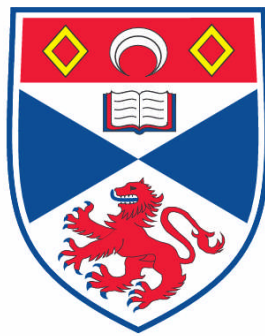


**WIDE ANGLE SEARCH FOR EXTRASOLAR PLANETS BY THE
TRANSIT METHOD**

Khalid Alsubai

**A Thesis Submitted for the Degree of PhD
at the
University of St. Andrews**



2008

**Full metadata for this item is available in the St Andrews
Digital Research Repository
at:**

<https://research-repository.st-andrews.ac.uk/>

Please use this identifier to cite or link to this item:

<http://hdl.handle.net/10023/521>

This item is protected by original copyright

**This item is licensed under a
[Creative Commons License](#)**

Wide Angle Search for Extrasolar planets by the Transit Method

Khalid Alsubai, Bsc, Msc
School of Physics and Astronomy
University of St Andrews

Submitted for the degree of Ph.D.

May 20, 2008

DECLARATION

I, Khalid Alsubai, hereby certify that this thesis, which is approximately 50000 words in length, has been written by me, that it is the record of work carried out by me and that it has not been submitted in any previous application for a higher degree. The English in this thesis has been corrected by professional proof readers for grammatical errors only.

Date Signature Of Candidate

I was admitted as a research student in January 2002 and as a candidate for the degree of Ph.D. in January 2002; the higher study for which this is a record was carried out in the University of St. Andrews between January 2002 and January 2008.

Date Signature Of Candidate

I hereby certify that the candidate has fulfilled the conditions of the Resolution and Regulations appropriate for the degree of Ph.D. in the University of St. Andrews and that the candidate is qualified to submit this thesis in application for that degree.

Date Signature Of Supervisor

In submitting this thesis to the University of St. Andrews I understand that I am giving permission for it to be made available for use in accordance with the regulations of the University Library for the time being in force, subject to any copyright vested in the work not being affected thereby. I also understand that the title and abstract will be published, and that a copy of the work may be made and supplied to any *bona fide* library or research worker.

Date Signature Of Candidate

ABSTRACT

The transit method is considered to be one of the most promising for discovering extrasolar planets. However, the method requires photometric precision of better than $\sim 1\%$. If we are able to achieve this kind of accuracy, then we are set to discover extrasolar planets. The uniqueness of my experiment will lead to the discovery of transiting planets around the brightest and most important stars quicker than the competitors in the field. The importance of the transit method stems from being able to supply many more planetary parameters than other methods which plays a crucial role in testing planet formation theories. This thesis is divided into eight chapters.

The first chapter provides a general background about transits and their theory. We discuss other methods of extrasolar planet detection, recent developments, future space missions, and what we have learned so far about properties of hot Jupiters. The second chapter details the theory of signals and noise on CCDs followed by the design of the PASS0 experiment. The third chapter reports on the difference imaging data pipeline that we developed and applied to a set of PASS0 data to search for transiting planets. The fourth chapter shows how we apply the PASS0 pipeline to SuperWASP data and improve on the accuracy obtained with their aperture photometry pipeline. The fifth chapter reports on the search for variable stars from the PASS0 and SuperWASP data sets that we consider in this thesis. In the sixth chapter we perform a transit search on the PASS0 and SuperWASP data sets and report the results. In the seventh chapter we use the PASS0 pipeline to process a full season of observing data from 2007 for two recent planet discoveries, WASP-7b and WASP-8b, that have not yet been announced. We analyse their lightcurves and predict their radii. Finally we conclude in the eighth chapter.

Contents

1	Extrasolar Planets	15
1.1	The Transit Method	15
1.2	Known Transiting Planets	19
1.2.1	HD 209458 b	19
1.2.2	Successful Ground-based Transit Search Experiments	19
1.2.3	Space-based Transit Search Experiments:	21
1.2.4	Using Transits to Determine Accurate Planet Radii	22
1.2.5	Using Transits to Detect and Characterise an Extrasolar Planet Atmosphere	22
1.3	The Radial Velocity Method	25
1.4	The Microlensing Method	26
1.5	Detection via Direct Imaging	27
1.6	The Pulsar Timing Method	28
1.7	The Formation of Hot Jupiters	29
1.8	Observed Properties of Extrasolar Planets	30
1.8.1	Planet Eccentricities	30
1.8.2	The Mass Function	32
1.8.3	Metal Rich Stars	33
2	Design of the PASS0 Experiment	37
2.1	Introduction	37
2.2	CCD Signal and Noise Modelling	37
2.2.1	Readout Noise	37
2.2.2	Bias Level	37
2.2.3	Bias Pattern	38
2.2.4	Dark Current	38
2.2.5	Photons	38
2.2.6	Pixel Noise	39
2.2.7	Measuring the CCD Gain	40
2.2.8	Signal-to-Noise Ratio	40
2.2.9	Lightcurve Noise	42
2.3	PASS: Permanent All Sky Survey	44
2.3.1	The Motivation and Ideas Behind PASS	44
2.3.2	PASS0: A Prototype PASS Experiment	45

2.3.3	Essential Considerations for Successful Non-Tracking Observations	51
2.3.4	Trailing and its Effect on Signal-To-Noise	55
2.3.5	Optimal Exposure Time for PASS0	57
2.3.6	Limitations due to Scintillation	58
2.3.7	A Theoretical Pass0 Noise Model	59
2.3.8	The Advantages of PASS0	60
2.3.9	The Disadvantages of PASS0	61
2.3.10	The First Pass0 Observation Run	61
3	PASS0 Data Reduction	63
3.1	The PASS0 Image Processing Pipeline	63
3.1.1	Stage 0: Preprocessing Calibrations	63
3.1.2	Stage 1: Reference Images and Astrometry	66
3.1.3	Stage 2: Image Subtraction	69
3.1.4	Stage 3: Measuring Difference Fluxes	71
3.1.5	Stage 4: Constructing the lightcurves:	72
3.2	Lightcurve Calibration	74
3.2.1	The String Method	77
3.2.2	PASSCAL	79
3.3	HD209458	83
4	Optimising SuperWASP Photometry	87
4.1	The SuperWASP Experiment	87
4.2	SuperWASP Observations and Reductions	87
4.3	Application of the PASS0 Pipeline	89
4.3.1	Adapting the PASS0 Pipeline	89
4.3.2	Comparing the Gaussian Preconvolution Tests	94
4.3.3	Testing the PASS0 Pipeline on Fake Image Data	98
4.3.4	Sub-Pixel Phase Map	101
4.3.5	Choosing the Best Gaussian Preconvolution	101
4.3.6	Image Subtraction Residuals	102
4.3.7	Further Lightcurve Calibration	103
4.4	Comparing the PASS0 and SuperWASP Pipeline Results	107
4.4.1	Comparing RMS Diagrams	107
4.4.2	Comparing the Lightcurves of XO-1	109
5	Variable Candidates	113
5.1	Introduction	113
5.2	Variables in the PASS0 Lightcurve Data	113
5.2.1	Identifying Variable Stars	113
5.2.2	Determining the Period of the Variable Stars	116
5.3	Variables in the SuperWASP Lightcurve Data	118
5.4	Conclusions	119

6	Transit Candidates	131
6.1	Introduction	131
6.2	Transit Search Algorithms	131
6.3	Transit Candidates in the PASS0 Lightcurve Data	132
6.4	Transit Candidates in the SuperWASP Lightcurve Data	141
6.5	Conclusions	143
7	WASP-7b and WASP-8b	147
7.1	Introduction	147
7.2	Reductions	147
7.3	Comparing the Lightcurves from the PASS0 and SuperWASP Pipelines	152
7.4	Fitting the Lightcurves from the PASS0 and SuperWASP Pipelines	161
7.5	Conclusions	162
8	Summary	163
A	Relation between Gaussian Sigma and FWHM	167
B	Number of Effective Pixels of a Gaussian PSF	169
C	Useful Equations	171

List of Tables

2.1	PASS0 CCD And Lens Evaluation	48
2.2	PASS0 And SWASP Star Counts	49
4.1	Gaussian convolution kernels	94
4.2	Final RMS Diagram Fits	107
5.1	PASS0 Variable Star Properties	124
5.2	PASS0 Variable Star Properties	125
5.3	SuperWASP Variable Star Properties	130
7.1	Pipeline Comparison for WASP-7b	151
7.2	Pipeline Comparison for WASP-8b	151
7.3	Fitted Planet Parameters for WASP-7b and WASP-8b	160

List of Figures

1.1	Geometry Of A Transit	16
1.2	Transit Of HD209458	17
1.3	Transit Duration	18
1.4	Transits Of HD209458 In Different Bandpasses	23
1.5	Phased Infrared Planet Flux	24
1.6	Radial Velocity Curve Of HD209458	25
1.7	Microlens Diagram	27
1.8	OGLE-05-390Lb	28
1.9	Eccentricity Against Orbital Size	30
1.10	Planet Mass Against Eccentricity	31
1.11	Eccentricity Against Period	32
1.12	Planet Mass and Period Histogram	33
1.13	Planet Mass Against Orbital Size	34
1.14	Planet Distribution As A Function Of Metallicity	36
2.1	Theoretical Signal-To-Noise Versus Exposure Time	41
2.2	PASS Design Concept	44
2.3	The PASS0 Camera In Tenerife	50
2.4	PASS0 Vignetting	52
2.5	PASS0 Sample Images And PSF	53
2.6	Example Trailing Apertures	54
2.7	S/N For A Single Trailed Observations	56
2.8	Total S/N For Many Trailed Observations	57
2.9	PASS0 Optimal Exposure Time	58
2.10	Scintillation Noise	59
2.11	PASS0 Theoretical RMS Diagram	60
3.1	The PASS0 PSF	64
3.2	FWHM and Sky Trends for PASS0 Data	65
3.3	DAOPhot Roundness Versus PASS0 y Pixel Coordinate	67
3.4	Star Trails On PASS0	68
3.5	Illustration Of Triangle Matching	70
3.6	PASS0 Difference Imaging Residuals	73

3.7	PASS0 Pipeline Flow Chart	75
3.8	PASS0 Lightcurve Calibrations With The String Method	76
3.9	RMS Diagrams For PASS0 Data	78
3.10	PASSCAL Patterns For PASS0 Lightcurves	81
3.11	PASS0 Lightcurve Calibrations With PASSCAL	82
3.12	Phased Lightcurves Of HD209458	85
4.1	Blending Characterisation In SuperWASP	88
4.2	The SuperWASP PSF	90
4.3	SuperWASP Difference Image Subregion	91
4.4	SuperWASP Difference Image	92
4.5	RMS Diagram For Different Blur Tests	95
4.6	Noise Parameters Versus Gaussian FWHM	96
4.7	RMS Scatter Versus Gaussian FWHM	97
4.8	Recovered Reference Fluxes From Fake Image Data	99
4.9	Recovered Difference Fluxes From Fake Image Data	100
4.10	SuperWASP Sub-Pixel Phase Maps	102
4.11	SuperWASP Difference Image Residuals	104
4.12	Tamuz Coefficients	105
4.13	RMS Diagrams For SuperWASP Data	108
4.14	Comparing Final Accuracy Results	109
4.15	Lightcurves Of XO-1	111
4.16	Phased Lightcurves Of XO-1	112
5.1	Histogram of the Number of Epochs in the PASS0 Lightcurves	114
5.2	RMS Diagram to Identify Variable Stars in the PASS0 Data	115
5.3	Normalised Cumulative Histogram of Lightcurve RMS	116
5.4	Example PASS0 Lightcurve Periodograms	117
5.5	Unphased PASS0 Variable Star Lightcurves	120
5.6	Unphased PASS0 Variable Star Lightcurves	121
5.7	Phased PASS0 Variable Star Lightcurves	122
5.8	Phased PASS0 Variable Star Lightcurves	123
5.9	RMS Diagram to Identify Variable Stars in the SuperWASP Data	126
5.10	Normalised Cumulative Histogram of Lightcurve RMS	127
5.11	Unphased SuperWASP Variable Star Lightcurves	128
5.12	Phased SuperWASP Variable Star Lightcurves	129
6.1	AoVtr Statistic Versus Magnitude For $N_H = 15$	133
6.2	AoVtr Statistic Versus Magnitude For $N_H = 30$	134
6.3	Transit Candidates for $N_H = 15$	137
6.4	Transit Candidates for $N_H = 30$	138
6.5	AoVtr Statistic Versus Magnitude For $N_H = 15$	139
6.6	AoVtr Statistic Versus Magnitude For $N_H = 30$	140
6.7	Transit Candidates from K07	142

6.8	Transit Candidates for $N_H = 15$	145
6.9	Transit Candidates for $N_H = 30$	146
7.1	RMS Diagrams for WASP-7b	149
7.2	RMS Diagrams for WASP-8b	150
7.3	Unfiltered Lightcurve for WASP-7b	154
7.4	Unfiltered Lightcurve for WASP-8b	155
7.5	Lightcurve Correlations for WASP-7b	156
7.6	Lightcurve Correlations for WASP-8b	157
7.7	Lightcurve for WASP-7b	158
7.8	Lightcurve for WASP-8b	159

Chapter 1

Transit Detection And Observed Properties Of Extrasolar Planets

The prime experiment that we report in this thesis is based on the aim of detecting extrasolar planets using the transit method. However, there are many available methods to detect extrasolar planets and a number of them have already had success in planet detections, some being more successful to date than others. In the introduction to the thesis we discuss in relative detail only the transit method (central to the thesis), the radial velocity method (the most successful method to date) and the microlensing method (which is starting to yield planets). Some other methods are not mentioned but the list is not complete since the aim of this thesis is not to review the whole field of extrasolar planets.

1.1 The Transit Method

When a planet passes in front of its parent star it blocks part of the star flux. To observe such a phenomenon from another star system at a great distance from the planet, the observer has to be within a very restricted region of space. Therefore any planet around a star does not necessarily transit its host and we will only observe a small fraction of planets as transiting planets. The decrease in luminosity of the host star when the planet transits is also of the order of $\sim 1\%$ for a Jupiter-sized planet around a solar-type star which requires high photometric precision observations carried out during and after the transit event.

In the following analysis of the transit phenomena we will assume that planetary orbits are circular and that the surface brightness, mass, and radius of the planet are small compared to that of the parent star. We will also assume that the orbital radius is much larger than the size of the parent star itself.

A planet with radius R_P orbits a star of radius R_* and mass M_* at an orbital radius a . A transit of the stellar disk will be seen by an observer only if the orbital plane is at the correct inclination to the line of sight (see Figure 1.1). Mathematically the inclination i must satisfy the following:

$$a \cos i \leq R_* + R_P \tag{1.1}$$

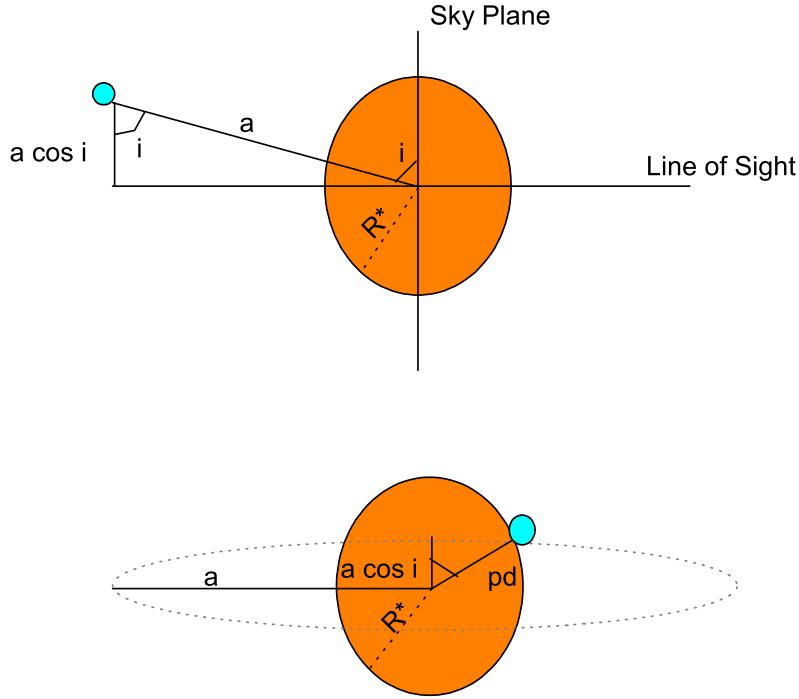


Figure 1.1: The geometry of a transit event of inclination i and orbital radius a as seen from the side (top) and from the observer's point of view (bottom) at a moment when the planet lies at a projected distance $d(t)$ from the star centre.

Since $\cos i$ is the projection of the vector perpendicular to the orbital plane onto the hemisphere of the sky and this is distributed uniformly over the surface of the sky hemisphere, it is equally likely to take on any random value between 0 and 1. Therefore, for a set of planetary systems with arbitrary orientation with respect to the observer [69], the probability that the inclination satisfies the necessary geometry for a transit is given by:

$$\text{Geometric Transit Probability} = \frac{\int_0^{(R_*+R_P)/a} d(\cos i)}{\int_0^1 d(\cos i)} = \frac{R_* + R_P}{a} \approx \frac{R_*}{a} \quad (1.2)$$

The photometric depth of a transiting planet is determined by the fraction of the light from the star that is eclipsed. Assuming that the flux from the star is F before or after the transit, and that the planet creates a change in flux of ΔF , then the ratio of ΔF to F can be calculated by considering the ratio of the area of the planetary disk to that of the stellar disk as follows:

$$\frac{\Delta F}{F} = \left(\frac{R_P}{R_*} \right)^2 \quad (1.3)$$

Planet Transit of HD209458

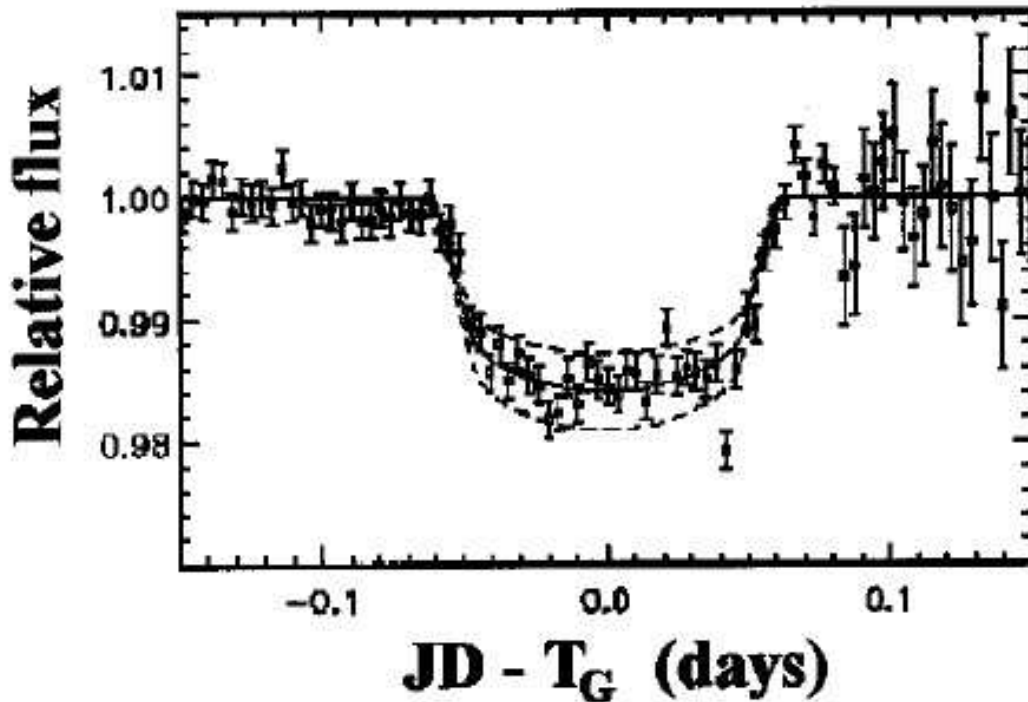


Figure 1.2: The transit lightcurve of HD209458b, taken from Charbonneau et al. 2000 [14].

This equation ignores the effect of limb darkening, and shows that the luminosity of the host star during transit is reduced by the square of the ratio of planet to star radius.

Figure 1.2 shows an typical transit lightcurve. In fact it is the discovery lightcurve for the first known transiting planet taken from Charbonneau et al. 2000 [14]. The period P of the transiting planet can be determined very simply by observing two or more consecutive transits and the period is then simply the time between the transits. The transit itself yields the duration of the event or it can be derived using the theory presented in Figure 1.3. This figure shows that the planet subtends an angle of 2θ radians during a transit, out of the angle of 2π radians that it subtends during a full orbit. The duration of a transit t_T is therefore given by:

$$t_T = \frac{P\theta}{\pi} \quad (1.4)$$

From Figure 1.3(b) the height of the centre of the transit from the centre of the star (also called

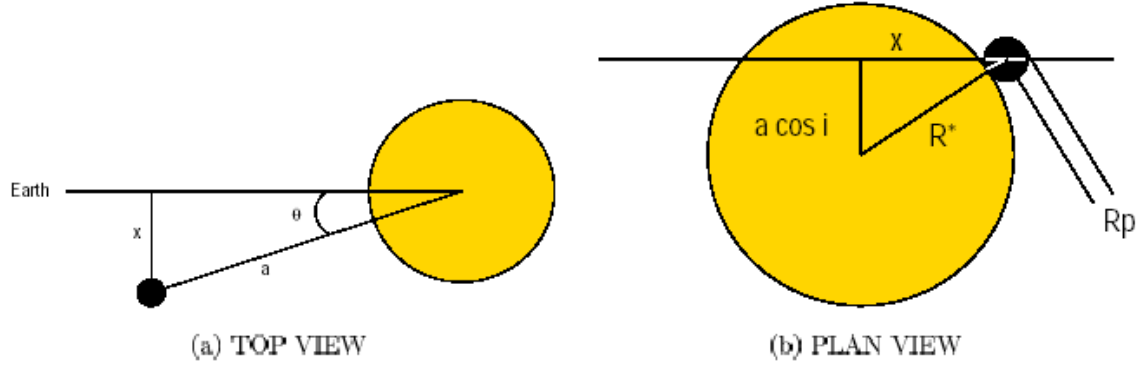


Figure 1.3: The transit duration is set by the fraction of the total orbit (left) for which a portion of the planet eclipses the stellar disk (right).

the impact parameter) is $a \cos i$ and we may solve for the distance x using the Pythagorean rule:

$$x^2 = (R_* + R_p)^2 - (a \cos i)^2 \quad (1.5)$$

Then from Figure 1.3(a) we can calculate θ using simple trigonometry as:

$$\theta = \arcsin \left(\frac{\sqrt{(R_* + R_p)^2 - (a \cos i)^2}}{a} \right) \quad (1.6)$$

Rewriting the equation for transit duration (Equation 1.4) using Equation 1.6 and assuming that θ is a small angle such that $\sin \theta \approx \theta$, then we get:

$$t_T = \frac{P \sqrt{(R_* + R_p)^2 - (a \cos i)^2}}{\pi a} \quad (1.7)$$

For the situation that $a \gg R_* \gg R_p$, which is generally true, Equation 1.7 becomes:

$$t_T = \frac{P}{\pi} \sqrt{\left(\frac{R_*}{a}\right)^2 - \cos^2 i} \leq \frac{PR_*}{\pi a} \quad (1.8)$$

We can get the mass of the host star M_* from spectroscopy to determine the spectral type and then use the mass-radius relation for (Sun-like) main sequence stars to get the star radius R_* . It is known that this relationship is given by the approximation:

$$R_* = f(M_*) \approx M_* \frac{R_\odot}{M_\odot} \quad (1.9)$$

With the star mass and radius we can then calculate the orbital radius of the planet using Kepler's law:

$$P^2 = \frac{4\pi^2 a^3}{GM_*} \quad (1.10)$$

The above equations are what are needed to analyse the lightcurve of a transiting planet and can be used to obtain interesting properties like the planet radius and orbital period. The inclination of the orbit of a transiting planet can be obtained from the lightcurve which is very important when combined with the detection of radial velocity variations since it leads to a real estimate of the planet mass, not just a minimum mass estimate (see Section 1.3).

1.2 Known Transiting Planets: HD 209458 b and Others

1.2.1 HD 209458 b

On November 12th 1999, a team led by G. W. Henry, G. Marcy, R. P. Butler and S. S. Vogt, announced the discovery of the first transiting planet around the star HD209458 (IAU Circular 7307). In fact the discovered planet had been observed previously by Brown, T and Charbonneau, D. between the 9th to 16th of September 1999 through the STARE project. HD209458 is at 47 parsecs from the Sun in the constellation of Pegasus, and it is very similar to our Sun since it has almost the same mass at $\sim 1.05 M_{\odot}$ and spectral type G0V. The apparent magnitude of the star is 7.65.

The planet was first detected by measuring the radial velocity variations of the star using the Keck telescope. The sinusoidal periodicity in the velocity versus time curve with amplitude ~ 81 m/s indicated the presence of a planet. Fits to the curve implied that the mass of the planet is $\sim 0.62 M_{\text{JUP}}$ at an orbital distance of ~ 0.046 AU (IAU Circular 7307). Photometric observations were carried out at the times of transit predicted from the radial velocity data. These observations reveal a magnitude dip of ~ 0.02 mag (or approximately 2%). Both Henry et al. 2000 [32] and Charbonneau et al. 2000 [14] can claim this first detection of a transiting planet, although the Charbonneau et al. data set is much more convincing and reliable since they observed two full transits whereas Henry et al. only observed the start of one transit.

These data allowed the teams to derive a planetary radius of $1.42 R_{\text{JUP}}$, and orbital inclination $\sin i > 0.993$. The actual mass of the planet was therefore calculated to be $\sim 0.62 M_{\text{JUP}}$.

Knowing the mass and radius of the planet we can calculate the density and we get $\sim 0.27 \text{ g/m}^3$; this classifies it as a gas giant. The interesting fact is that despite having a mass of only $\sim 62\%$ that of Jupiter, the radius is $\sim 60\%$ larger than that of Jupiter. This agrees perfectly with theories that anticipated a bloated planet at this close distance to the host star [28].

1.2.2 Successful Ground-based Transit Search Experiments

An up to date list of extrasolar planets is kept at “The Extrasolar Planets Encyclopedia” maintained by J.P. Schneider [102]. The web address for this very valuable resource is <http://exoplanet.eu/>.

OGLE

The Optical Gravitational Lensing Experiment (OGLE; [88]) uses the 1.3 m Warsaw telescope located at Las Campanas Observatory in Chile. The telescope has an imaging camera with a $4\text{K} \times 4\text{K}$ CCD, and their configuration of the telescope and CCD gives a $35' \times 35'$ field of view (FOV). The main aim of the experiment is to actually detect planets from small deviations in

standard microlensing events, but also the data is useful for searching for variables and transiting planets because each field is visited a few and/or many times during one night over many years of observing seasons. In the first few years of the survey, many transit candidates were announced [89] but after a while it became clear that a large fraction of these are systems that have lightcurves mimicking a transiting planet (e.g. [86]). However, as of November 2007, OGLE has led to the discovery of 7 transiting extrasolar planets close to the Galactic plane (see the website at <http://www.astrouw.edu.pl/~ogle/>).

HAT

The Hungarian Automated Telescope Network (HATNet; [5]) uses a $2K \times 2K$ CCD with a 11 cm diameter commercial lens. The FOV is 8×8 square degrees. There are 3 instruments located around the Earth, one at the Fred Lawrence Whipple Observatory (FLWO) in the US, one at the Mauna Kea observatory in Hawaii, and one at the WISE observatory in Israel. As of November 2007, the HAT network has discovered 6 extrasolar planets transiting their parent stars (see the website at <http://www.cfa.harvard.edu/~gbakos/HAT>).

SuperWASP

The acronym WASP stands for Wide Angle Search for Planets consortium [79] and it has a very similar concept as that of HAT. The cameras use a similar lens (also commercial) but with a better quality CCD. Currently there are two SuperWASP sites and at each site there are 8 cameras mounted on a single robotic equatorial mount. Each camera has a field of view of 7.8×7.8 square degrees. More details about the SuperWASP experiment and the prototype experiment WASP0 are described at the beginning of Chapter 4. As of November 2007, SuperWASP has discovered 5 extrasolar planets (see the website at <http://www.superwasp.org/>).

TRES

TRES stands for the Trans-Atlantic Exoplanet Survey [4] and the experiment consists of a network of three small-aperture telescopes searching the sky for transiting planets (Sleuth at the Palomar Observatory, Southern California, USA; PSST at the Lowell Observatory, Northern Arizona, USA; STARE at the Teide Observatory, Canary Islands in Spain). The small telescopes have an $f/2.8$ lens with a 10 cm aperture that has a field of view of 6×6 degrees coupled with a 2048×2048 back-illuminated CCD. As of November 2007, TRES has discovered 3 planets (see the website at <http://www.astro.caltech.edu/~ftod/tres/tres.html>).

XO

The XO experiment [50] is similar to HAT and Superwasp in the kind of lens they are using. However, they use 2 cameras with $1K \times 1K$ pixel CCDs, so that the FOV is about 7.2×7.2 square degrees. The experiment is located on the summit of Haleakala on Maui, Hawaii and started observing in September of 2003. The observational technique is different to other surveys in that the CCD uses a drift scan mode where the CCD is continuously read out at the sidereal

rate removing the need for tracking of observations. As of November 2007, XO has discovered 3 planets (see the website at <http://www-int.stsci.edu/~pmcc/xo/>).

1.2.3 Space-based Transit Search Experiments:

SWEEPS

The acronym SWEEPS stands for the Sagittarius Window Eclipsing Extrasolar Planet Search. This team uses the Hubble Space Telescope (HST) to search for transiting planets towards the centre of the Milky Way. This experiment has proved that extrasolar planets can exist anywhere in the Galaxy [70]. However spectroscopic confirmation of the transit candidates via radial velocity measurements is a difficult challenge because the faintness of the stars puts them beyond even some of the largest ground-based telescopes. As of November 2007, SWEEPS has discovered 2 transiting planets (see the website at http://www.nasa.gov/mission_pages/hubble/exoplanet_transit.html).

The COROT Mission

The COROT space mission has two objectives:

- Stellar seismology, or the detection and measurement of stellar vibrations.
- The search for planets around stars other than the Sun.

Both objectives require the same technique of very high precision stellar photometry (one hundred times better than that which can be achieved from the best observatories on Earth), and continuous observations of the same part of the sky over very long periods (at least 150 days). This is impossible from the Earth, since the Earth's orbital motion around the Sun only allows us to observe the same part of the sky for 6 to 8 months. . . and only at night (except at the poles)!

By creating an observing program that consists of observing, in a systematic way, many fields of 12000 stars, it has been estimated that about one hundred hot Jupiter planetary systems can be detected, along with a few dozen small/terrestrial planets. The first extrasolar planet detection from COROT was in May of 2007. The planet was named COROT-Exo-1b [101] with an orbital period of ~ 1.5 d indicating that it is a very hot Jupiter (since it also has a radius of 1.78 times that of Jupiter). The host star is a main sequence star very similar to our Sun. COROT-Exo-1b is the only planet discovered by the COROT mission as of November 2007 (see the website at <http://smc.cnes.fr/COROT/>).

The Kepler Mission

The Kepler Mission is specifically designed to survey the extended solar neighborhood to detect and characterize hundreds of terrestrial and larger planets in or near the habitable zone, and provide fundamental progress in our understanding of planetary systems. The results will yield a broad understanding of planetary formation, the frequency of formation, the structure of individual planetary systems and the generic characteristics of stars with terrestrial planets.

The scientific goal of the Kepler Mission is achieved by surveying a large sample of dwarf (main-sequence) stars to:-

- Determine the frequency of terrestrial and larger planets in or near the habitable zone; distributions of planet sizes, semi-major axis, albedo, size, mass, and density of short-period giant planets.
- Determine the properties of those stars that harbor planetary systems.

Kepler is predicted to be able to measure stellar flux with a fractional precision of the order of 10^{-5} over the typical transit duration for terrestrial planets (~ 13 hours). The mission will use a differential photometer to continuously monitor the brightness of $\sim 10^5$ dwarf stars for up to 4 years, and hence it is expected to generally see ~ 4 transits of a terrestrial planet in the habitable zone of a Sun-like star (since observations are not interrupted by the day-night and seasonal cycle). The launch of the mission is scheduled for the beginning of 2009 (see the website at <http://kepler.nasa.gov/>).

1.2.4 Using Transits to Determine Accurate Planet Radii

Recently Knutson et al. 2007 [41] gathered 1066 spectra over four distinct transits of HD209458 with the STIS spectrometer on the Hubble Space Telescope with synthesised multiple-bandpass photometry (see Figure 1.4). Assuming the stellar mass-radius relation from Cody & Sasselov 2002 [18], and theoretical models for limb darkening to significantly improve the estimates of the radius and orbital inclination of HD 209458b, they find that the radius of HD 209458b is $1.320 \pm 0.025 R_{\text{JUP}}$ which is a factor of two more precise than previous measurements. Knutson et al. 2007 find a density for the planet of $0.345 \pm 0.05 \text{ g/cm}^3$. The planet's inclination is found to be $86.929^\circ \pm 0.010^\circ$, a factor of three more precise than previous measurements.

The above example is a good illustration of how the transit method can be used to measure accurate planetary radii. From these measurements the planet mass-radius relationship can be accurately explored which is necessary in order to carefully investigate various planet formation scenarios.

1.2.5 Using Transits to Detect and Characterise an Extrasolar Planet Atmosphere

One of the aims of studying extrasolar planets is to learn about the composition of the planet and its atmosphere. By studying the absorption-line spectra of the star during and out of transit, it is possible to construct the absorption line spectra of the planet [12]. This method has been used to detect elements such as C, O and Na in the atmosphere of HD209458 [15] and to learn that HD209458 is losing elements from its atmosphere as it is blown away due to the planet's proximity to its host star [93]. There is even some evidence that the atmosphere of the planet takes the shape of a comet. For instance, Vidal-Madjar et al. 2003 [92] found that the depth of the transit is $\sim 15\%$ if the transit is observed at the wavelength of the Lyman α transition of the hydrogen atom (compared to the $\sim 1.5\%$ dip in visible light). This means that the hydrogen of the planet extends out past the Roche limit and the planet must therefore be losing its atmosphere.

Related to the idea of trying to detect an extrasolar planet atmosphere is the recent detection by the Spitzer Space Telescope of the secondary eclipse of HD209458 [21]. The secondary eclipse in this case is the obscuration of the planet by the star. Since this extrasolar planet is so close to its parent star, it is expected to be very hot and the secondary eclipse is therefore much deeper in

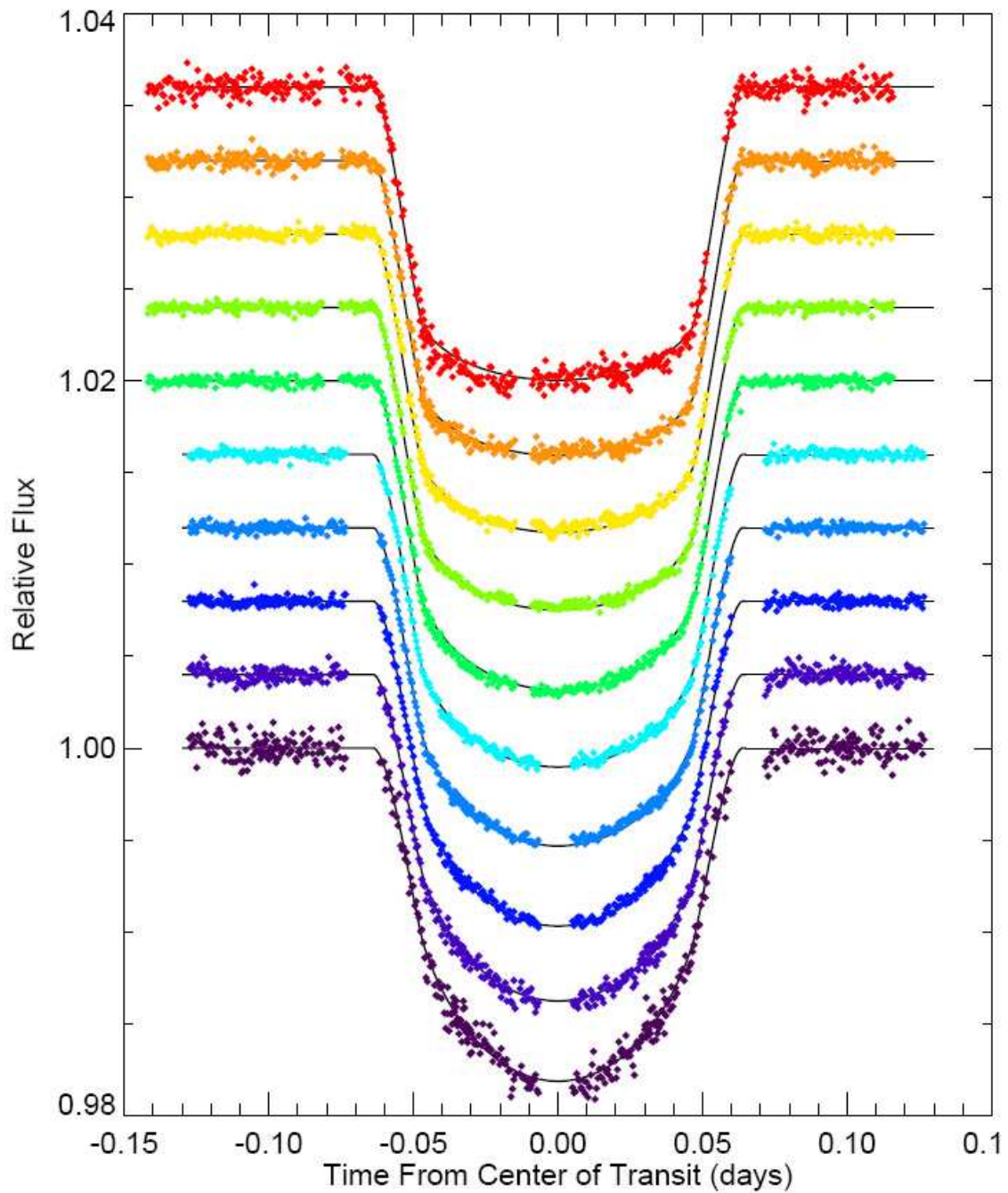


Figure 1.4: Normalized data for the transit curves of HD209458 observed by Knutson et al. 2007 in ten bandpasses. Theoretical fitted transit curves are overplotted. Each bandpass contains data from two separate observation visits from HST. Each successive transit curve is offset by 0.004.

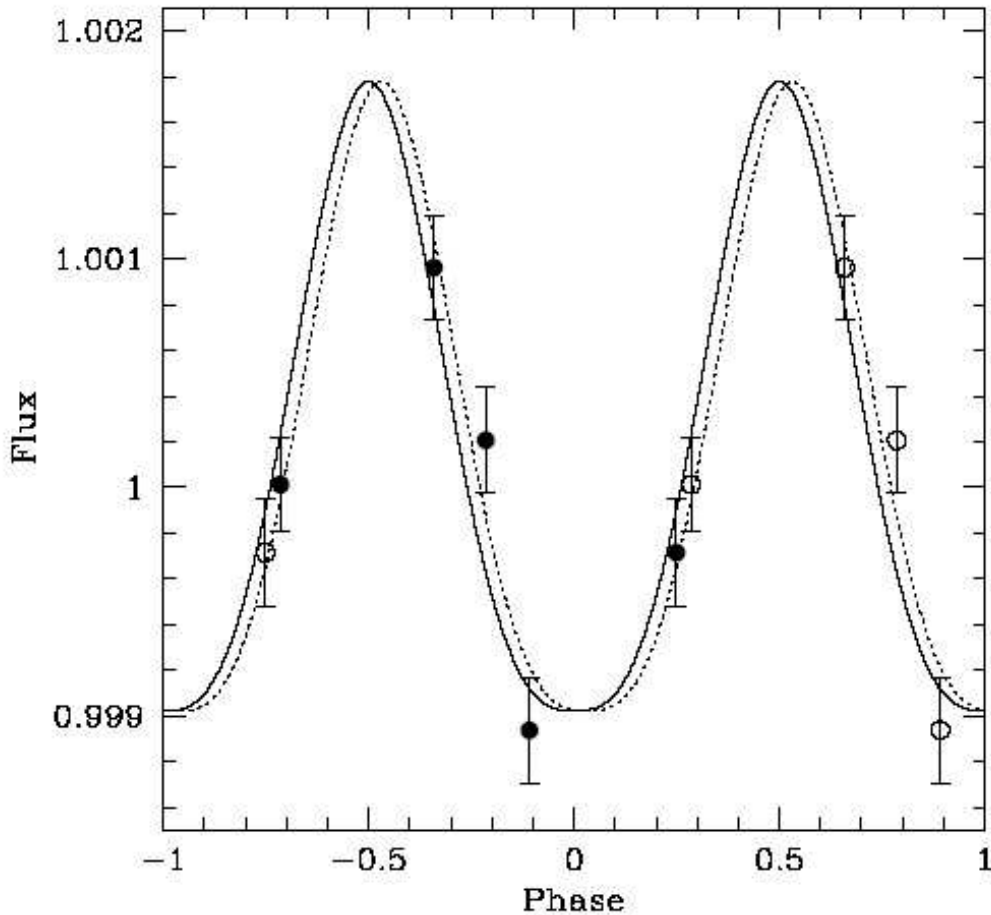


Figure 1.5: The normalised infrared flux of ν Andromeda b as a function of orbital phase [30].

the infrared than in the visible, which is what has led to its successful detection. The planet's infrared flux confirms its hot temperature at ~ 1150 K.

The star ν Andromeda is orbited by three known planets, the innermost of which has an orbital period of 4.617 days. Again infrared observations with the Spitzer Space Telescope have detected the emission from the hot atmosphere and it was found that the emission varies with the phase of the planet [30]. This indicates that there is a large temperature difference between the day and night side of the planet. Figure 1.5 shows the normalised variation in infrared flux of the planet as a function of phase.

Finally we would like to mention the important discovery of water vapour in the atmosphere of the hot Jupiter HD189733b while it was transiting its parent star [83]. The analysis by Tinetti et al. 2007 of Spitzer observations shows that absorption by water vapour is the most likely cause of the wavelength-dependent variations in the effective radius of the planet at the infrared wavelengths $3.6 \mu\text{m}$, $5.8 \mu\text{m}$ and $8 \mu\text{m}$.

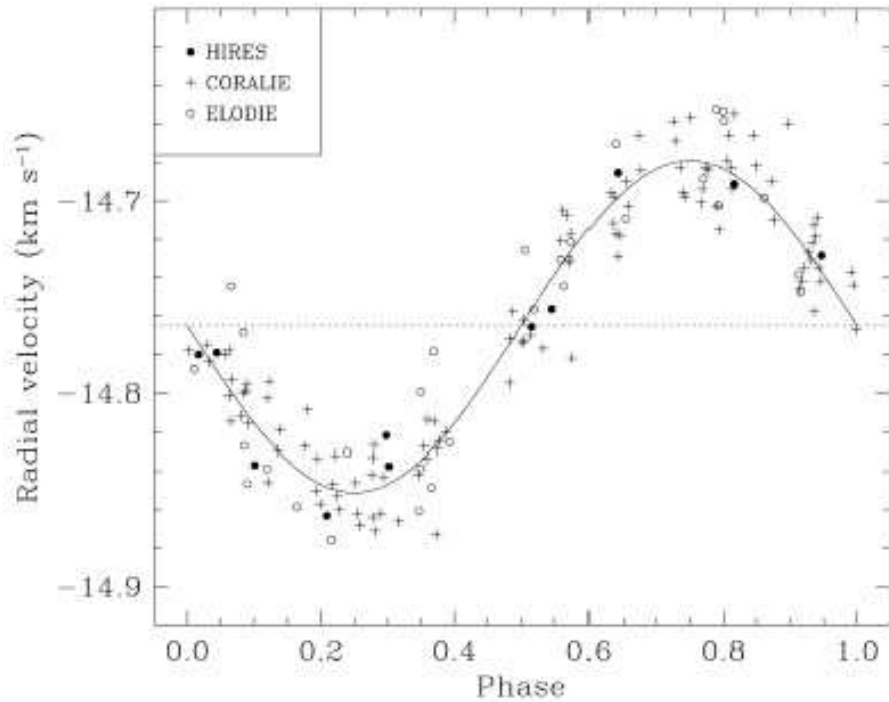


Figure 1.6: The radial velocity curve of HD209458 taken from Mazeh et al. 2000 [49]

1.3 The Radial Velocity Method

The majority of the known extrasolar planets around main sequence stars have been discovered by the radial velocity method. The method is based on the fact that an orbiting planet perturbs the host star in such a way that the star also orbits the combined centre of mass of the system. The motion of the star creates a Doppler shift in the spectral lines of the star which shifts the lines towards the red when the star is moving away from the observer and shifts the lines towards the blue when the star is moving towards the observer. Since the planetary motion is periodic then so is this Doppler shift.

By observing spectra of the host star over the course of an orbital period, we can measure the radial velocity of the star at various orbital phases from the Doppler shift of the spectral lines relative to some reference lines at rest on the Earth. The radial velocity curve will then look similar to that shown in Figure 1.6 which is taken from a follow-up paper on the discovery of HD209458b by Mazeh et al. 2000 [49]. From the radial velocity curve we can calculate the radial velocity semi-amplitude K of the star which is related to the star mass M_* , planet mass M_p , inclination i , period P and eccentricity e by the equation:

$$K = \left(\frac{2\pi G}{P} \right)^{1/3} \frac{M_p \sin i}{(M_p + M_*)^{2/3}} \frac{1}{(1 - e^2)^{1/2}} \quad (1.11)$$

We may also determine P from the radial velocity curve, and the star mass M_* can be estimated from determining the spectral type of the host star from the radial velocity spectra.

Also, if we assume a circular orbit ($e = 0$) and that $M_P \ll M_*$ then Equation 1.11 reduces to:

$$K = 28.4 \left(\frac{P}{1 \text{ year}} \right)^{-1/3} \left(\frac{M_P \sin i}{M_{\text{JUP}}} \right) \left(\frac{M_*}{M_{\odot}} \right)^{-2/3} \text{ m s}^{-1} \quad (1.12)$$

Measuring K allows us to calculate the minimum planet mass $M_P \sin i$ and Kepler's third law in Equation 1.10 can be used to determine the orbital radius a of the planet. We refer to $M_P \sin i$ as the *minimum* planet mass since $\sin i$ can only take values between 0 and 1 for inclinations between 0° and 90° which implies that $M_P \sin i$ is always smaller than M_P . Note that in the case of a planet with an eccentric orbit, the eccentricity can be determined from the shape of the radial velocity curve by fitting the correct model to the data.

We consider the example of Jupiter orbiting the Sun. This causes a $K = 12.5 \text{ ms}^{-1}$ semi-amplitude radial velocity with a period of 11.9 years. In the case of Earth orbiting the Sun, K is about 0.1 ms^{-1} . Our current limit on radial velocity accuracy is about $K = 3 \text{ ms}^{-1}$ so Jupiter is certainly detectable if we observe for long enough, but Earth is not detectable by this method.

Limitations of the radial velocity method include the fact that if the orbital systems that we observe are seen face on ($i = 0$) then there is no radial oscillation, and since high signal-to-noise (S/N) spectra are required to make the radial velocity measurements, observations are limited to bright stars typically brighter than 9th magnitude in the visible. Equation 1.12 shows that radial velocity measurements favour the detection of systems with massive planets, less massive stars and short periods.

1.4 The Microlensing Method

If two stars are correctly aligned with the Earth, where the first is in the background (the source star) while the second is in the foreground (the lens star), then the intervening lens star will gravitationally bend the light of the more distant source star (see Figure 1.7). An observer of this situation will see the source star in a magnified state. Since both stars will be moving relative to each other and the observer, the magnification of the source star is constantly changing and will reach a peak at the position of closest alignment. In fact the source star will show a typical symmetrical lightcurve of magnification and demagnification through a peak.

In our Galaxy, source stars tend to be in the Galactic bulge and lens stars somewhere in between, and the geometry of the events is such that both stars are aligned within the size of the point spread function (PSF) of a ground based observation. Therefore, from the ground, both the lens and the source star appear as one point source, and these events are termed "microlenses". When the lens star has an accompanying planet that also passes close to the line of sight between the source star and the observer, there is another magnification event due to the planet. This event appears as a deviation in the standard microlens lightcurve, and the deviation lasts up to a couple of days for Jupiter-mass planets and a few hours for Earth mass planets. The great potential of this method is in detecting Earth mass planets because the microlens lightcurve deviation size has the potential to be infinite no matter what the mass of the planet.

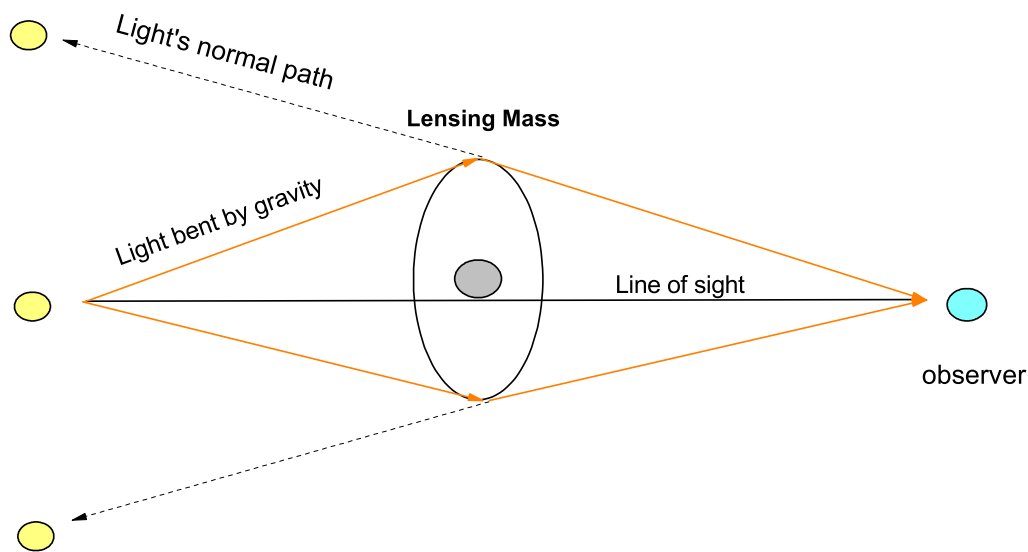


Figure 1.7: Diagram showing the bending of light towards an observer by an intervening massive object. The massive object acts like a lens for the light from the distant source.

As of November 2007, only four planets have been detected by the microlensing method, three of which have masses in the range of gas giants [8],[90],[27]. The real potential of the microlensing method was demonstrated in 2006 with the publication of a very low mass planet near the habitable zone of its parent star [6]. The best fit planet model has a planet mass of $5.5 M_{\text{EARTH}}$ at ~ 2.6 AU from the host M star. This planet is calculated to have a temperature of ~ 50 K which, combined with its mass estimate, makes it most likely to be a frozen super-Earth (rocky planet). The lightcurve of the discovery microlens lightcurve is presented in Figure 1.8 and it shows the standard microlens lightcurve with a zoom on the detected planetary deviation (taken from [22]).

1.5 Detection via Direct Imaging

This method is the most direct way of detecting an extrasolar planet since with this method you are looking to detect photons reflected directly from the planet surface, rather than trying to detect some indirect signal showing the presence of a planet. However, since the star outshines a planet in brightness by billions of times in the optical wavelengths because a planet only reflects light, the imaging of a planet close to such a bright source is very difficult.

In the infrared the contrast between the star and planet luminosities is less at around a million. Using coronagraphs to block out the star's light and adaptive optics to improve resolution has

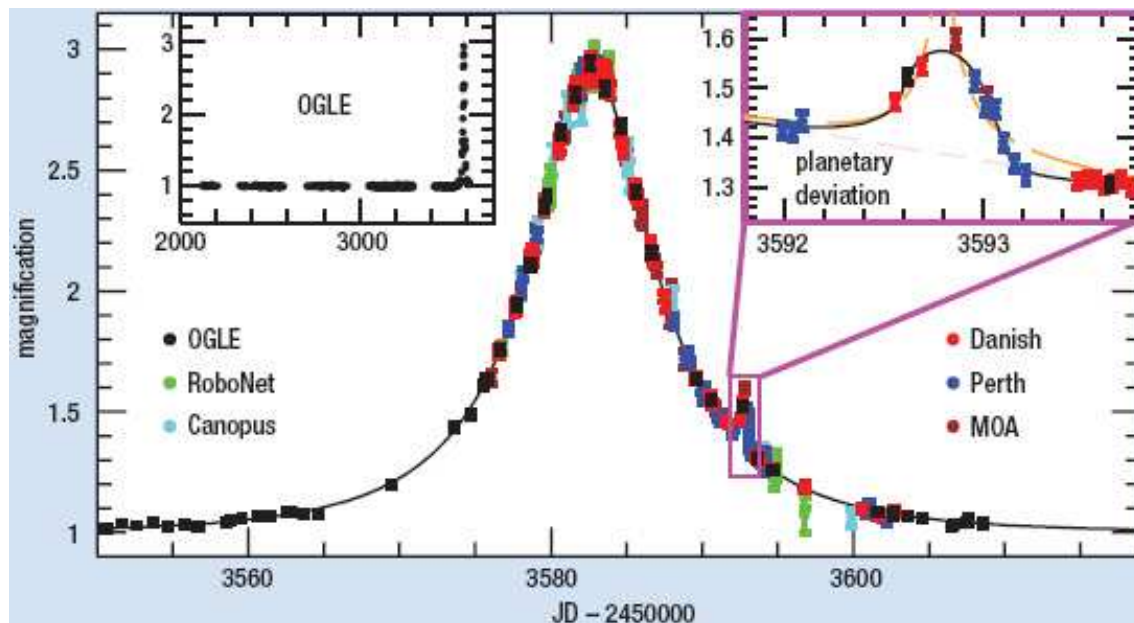


Figure 1.8: The microlens lightcurve that lead to the discovery of the ~ 5.5 Earth mass extrasolar planet OGLE-05-390Lb, taken from [22].

lead to the first detection of an exoplanet [16]. The planet orbits the brown dwarf 2M1207 in the constellation of Taurus. In 2005, GQ Lup b was the second exoplanet to be discovered by the direct detection imaging method [57] and in the same year the third planet discovered by this method was AB Pic b [17]. As of November 2007, there are four known planets detected by direct imaging [7].

1.6 The Pulsar Timing Method

Despite the success of other methods in detecting extrasolar planets, the pulsar timing method deserves a mention because it lead to the first detection of an extrasolar planet, which happened in 1992 by Wolszczan A. & Frail D [96] who used this method to discover planets around a pulsar. A pulsar emits radio beams of radiation as it spins rapidly. If this beam passes through the line of sight during the pulsar rotation period, then the Earth observer receives a brief radio pulse repeated at the period of the pulsar spin. Pulsars can have periods from 10 ms to 10 s and the pulses are very regular. The movement of the pulsar due to an orbiting companion can be detected by the delays caused in the reception of the radio pulses and the sensitivity can reach down to planet masses smaller than that of the Earth. The disadvantage of the method is that the number of known pulsars is very small due to the fact that very few are aligned correctly to be beaming at the Earth. As of November 2007, there are 5 known planets detected using this method.

1.7 The Formation of Hot Jupiters

Standard planet formation theory (e.g. [63], [10], [45]) predicts that giant planets like Jupiter and Saturn should be formed at distances of 3 to 5 AU from the host star (for Sun-like stars). This is because the accretion process for giant planets requires core accretion involving ice grains. At distances closer than ~ 4 AU the ice grains cannot form because the temperature is too high due to the proximity of the host star. In the interior part of the accretion disk only dust and silicates can accrete to form planets. Gas is blown out of the inner parts by the strong stellar wind from the young star. Further out in the accretion disk gas can be accreted by the protoplanets because of the weaker stellar wind and the higher mass of the accretion cores. Hence the theory predicts that gas giants should form beyond the inner parts of the system.

However the existence of short-period giant planets of low density (like HD290458b) contradicts the standard planet formation theory. To adapt the standard theory to account for hot Jupiters, a scenario is required in order to explain how gas giants end up close to the host stars. The idea of planetary migration has been discussed extensively in publications over the last decade as a most likely explanation. However the main problem with the idea of inward migration of gas giants is that it is not clear what process stops the migration at such small distances to the host star. Why does the gas giant simply not fall into the star?

Some ideas have been put forwards in order to explain how such migration braking may come about [48]:

- A central magnetic cavity around the star extending out to the edge of the accretion disk can stop migration naturally [76].
- Many giant planets form at the same time, but most of them fall into the central star and when the disk disappears some giant planets remain [56].
- A mass transfer process via the Roche lobe, or by an exchange of angular momentum, between the planet and its parent star may cause a braking effect [44], [87].
- Planet evaporation as a result of its gas reaching escape velocity would make the planet lose mass and consequently move closer to its parent star to conserve momentum [59].

There are some formation scenarios that offer an explanation for hot Jupiters but do not use migration:

- Jumping Jupiters: If many giant planets have formed at the same time, then there would be a chaotic interaction between them that may eject some from the system and send others into very close orbits around the parent star [94], [53].
- In situ formation: If giant planets are able to form much faster than predicted by the standard theory, then they may be able to form at very close distances to the host star [97], [98], [31].

It is very clear that planet formation theories are not sufficiently developed in order to explain the variety of planetary systems that we have detected to date. This is why it is important to detect as many planets as possible in order to build up statistics about planets of different types orbiting different types of host stars in many different configurations. The statistics may then lead to being able to constrain various planet formation and/or migration scenarios.

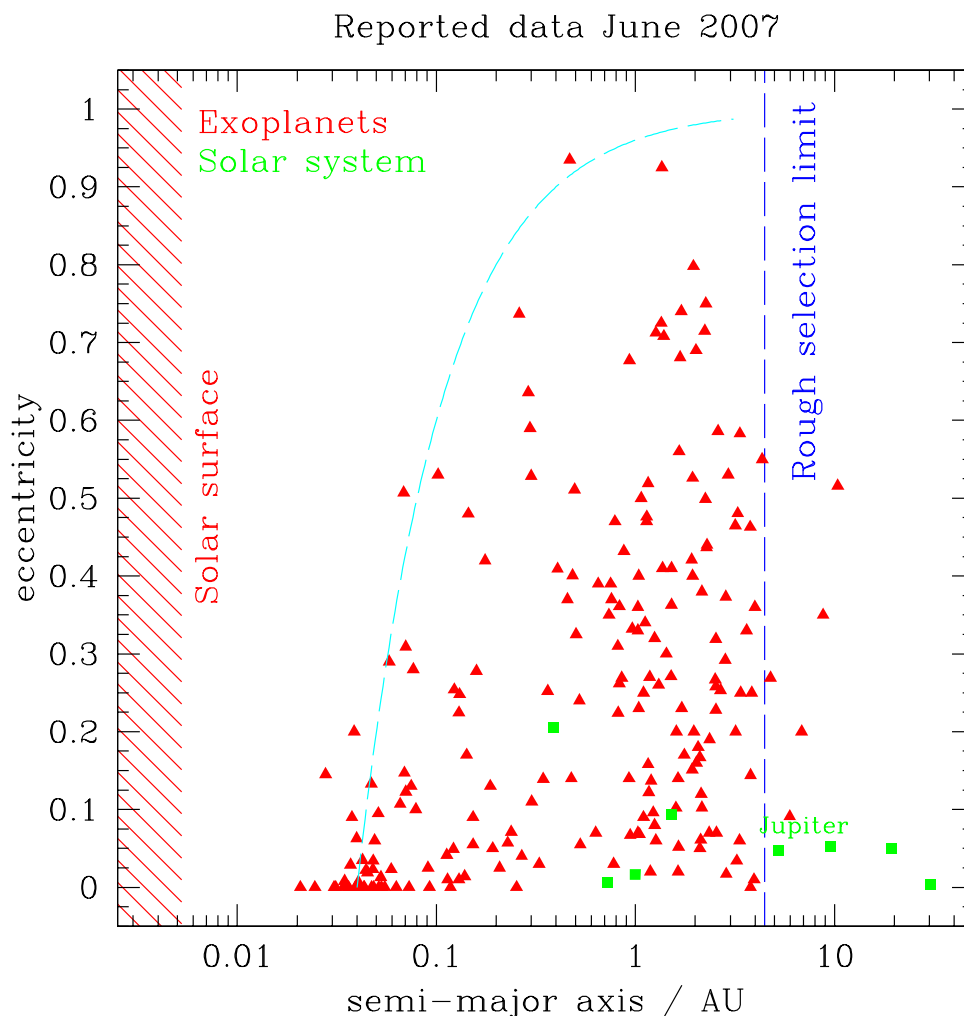


Figure 1.9: Plot of orbital eccentricity against semi-major axis in AU for known extrasolar planets detected by the radial velocity method (red triangles). Solar system planets are also plotted (green squares). The plot was taken from the website by Phil Armitage in the reference [104].

1.8 Observed Properties of Extrasolar Planets

1.8.1 Planet Eccentricities

The definition for orbital eccentricity is the ratio between the semi-major axis of the ellipse and the distance from the centre to either of the foci of the ellipse. The eccentricity has a value of zero for a circular orbit and can take a value between zero and one for an elliptical orbit.

Extrasolar planets appear surprisingly diverse and different from our Solar System. If we look at Figure 1.9 where the orbital eccentricity is plotted against orbital distance, we don't see any

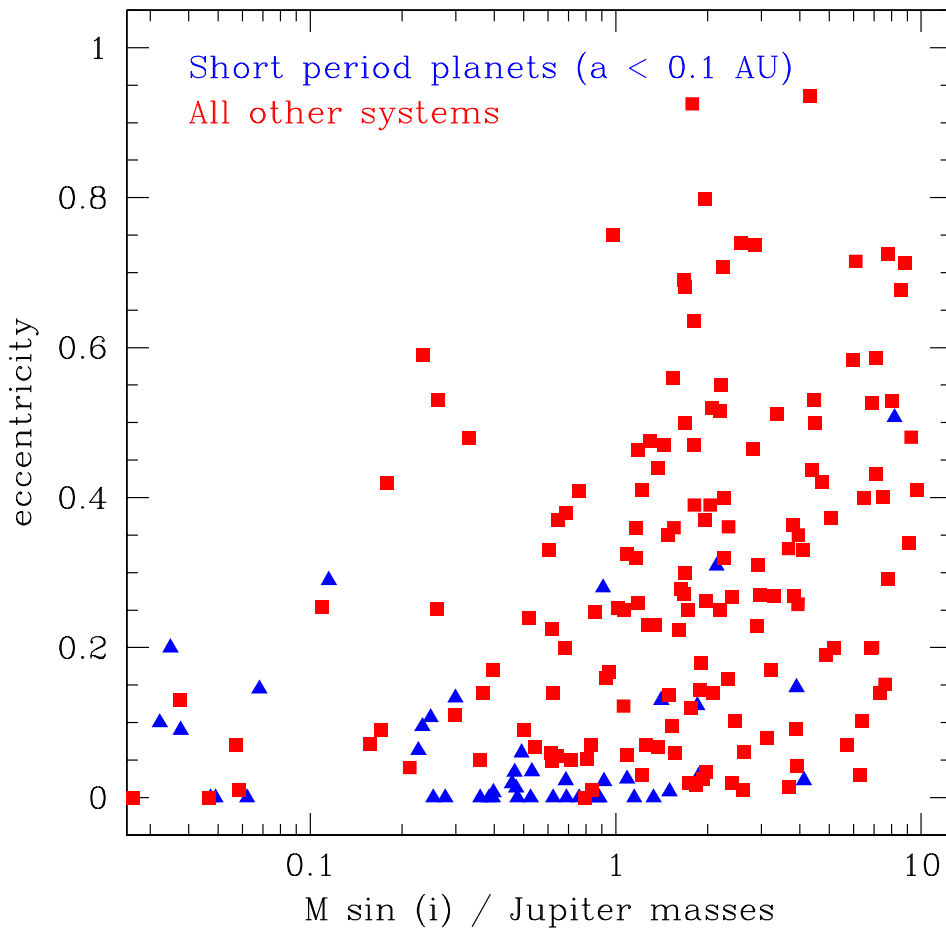


Figure 1.10: Plot of $M_P \sin i$ against orbital eccentricity for known extrasolar planets detected by the radial velocity method. Short-period planets ($a < 0.1$ AU) are plotted as blue triangles and all other systems are plotted as red squares. The plot was taken from the website by Phil Armitage in the reference [104].

clear relationship. However, with more study it becomes clear that hot Jupiters which have an orbital radius of less than ~ 0.1 AU have near-circular orbits similar to those in our Solar System. This is to be expected due to tidal circularising of orbits which is on a short timescale so close to the parent star. Figure 1.9 also shows the bias of the radial velocity method towards very close-in planets. A trend can also be seen that the range of eccentricities increases with semi-major axis.

Also, in Figure 1.10 we can see the absence of planets that have masses of below 0.1 Jupiter masses with an eccentricity of more than 0.2 although planets of any mass in the known range can have small eccentricities. This figure shows that higher-mass planets tend to have higher

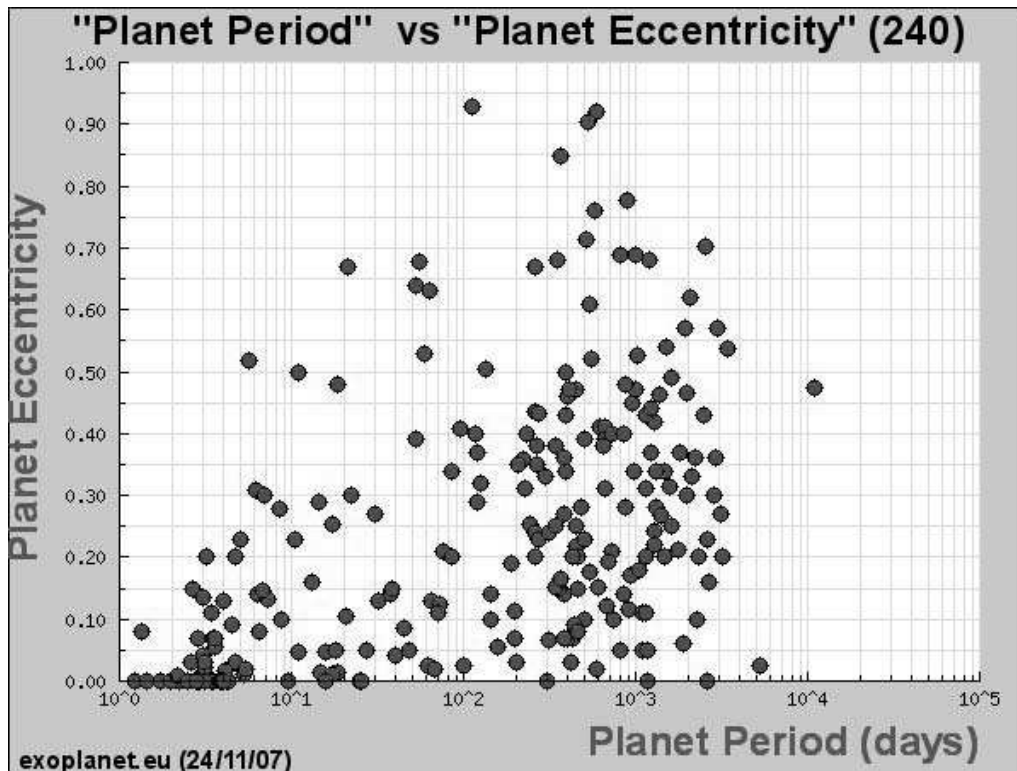


Figure 1.11: Plot of orbital eccentricity against period for known extrasolar planets detected by the radial velocity method. The plot was taken from the extrasolar planet encyclopedia website [102].

eccentricity orbits.

Figure 1.11 confirms the trends seen in Figures 1.9 and 1.10. For short periods of 1 to 10 days there are very few planets with an eccentricity of more than 0.2, but as the period increases above 10 days, the scatter in the eccentricities also increases.

1.8.2 The Mass Function

Radial velocities only give the minimum masses of the extrasolar planets $M_P \sin i$. However, we can still analyse the statistics of the planet minimum mass distributions. The top panel in Figure 1.12, which is a histogram of extrasolar planet mass corrected for the $\sin i$ term, shows that low mass planets are more common than high mass planets. The bottom panel of the same figure, which is a histogram of orbital period, also shows that short-period planets are more frequent than long period planets. Neither of these observed trends are due to biases in the radial velocity method since radial velocity surveys have been observing for upwards of 10 years and therefore planets with periods of at least 10 years are within range of the surveys. Also, radial-velocity detections favour higher-mass planets, not lower-mass planets.

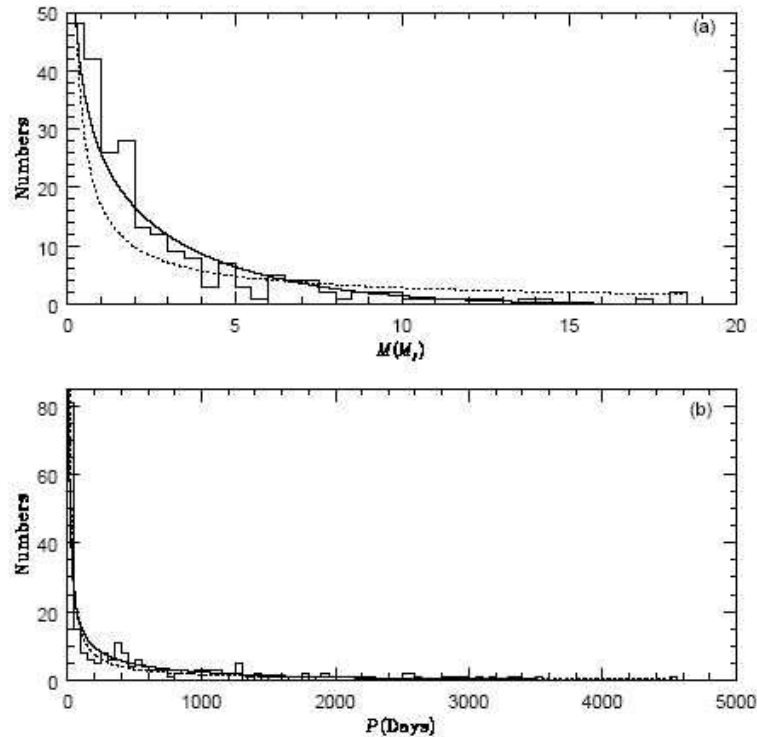


Figure 1.12: Histograms of planet mass (top) and orbital period (bottom), taken from Sotin et al. 2007 [80].

In Figure 1.13 we show a plot of planet minimum mass against orbital semi-major axis for radial velocity planets (red triangles) and solar system planets (green squares). Here the lower mass limits of the radial velocity method with current technology become very clear. At an accuracy of $\sim 3 \text{ m s}^{-1}$, which is the current limit, we can detect Jupiter and maybe Saturn, but other Solar system planets would be out of reach. Even though we may be able to improve on the accuracy of the radial velocity method with technological advancements, there may be a fundamental limit to the radial velocity method in that stars can show a radial velocity jitter of up to $\sim 20 \text{ m s}^{-1}$ themselves which would hide any smaller planetary signal [95]. Radial velocity jitter is dependent on the stellar spectral type and activity level, and for G and F main sequence stars is generally less than 2 m s^{-1} .

1.8.3 Metal Rich Stars

During the first few years after the first radial velocity planet discovery, it was noticed that there is a tendency to discover planets that orbit metal rich stars ([25],[26]; stars with the same or higher

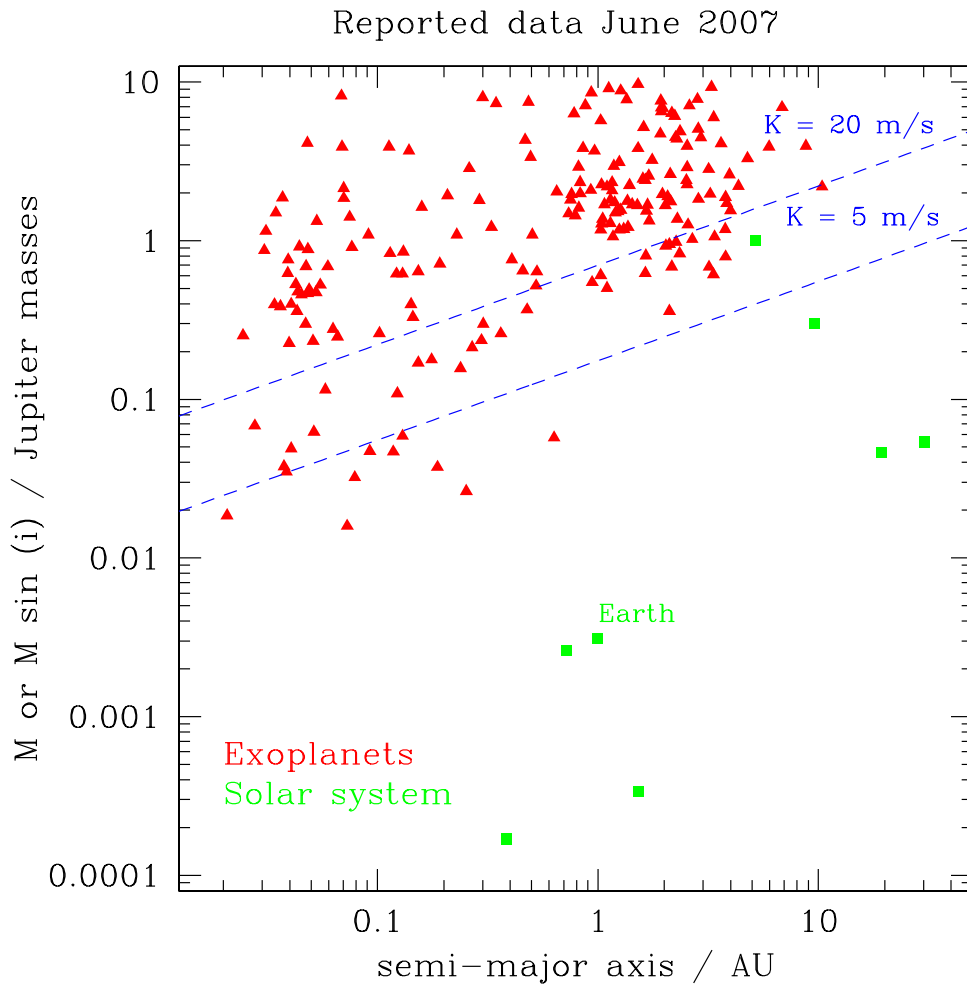


Figure 1.13: Plot of minimum planet mass against semi-major axis for radial velocity planets (red triangles) and solar system planets (green squares). The dashed blue lines mark radial velocity curve semi-amplitudes of 20 m s^{-1} and 5 m s^{-1} . The plot was taken from the website by Phil Armitage in the reference [104].

metal content than our Sun). With the growing number of detected planets, this early trend was confirmed [71] and strengthened by a homogeneous metallicity determination for a set of planet-hosting and comparison stars [72]. The abundance ratios of “non-Iron” chemical elements in the stellar atmosphere ($[\text{Li}/\text{H}]$, $[\text{C}/\text{H}]$ and $[\text{N}/\text{H}]$) are found to be comparable for stars with and without planets [71],[72].

This observation fits in well with the idea that an abundance of heavier elements would favour planet formation. An intensive HST survey of the very metal poor globular cluster 47 Tuc ($[\text{Fe}/\text{H}] \approx -0.7$) failed to detect any transits whereas several dozens were expected [24]. It should be

noted however, that in the case of 47 Tuc, the absence of planets could be due to the clusters high stellar density in the monitored region. Close stellar neighbours could prevent the formation of the protoplanetary disk. However, some debate of the theory has been made in the light of the discovery of a very old planet in the M4 globular cluster [82] since the stars in this cluster have a heavy element fraction that is 1/20th of the value for the Sun. Another scenario to explain the association of planets with metal rich stars is that the migration process which happens early on in the time of planet formation was without a braking mechanism and that many of the protoplanets ended their lives being engulfed by their parent stars [35].

D. Fischer & J. Valenti 2005 [23] analyse carefully the dependence of the probability of finding giant planets around stars as a function of metallicity. Figure 1.14 shows plots of the percentage of stars hosting a giant planet as a function of metallicity [Fe/H]. The data used to produce these plots consists of 850 stars for which radial velocity measurements have been made that would ensure the detection of planets with masses high enough to cause 30 m s^{-1} semi-amplitude radial velocity curves with periods of 4 years or less. It is very obvious that for stars with $[\text{Fe}/\text{H}] < 0.5$, the probability of finding a giant planet is very small indeed, whereas for Solar metallicity this probability rises to $\sim 3\%$ and for $[\text{Fe}/\text{H}] > 0.3$ the probability is up to 15%. The relationship that they are able to derive from this data for the range $-0.5 < [\text{Fe}/\text{H}] < 0.5$ is as follows:

$$P(\text{Giant planet companion}) = 0.03 \left[\frac{N_{\text{Fe}}/N_{\text{H}}}{(N_{\text{Fe}}/N_{\text{H}})_{\odot}} \right]^2 \quad (1.13)$$

Thus the probability of a star hosting a giant planet is proportional to the square of the number of iron atoms.

It is interesting that particle collision rates are also proportional to the square of the number of particles, which suggests a physical link between dust particle collision rates in the primordial disk and the formation rate of gas giant planets. This strengthens the argument that high metallicity in stars with planets is inherited from the primordial cloud, rather than an acquired property, and that gas giant planets form by accretion rather than gravitational instabilities in a gaseous disk.

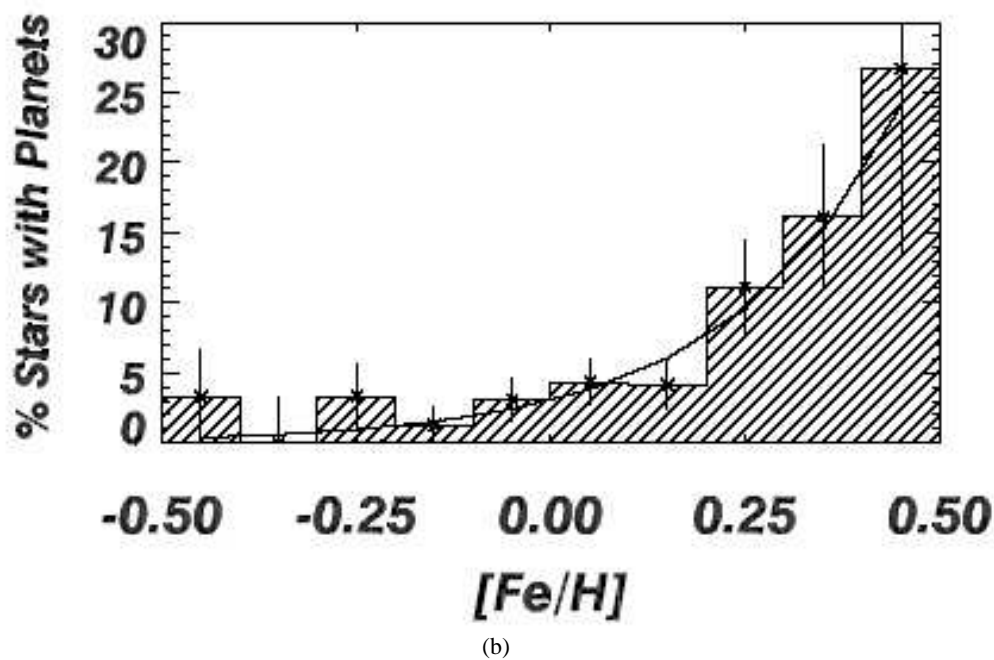
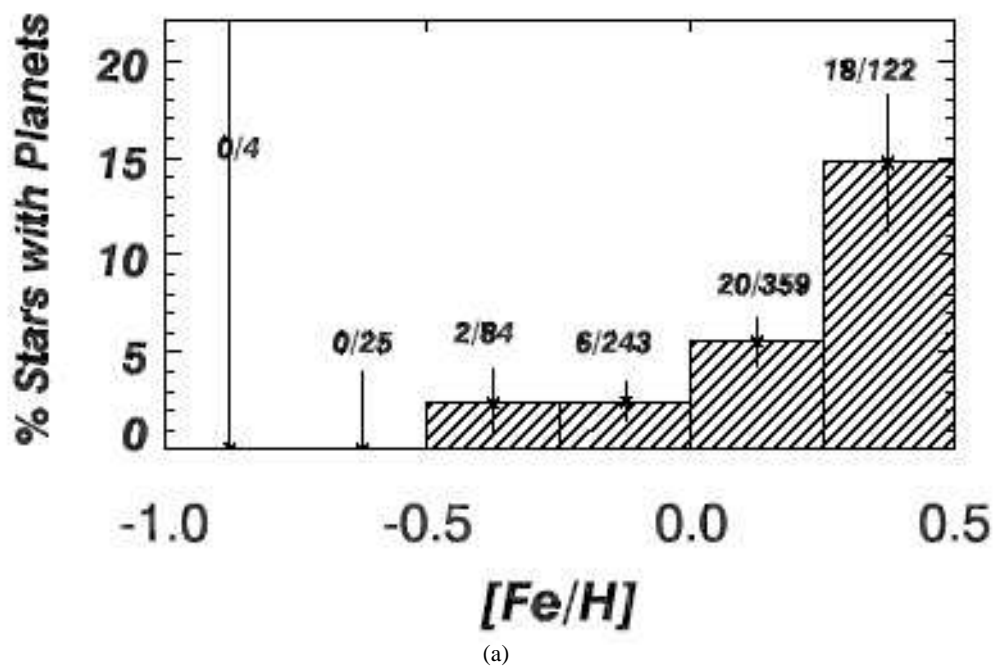


Figure 1.14: Plots of the probability of finding a giant planet as a function of metallicity of the host star. The plots are constructed from a uniform sample of 850 stars and the ratio labelled over each bin is the number of planets to stars in each bin.

Chapter 2

Design of the PASS0 Experiment

2.1 Introduction

This chapter is divided into two parts. The first part deals with the sources of observational noise for a charge-coupled-device (CCD) detector and the theory behind them. In the design of our experiment, we need to reduce the effects of the various noise sources as much as possible in order to reach the $\sim 1\%$ precision required to detect planetary transits. The second part of the chapter is an introduction to the idea and design of PASS0, and the challenges that we face in order to get PASS0 to achieve its maximum precision.

2.2 CCD Signal and Noise Modelling

2.2.1 Readout Noise

On reading out a CCD pixel, noise is introduced into the signal from two sources:

1. The on-chip amplifier produces a statistical distribution of values centred on a mean value when converting from the analogue signal to a digital signal. Hence, even on reading out the same pixel twice with identical charge, a slightly different digital answer may be produced.
2. The output electronics themselves introduce spurious electrons into the readout process, producing unwanted random fluctuations in the output signal.

The readout noise, generally denoted by σ_{RON} , generally follows a Normal distribution. Hence it is quoted as a one-sigma value in electrons. It can be measured as the standard deviation of a bias frame, where a bias frame is a zero-second exposure with the shutter closed. The readout noise for the PASS0 camera with the Apogee U10 CCD is $\sim 9 e^-$ (see Section 2.3.10).

2.2.2 Bias Level

The readout electronics apply a non-zero voltage to the CCD and the consequence of this is that on readout, the pixel values include an additive bias level. This bias level can vary from image to

image and hence a few extra read cycles are performed before or after reading the real physical pixels in order to quantify this level. This area of the image is called the overscan region, and the mean of this area is an estimate of the bias level. Images without an overscan region can be corrected for bias level by taking bias frames interspersed between the actual observations. This is the tactic we use with the PASS0 CCD which does not possess an overscan region.

2.2.3 Bias Pattern

On some CCDs there is a fixed pattern in the bias frames which will need to be removed from the science images by subtraction of the pattern. The easiest way to do this is to construct a master bias frame by combining many bias images together using the median or mean, which results in a high S/N estimation of the bias pattern.

2.2.4 Dark Current

The electrons in the silicon of a CCD may be thermally agitated and freed, consequently to be collected in the potential well of a pixel. Hence these thermal electrons accumulate along with the signal to be measured, and constitute a dark current. Clearly the dark current is a strong function of CCD temperature, and can be minimised by cooling down the CCD as much as possible. The cooling system of the PASS0 camera for instance achieves a CCD temperature of $-20\text{ }^{\circ}\text{C}$, which strongly suppresses the dark current for the CCD, but is not enough cooling to reduce it to a negligible level.

Characterising the dark current of a CCD at a particular temperature can be done by integrating the CCD for a certain time (usually the same integration time as the science observations) with the shutter closed so as to only accumulate thermal electrons. A large number of dark images can be combined to create a masterdark image which can be scaled to each science image using the relative exposure times and subtracted, since dark current is an additive effect.

The presence of a dark current can also introduce extra Poisson noise from the random nature of the thermal electrons. The thermal noise is usually denoted by σ_{TH} and it is given by:

$$\sigma_{\text{TH}} = \sqrt{D(x, y) \Delta t} \quad (2.1)$$

where $D(x, y)$ is the number of thermal electrons generated per second as a function of x and y position on the CCD, and Δt is the exposure time.

2.2.5 Photons

When the shutter on a CCD is opened, photons arrive at the CCD and knock electrons from the silicon valence bands, which are subsequently collected in the potential wells of the pixels. Photons in CCD observations arrive from two sources, sky background emission and astronomical objects. Independent of the source of the photons, the photons arrive in a random manner with a Poisson distribution. Hence, for a pixel of sensitivity F receiving a flux of X photons per second, XF photo-electrons per second are produced and the photon noise σ_{PH} amounts to $\sqrt{XF \Delta t}$ in a Δt second exposure.

Each pixel in a CCD has a slightly different sensitivity to photons. This non-uniformity in detector sensitivity can be characterised by imaging a bright uniform source (like the twilight sky). These type of images are called flatfields, and they may be combined, usually via the median to avoid bright stars, into a high signal-to-noise master flatfield which maps the sensitivity variations. The master flatfield, after appropriate normalisation, is then used to correct the non-uniform sensitivity by dividing it into the science images.

The model for a raw CCD pixel value $Z(x, y)$ in electrons, taking into account all of the above sources, may be written as:

$$Z(x, y) = B(x, y) + D(x, y) \Delta t + X(x, y) F(x, y) \Delta t \quad (2.2)$$

where $B(x, y)$ represents the bias pattern including the bias level (electrons), $D(x, y)$ is the dark current per second, $X(x, y)$ represents the distribution of incoming photons per second, $F(x, y)$ is the master flatfield (dimensionless) and Δt is the exposure time in seconds. The calibrated CCD pixel value $X(x, y)$ in electrons per second is therefore given by:

$$X(x, y) = \frac{Z(x, y) - B(x, y) - D(x, y) \Delta t}{F(x, y) \Delta t} \quad (2.3)$$

During the analogue to digital conversion in a CCD, electrons get converted to counts (or ADUs) at a rate of G electrons per ADU. The value of G is referred to as the CCD gain. Equations 2.2 and 2.3 can be used in either units of electrons or ADUs. The gain for the PASS0 camera with the Apogee U10 CCD is $\sim 2.3 \text{ e}^-/\text{ADU}$ (see Section 2.3.10).

2.2.6 Pixel Noise

Combining all of the above discussion, we can write an expression for the noise in the raw pixel value σ_Z in electrons as:

$$\sigma_Z^2(x, y) = \sigma_{\text{RON}}^2 + \sigma_{\text{TH}}^2 + \sigma_{\text{PH}}^2 \quad (2.4)$$

All of σ_{RON} , σ_{TH} and σ_{PH} have units of electrons. Using the expressions $\sigma_{\text{TH}} = \sqrt{D(x, y) \Delta t}$ and $\sigma_{\text{PH}} = \sqrt{X(x, y) F(x, y) \Delta t}$ gives:

$$\sigma_Z^2(x, y) = \sigma_{\text{RON}}^2 + D(x, y) \Delta t + X(x, y) F(x, y) \Delta t \quad (2.5)$$

Converting all quantities to ADU and ADU/s gives:

$$\sigma_Z^2(x, y) = \sigma_{\text{RON}}^2 + \frac{D(x, y) \Delta t}{G} + \frac{X(x, y) F(x, y) \Delta t}{G} \quad (2.6)$$

The process of calibrating the CCD pixel values via Equation 2.3 affects the pixel noise model as follows:

$$\sigma_X^2(x, y) = \frac{\sigma_{\text{RON}}^2}{(F(x, y) \Delta t)^2} + \frac{D(x, y)}{F(x, y)^2 G \Delta t} + \frac{X(x, y)}{F(x, y) G \Delta t} \quad (2.7)$$

Again we are using ADU units in place of electrons (e^-), and ADU/s in place of e^-/s , where appropriate. From now on in the analysis we only consider units of ADU and ADU/s.

2.2.7 Measuring the CCD Gain

At this point we are in the position to be able to measure the CCD gain using Equation 2.7. The simplest way to do this is to take two consecutive and identically-exposed bias-corrected flatfields F_1 and F_2 and form the difference image $\Delta F = F_1 - F_2$. The exposure level H of the two flatfields can be measured by taking the mean of the central region. We are able to measure the noise $\sigma_{\Delta F}^2(x, y)$ on the difference image, which is free from a flatfield pattern since it is the difference of two flat fields taken under exactly the same conditions. Assuming that the master flatfield is approximately 1 and that the dark noise is negligible, then we get:

$$G = \frac{2H}{\sigma_{\Delta F}^2(x, y) - 2\sigma_{\text{RON}}^2} \quad (2.8)$$

This method may be repeated with numerous pairs of flatfields in order to get a set of gain measurements for the CCD from which the mean gain can be calculated. The gain for the PASSO camera with the Apogee U10 CCD is $\sim 2.3 \text{ e}^-/\text{ADU}$ (see Section 2.3.10).

2.2.8 Signal-to-Noise Ratio

The photons from an astronomical source are rarely confined to a single pixel. The signal is spread over a small area of the CCD consisting of a group of pixels, and the distribution of the photons is defined by the combination of the source light distribution and the combined point-spread function (PSF) from the atmosphere and instrument. For stars, which are effectively point sources, the photons are simply distributed via the PSF.

If we assume that we have a signal of N_* detected photo-electrons per second from a star, then in Δt seconds we obtain $N_*\Delta t$ photo-electrons on the CCD. These photo-electrons are spread out over n_{pix} pixels, which each contain a sky background signal of $N_{\text{SKY}}\Delta t$ photo-electrons. By assuming that the noise contribution from the dark current is negligible (for a low dark current), then the theoretical signal-to-noise (S/N) that we may get when measuring $N_*\Delta t$ is:

$$\frac{S}{N} = \frac{N_*\Delta t}{\sqrt{N_*\Delta t + n_{\text{pix}}(N_{\text{SKY}}\Delta t + \sigma_{\text{RON}}^2)}} \quad (2.9)$$

Note that here σ_{RON} has units of electrons, as in the rest of this subsection. This equation is called the ‘‘CCD Equation’’ [55], and there are various formulations of this equation in the literature (e.g., [58] and [29]).

We may rewrite Equation 2.9 for two cases when various noise sources dominate. Generally readout noise contributions never dominate sky noise contributions since there is always an appreciable sky background signal. In the case where the star is bright, and its photons dominate the sky photons, $N_*\Delta t \gg n_{\text{pix}}N_{\text{SKY}}\Delta t$, then we have:

$$\frac{S}{N} = \sqrt{N_*\Delta t} \quad (2.10)$$

yielding the expected result for a measurement of a single Poisson behaved value. In the case where the sky background is bright enough to dominate the star photons, $N_*\Delta t \ll n_{\text{pix}}N_{\text{SKY}}\Delta t$,

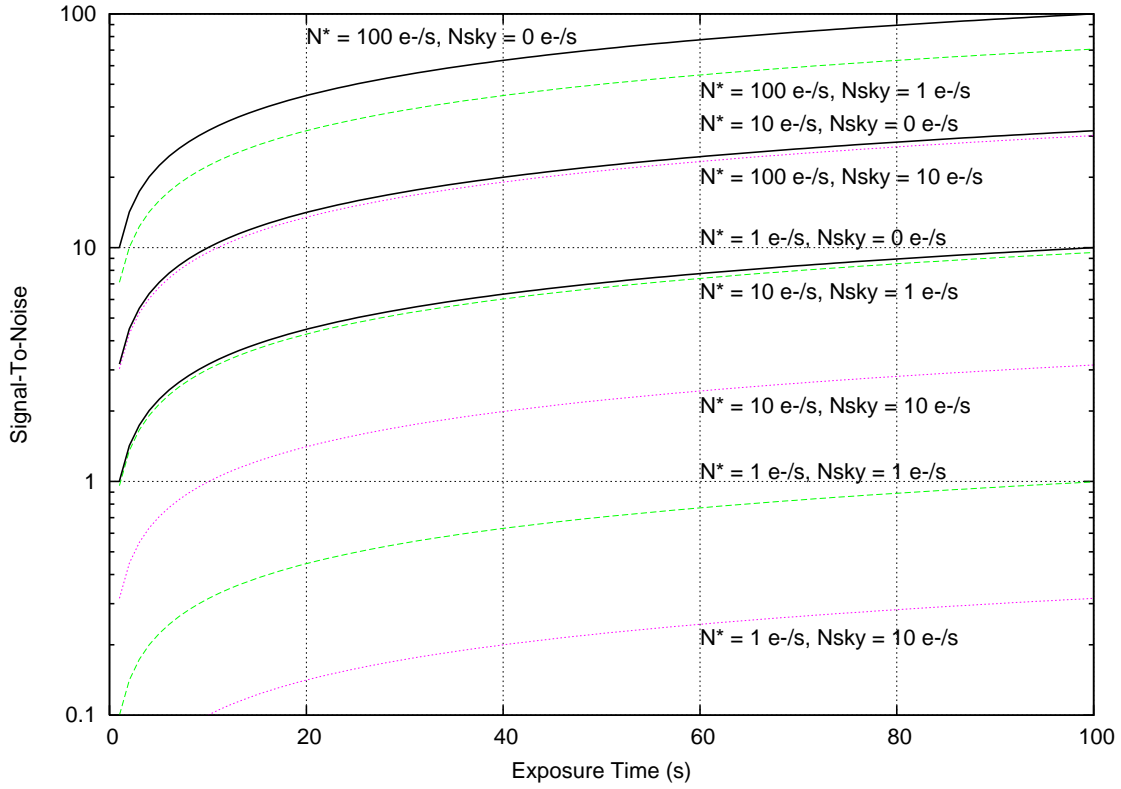


Figure 2.1: Example plot of signal-to-noise versus exposure time for a star signal spread out over a 100 pixel area (regardless of shape). The various values for N_* and N_{SKY} are labelled on the different curves. All curves are proportional to $\sqrt{\Delta t}$. It is assumed that the CCD does not saturate.

then we have:

$$\frac{S}{N} = N_* \sqrt{\frac{\Delta t}{n_{\text{pix}} N_{\text{SKY}}}} \quad (2.11)$$

In both cases, the signal-to-noise of the star signal only grows as $S/N \propto \sqrt{\Delta t}$. In Figure 2.1, we show the evolution of the signal-to-noise versus time for a set of stars with different fluxes and measured under different sky background conditions. Readout noise is considered negligible and saturation is ignored.

At this stage we note that given a desired S/N , we may calculate the required exposure time in order to achieve this by inverting Equation 2.9 and solving the quadratic equation. Consequently

we find that:

$$\begin{aligned}
 \Delta t &= \frac{-B + \sqrt{(B^2 - 4AC)}}{2A} \\
 A &= N_*^2 \\
 B &= - (S/N)^2 (N_* + n_{\text{pix}} N_{\text{SKY}}) \\
 C &= - (S/N)^2 n_{\text{pix}} \sigma_{\text{RON}}^2
 \end{aligned} \tag{2.12}$$

2.2.9 Lightcurve Noise

Here we derive the expected scatter in the lightcurves as a function of star brightness. These calculations are necessary because they help to define the theoretical best precision that we can reach in our lightcurves, in the case that we have a “perfect” data reduction pipeline. Since our pipeline will not be perfect, these calculations will allow us to assess the quality of our reductions. The result also depends on the method used to perform photometry on the calibrated CCD images. We get a different result for aperture photometry as opposed to optimal PSF scaling. We derive both results below.

We start by assuming that we have a CCD detector with readout noise σ_{RON} in ADU and gain G . We assume that the dark current is negligible so that $D(x, y) \approx 0$, that the flatfield is $F(x, y) \approx 1$ and we use a single exposure time of Δt seconds. We represent the sky counts (ADU/s/pix) as $S(t)$ where t is the time of observation, and the star counts (ADU/s) by $N_*(t)$. Our pixel noise model then becomes (using Equation 2.7):

$$\sigma_X^2(x, y, t) = \frac{\sigma_{\text{RON}}^2}{\Delta t^2} + \frac{X(x, y, t)}{G \Delta t} \tag{2.13}$$

where $X(x, y, t)$ and $\sigma_X(x, y, t)$ represent the calibrated pixel value and its error bar (in units of ADU/s), as functions of pixel coordinates x and y .

In aperture photometry, we measure the star flux by placing a circular aperture of radius R pixels at the position of the star, summing the counts in this area and subtracting the sum of the sky counts in this area. The sky background level can be estimated using a larger annulus around the star aperture and calculating the median of these pixels (to protect from other objects contaminating the sky flux). The number of pixels in the star aperture is simply πR^2 pixels. To summarise this process in an equation we may write:

$$N_*(t) = \sum_{x,y} X(x, y, t) - \pi R^2 S(t) \tag{2.14}$$

Here we are assuming that the size of the aperture is sufficient to enclose all star counts from the

point-spread function. Using Equation 2.13, the variance of $N_*(t)$ is given by:

$$\begin{aligned}\sigma_{N_*}^2(t) &= \sum_{x,y} \sigma_X^2(x,y,t) \\ &= \frac{\pi R^2 \sigma_{\text{RON}}^2}{\Delta t^2} + \frac{\pi R^2 S(t)}{G \Delta t} + \frac{N_*(t)}{G \Delta t}\end{aligned}\quad (2.15)$$

In astronomy we usually work in magnitudes, and we convert the flux to a magnitude $m(t)$ via the relation:

$$m(t) = M_0 - 2.5 \log(N_*(t)) \quad (2.16)$$

where M_0 is some zeropoint magnitude. The zeropoint may vary from image to image, and is usually determined from a set of standard stars in the field of view. The corresponding error bar on $m(t)$, denoted by $\sigma_m(t)$, is given by:

$$\sigma_m(t) = 1.0857 \frac{\sigma_{N_*}(t)}{N_*(t)} \quad (2.17)$$

The root-mean-square (RMS) uncertainty in the mean level of a lightcurve σ_{LC} may be calculated from:

$$\sigma_{\text{LC}}^2 = \frac{\sum_t \sigma_m^2(t)}{N_{\text{IM}}} \quad (2.18)$$

where N_{IM} is the number of images in the sequence. By combining Equations 2.15, 2.17 and 2.18, we may derive:

$$\sigma_{\text{LC}}^2 = \frac{1.0857^2}{N_{\text{IM}}} \left(\frac{\pi R^2 \sigma_{\text{RON}}^2}{\Delta t^2} \sum_t \frac{1}{N_*(t)^2} + \frac{\pi R^2}{G \Delta t} \sum_t \frac{S(t)}{N_*(t)^2} + \frac{1}{G \Delta t} \sum_t \frac{1}{N_*(t)} \right) \quad (2.19)$$

In PSF photometry, we measure the star flux by fitting a PSF model at the position of the star. This PSF model is usually previously constructed from fits to suitable bright and isolated stars. Fits may be analytical, empirical or some combination. We consider the case where a known empirical PSF is simply scaled to the star at its already known position, and where the scaling is done using the optimal scaling formula. This case corresponds to the difference imaging pipeline we use to reduce our data later on (see Section 3.1). Since we are measuring difference images (see Sections 3.1.3 and 3.1.4), the flux we are measuring is a difference flux, which we denote as $\Delta f(t)$, with units ADU per second.

We represent the PSF as the function $P(x, y, t)$. Then, using the optimal scaling formula, we may measure $\Delta f(t)$ as:

$$\Delta f(t) = \frac{\sum_{x,y} X(x,y,t)P(x,y,t)/\sigma_X^2(x,y,t)}{\sum_{x,y} P(x,y,t)^2/\sigma_X^2(x,y,t)} \quad (2.20)$$

The associated variance is given by:

$$\sigma_{\Delta f}^2(t) = \frac{1}{\sum_{x,y} P(x,y,t)^2/\sigma_X^2(x,y,t)} \quad (2.21)$$

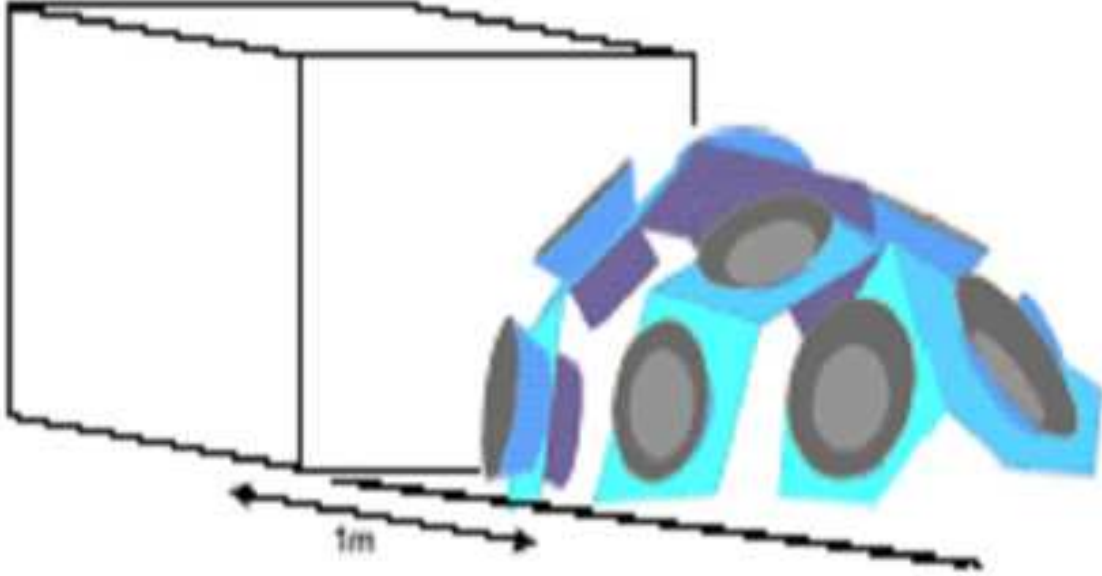


Figure 2.2: A diagram showing the design concept of the PASS instrument

Note that again, $\sigma_X^2(x, y, t)$ is given in Equation 2.13 as our pixel noise model. In difference imaging, the total star flux $N_*(t)$ may be obtained from the following equation (see Section 3.1.4):

$$N_*(t) = F_{\text{ref}} + \frac{\Delta f(t)}{p(t)} \quad (2.22)$$

where F_{ref} is the star flux as measured on the reference image in ADU/s (see Section 3.1.2, and $p(t)$ is the photometric scalefactor (see Section 3.1.4). Therefore the error on $N_*(t)$ is given by:

$$\sigma_{N_*}^2(t) = \frac{1}{p(t)^2 \sum_{x,y} P(x, y, t)^2 / \sigma_X^2(x, y, t)} = \frac{\sigma_{\Delta f}^2(t)}{p(t)^2} \quad (2.23)$$

To calculate the final noise in the lightcurve σ_{LC} , we need to use Equations 2.17 and 2.18. There is no simple analytical expression for σ_{LC} as in the aperture photometry case.

2.3 PASS: Permanent All Sky Survey

2.3.1 The Motivation and Ideas Behind PASS

The primary goal and original envisioned idea of the Permanent All Sky Survey (PASS) is to detect *all* transiting hot Jupiters in the entire sky, complete for host stars between 5.5-10.5 mag, with transits deeper than ~ 10 mmag, and with periods up to 1 week [20]. To achieve all-sky coverage, at least two sites are required, and so we consider here how the experiment would be set up at a single site. The sky above 30° elevation may be observed simultaneously using an array of CCD cameras

of short focal length (approximately 50 mm and f-ratio $f/1.4$) orientated in different directions. The CCD cameras would be fixed on a sturdy platform, ensuring the mechanical stability and simplicity of the instrument, and a completely removable enclosure would be used to protect the instrument when not in use. Figure 2.2 shows how PASS might look in reality.

One key in the design of PASS would be the synchronization of the start of each exposure with Local Sidereal Time (LST). By ensuring that images are always taken at a fixed set of LSTs, stars will trail over exactly the same CCD pixels for a given LST on different nights. The resulting photometry of stars at the same LST will then avoid systematic errors, such as flatfielding errors, that do not vary from night to night. Also groups of images from a single LST are directly comparable and already aligned with each other.

The data collected by PASS will not just be useful for planet hunting, but will also supply information about any variability in the field, whether they be variable stars, moving objects, or transient events. PASS will provide a temporal spacing of around 30 seconds between data points, allowing the characterisation of variable stars with periods as short as half an hour and as long as years, depending on the length of operation of PASS (which will hopefully be indefinite). Moving objects, such as asteroids, will drift slowly through the field of view, and astrometry and photometry can be performed on such objects. Transient events may appear in just one image, but the all sky coverage and high duty cycle will ensure the observation of events brighter than ~ 10 th magnitude.

PASS is not the first project to attempt all-sky surveillance. The All Sky Automated Survey (ASAS; [64]) observes the whole southern sky once every two days, and provides reliable photometry down to ~ 14 mag. This survey has published the discovery of many variable stars (e.g, [65], [66]). The RAPTOR survey [91] is a spatially distributed system of autonomous robotic telescopes that is designed to monitor the sky for optical transients. The Kilodegree Extremely Little Telescope (KELT; [60]) is a survey for planetary transits of bright stars (8-10 mag) using a small-aperture wide-field ($26^\circ \times 26^\circ$) robotic telescope. The camera achieves coverage of $\sim 25\%$ of the northern sky by cycling through a fixed set of observation fields. The project has produced ~ 4 transit candidates [61], none of which have been proven to be planets. Finally, it should be noted that there has already been one transit detection experiment similar in design to PASS. This was the South Pole Exoplanet Transit Search [13] that uses a large-format CCD and a fast $f/1.5$ 300 mm focal length lens to give a seven degree field-of-view. No results have been reported to date.

2.3.2 PASS0: A Prototype PASS Experiment

Our prototype PASS experiment, which we name PASS0, was constructed with a single CCD and lens combination. The aim of PASS0 was to test the ideas behind the PASS experiment. Our first task was to evaluate the CCD detector and lens combination that would be used, and compare it to that used by the SuperWASP experiment.

We consider four different commercial CCDs from Apogee (AP47P, AP8P, AP10 and AP9E) with different Nikon lenses with fixed focal lengths 35 mm, 50 mm and 85 mm. Each lens is considered at its maximum aperture (or f-stop), which are $f/1.4$, $f/1.2$ and $f/1.4$ for the 35 mm, 50 mm and 85 mm focal length lenses respectively. For each lens and CCD combination, we carry out the following evaluation of the potential planet catch.

For each CCD we are given information by the manufacturer on quantum efficiency (QE), the size/dimensions of the CCD in pixels and the pixel size in microns. This information is listed in Table 2.1 for the CCDs that we have chosen to evaluate. We also list in the table the focal length of each lens used in the evaluation, along with its maximum aperture. We proceed to evaluate the CCD and lens combinations by calculating the following quantities using the recipe we describe below.

To calculate the pixel size in arcseconds Δ_{arc} , we use the relation:

$$\Delta_{\text{arc}} = \left(\frac{3600 \times 180}{1000 \times \pi} \right) \times \left(\frac{\Delta_{\mu}}{f_1} \right) \quad (2.24)$$

where Δ_{μ} is the pixel size in microns and f_1 is the focal length of the lens in mm. The field-of-view, FOV, in degrees of each camera is given by:

$$\text{FOV} = \sqrt{D_x D_y} \times \frac{\Delta_{\text{arc}}}{3600} \quad (2.25)$$

where D_x is the CCD size in the x -direction in pixels, and D_y is the CCD size in the y -direction in pixels. However, for PASS0, where stars trail across the CCD, this FOV would need scaling according to how long it takes for a star to trail across the CCD and the length of an observing night. For simplicity we do not make this adjustment, especially since we are trying to compare various CCD and lens combinations. To calculate the sky magnitude M_{SKY} , assuming a standard sky magnitude per square arcsecond of 18, and assuming a typical FWHM of 2 pixels for the PSF, we use:

$$\begin{aligned} M_{\text{SKY}} &= 18 - 2.5 \log(A) \\ A &= N_{\text{eff}} \Delta_{\text{arc}}^2 \\ &= \left(\frac{\pi}{2 \ln(2)} \right) \times 4 \Delta_{\text{arc}}^2 \end{aligned} \quad (2.26)$$

where N_{eff} is the number of effective pixels of a Gaussian PSF. To get this result we have used Equation B.8 from the Appendix B.

We now require to calculate the magnitude of the faintest star for which we can detect transits at a signal-to-noise ratio (SNR) of 10. We start by assuming that our typical hot Jupiter has the same radius as Jupiter, a period of 4 days and orbits a star with the same radius as our Sun. We also assume that our survey observes for 30 nights (so that finally we can quote the number of planets we expect to detect on a per month basis) and on average 6 hours per day. Using Equations 1.3 and 1.8, we get a transit depth of ~ 10 mmag, a transit duration of ~ 2.88 hours and ~ 1.9 transits observed in one month on average. Taking Vega as our standard star with magnitude zero and a photon flux of approximately 10^3 photons per cm^2 per sec per \AA at 5500 \AA , then for a bandwidth of 1000 \AA , we calculate the number of counts per second V_{cps} arriving at the detector for a zero

magnitude point source object as:

$$\begin{aligned} V_{\text{cps}} &= 10^6 \times Q \times \left(\frac{\pi}{4}\right) \times D_1^2 \\ D_1 &= \frac{f_1}{10 f_s} \end{aligned} \quad (2.27)$$

where Q is the detector quantum efficiency, D_1 is the lens diameter in cm and f_s is the lens f-stop. The counts per second due to sky background S_{cps} are then calculated via:

$$S_{\text{cps}} = V_{\text{cps}} \times 10^{-0.4 M_{\text{SKY}}} \quad (2.28)$$

and the number of sky counts received during the transit duration S_T is then given by:

$$S_T = S_{\text{cps}} t_T \quad (2.29)$$

where t_T is the transit duration in seconds. In a similar way we can derive:

$$C_T = V_{\text{cps}} \times 10^{-0.4 M_*} \times t_T \quad (2.30)$$

where C_T is the star counts during one transit. Using Equation 2.9 (ignoring readout noise), we get the signal-to-noise for one transit SNR_1 as:

$$\text{SNR}_1 = \left(\frac{C_T}{\sqrt{C_T + S_T}} \right) \delta_T \quad (2.31)$$

where δ_T is the fractional transit depth. For more than one observed transit we derive a signal-to-noise SNR_N given by:

$$\text{SNR}_N = \text{SNR}_1 \sqrt{N} \quad (2.32)$$

where N is the number of observed transits. Our requirement is that we can detect multiple transits at a SNR of 10. We can rearrange Equations 2.30, 2.31 and 2.32 to get a quadratic equation for the number of star counts during one transit:

$$C_T^2 - B^2 C_T - B^2 S_T = 0 \quad (2.33)$$

$$B = \frac{\text{SNR}_N}{\delta_T \sqrt{N}} \quad (2.34)$$

The quadratic equation can be solved in the standard way and we take the positive solution to get:

$$C_T = \left(\frac{B}{2} \right) \times \left(B + \sqrt{B^2 + 4S_T} \right) \quad (2.35)$$

Finally, the faint star limit for a SNR of 10 is calculated from:

$$M_* = -2.5 \log \left(\frac{C_T}{V_{\text{cps}} t_T} \right) \quad (2.36)$$

Table 2.1: Evaluation of each CCD and lens combination, listing useful quantities to be taken into account when designing the survey.

CCD	Lens	QE	Dimensions (pixel)	Pixel Size (micron)	Pixel Size (arcsec)	FOV (deg)	Sky Magnitude	Faint Star Magnitude Limit	Distance (pc)	Number Of Stars ($\times 10^3$)	Planet Discoveries Per Month
AP47P	35mm, f/1.4	0.7	1024x1024	13.3	78.4	22.3	6.14	9.08	75	1.07	0.55
AP8P	35mm, f/1.4	0.7	1024x1024	24.0	141.4	40.2	4.85	8.45	56	1.47	0.76
AP10	35mm, f/1.4	0.3	2048x2048	14.0	82.5	46.9	6.02	8.55	59	2.27	1.18
AP9E	35mm, f/1.4	0.5	2048x2048	9.0	53.0	30.2	6.98	9.29	83	2.64	1.37
AP47P	50mm, f/1.2	0.7	1024x1024	13.3	54.9	15.6	6.91	10.02	116	1.94	1.00
AP8P	50mm, f/1.2	0.7	1024x1024	24.0	99.0	28.2	5.63	9.40	87	2.65	1.37
AP10	50mm, f/1.2	0.3	2048x2048	14.0	57.8	32.9	6.80	9.50	91	4.13	2.14
AP9E	50mm, f/1.2	0.5	2048x2048	9.0	37.1	21.1	7.76	10.24	128	4.80	2.49
AP47P	85mm, f/1.4	0.7	1024x1024	13.3	32.3	9.2	8.06	11.00	182	2.60	1.35
AP8P	85mm, f/1.4	0.7	1024x1024	24.0	58.2	16.6	6.78	10.38	137	3.56	1.85
AP10	85mm, f/1.4	0.3	2048x2048	14.0	34.0	19.3	7.95	10.47	143	5.52	2.86
AP9E	85mm, f/1.4	0.5	2048x2048	9.0	21.8	12.4	8.91	11.22	201	6.40	3.32

Table 2.2: Evaluation of the number of star counts for the PASS0 and SWASP cameras in various magnitude ranges and observational directions. The column headed M represents the apparent magnitude range considered extending 0.5 magnitudes either way around the listed magnitude. The columns headed with b correspond to different Galactic latitudes and we only consider the Galactic longitude of 90° (in the Galactic plane perpendicular to the Sun-Galactic centre line).

	AP10 with 50mm,f1.2		SWASP with 200mm,f1.8	
M	b = 0	b = 90	b = 0	b = 90
4	83	18	3	0
5	200	35	13	2
6	331	148	19	4
7	1500	382	90	21
8	3852	944	229	65
9	13484	2196	806	146
10	38730	4650	2316	253
11	93839	9547	5612	533
12	175694	16088	10508	942
Total	327713	34008	19596	1966

Using the faint star magnitude limit, we can now calculate the distance d , in parsecs, out to which we can detect a transiting planet at a SNR of 10 using the following equation for solar-type stars:

$$d = 10^{1+(M_*-4.7)/5} \quad (2.37)$$

Here we have ignored Galactic extinction because of the relatively small distances involved (< 300 pc). The solid angle Ω corresponding to the FOV of the survey calculated earlier can be obtained from:

$$\Omega = \left(\frac{\text{FOV}}{180/\pi} \right)^2 \quad (2.38)$$

The volume of the survey V in cubic parsecs is then given by:

$$V = \left(\frac{\Omega}{3} \right) d^3 \quad (2.39)$$

The average density of main sequence stars in the solar neighbourhood is ~ 0.05 stars per parsec³. Hence the number of stars N_* in the survey is given by:

$$N_* = 0.05V \quad (2.40)$$

We can now make the assumption that $\sim 0.5\%$ of stars host a hot Jupiter, and using Equation 1.2 we get a transit probability of ~ 0.10 for our assumed hot Jupiter. Since we have considered observations over a period of 30 days, we can estimate the number of planets detected per month N_{ppm} as:

$$N_{\text{ppm}} = 0.005 \times 0.10 \times N_* \quad (2.41)$$



Figure 2.3: The PASS0 camera in its enclosure at the Teide observatory in Tenerife.

In Table 2.1, we present the most important quantities from those we calculated above. In choosing the CCD and lens combination we used to construct PASS0, we tried to balance a number of important considerations. The main aim of the PASS project is to maximise the discovery rate of extrasolar planets. For this reason it is obvious that the AP9E CCD is the best choice for the detector regardless of the chosen lens. This CCD achieves the best planet discovery rate because of its relatively high quantum efficiency and its large field of view. However, we also want to design the PASS experiment to be complementary to the SuperWASP project rather than to be in competition. The SuperWASP cameras target stars from 9th to 15th magnitude and mainly expect to discover planets in the 9th to 12th magnitude range. For this reason we want to avoid overlap of the survey magnitude limits between the projects and the AP9E CCD goes too deep for our aims. The next best choice is the AP10 CCD which also happens to be the WASP0 CCD. This CCD supplies the largest field of view regardless of the lens used, and combined with the fact that it is $\sim 30\%$ cheaper (at the time of purchase) than the AP9E CCD, we have opted for the AP10 CCD.

The choice of lens is also based on the above considerations. The 85mm lens goes deep enough to overlap the SuperWASP magnitude range with the AP10 CCD and its field of view becomes restrictive, and so we do not choose this lens. The 35mm lens provides a large field of view, but with the f-stop available at 1.4, the lens is slower than the 50mm lens at f-stop 1.2 (i.e. it has a smaller diameter) and this increases the exposure time necessary in order to reach a specified S/N. We want to minimise the exposure time for efficiency and also to minimise trailing since the longer the star trails the smaller S/N that we can achieve and the more blending that the stars suffer

from. Finally the 35mm lens suffers from the most vignetting and aberrations which will limit the quality of the photometry that we can perform. Hence we choose the 50mm lens with f-stop of 1.2.

Finally we compare the idea of the PASS0 experiment to the SWASP experiment by a simple comparison of the number of stars that will be surveyed at various magnitude intervals. We do this by using the Besancon model for the Galaxy [68], and quote the results of the star counts for each magnitude range and observing direction. The Besancon model is the generally accepted model of the Galaxy star population used in many astrophysical applications and we refer the interested reader to the relevant publication of Robin et al. 2003 [68] for the model details. In Table 2.2 we present the results of the Besancon model simulations carried out using the interactive webpage at <http://bison.obs-besancon.fr/modele/>. The results indicate that in the primary magnitude range of PASS0 from 6th to 9th magnitude the PASS0 experiment will survey approximately 20 times as many stars as the SWASP experiment per camera showing its superiority for this magnitude range.

In Figure 2.3 we show a picture of the PASS0 camera as it was finally constructed with the U10 CCD (a better CCD, see Section 2.3.10) and 50mm lens in its enclosure at the Teide observatory in Tenerife.

2.3.3 Essential Considerations for Successful Non-Tracking Observations

In carrying out a very wide field survey we face many challenges that we need to overcome. The commercial lens that we use for PASS0 suffers from optical vignetting and spherical aberration. Vignetting reduces the S/N towards the edges of the images and spherical aberration deforms the PSFs of the stars towards the edges of the images.

In Figure 2.4 we show a 2D polynomial fit to the sky background of a typical PASS0 image taken at f-stop of 1.2 which clearly illustrates the magnitude of the vignetting. Ideally the sky background should be flat. This vignetting is also visible in the image shown at the top in Figure 2.5 which was taken with an f-stop of 1.2. In the same image we can see that the star PSFs are being deformed towards the edge of the image, which is a bigger effect than the short star trails in the 20 second exposures.

The easiest way to reduce the problems with the vignetting and lens aberrations is to step up the f-stop. The image shown at the bottom in Figure 2.5 has been taken with an f-stop of 2, and now the vignetting amplitude is greatly reduced and the star PSFs are not distorted towards the edges of the CCD. However, by stepping down from an f-stop of 1.2 to an f-stop of 2, the lens diameter decreases by a factor of 0.6, and consequently the S/N we can achieve in a fixed exposure time falls by a factor of 0.36. If we can develop methods to cope with the vignetting and PSF deformations when doing the image reductions and data photometry, then it is clear that we should still choose an f-stop of 1.2 to maximise our S/N.

Our approach to calibrating properly the lens vignetting involves obtaining a set of high quality flatfields. Twilight sky flats are not suitable because they produce a large sky background gradient since the sky is not sufficiently uniform over the PASS0 large field of view. Also, since twilight is restricted to a short time period of about half an hour, only a limited number of flat fields may be obtained. Finally, stars appear in the twilight flat field images since the lens is a fast lens, and these stars will interfere in constructing a high quality master flat field. Our solution has been to construct a large white screen of light diffuser material which we use as a source of uniform

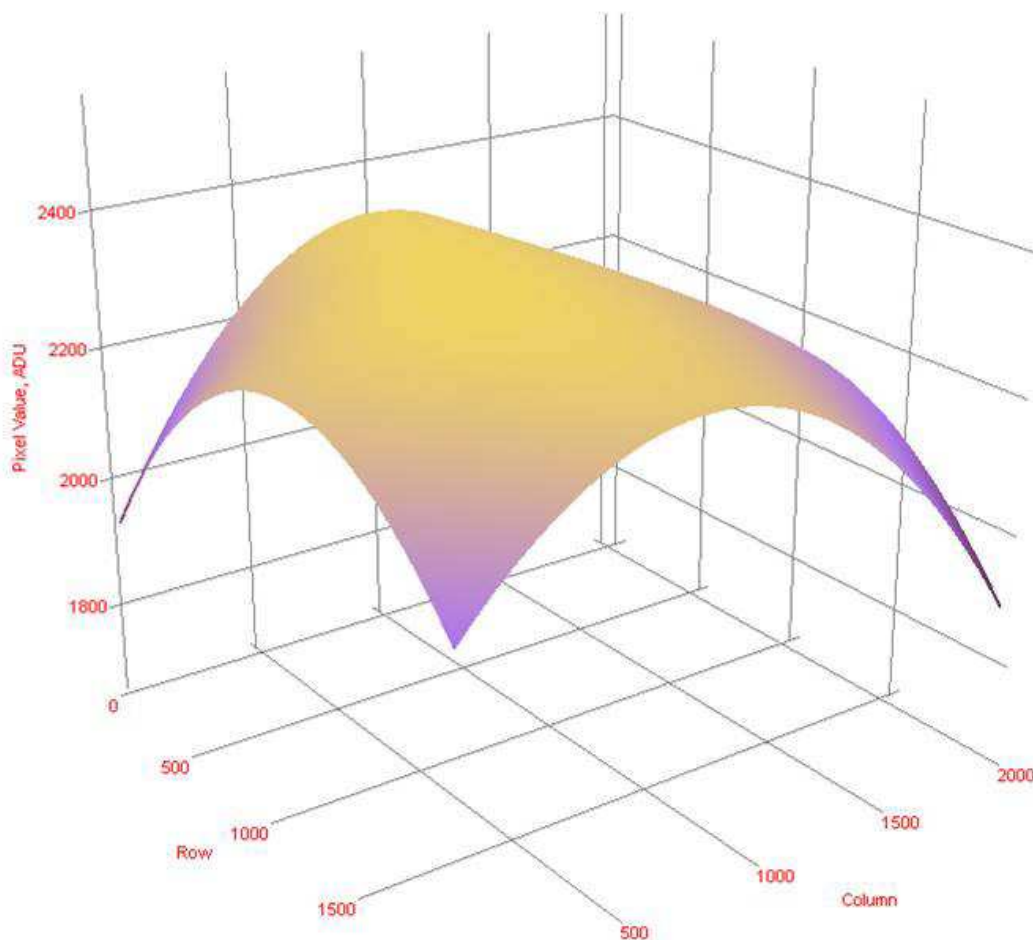


Figure 2.4: Plot of a 2D polynomial fit to the sky background of a PASS0 image taken at f-stop 1.2. The effect of the lens vignetting is to create a sky background that reaches a peak in the middle of the CCD and falls off towards the edge of the CCD. Ideally the sky background should be flat.

illumination. Many flat fields may be taken at once using this device which allows us to construct a very high S/N master flat field of a truly uniform source. Note that flat fields are all taken at the same CCD temperature for consistency and this temperature is below 20 degrees Celsius.

Next we consider the photometry method that we intend to use for the PASS0 image data. Aperture photometry is possibly the simplest method and we make some initial tests on a WASP0 image of 60 second exposure using the AP10 CCD. The first challenge was to design the correct aperture for a trailing star and we did this by redesigning the aperture used in the WASP0 pipeline as shown in Figure 2.6. It is clear from the image that many apertures overlap, a situation that is worsened by the trailing. For PASS0 with a much larger pixel scale, this problem will be much worse.

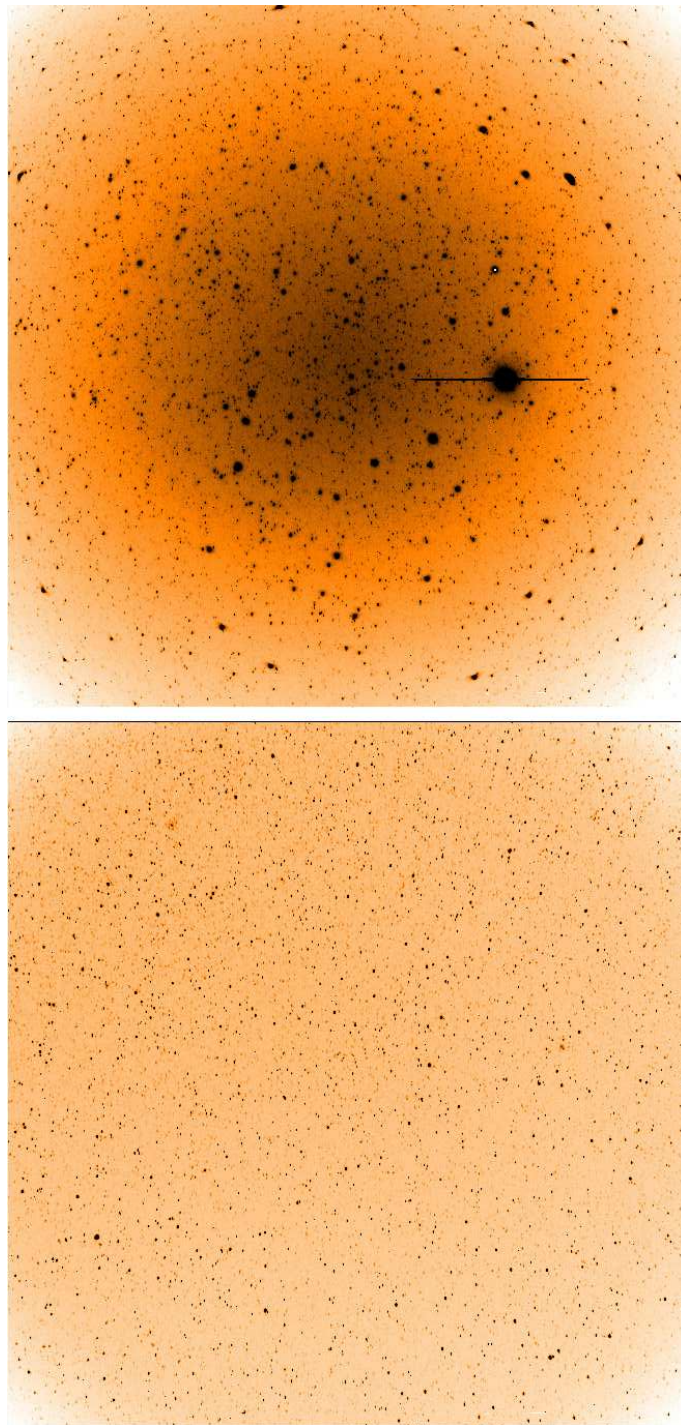


Figure 2.5: **Top:** PASS0 20 second image using a f-stop of 1.2. **Bottom:** PASS0 20 second image using a f-stop of 2.

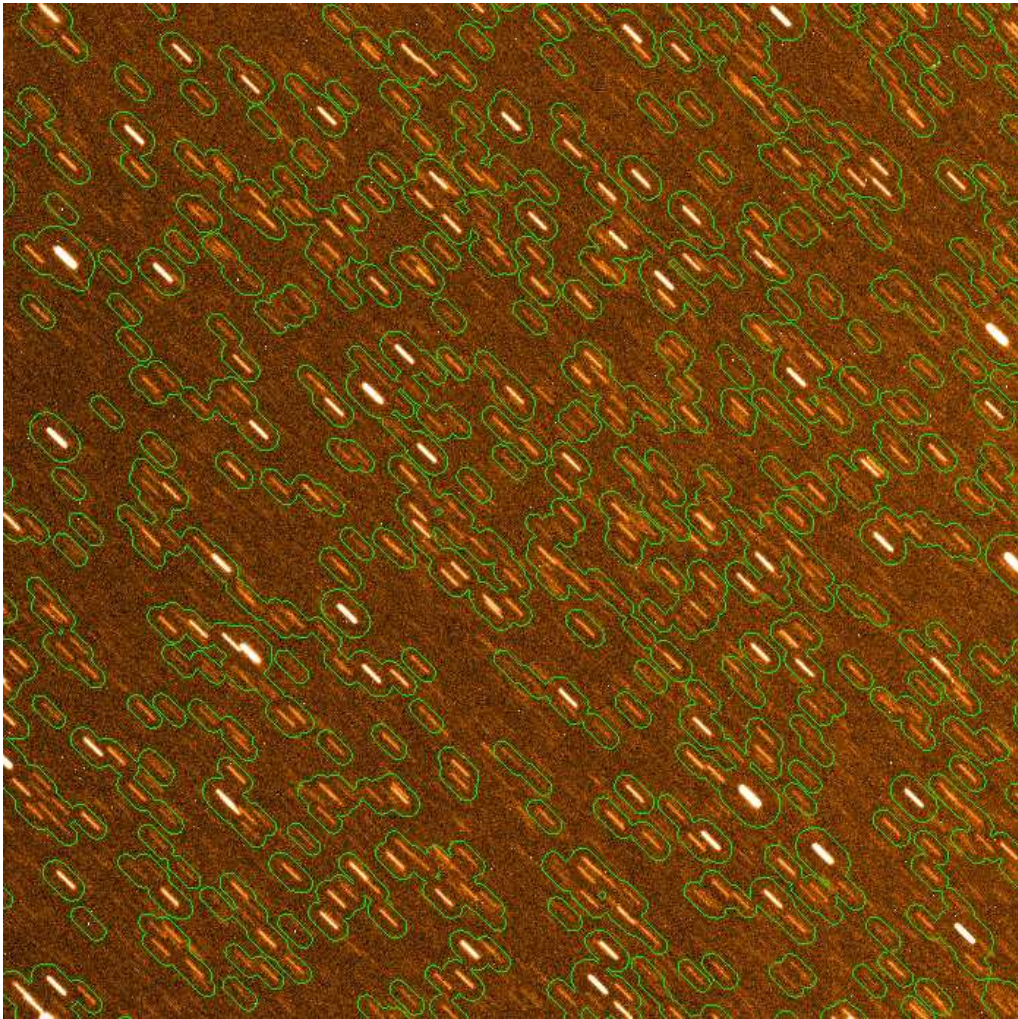


Figure 2.6: A WASP0 60 second image with example apertures to be used for aperture photometry. The 180 mm lens FOV is $9^\circ \times 9^\circ$ with a diameter of 6.30 cm and aperture f/2.8. The WASP0 camera uses the AP10 CCD.

At this point we see that the image subtraction method (see Chapter 3) can reduce the problem of the blending of stars since all constant stars are removed in the difference images, and measuring the difference images of variable stars is then a much cleaner process. Only blend stars that lie within the PSF of the star being considered will continue to affect the lightcurve. Also, by combining the image subtraction method with an optimal PSF scaling on the difference images in order to measure the differential fluxes, we can achieve a better signal-to-noise ratio than aperture photometry (because aperture photometry is not optimal). It is clear that for the experiment to work we will need to create a pipeline that uses difference imaging.

2.3.4 Trailing and its Effect on Signal-To-Noise

Star trailing is the obvious consequence of stationary observations. The main effect of the trailing will be to spread out the star photons over a larger area of sky increasing the sky noise that needs to be taken into account when calculating the S/N of an observation. The longer the exposure time, the longer the trail and consequently the more sky noise that is added to the overall noise. The length of a star trail in a certain exposure time depends on where we look on the sky, since stars trail at the fastest rate on the celestial equator and at their slowest rate at the celestial poles.

In this section we try to quantify the effect of star trailing on the S/N of the observations. We assume the values listed in Table 2.1 for the AP10 CCD and 50mm f/1.2 lens that we used for constructing PASS0. We calculate the Vega counts per second from Equation 2.27 and divide by the CCD gain (15.5 e⁻/ADU) to get 2.639×10^5 ADU/s. We can then calculate the star ADU per second C_{ADUps} for a star of magnitude m using:

$$C_{\text{ADUps}} = 2.639 \times 10^5 \times 10^{-0.4m} \quad (2.42)$$

To calculate the sky counts in ADU per second per pixel S_{ADUpspp} we use:

$$\begin{aligned} S_{\text{ADUpspp}} &= 2.639 \times 10^5 \times 10^{-0.4M_{\text{SKY}}} \\ M_{\text{SKY}} &= 18 - 2.5 \log(\Delta_{\text{arc}}^2) \end{aligned} \quad (2.43)$$

and we note that each pixel is of size 57.8'' (from Table 2.1).

Now we consider the case of no trailing which corresponds to ‘‘normal’’ observations (by WASP0 for example) and to PASS0 when it is observing towards the celestial pole ($\delta = 90^\circ$). We want to calculate the signal-to-noise of an observation, using optimal PSF scaling, and as a function of exposure time, which will involve the use of Equations 2.13, 2.20 and 2.21. To do this we assume that the typical FWHM of the untrailed PSF is 2 pix and use this to generate a normalised Gaussian PSF for the PSF function $P(x, y)$. We then use the known sky flux and star flux to generate a model image, which becomes the term $X(x, y)$. Finally we take the AP10 CCD readout noise to be 1.3 ADU. The signal-to-noise SNR we calculate as:

$$\text{SNR} = \frac{N_*}{\sigma_{N_*}} \quad (2.44)$$

In Figure 2.7 we plot the calculated signal-to-noise for a non-trailed image as a function of exposure time for three example stars of magnitudes 7, 8 and 9 (solid curves).

To calculate the S/N for a trailed star image, we simulate the trail by summing many Gaussian PSFs shifted relative to each other and along the direction of the trail. The trail image is then renormalised to give $P(x, y)$ and used together with the sky flux and star flux to calculate $X(x, y)$. The trail length L_{trail} , in pixels, is calculated using the equation:

$$L_{\text{trail}} = \left(\frac{360 \times 60 \times 60}{24 \times 60 \times 60} \right) \times \left(\frac{\Delta t \cos \delta}{\Delta_{\text{arc}}} \right) \quad (2.45)$$

where δ is the declination of the observation. There is no trailing at the celestial pole ($\delta = 90^\circ$) and the fastest trailing occurs at the celestial equator ($\delta = 0^\circ$). In Figure 2.7 we plot the calculated

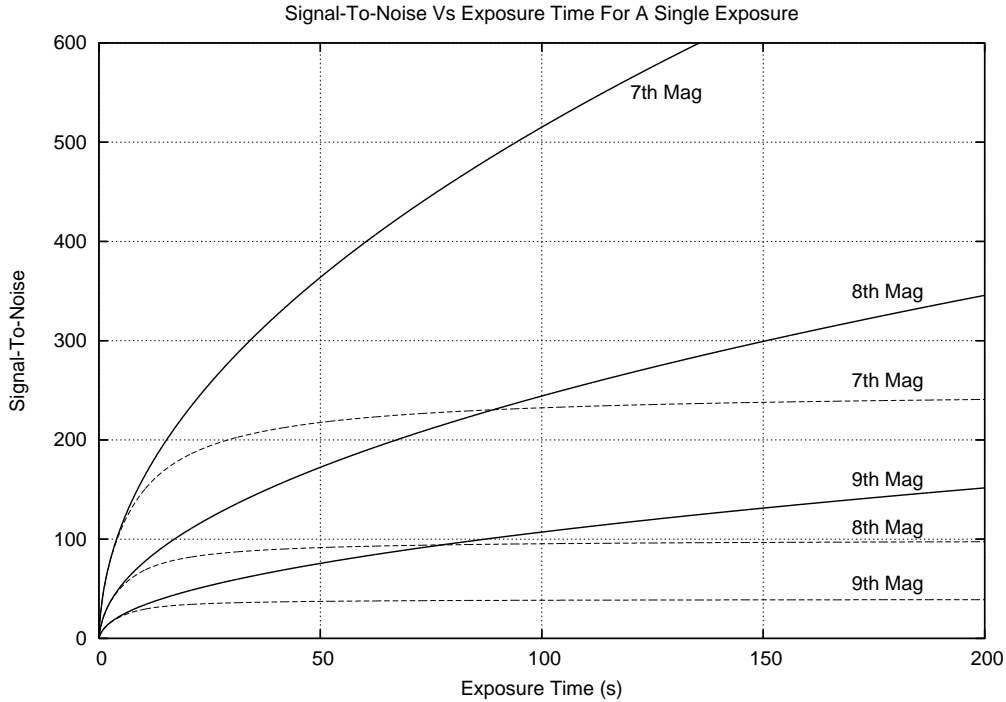


Figure 2.7: The S/N as a function of exposure time for a single image with no trailing (solid curves) and trailing at the celestial equator (dashed curves). Each curve corresponds to a star of a different magnitude (7, 8 or 9) and all the curves correspond to the PASSO camera.

signal-to-noise for trailed images at the celestial equator for three example stars of magnitudes 7, 8 and 9 (dashed curves). The plot shows that, for a single exposure, the effect of the trailing is that the S/N converges towards a maximum S/N and does not continue increasing with exposure time. It is clear that after about 50 s, the gains in S/N for the trailed images are very small.

Our conclusion from Figure 2.7 is that exposure times for PASSO should be kept on the short side for efficiency of the observations. However, we cannot have very short exposure times because the CCD has a readout time of ~ 10 s. In Figure 2.8, we plot the total S/N over 1 hour of observations as a function of exposure time of an individual exposure, taking into account a readout time of 10 s. The solid curves correspond to stars of 7th, 8th and 9th magnitude without trailing and the dashed curves to the same stars but with the trailing at the celestial equator (maxima are marked by solid black circles). The curves are calculated by taking the previous calculations of signal-to-noise for one exposure and multiplying this by $\sqrt{N_{\text{IM}}}$ where N_{IM} is the number of images taken in 1 hour (including the readout time of 10 s). The number of images with exposure time Δt taken in 1 hour is simply $N_{\text{IM}} = 3600/(\Delta t + 10)$. We conclude from Figure 2.8 that for trailed images there is an optimal exposure time for the individual images for which the total S/N during an observing run is maximised, and that for PASSO this optimum exposure time will be about 10 s to 15 s.

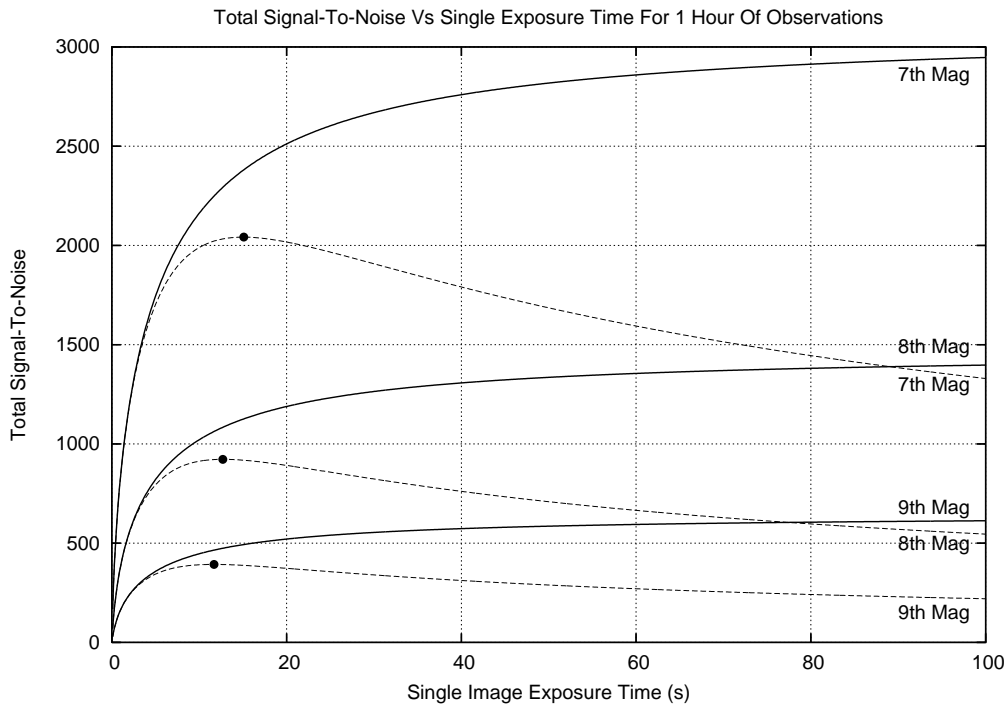


Figure 2.8: The total S/N as a function of the single image exposure time for 1 hour of observations. No trailing is shown by the solid curves and trailing at the celestial equator is shown by the dashed curves. Maxima are marked by solid black circles. Each curve corresponds to a star of a different magnitude (7, 8 or 9) and all the curves correspond to the PASS0 camera.

2.3.5 Optimal Exposure Time for PASS0

We now try and predict the optimal exposure time for the PASS0 camera. We can consider observing sites at the equator, at 30 degrees latitude (Teide Observatory in the Canary Islands), at 60 degrees latitude (St. Andrews University) and at the poles. In Figure 2.9 we show a figure similar to Figure 2.8. We show the predicted S/N over 1 hour of observations as a function of the single image exposure time for a PASS0 camera pointing at zenith for each of our example observing sites (see labels), and for example stars of magnitudes 7 (solid curves), 8 (dashed curves) and 9 (dotted curves). Again, maxima are marked by solid black circles.

Ignoring the poles as an observing site (since this is equivalent to tracking observations), the optimal exposure time for PASS0 lies between 10 s and 25 s depending on the observing site. As we will see in the next Section, we also need to minimise scintillation noise, which is smaller for longer exposure times. Hence we adopt a 20 s exposure time for the PASS0 experiment which also allows 10 s for readout and saving the image to the hard drive in any 30 s observing window.

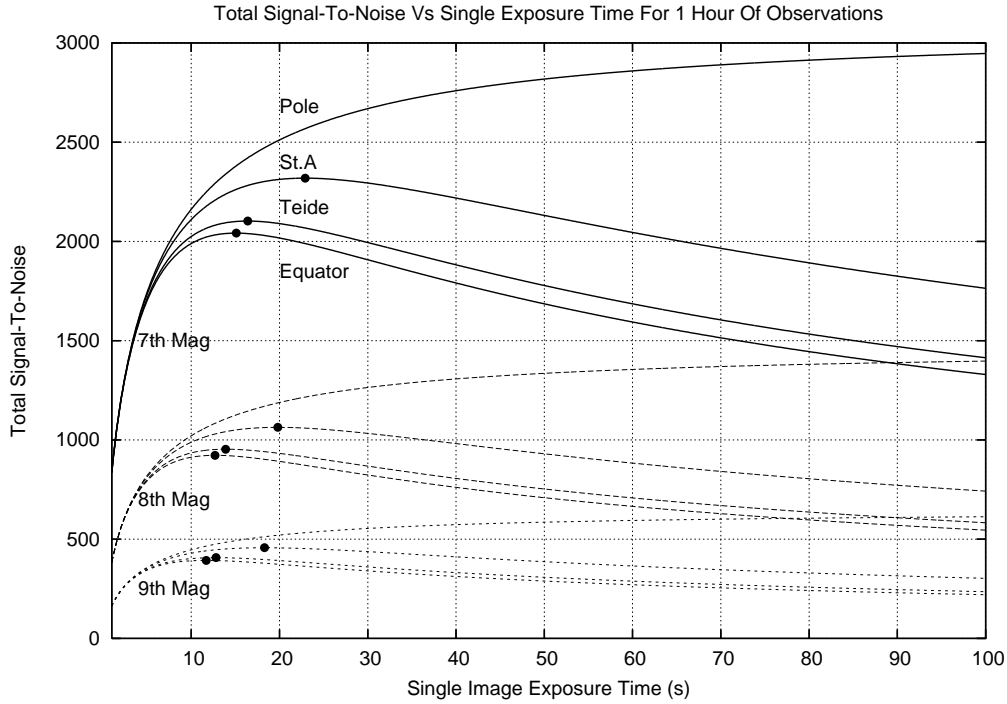


Figure 2.9: The total S/N as a function of the single image exposure time for 1 hour of observations. Here we consider three example stars of magnitudes 7 (solid curves), 8 (dashed curves) and 9 (dotted curves). Maxima are marked by solid black circles. For each star we consider four observing sites, the poles, St. Andrews, the Teide Observatory and the equator. The observations at each site are assumed to be made towards the zenith.

2.3.6 Limitations due to Scintillation

For PASS0 with its small aperture of diameter 4.17 cm, scintillation noise is an important contribution to the overall observation noise. This noise term contributes equally at all star magnitudes and hence its impact is worst on the brightest stars where other noise sources are smallest. We can calculate the contribution to the overall noise due to scintillation using the equation of Young 1967 [99]:

$$\sigma_{\text{SCINT}} = 0.09 d^{-2/3} X \exp(-h/h_0) \sqrt{1/(2\Delta t)} \quad (2.46)$$

where σ_{SCINT} is the RMS scintillation noise in magnitudes, d is the telescope diameter in cm, X is the airmass, h is the observatory height in m, $h_0 = 8000$ m and Δt is the exposure time in s. At the time we were doing our simulations, it was not clear where the PASS0 experiment would be located. However we can now update our simulations to the Teide observatory which has an altitude of ~ 2400 m.

In Figure 2.10 we consider the size of the scintillation noise as a function of exposure time, and we plot curves for an airmass of 1 (observations at zenith; solid curve), an airmass of 1.15 (ele-

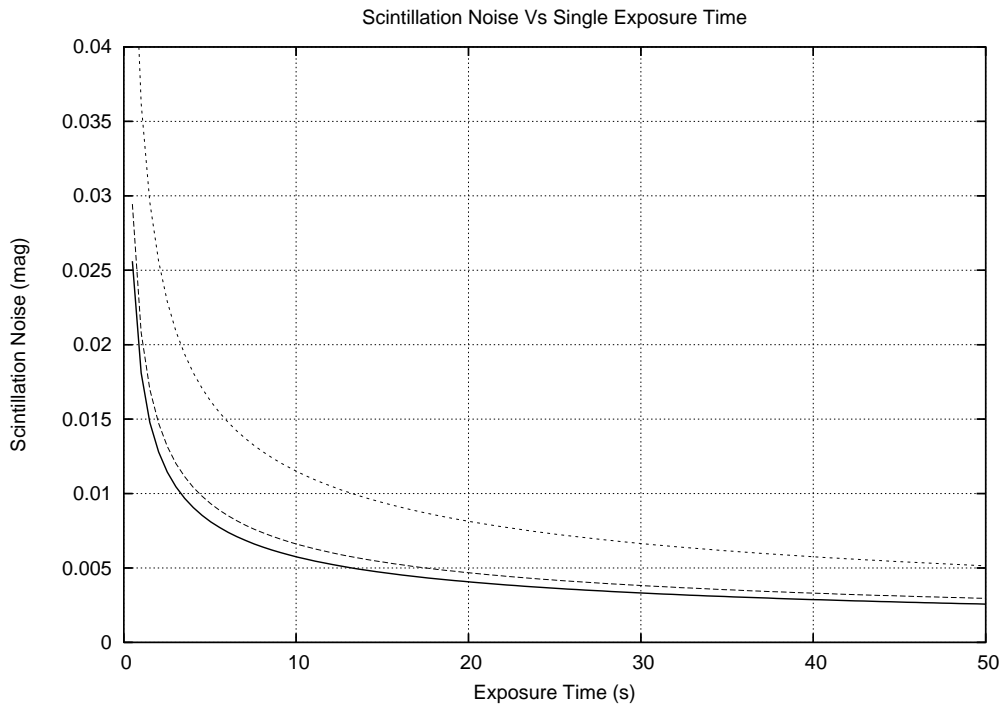


Figure 2.10: The scintillation noise as a function of the single image exposure time and airmass. The solid curve represents an airmass of 1 (observations at zenith), the dashed curve represents an airmass of 1.15 (elevation of 60 deg) and the dotted curve represents an airmass of 2 (elevation of 30 deg). This noise source affects all stars equally and so impacts most the photometry of the brightest stars where other noise sources are smallest.

vation of 60 deg; dashed curve) and an airmass of 2 (elevation of 30 deg; dotted curve). For transit searches we are looking at signals of 0.5-2%, and so a scintillation noise of above ~ 0.005 mag is undesirable. This constraint indicates that we require exposure times of at least ~ 13 , ~ 18 and ~ 50 s at airmasses of 1, 1.15 and 2 to keep scintillation noise at a reasonable level. However, from Figure 2.8 we have seen that there will be an optimal exposure time for S/N considerations of ~ 10 -15 s. Hence the original idea of PASS with many cameras at one site is not optimal, or even viable, since the ones pointing below elevations of 60 deg will be compromised by scintillation noise. For the future, the idea of PASS will have to be based on a network of individual cameras based at different sites around the globe that all point at zenith.

2.3.7 A Theoretical Pass0 Noise Model

In this section we make some simple assumptions about the PASS0 observations to predict the theoretical photometric accuracy that we may achieve. The observing site was chosen to be Teide Observatory in the Canary Islands and so we assume the latitude of 30 degrees and observations at zenith. We take the adopted exposure time of 20 s and again assume a standard sky magnitude

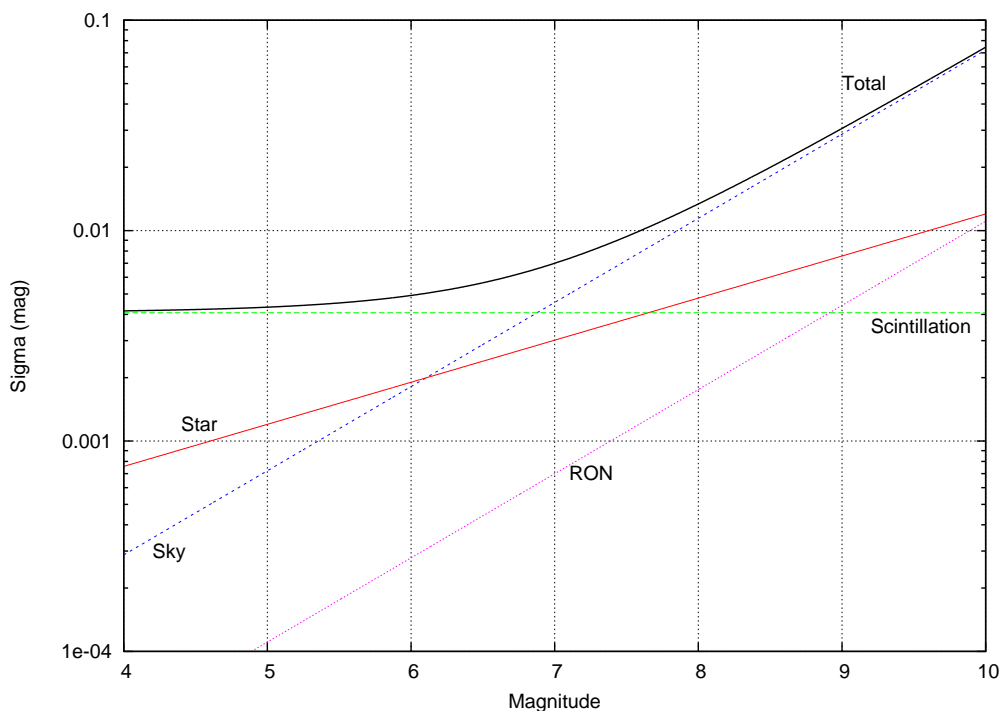


Figure 2.11: The predicted theoretical noise sources as a function of magnitude for PASS0 based at the Teide Observatory in the Canary Islands and pointing at zenith. The various noise sources are labelled appropriately.

of 18 per square arcsec. Using the equations from Sections 2.2.9 and 2.3.2 we calculate the dependence of each noise source on star magnitude and plot these curves in Figure 2.11. The red curve represents star photon noise, the blue curve represents sky photon noise, the green curve represents scintillation noise (calculated using Equation 2.46) and the purple curve represents readout noise. The total noise is represented by the solid black curve.

Figure 2.11 shows that scintillation noise is dominant for stars brighter than 7th magnitude and that sky noise is dominant for stars fainter than 7th magnitude. The scintillation noise is likely to be an underestimate since the PASS0 field of view is ~ 33 degrees, which gives a range of airmasses between 1 and 1.04

2.3.8 The Advantages of PASS0

- PASS0 has the widest FOV at $32^\circ \times 32^\circ$ of all current experiments searching for transiting planets.
- PASS0 searches for planets around the brightest stars in the sky from 4th to 10th magnitude which are not generally targets of other wide field transit surveys that go slightly deeper. Hence PASS0 is complementary to other wide field transit surveys.

- PASS0 is designed to observe in a stationary mode and therefore a simple fixed base is required. This is very attractive economically. The other advantage of not tracking on the sky is that this set up eliminates the risk of errors from bad tracking.
- The stationary observing mode offers a very good way to calibrate the data. Since observations are synchronised to specific LSTs, stars will be in the same position in the sky and at the same place on the CCD at specific LSTs. Hence the sources of any systematic errors can be easily quantified since they are repeatable each day and will be functions of LST.
- The photometry pipeline that will be developed for PASS0 will be an interesting application of photometry to non-round/trailed star PSFs.
- PASS0 has the potential to be used at multiple sites around the globe since CCDs are getting cheaper along with commercial lenses. This opens the possibility for all sky coverage all year round, and opens the door for amateur astronomers and high schools to participate in the project.
- A PASS0 experiment placed at either the North or South pole, and pointing at the zenith, will suffer from very little trailing, giving all the added advantages of tracking observations, but without physically tracking. We suggest that this should be the site of choice for any follow-up PASS0 experiment.

2.3.9 The Disadvantages of PASS0

- Since we are using small aperture lenses of the order of 4.1 cm diameter, scintillation noise seriously affects the accuracy of the photometry that we can achieve with the brighter stars. Hence PASS0 observations will be limited to near the zenith at any observing site, since the size of the scintillation effect increases in proportion to airmass (Figure 2.10).
- The star trailing serves to limit the S/N that can be achieved on the star photometry (Figure 2.9). Photometry on trailed stars is not as accurate as on non-trailed stars due to the increase in sky noise mixed with the star photon noise.
- Wide field observations suffer from vignetting and aberrations which can cause problems for optimising the photometry pipeline (Figures 2.4 and 2.5).
- The large pixel size (~ 1 arcmin) means that each observed star will be blended with many other stars, mostly fainter ones. The trailing serves to make this effect worse. Hence any photometric pipeline will need to deal with this blending or take it into account.
- Individual stars can only be observed from one chip each night during the time it takes for the star to cross the chip (only ~ 2 hours near $\delta = 0^\circ$).

2.3.10 The First Pass0 Observation Run

In the final design of PASS0, a new and better CCD was purchased with exactly the same characteristics as the AP10 CCD except that it had a better gain (at $2.3 e^-/ADU$), no bad columns and a

more efficient cooling system. The CCD was the Apogee U10 CCD and it has a readout noise of ~ 4 ADU.

The PASSO camera is controlled by a computer that runs a fully automatic observing script written in VISUAL BASIC. The computer clock is not very accurate and can be in error with UT by up to a few minutes. Also, at the PASSO site at the Teide Observatory, there is no internet access. This means that we opted to measure the UT time to within a tenth of a second using a global positioning device (GPS) and convert this to LST. The computer then uses the LST to start a 20 s exposure at the beginning of each minute of LST, and exactly 30 seconds later. The 10 seconds of dead time are sufficient for the camera to be read out and the image saved to disk. The observing script is also written to stop observing during the day, and to automatically take dark and bias frames at specified times. Also the observing script only allows the observations to start when the CCD has reached below a temperature of -20 degrees Celsius. Finally, flat fields need to be taken manually because of the use of the white light diffuser screen.

The observations taken and analysed in this thesis span the nights of the observing run from the 29th of June 2005 to the 16th July 2005 inclusive. A total of 3426 science images were taken between the LST times of 20:55:00 and 23:06:00 each night. This data set was intended as a test of the ideas of PASSO and to allow the development of a data pipeline, which is described in the next chapter. For this reason the field containing the transiting planet HD209458b was observed to see if we can recover the transit signal. However, this field centre was not at zenith but at an airmass of 1.08, which means that the airmass varies from 1.005 to 1.28 across the FOV, and that the scintillation noise can vary from 4.1 mmag to 5.2 mmag over the field. The data set we describe was not necessarily intended to be used to search for transit candidates, although we attempt this in Chapter 6.

Chapter 3

PASS0 Data Reduction

3.1 The PASS0 Image Processing Pipeline

We have developed a custom made image processing pipeline for the PASS0 camera in order to automatically reduce the large amounts of data per night of good-weather observations (~ 8 Gb per night in summer; ~ 11 Gb per night in winter). The pipeline is split into various stages, each of which we describe in detail below.

3.1.1 Stage 0: Preprocessing Calibrations

The standard CCD calibrations are controlled by a Visual Basic script that invokes the `MAXIM DL` astronomical image processing application (by Diffraction Limited). The script works on a per night basis, and as a first step, sorts the observations by image type for the current night under consideration. All bias frames are collected and averaged to create a master bias frame. Similarly all dark frames for a particular night are debiased using the master bias frame and then averaged together to create a master dark frame. The master bias and master dark frames are then subtracted off all the flat frames and science images. The script creates a master flat field for the night by normalising each corrected flat field and median combining them. Finally, the master flat field is divided in to each science frame to produce a set of calibrated science images.

At this stage the data are organised by night of observation, but in order to be useful for the PASS0 experiment we need to reorganise the data by the LST of observation. A master list of LSTs is used to reorganise the science images, and the master list of LSTs is constructed from the set of LSTs over all nights that were observed.

An initial approximate astrometric solution for each science image is derived using the program `pinpoint` [103], and the RA and DEC of the image centre are added to the image header. Further astrometric calibration is required since the PASS0 lens exhibits strong barrel distortion, and the star centroids are less certain due to the star trailing in each image. This is done later on (see Section 3.1.2).

To perform photometry on the science images we have chosen the image subtraction method [2],[3], which is known to deliver better precision than either aperture photometry or PSF fitting, especially in the case of crowded stellar fields like that of PASS0 (for example, see [52]). The

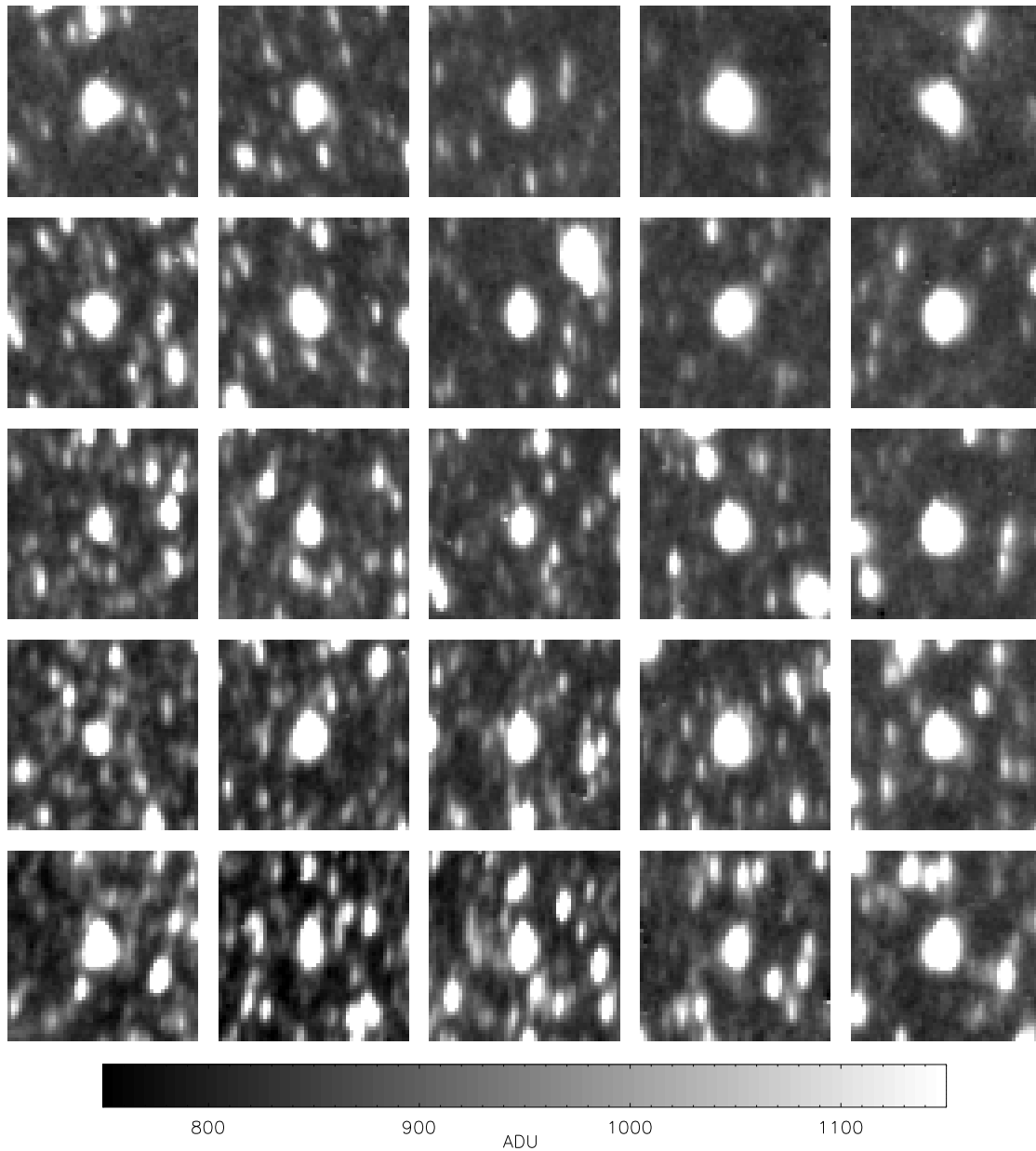


Figure 3.1: A grid of typical star images (PSFs) taken from a corresponding grid of positions on a typical PASS0 calibrated science image. Each image stamp is 50×50 pixels. Note that all stars are blended to some degree.

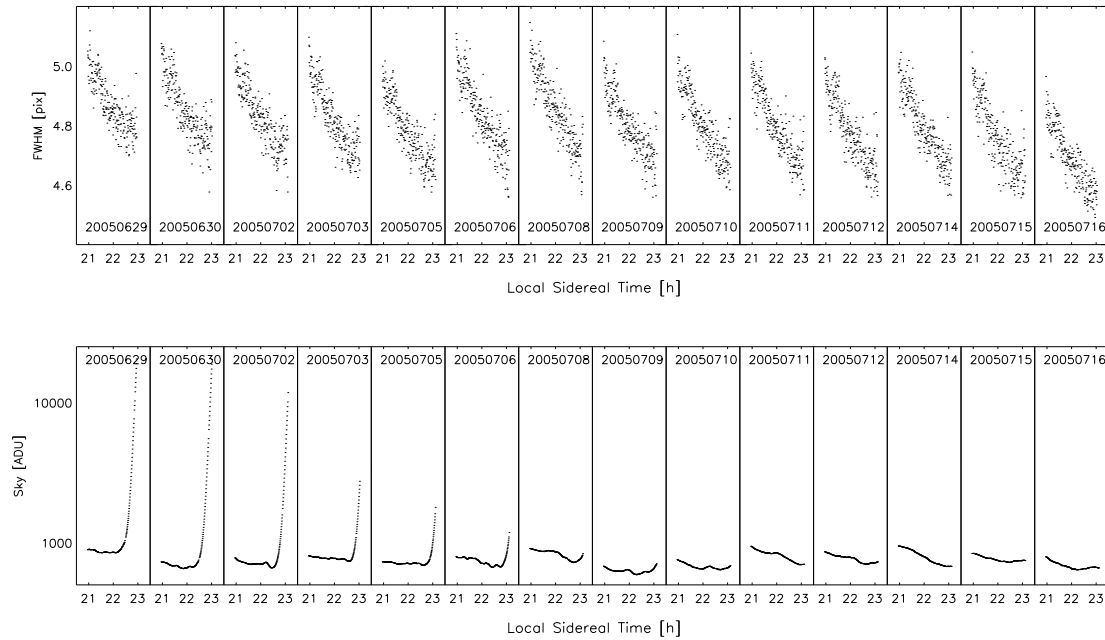


Figure 3.2: Plot of trends in FWHM and sky background level in the science frames against LST for each night of our PASS0 data.

image subtraction method is flexible enough to deal with the complexity of the PASS stationary mode and lens deformation, which complicate the shape of the PSF, and its stability across the CCD, because the method models the differences in the PSF between frames, not the PSF itself. In Figure 3.1, we illustrate the complicated PSF shape as a function of position on the PASS0 CCD. Note that all stars are blended to some degree, and for this figure we have tried to show relatively unblended bright stars.

Image subtraction also has another important advantage over aperture photometry. Aperture photometry has a larger confusion radius (smallest angular distance between two resolvable stars [40]) when considering blended objects, since a blend can be considered as any contaminating star within the photometric aperture, which usually has a radius of at least 1.5 FWHM in order to contain all the star flux. The confusion radius for image subtraction is determined by the PSF fitting on the reference image which can separate sources usually down to at least one FWHM or better. Only for sources closer than this will the reference flux become contaminated by a blending source, which in turn affects the image subtraction lightcurves. This advantage in terms of reducing the effects of blending is important because Kiss & Bedding [40] have shown that up to 50% of stars in typical wide-field transit surveys can be affected by blending objects within 3 magnitudes.

3.1.2 Stage 1: Reference Images and Astrometry

For the difference image analysis (DIA), we have opted to use the core elements of the software described in Bond et al. [9] and in Bramich et al. [11]. It is worth mentioning that a similar software package is available called ISIS by C. Alard [2], [3]. However, we prefer the Bond & Bramich DIA package (from now on BBDIA), since it uses PSF fitting on the difference images to measure the difference flux, which is more suitable for measuring a trailed PSF than the circular aperture photometry employed by ISIS. The difference imaging part of the PASS0 pipeline is organised into three consecutive stages. The first stage involves the analysis of each reference image including astrometry which is described in this section. The second stage is producing the difference images and the third stage consists of measuring the difference fluxes.

In order to employ difference imaging, we are required to choose a reference image for each set of images grouped by common LST. The reference frame is selected by measuring the mean FWHM (Full-Width Half-Maximum) and the sky background level in the science frames, and choosing the night that yields the smallest average FWHM and the smallest average sky background level. The FWHM we measure is along the long-axis direction of the PSF which is also in the y direction on the CCD. Figure 3.2 shows the trends of FWHM and sky background level against LST for each night of PASS0 data. Notice that the FWHM improves by a small but significant amount (up to 0.2 pix) over the two hours of observations. This trend has two possible explanations, the first of which is that the camera focus may depend on temperature, and the temperature drops as the night continues. However the exactly repeated pattern implies that our second explanation is probably more likely. There is an area of sky with a much higher concentration of stars (due to being close to the Galactic plane). This area of stars starts off near the edge of the CCD where the FWHM is worse and moves towards the centre of the CCD where the FWHM is better. These stars dominate the mean FWHM calculation and hence the observed decrease in mean FWHM.

We have found that choosing the best night overall to define the reference frame instead of the best frame per LST minimizes differences in extinction and seeing between the reference frames in consecutive LSTs, and therefore provides consistency in the measurements of the instrumental magnitudes on the reference frames. Also, we found that the rate of matching stars between consecutive LSTs is much better if all the reference frames belong to the same night. From the evidence presented in Figure 3.2, we choose the night of the 16th July 2005 as the reference night (2005-07-16). Finally, we cannot consider combining images from the same LST on various nights in order to make a high signal-to-noise reference frame since our data set was taken on nights with different weather quality, with only one set of observations in pristine conditions, and we would need at least two very high quality nights. By combining reference frames, this can also create a fundamental problem for variable stars.

Stars are detected in each reference image using the DAOFind algorithm available within IRAF, which produces a list of stars along with corresponding x and y coordinates (DAOFind is part of the DAOPHOT stellar PSF fitting package developed by Stetson [77]). We note that with the trailed PSF, the definition of what constitutes a star within DAOPHOT needs to be modified. Detected objects have a measured quantity called “round” defined by the following equation:

$$R = \frac{h_x - h_y}{(h_x + h_y)/2} \quad (3.1)$$

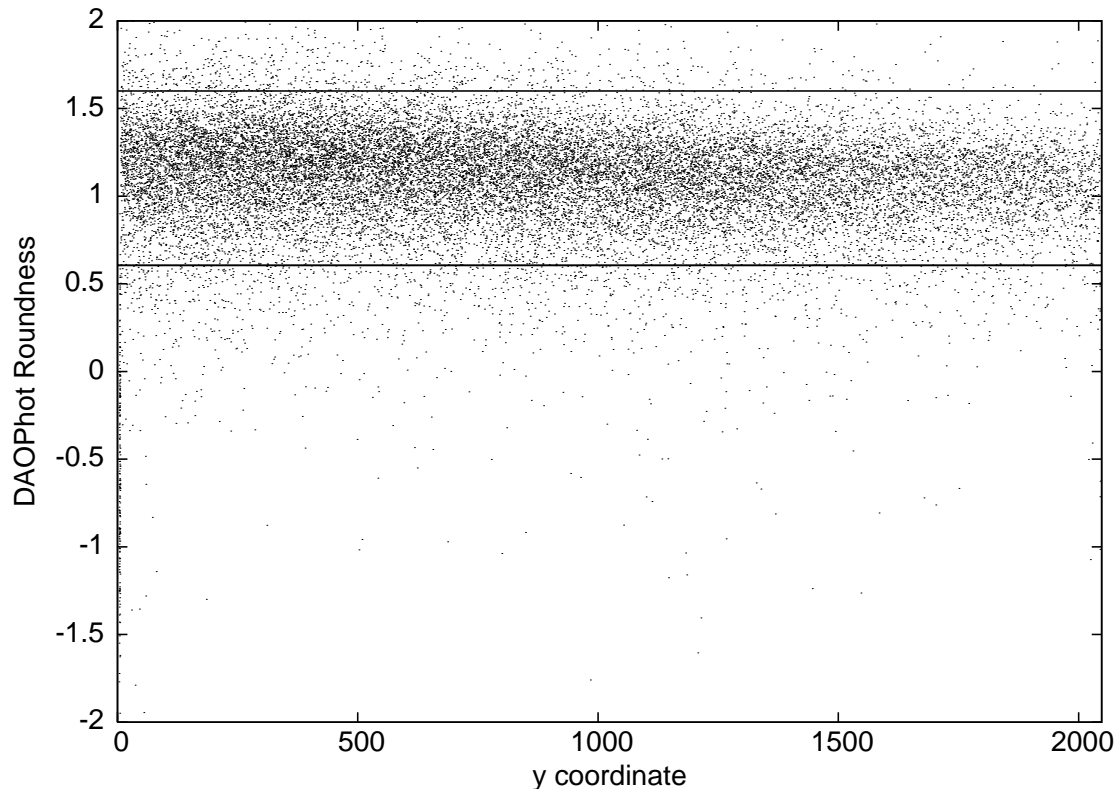


Figure 3.3: Plot of DAOPhot roundness statistic R versus y pixel coordinate. Horizontal continuous lines mark the range of acceptable roundness values.

where R is the roundness, h_x and h_y are the heights of the gaussians fitted to the projected flux distributions in the x and y directions respectively. An object elongated in x will have R less than zero, and an object elongated in y will have a value of R greater than zero. Stars, with radially symmetric PSFs, are normally found by only choosing objects with R in the range -1 to 1.

In fact the stars trail across the chip in the y direction leading to elongated PSFs in the y direction. This is visible in Figure 3.1. Also, when we plot the DAOPHOT roundness R versus the y pixel coordinate for the objects detected on a single reference image in Figure 3.3, we find that R takes on values around a median of ~ 1.1 , a positive value indicating that the PSFs are elongated in the y direction. Hence we only accept objects as stars if they have a value of R in the range 0.6 to 1.6 (this range is delimited in Figure 3.3 by two horizontal continuous lines).

The noticeable gradient in R with the y pixel coordinate in Figure 3.3 may be explained by the fact that as stars trail from small y to large y , the trail is not straight but slightly curved due to the Earth's rotation. We illustrate this in Figure 3.4 by plotting the tracks of a random set of stars across the CCD. We also mark on the track of the known star HD209458 hosting a transiting planet. As you can see, this star fully crosses the chip in the course of the observations, and so the lightcurve for this star is of maximum duration on each night (~ 2 hours each night).

The DAOPHOT package, from within IRAF, is used to measure the instrumental fluxes of

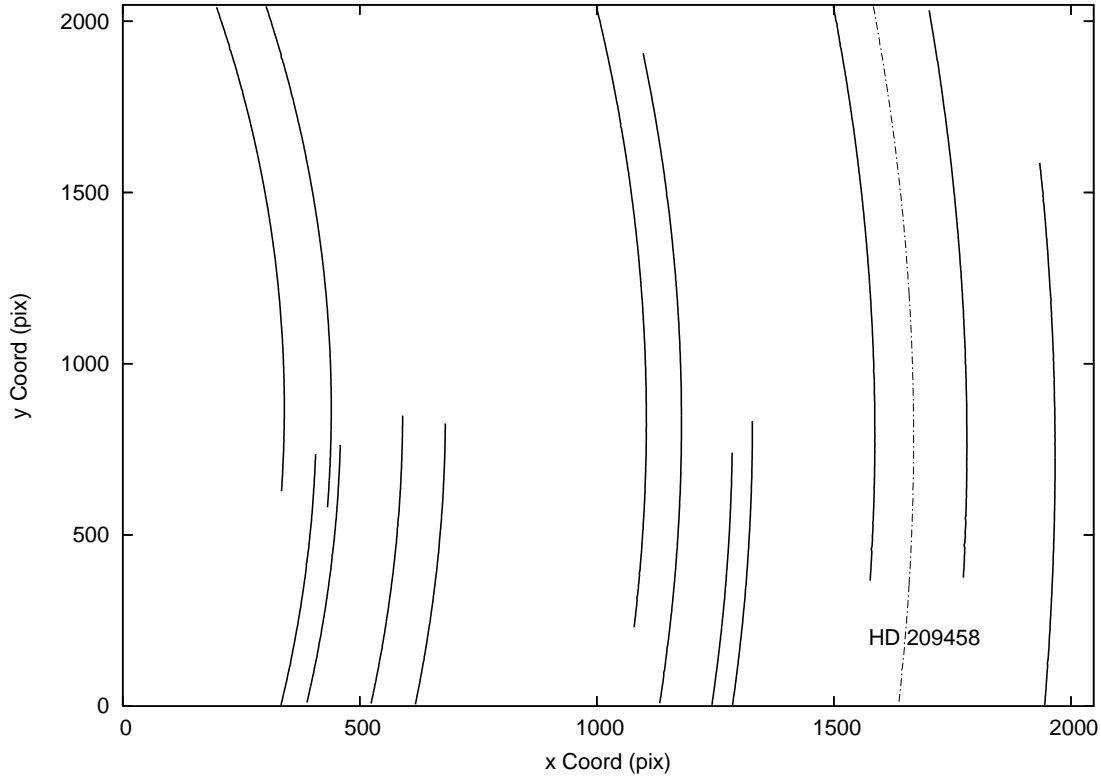


Figure 3.4: Plot of star tracks across the PASS0 CCD for a few random stars. The track for HD209458 is plotted as a dot-dashed curve.

the detected stars on the reference images via PSF fitting. For each reference image, the software works by automatically choosing 175 bright PSF stars. The PSF stars are then fitted with a “penny2” function, which is allowed to vary quadratically with position, and a lookup table of residuals. The neighbours of the PSF stars are then subtracted using this solution, and a new PSF function is solved for. This new solution is used to measure the instrumental fluxes and accurate positions of all stars on the reference image. The result is a set of reference images with corresponding star lists that report reference fluxes and positions.

A full astrometric solution for each reference image is derived using the WASP0 astrometric pipeline. The declination of a PASS0 field is the same at all LSTs and on all nights, and we use the initial estimate of the declination present in the image headers as a first approximation for the field centre. The right ascension of a PASS0 field is constantly changing and is given by:

$$\Theta = h + \alpha \quad (3.2)$$

where Θ represents local sidereal time, h is hour angle, and α is the right ascension. In this experiment, PASS0 was pointed at the sky vertically overhead (the zenith), toward the local meridian. In this case, $h = 0$ and $\Theta = \alpha$. Therefore, by measuring the LST, we are approximately measuring the right ascension of the field centre.

Our experiment requires a high precision measurement of the LST so that we can time exactly when to start each exposure and calculate an accurate right ascension. To overcome this problem we have used a GPS device to supply the observing script with the precise location and current time (UT). The calculated RA and constant declination of the field centre are written to each image header.

The WASP0 astrometric pipeline uses its own object detection routine (`extractor` from the STARLINK package) to create a coordinate list of the brightest 200 stars for each PASS0 science image, along with their approximate instrumental magnitudes. Using the approximate field centres from the image headers and known PASS0 field orientation, the WASP0 astrometric pipeline attempts to match the 200 brightest stars in each image to objects in the Tycho-2 Catalogue [33]. This catalogue has an astrometric precision of better than ~ 60 mas and a photometric precision of better than ~ 0.1 mag for all stars in the catalogue, which is more than required for matching with PASS0. Also, the magnitude range of Tycho-2 is from ~ 2 mag to ~ 11 mag in the optical, which matches well with the PASS0 magnitude range from ~ 4 mag to ~ 12 mag.

To accomplish the task of matching stars between the Tycho-2 catalogue and those detected on the science image, the WASP0 astrometric pipeline employs a similar triangles technique described in Quine & Durrant-Whyte [67]. Triangles formed by Tycho-2 stars and image stars are matched by shape (where triangle shape is defined by the internal angles), and the process is aided by the prior knowledge of the PASS0 camera pixel scale, and the estimated instrumental star magnitudes. To illustrate the idea of matching similar triangles, we present the matched triangles for a typical WASP0 image in Figure 3.5 (courtesy of A. Collier Cameron and J. Irwin).

The set of matching triangles is converted into a list of matching stars from which an initial 4-parameter astrometric solution is derived describing the translation, scaling and rotation of the CCD coordinates in the tangent plane. This solution allows the cross-identification of many more stars with their Tycho-2 counterparts. The location of the optical axis on the sky and on the CCD, along with the barrel-distortion coefficient, are refined iteratively and a final 6-coefficient astrometric fit is computed, correcting for any small amount of image shear that may be present. A great advantage to our fixed observing mode is that at the same LST, stars are at exactly the same position regardless of the amount of camera distortion, and for difference imaging this avoids the need to pre-align images and use image resampling.

3.1.3 Stage 2: Image Subtraction

The second stage of the PASS0 BBDIA pipeline starts by adding various header keywords that are required by BBDIA to the science image headers. Also, each debiased and flat-fielded science image has its sky background fitted with a 2D polynomial of order 6. The fitted surface is then subtracted from the science image to leave the background flat and essentially with a zero mean value. The BBDIA code requires positive pixel values due to the fact that bad pixels are identified with a value of -1 and hence a constant background, derived from the previous fit, is added back to the science images.

The image subtraction method relies on accurately matching the PSF between the current science image and the corresponding reference image. The reference image, by construction, has the best seeing (smallest FWHM PSF) and it therefore needs to be convolved (blurred) with a

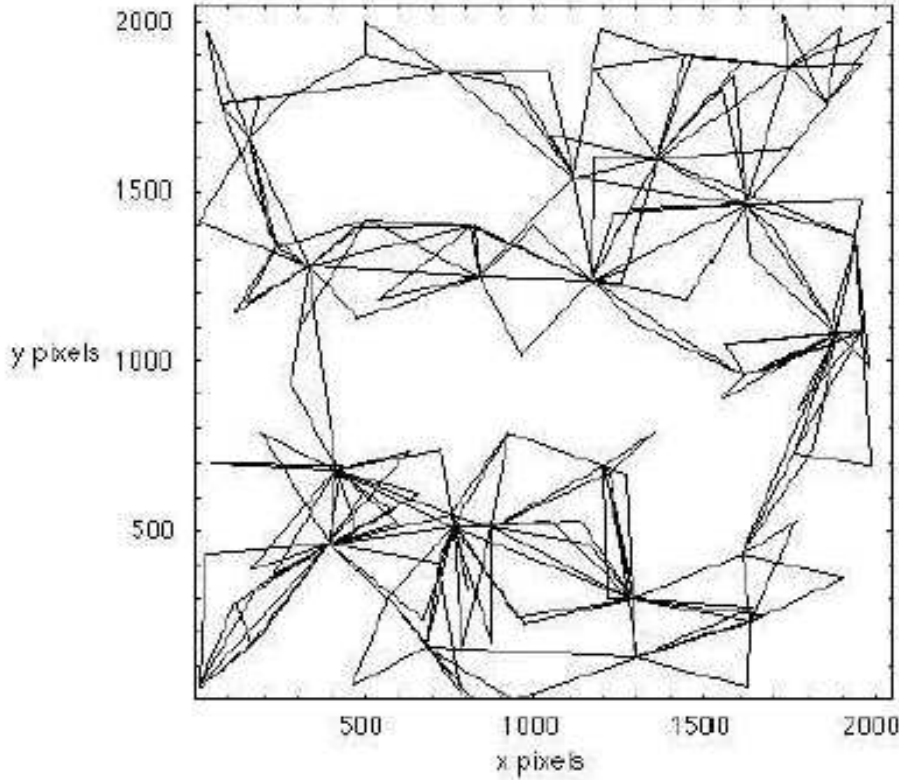


Figure 3.5: Set of triangle matches that have been successfully determined for a typical WASP0 image (courtesy of A. Collier Cameron and J. Irwin).

convolution kernel in order to match the current science image. This relation can be written as:

$$R \otimes K(x, y) + B(x, y) = I(x, y) \quad (3.3)$$

where $R \otimes K(x, y)$ is the reference image convolved with the kernel $K(u, v, x, y)$ with kernel coordinates u and v (\otimes is the symbol for convolution), $B(x, y)$ is the differential background, and $I(x, y)$ is the current science image. The convolution of the reference image R with the kernel K is defined by:

$$R \otimes K(x, y) = \int \int R(x - u, y - v) K(u, v, x, y) du dv \quad (3.4)$$

The BBDIA package solves for a spatially variable kernel as a sum of 3 Gaussians with sigmas 0.7, 1.3 and 2.1 pix, multiplied by polynomials of degree 6, 4 and 2 (respectively) in u and v , and further multiplied by a polynomial of degree 2 in x and y . The differential background B is modelled in BBDIA as a polynomial of degree 2. Difference images $D(x, y)$ are constructed as:

$$D(x, y) = I(x, y) - R \otimes K(x, y) - B(x, y) \quad (3.5)$$

A star that has stayed constant in brightness between the reference image and the current science image should leave no residual counts on the difference image. Hence, a field with no variable objects should result in a difference image composed entirely of noise (readout noise and photon noise). In fact, only variable stars should show a residual PSF on a difference image, positive or negative depending on whether an object increased or decreased in brightness with respect to the reference image. The flux contained in the residual PSF, called the difference flux, may consequently be measured. A small number of non-variable stars will not have a completely clean subtraction. This may be caused by small misalignments between images, although this is compensated for in the kernel solution process.

In the PASS0 BBDIA pipeline, we opted to split each image into four square sections and solve for the kernel and differential sky background in each section. This was found to produce “cleaner” image subtractions than simply solving for the kernel and differential sky background for the image as a whole.

Also, as a final step, a high signal-to-noise ratio empirical PSF for the reference image is constructed for a 3 by 3 grid in each section by stacking a set of suitably resampled stamps centred on bright and relatively isolated stars. This means that there are 36 empirical PSFs corresponding to a 6 by 6 grid for each reference image. Each PSF is 27×27 pixels in size which easily includes the full PASS0 trailed PSF shape. The empirical PSF is constructed for use in measuring the difference images, after modification with the kernel function to produce a PSF for each star on each science image (see Section 3.1.4).

3.1.4 Stage 3: Measuring Difference Fluxes

In BBDIA, difference fluxes are measured using the empirical PSF constructed for each square section of the reference image in Stage 2 (Section 3.1.3). For each star to be measured, the corresponding empirical PSF is resampled at the fractional pixel coordinates of the star, and then it is convolved with the kernel derived in Stage 2. The convolved PSF is then optimally scaled to the difference image at the already known position of the star on the reference image (fixed position PSF photometry). The optimal scale factor Δf of the normalised convolved PSF $P(x, y)$ is given by:

$$\Delta f = \frac{\sum_{x,y} P(x, y) D(x, y) / \sigma^2(x, y)}{\sum_{x,y} P(x, y)^2 / \sigma^2(x, y)} \quad (3.6)$$

and the variance $\sigma_{\Delta f}^2$ is given by:

$$\sigma_{\Delta f}^2 = \frac{1}{\sum_{x,y} P(x, y)^2 / \sigma^2(x, y)} \quad (3.7)$$

where the $\sigma(x, y)$ are calculated from the CCD noise model. If the empirical PSF is normalised to a sum of 1 over all pixels, then Δf supplies an estimate of the difference flux for the star under consideration. A 3σ clip on the residuals of the scaling is performed, and one pixel rejected. The scaling and rejection is repeated until no more pixels are rejected, and the final value for Δf is taken to be the difference flux.

The total flux F_{tot} for a star with difference flux Δf and reference flux F_{ref} (where the reference flux is the star flux as measured on the reference image as described in Section 3.1.2) is given by:

$$F_{\text{tot}} = F_{\text{ref}} + \frac{\Delta f}{p} \quad (3.8)$$

where all fluxes have units of ADU/s and $p(x, y) = \sum_{u,v} K(u, v, x, y)$ is the photometric scale-factor (integral of the kernel solution over u and v). The photometric scale factor $p(x, y)$ is forced to be a constant p for the image by appropriate normalisation of the kernel basis functions in the kernel model. The total flux is converted to a magnitude using the standard relation:

$$M = M_0 - 2.5 \log(F_{\text{tot}}) \quad (3.9)$$

where M is the calibrated magnitude, and M_0 is the zeropoint magnitude (magnitude of a star that gives 1 ADU/s). We are only interested in obtaining a rough absolute calibration of the PASS0 instrumental magnitudes for the purpose of hunting for transits and so we simply determine M_0 from the mean difference between the PASS0 instrumental magnitudes and the Tycho-2 catalogue magnitudes for the brightest 200 stars on the reference image. With this method we obtain $M_0 \approx 15.75$.

In Figure 3.6, we show five image stamps (columns) centred on each of 9 stars (rows) taken from a 3x3 grid on the reference image (where the reference image in this case corresponds to the LST 21:52:30). The first image stamp is a cutout from the reference image (observed on 2005-07-16). The second image stamp is a cutout from a typical science image (observed on 2005-07-06 at LST 21:52:30). The third image stamp is a cutout from the difference image showing the residuals at the position of each star. The fourth image stamp is the difference image with the optimally scaled empirical PSF subtracted at the position of the central star, which shows the quality of the PSF model used to measure the difference image. The fifth image stamp shows the fourth image stamp normalised by the pixel sigmas determined from the CCD noise model. It is clear that our method for measuring the difference images is working acceptably since the fifth image stamp looks like pure noise with no obvious residuals. Included is a clear example of a variable star in the third row and a moving object (maybe a satellite) in the fourth row. Notice how the variable star is correctly subtracted in the difference images in the third row.

3.1.5 Stage 4: Constructing the lightcurves:

At this stage we have a separate reference image with a corresponding star list for each LST, and time series photometry for each star in each star list. In order to construct full lightcurves across all LSTs, we must first match the stars between the different LST star lists, and then extract the relevant photometry to a single file for each unique star. This is most logically done by matching stars between consecutive LSTs and cumulatively building up the lightcurves, since during the course of the night stars drift onto the detector, across and off the detector.

Below we describe the algorithm, employed in the CSHELL script “extract.csh” and in the PERL subprogram “construct_raw_lc.pl”, that is used to construct full lightcurves:

- (1) For each LST, starting at the earliest LST and stepping in time order to the latest LST, the program carries out steps (2) to (8)

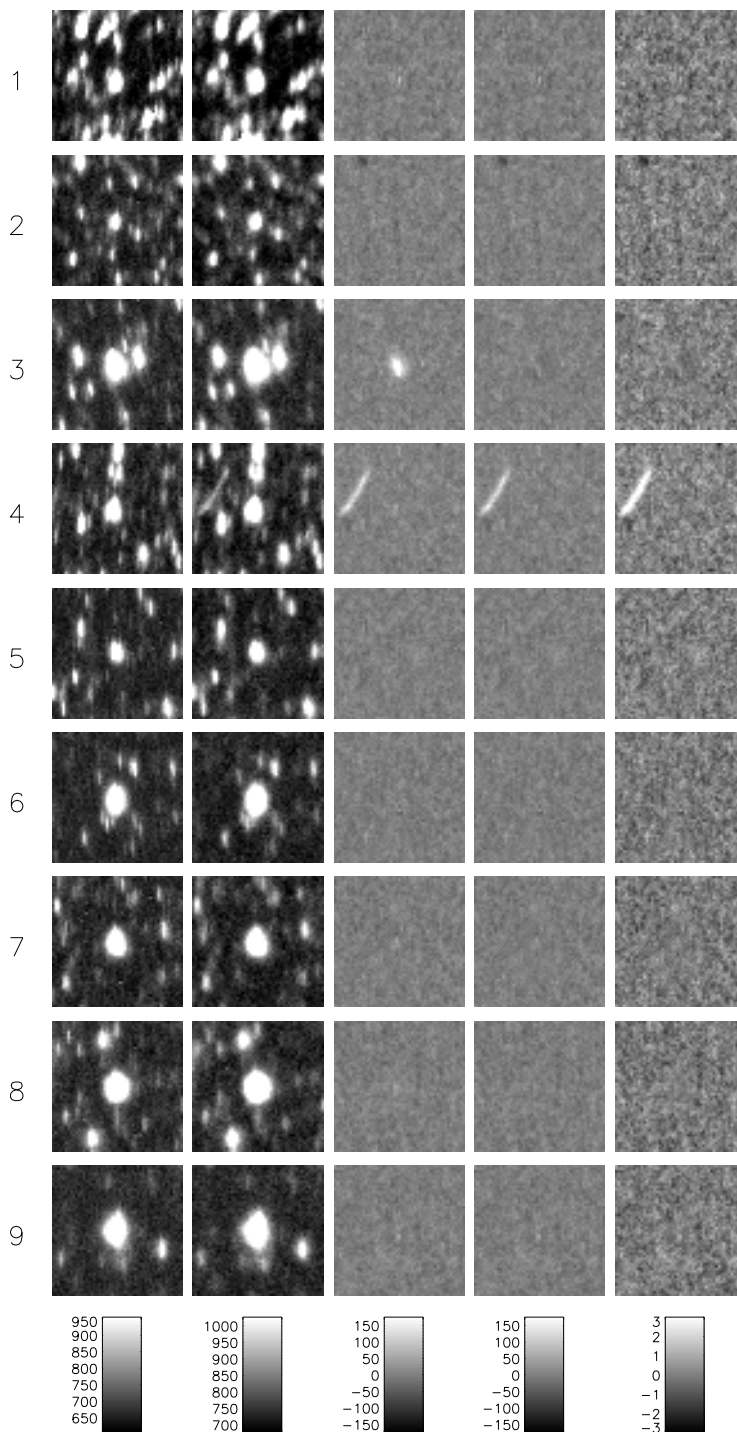


Figure 3.6: Five image stamps (columns) centred on each of 9 stars (rows). The first image stamp is a cutout from the reference image on 2005-07-16 at LST 21:52:30. The second image stamp is a cutout from a typical science image on 2005-07-06 at LST 21:52:30. The third image stamp is a cutout from the difference image. The fourth image stamp is the difference image with the optimally scaled empirical PSF subtracted at the position of the central star. The fifth image stamp shows the fourth image stamp normalised by the pixel sigmas determined from the CCD noise model.

- (2) The program checks that a Tycho-2 catalogue file exists for the current LST, indicating that the derivation of the astrometric solution was successful.
- (3) The program makes a list of the current set of lightcurves.
- (4) For each star in the Tycho-2 catalogue file for the current LST, the program carries out steps (5) to (8)
- (5) The program calculates two (x, y) pixel coordinates of the current star from the Tycho-2 catalogue file corresponding to the beginning and the end of the star trail, and calculates the average pixel position.
- (6) The program searches for the lightcurve file of the current Tycho-2 star in the list of lightcurves. If the Tycho-2 star does not have a corresponding lightcurve, then an empty lightcurve file is created, and the lightcurve name is added to the list of lightcurves.
- (7) The program reads in the DAOPhot star list for the current LST and finds the star in this list that is closest to the average coordinates of the current Tycho-2 star. If this star is less than 2.5 pixels away from the current Tycho-2 star, then a match is considered to have been found, and the program continues by extracting the photometry in step (8). Otherwise the program moves on to the next Tycho-2 star.
- (8) The program extracts the photometry and trend information for the current Tycho-2 star from the BBDIA data files using the star match found in step (7). This information is written to the corresponding lightcurve file.

The whole PASS0 pipeline is summarised in the flow chart shown in Figure 3.7.

3.2 Lightcurve Calibration

Each LST for which we make observations uses a separate reference frame in the PASS0 pipeline, which means that a different reference flux is obtained for each star at each LST. The reference flux for a particular star is dependent on the LST due to changes in airmass, atmospheric extinction, position on the detector and possible intrinsic variability. This problem is illustrated in Figure 3.8 where, in the top row of panels, we show how the reference flux for star 3185-1155-1 (left) and 2679-0493-1 (right) varies as a function of LST (open circles). Star 3185-1155-1 is a typical constant star with mean magnitude 7.44 mag and star 2679-0493-1 is a variable star with mean magnitude 8.33 mag.

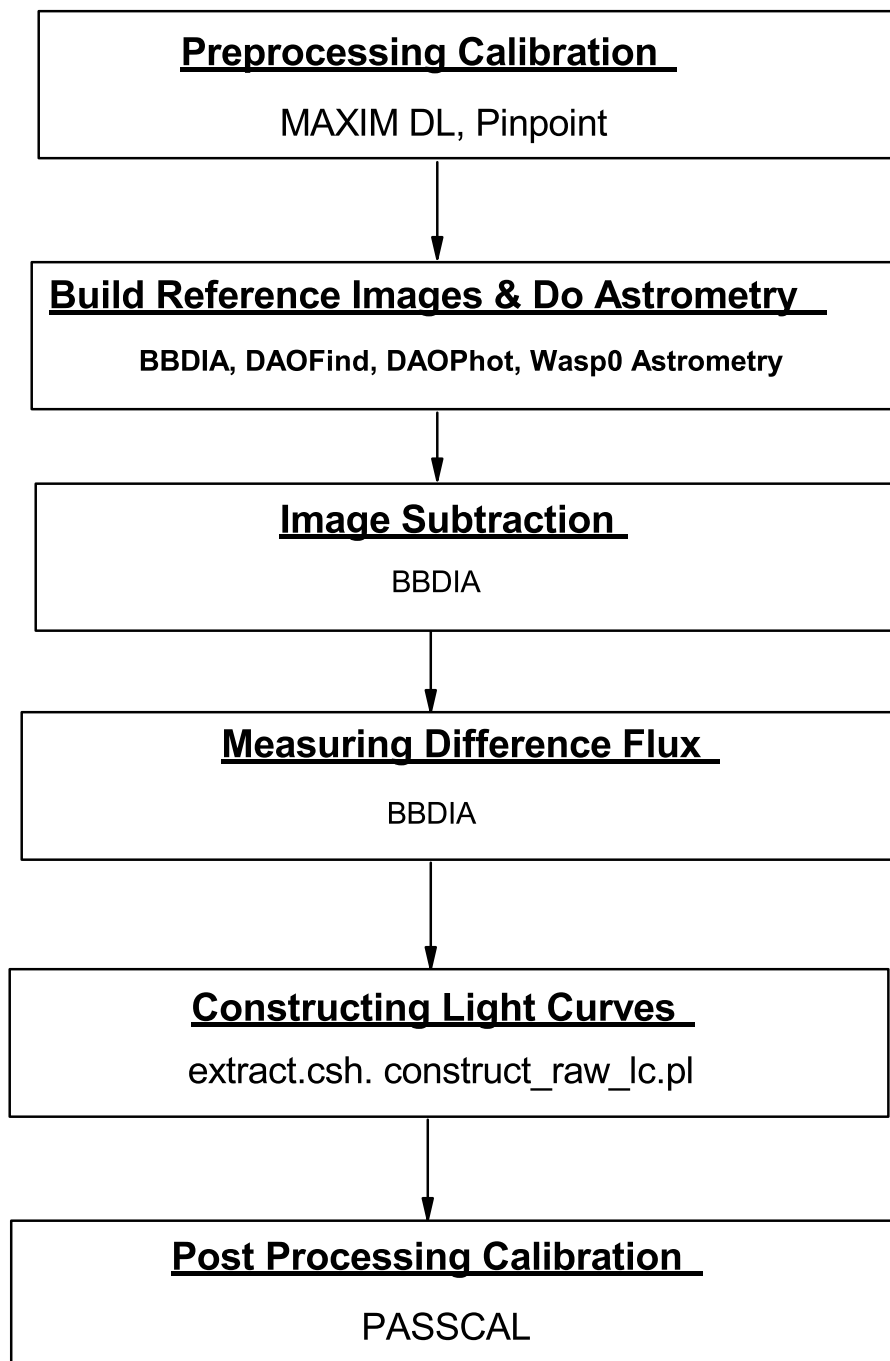


Figure 3.7: A flow chart of the PASS0 pipeline.

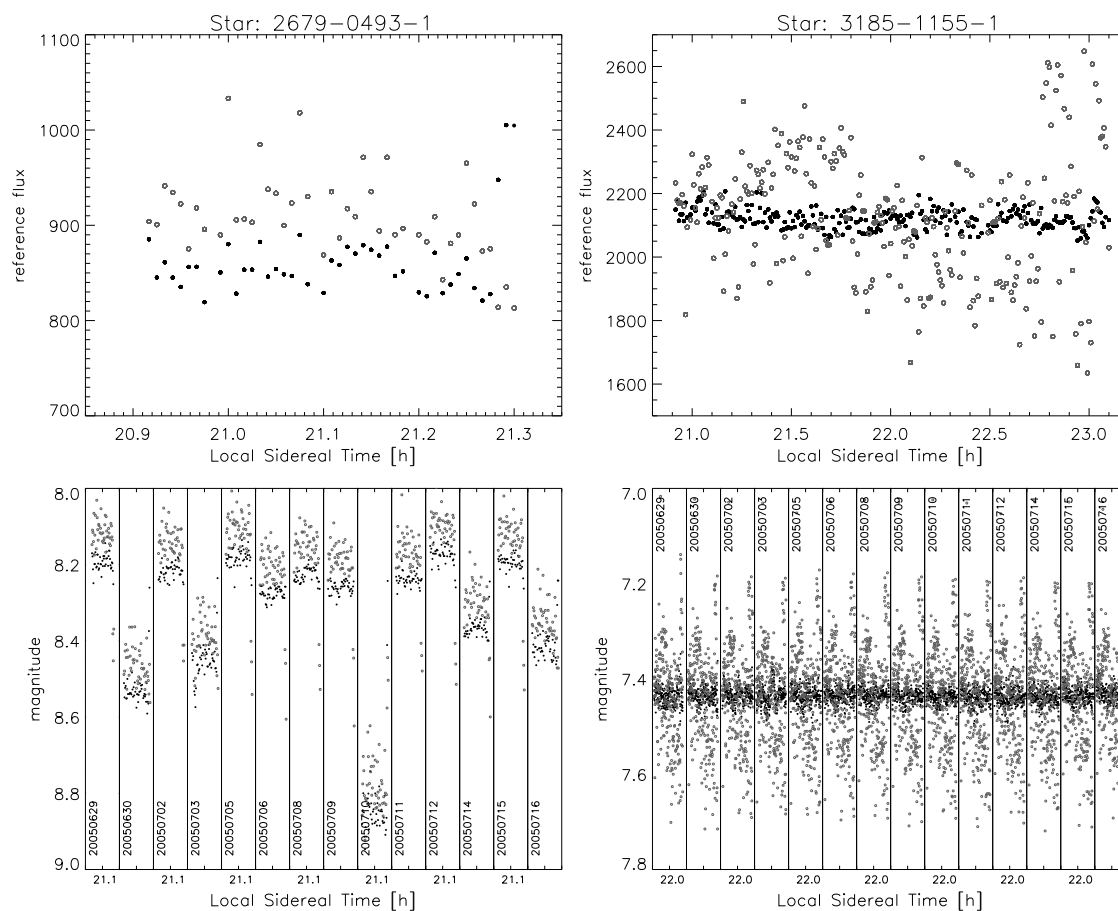


Figure 3.8: In the top two panels we plot the reference flux on the reference night against LST for two stars, a constant star (3185-1155-1 on the right) and a variable star (2679-0493-1 on the left). The open circles represent the reference fluxes before application of the string method, and the solid black circles represent the reference fluxes after application of the string method. In the bottom two panels we present lightcurves of both stars before (open circles) and after (solid black circles) the application of the string method.

The effect that LST-dependent reference fluxes have on the lightcurves is shown in the bottom two panels for the two stars, where we show the full lightcurves of the stars (open circles). Close examination of the open symbol lightcurves in Figure 3.8 indicates that there is an LST-dependent pattern that repeats on each night, greatly increasing the scatter in the lightcurve of every star, including many stars that have no intrinsic variability. Hence we have investigated various methods for calibrating the lightcurves and removing systematic trends that may be present.

3.2.1 The String Method

Our first attempt at calibrating the PASSO lightcurves consists of trying to determine what corrections need to be applied to the reference fluxes in order to remove their LST dependence. The method we use is applied on a star by star basis since each star experiences unique changes in air-mass, extinction and position, especially across such a wide field, and each star enters and leaves the CCD at a different LST.

Consider a single star with observations at N LSTs on each night over a period of M nights. Then we have MN data points, and we require $N - 1$ factors to correct the N reference fluxes. So long as M is greater than 1 then we are guaranteed to be able to determine the factors.

We apply a minimization technique based on the idea behind the string length technique used for determining periods in periodic variables with unknown forms of variations [43]. Stars are most likely constant but they may also be variables of any type and hopefully transit candidates. Hence we cannot make any prior assumption about the lightcurve shape. Instead we calculate a string length between consecutive data points and sum the lengths to get a total length d given by:

$$d = \sum_{i=1}^{NM-1} m_{i+1} - m_i \quad (3.10)$$

where m_i are the lightcurve magnitudes. Then we use the AMOEBA algorithm to adjust the reference flux factors K_j in order to minimize this total string length by recalculating the lightcurve magnitudes as follows:

$$m_i = M_0 - 2.5 \log \left(K_j F_{\text{ref},j} + \frac{\Delta f_i}{p} \right) \quad (3.11)$$

where $F_{\text{ref},j}$ is the relevant reference flux for the LST j that applies to the data point i .

To help illustrate why we do this, imagine the data points as beads threaded by a string. The beads are allowed to move vertically in small groups (grouped by LST). By pulling the string taught you try to minimize the string length between the beads and the system will settle into its natural shape. This shape depends on the underlying variations in the light from the star. Since we are only interested in adjusting the reference fluxes, we do not consider the dependence of the string length on epoch of observation.

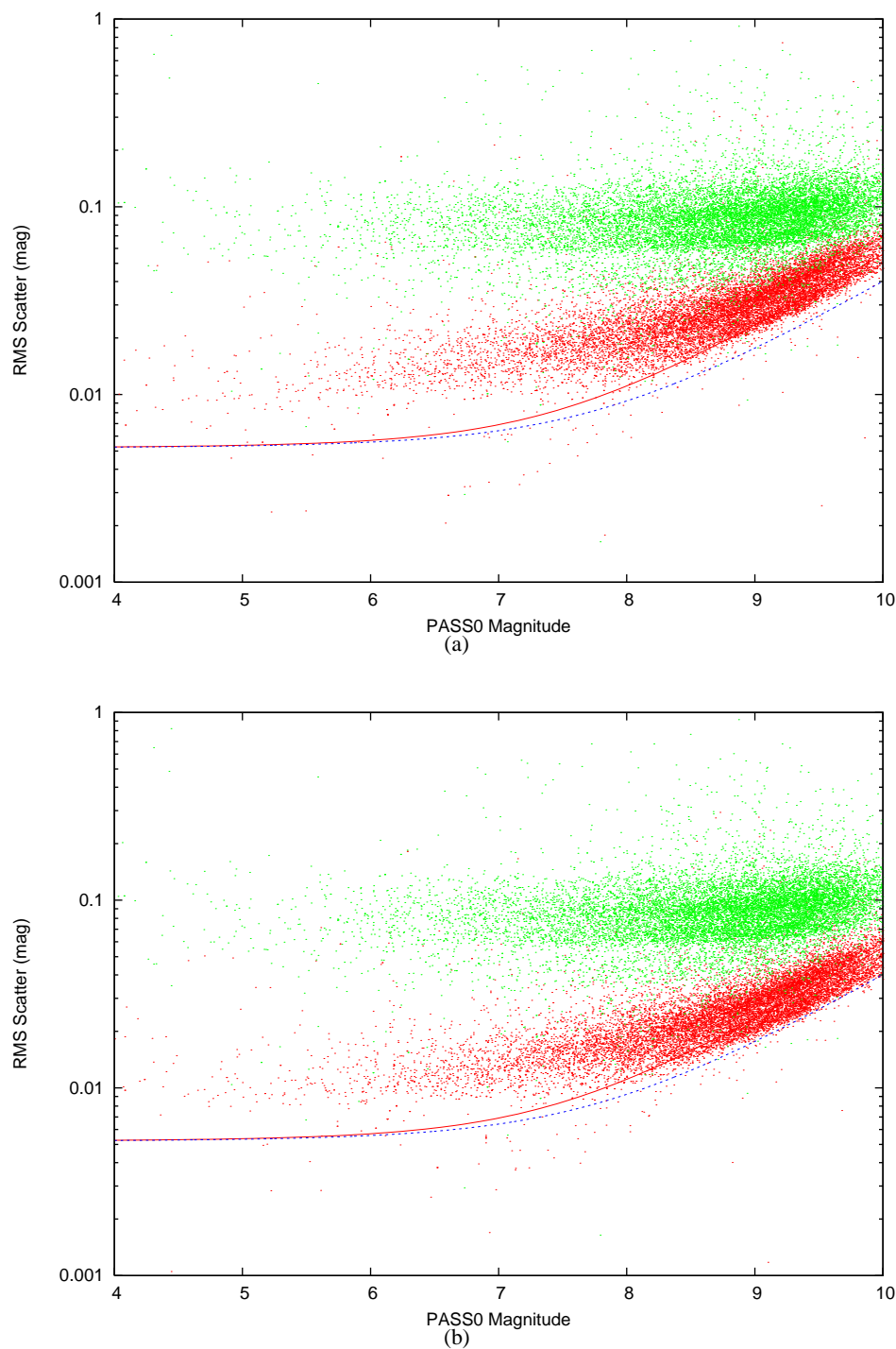


Figure 3.9: **(a)**: Plot of RMS scatter against mean magnitude for the PASS0 lightcurves before (green points) and after (red points) calibration using the string method. The red line shows the aperture photometry theoretical limit using the special extended aperture suitable for the trailed star images, and the blue dashed line shows the theoretical PSF photometry limit calculated using the known PASS0 PSF. Scintillation noise at 5.2 mmag has been included. **(b)**: The same as (a) except that the red points now represent the PASS0 lightcurves after calibration with PASCAL.

In Figure 3.8 we also show the reference fluxes (top panels) and lightcurves (bottom panels) for the two example stars after calibration with the string method (solid black points). In correcting the reference fluxes using the string method, it is now obvious which star is the constant star and which star is the variable star.

In Figure 3.9(a) we plot the RMS scatter in the lightcurves versus PASS0 mean magnitude (calibrated to Tycho-2 catalogue magnitudes). The green points show the RMS scatter for the raw lightcurves from the pipeline, and the red points show the improvement after applying the string method that we have developed. In calculating the theoretical aperture photometry limit we have assumed that a special aperture is necessary. This aperture consists of a rectangle with a semicircle at each end (on the ends in the direction of the star trail; see Figure 2.6). The aperture is defined by the diameter of the semicircles and the length of the rectangle. For observations near the celestial equator we calculate that the trailing in 20 seconds requires a rectangle of length ~ 5.2 pix (or ~ 5.0 arcmin; see Equation 2.45) and the PASS0 PSF requires a semicircle diameter of 7.0 pix (exactly the same size as for the SuperWASP pipeline in Chapter 4). The theoretical aperture photometry limit is plotted in Figure 3.9(a) as the solid red line. Finally the theoretical PSF photometry limit is calculated using Equations 2.17, 2.18 and 2.23 with the known PASS0 PSF and it is plotted as the dashed blue line. A scintillation noise of 5.2 mmag (as calculated in Section 2.3.10) has been added in quadrature with the noise models to account for this effect.

It is clear from Figure 3.9(a) that the string method greatly improves the raw PASS0 lightcurves but it does not reach to the theoretical PSF photometry limit and it does only slightly better than the aperture photometry limit towards the faint end (from 9th mag and fainter). The spread in RMS at each magnitude is due to the fact that most PASS0 lightcurves have fewer epochs than the maximum number since stars drift on, over and off the CCD. Also, the wide field-of-view of the PASS0 camera means that each star has a slightly different airmass at each epoch and the varying amounts of scintillation noise present for each star contribute to this spread in RMS. The theoretical limits presented have been calculated assuming that all epochs are present in a lightcurve and that the scintillation noise is the same as that in the field centre for the whole field-of-view.

3.2.2 PASSCAL

As we have seen in Section 3.2.1, there is still room for improvement on the results obtained using the string method for calibrating the PASS0 lightcurves. Our second attempt at calibrating the PASS0 lightcurves takes a different and more logical approach to the problem where we attempt to model the flux correction factors as a function of LST, night of observation, and detector position using the lightcurves themselves. These factors may then be applied to the lightcurves to remove any systematic trends that are found.

We choose to model the flux correction factor K as a function of LST t , night of observation n and detector coordinates x and y . The form we choose for $K(t, n, x, y)$ is:

$$K(t, n, x, y) = k_1(t) k_2(n) k_3(x, y) \quad (3.12)$$

The most important correction factor is $k_1(t)$ since it allows for the fact that a different reference image is used for each LST and we have already seen some examples in Figure 3.8 of the systematic trends in the reference flux as a function of LST that need to be corrected. The $k_2(n)$

correction factor adjusts the brightness of all stars at all LSTs by a different amount for each night of observation, which models changes in extinction between nights. Since the airmass range for our PASS0 images is so small as PASS0 was pointed to near the zenith, we do not need to generalise this term to a 2-parameter extinction fit. However, for future data obtained for a pointing away from the zenith, this extension of the model may be necessary. The $k_3(x, y)$ factor allows for correction of star fluxes based on their current position on the detector, which is useful for modelling defects in the chip sensitivity which are not already corrected for by the flatfielding process.

We fit our flux calibration model to our lightcurve data $L(s, t, n)$ (where s represents each star) using iterated optimal scaling to solve for the three patterns $k_1(t)$, $k_2(n)$ and $k_3(x, y)$ in turn. Our model $M(s, t, n)$ for the lightcurve data is therefore:

$$M(s, t, n) = f(s) k_1(t) k_2(n) k_3(X(s, t, n), Y(s, t, n)) \quad (3.13)$$

where $f(s)$ is the mean flux of each star, and $X(s, t, n)$ and $Y(s, t, n)$ are the coordinates of the calculated centroid of star s at time t on night n . If the patterns $k_1(t)$, $k_2(n)$ and $k_3(x, y)$ are already known, then we may calculate $f(s)$ using optimal scaling:

$$f(s) = \frac{\sum_{t,n} L(s, t, n) k_1(t) k_2(n) k_3(X(s, t, n), Y(s, t, n)) / \sigma^2(s, t, n)}{\sum_{t,n} (k_1(t) k_2(n) k_3(X(s, t, n), Y(s, t, n)))^2 / \sigma^2(s, t, n)} \quad (3.14)$$

where $\sigma^2(s, t, n)$ are the lightcurve data variances. Hence, for our first iteration we calculate $f(s)$ by assuming $k_1(t) = k_2(n) = k_3(x, y) = 1$. We then calculate $k_1(t)$ and its variance $\sigma_{k_1}^2(t)$ using our estimated values of $f(s)$ and the optimal scaling formula again:

$$k_1(t) = \frac{\sum_{s,n} L(s, t, n) f(s) k_2(n) k_3(X(s, t, n), Y(s, t, n)) / \sigma^2(s, t, n)}{\sum_{s,n} (f(s) k_2(n) k_3(X(s, t, n), Y(s, t, n)))^2 / \sigma^2(s, t, n)} \quad (3.15)$$

$$\sigma_{k_1}^2(t) = \frac{1}{\sum_{s,n} (f(s) k_2(n) k_3(X(s, t, n), Y(s, t, n)))^2 / \sigma^2(s, t, n)} \quad (3.16)$$

We also normalise $k_1(t)$ as follows:

$$\frac{\sum_t \frac{k_1(t)}{\sigma_{k_1}^2(t)}}{\sum_t \frac{1}{\sigma_{k_1}^2(t)}} = 1 \quad (3.17)$$

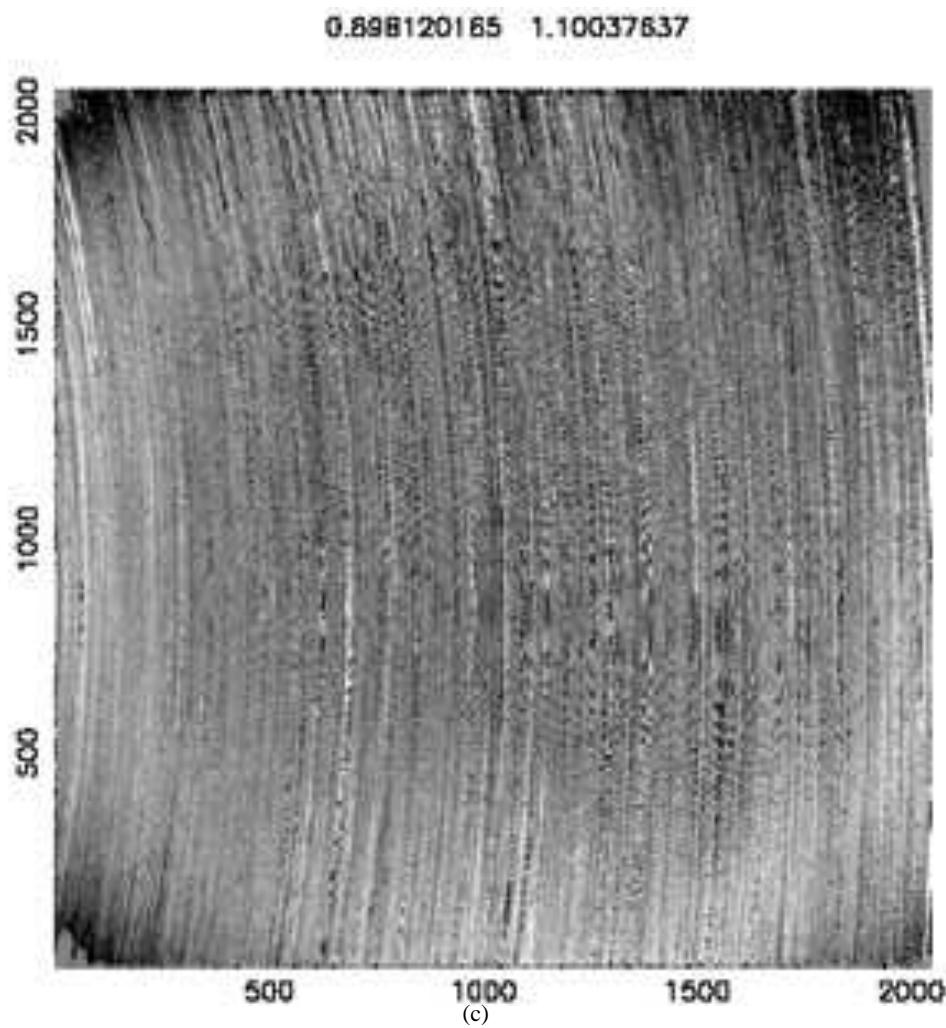
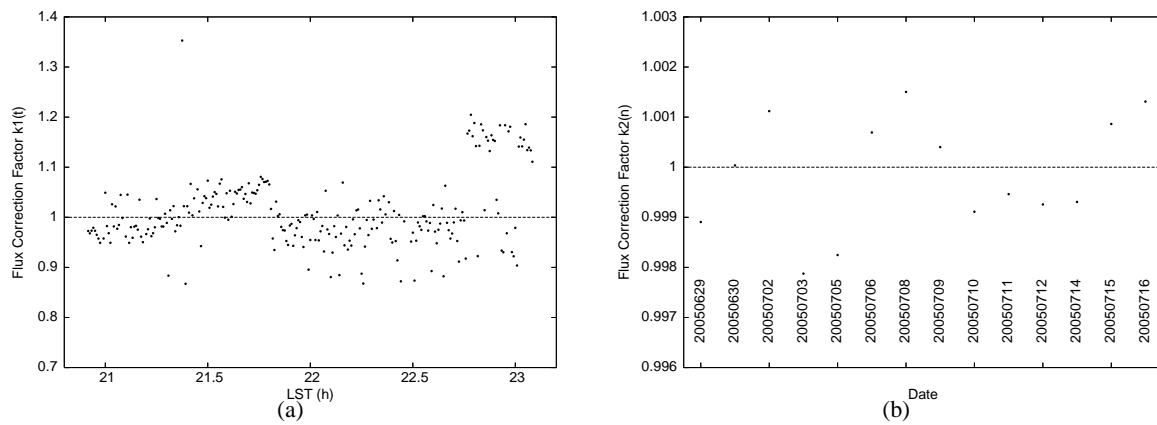


Figure 3.10: **(a)**: The flux correction factor $k_1(t)$ against LST (h). **(b)**: The flux correction factor $k_2(n)$ against observation date labelled directly on the plot. **(c)**: The flux correction factor $k_3(x, y)$ against x and y CCD coordinates as a grey scale image with a linear scale from 0.9 to 1.1.

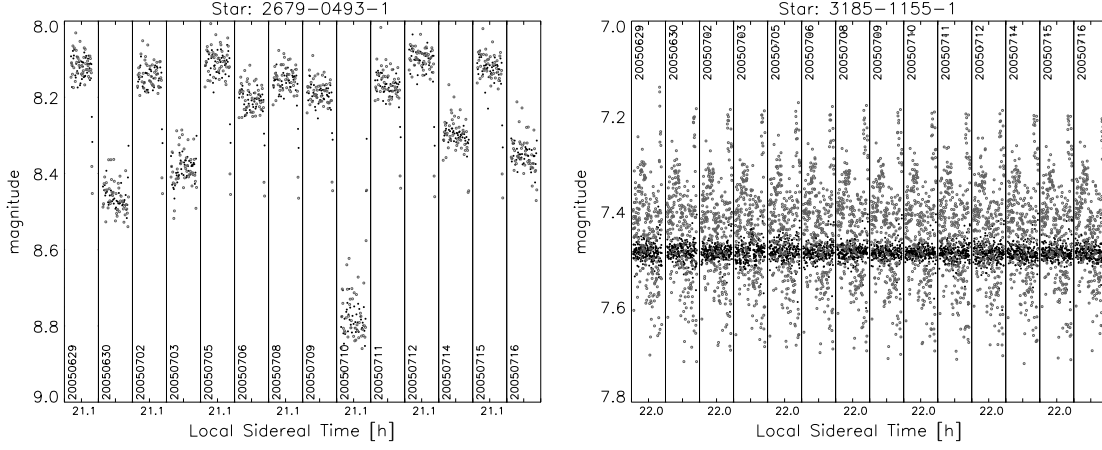


Figure 3.11: On the left we plot lightcurves of the variable star 2679-0493-1 before calibration with PASSCAL (open circles) and after calibration with PASSCAL (solid black circles). On the right we make the same plot but for the constant star 3185-1155-1.

Similarly we may calculate $k_2(n)$ and $\sigma_{k_2}^2(n)$ from the following equations:

$$k_2(n) = \frac{\sum_{s,t} L(s,t,n) f(s) k_1(t) k_3(X(s,t,n), Y(s,t,n)) / \sigma^2(s,t,n)}{\sum_{s,t} (f(s) k_1(t) k_3(X(s,t,n), Y(s,t,n)))^2 / \sigma^2(s,t,n)} \quad (3.18)$$

$$\sigma_{k_2}^2(n) = \frac{1}{\sum_{s,t} (f(s) k_1(t) k_3(X(s,t,n), Y(s,t,n)))^2 / \sigma^2(s,t,n)} \quad (3.19)$$

with normalisation:

$$\frac{\sum_n \frac{k_2(n)}{\sigma_{k_2}^2(n)}}{\sum_n \frac{1}{\sigma_{k_2}^2(n)}} = 1 \quad (3.20)$$

Finally we may calculate $k_3(x,y)$ and $\sigma_{k_3}^2(x,y)$ from the following equations:

$$k_3(x,y) = \frac{\sum_{s,n,t} L(s,t,n) f(s) k_1(t) k_2(n) w(x-X, y-Y) / \sigma^2(s,t,n)}{\sum_{s,n,t} (f(s) k_1(t) k_2(n))^2 w(x-X, y-Y) / \sigma^2(s,t,n)} \quad (3.21)$$

$$\sigma_{k_3}^2(x,y) = \frac{1}{\sum_{s,n,t} (f(s) k_1(t) k_2(n))^2 w(x-X, y-Y) / \sigma^2(s,t,n)} \quad (3.22)$$

where:

$$w(x-X, y-Y) = \exp\left(-\frac{(x^2 + y^2)}{2D^2}\right) / G \quad (3.23)$$

where the D is the sigma of the Gaussian and the factor G is chosen to enforce the normalisation:

$$\sum_{x,y} w(x-X, y-Y) = 1 \quad (3.24)$$

We normalise $k_3(x, y)$ using:

$$\frac{\sum_{x,y} \frac{k_3(x,y)}{\sigma_{k_3}^2(x,y)}}{\sum_{x,y} \frac{1}{\sigma_{k_3}^2(x,y)}} = 1 \quad (3.25)$$

By iterating the process of estimating $f(s)$, $k_1(t)$, $k_2(n)$ and $k_3(x, y)$ in turn, we progressively reconstruct the correction patterns. The iteration process is ended when the fractional change in any one element of $f(s)$, $k_1(t)$, $k_2(n)$ and $k_3(x, y)$ is less than 10^{-4} .

In Figure 3.10 we show plots of the functions $k_1(t)$, $k_2(n)$ and $k_3(x, y)$. The function $k_1(t)$ shows a systematic pattern of up to $\sim 20\%$ and is therefore the most important correction (Figure 3.10(a)). The function $k_2(n)$ shows an amplitude of only $\sim 0.2\%$ and is therefore an insignificant correction in comparison to $k_1(t)$. This is what is expected if the difference imaging pipeline is determining the correct atmospheric extinction for each image via the photometric scale factor. The function $k_3(x, y)$ shows a clear pattern of amplitude $\sim 10\%$ that is approximately a function of the distance from the centre of the CCD. It is probably the result of a difference between the actual vignetting and that taken out by the flatfield.

In Figure 3.9(b) we show the RMS diagram for the PASS0 lightcurves calibrated with the PASSCAL procedure (red points). In the same figure we also show the RMS of the raw PASS0 lightcurves along with the previously calculated aperture and PSF photometry theoretical limits. We have clearly improved on the string method in our calibrations which is to be expected since the methodology behind PASSCAL is based on a model specific to the PASS0 experiment. For ~ 8.8 mag and fainter we are starting to reach the theoretical PSF photometry limit, and from ~ 8.2 mag and fainter we are doing better than the theoretical aperture photometry limit. However at the bright end, the photometry has an RMS of ~ 0.01 mag independent of magnitude. It is most likely that the photometric accuracy is being limited by scintillation down to about 8th magnitude.

In Figure 3.11 we replot the lightcurves of the variable star 2679-0493-1 (left) and the constant star 3185-1155-1 (right) before (open circles) and after (solid black circles) calibration by the PASSCAL routine. The improved quality of the lightcurve of the constant star compared to the lightcurve after calibration by the string method (see Figure 3.8 bottom right) is quite clear.

Future improvements to PASSCAL which are possible, but have not been implemented to date, would include downweighting stars that are clearly variable, downweighting images with large residuals (indicating clouds), and expanding the flux correction model to include colour-dependent correction functions using the Tycho B and V magnitudes.

3.3 HD209458

In the last section of this chapter we mention briefly the lightcurve of HD209458. This transiting planet, the first that was discovered, is present in the PASS0 data that we analysed. The lightcurve of HD209458 has 3426 data points, which is the maximum number, since the star is present on all PASS0 images. In Figure 3.12 we plot the PASS0 lightcurve of HD209458 phased on its period of 3.5247484 d and using a transit epoch of $T_0 = 2451659.93677$ d. These transit ephemerides are taken from Agol & Steffen 2007 [1] who reanalyse all public HST data on HD209458 transits including 13 transit events from 2001 to 2006. The transit event is clearly visible in the PASS0 lightcurve even though we have only caught the first half of one transit on one night (20050630).

We use further transit parameters listed by Agol & Steffen 2007 to calculate a model transit lightcurve. We take the published values for the planet-to-star radius ratio of 0.12, the orbital radius to star radius ratio of 8.883 and the inclination of 85.845° to calculate a model transit lightcurve using the equations of Mandel & Agol 2002 [47]. We also assume a linear limb darkening coefficient of 0.5 as quoted in the original discovery paper [14] for HD209458 as a decent approximation. We plot the model transit lightcurve as the black curve in Figure 3.12. It is encouraging to see that the data follow the model to within the photometric accuracy. We leave the search for variables and transit candidates in the PASS0 lightcurves to Chapters 5 and 6.

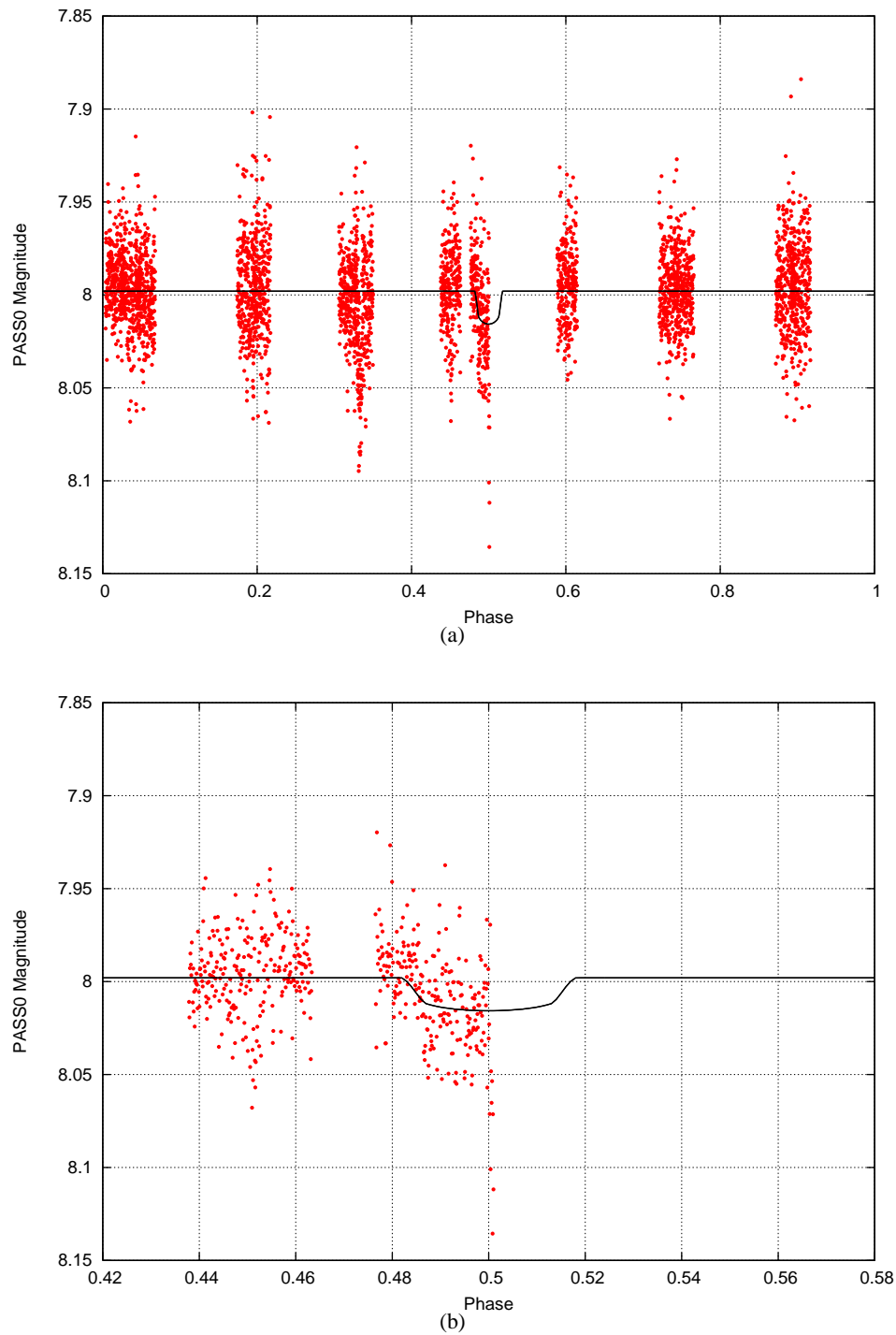


Figure 3.12: **(a)**: Phased lightcurve of HD209458 calibrated using `PASSCAL` (red points). The black curve is the model lightcurve using published transit parameters. **(b)**: Zoom around the transit event of the phased lightcurve of HD209458 (red points). Again the black curve is the model lightcurve using published transit parameters.

Chapter 4

Optimising SuperWASP Photometry

4.1 The SuperWASP Experiment

As described in Chapter 1, SuperWASP, among other wide field surveys, was initiated after the discovery of the first transiting planet around HD209458 [14]. The initial phase of the SuperWASP project was the construction of a prototype system called WASP0. The instrument consisted of a 200mm, f/2.8 Nikon telephoto lens with an AP10 CCD from Apogee. WASP0 was observationally tested both on La Palma in the Canary Islands and at the Kryoneri Observatory in Greece. A handful of transit candidates and many variable stars have been discovered using the prototype [36], [37], [38].

After fine tuning the prototype system and observing procedure, and while developing the reduction pipeline, the WASP consortium were able to get sufficient funds to build multi-detector SuperWASP cameras for the La Palma site. The SuperWASP instrument is made of 8 cameras each containing a back-illuminated CCD from the company Andor of Belfast. Each CCD is 2048x2048 pixels with a pixel size of $13.5\mu\text{m}$ equating to a pixel scale of $13.7''$ per pixel. The camera lens is a 200mm, f/1.8 Canon telephoto lens. Each camera has a field of view of $7.8^\circ \times 7.8^\circ$.

The fields monitored are selected to avoid the crowded Galactic plane regions, and the ecliptic plane (to avoid the Moon and planets). Data reduction is fully automated using a purpose built pipeline [62]. The photometric output is stored in, and exploited from, the SuperWASP data archive held at the University of Leicester. During the 2004 season ~ 6.7 million lightcurves were observed.

4.2 SuperWASP Observations and Reductions

The transiting planet XO-1b [51], the first planet discovered by the XO team [50], is a perfect candidate for comparing the accuracy of photometric reductions using the SuperWASP pipeline and the PASS0 pipeline. The planet transits an 11th magnitude G1 main sequence star with a period of 3.941534 ± 0.000027 d, transit depth of $\approx 2\%$ and duration of ≈ 0.1 d. Hence the target star is bright enough for observation by SuperWASP, the planet is a short-period hot Jupiter, and the transit depth should produce an easily recoverable signal in the SuperWASP data.

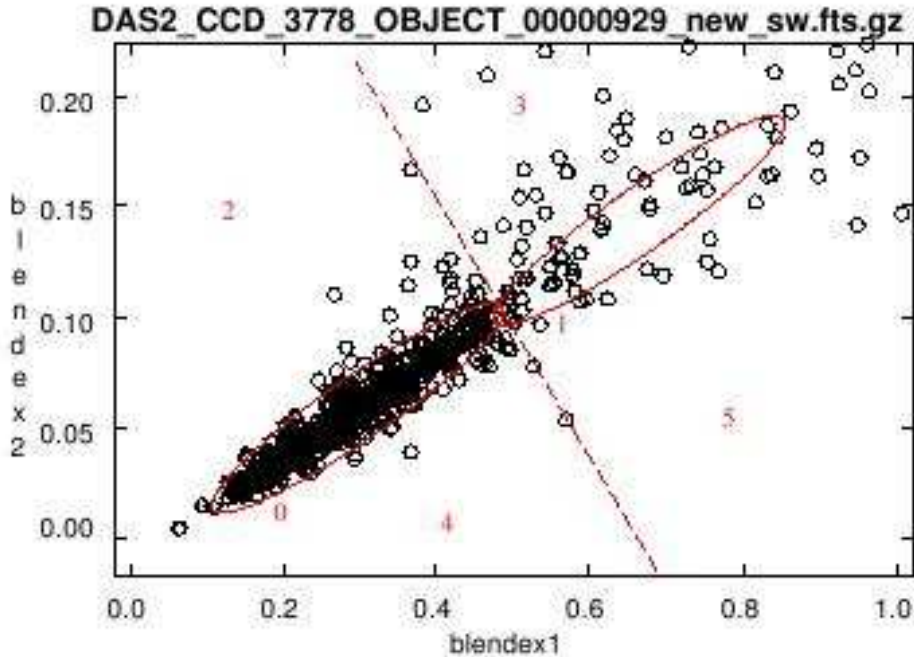


Figure 4.1: Plot of the blending indices Blendex1 and Blendex2 for one particular SuperWASP image. The stars considered to be unblended lie in the locus labelled by a “0”. Figure courtesy of A.C. Cameron.

Up until the end of 2004, the SW-N observing station made 8775 observations of fields containing the star XO-1, including observations of 11 separate transit events. We chose to reconsider 688 of 4585 available images from one specific camera, which were taken over a 15 night period between UTC dates 1st-15th June 2004. This time period includes observations of four transit events, two of which are fully covered and the other two are partially covered. The most densely covered transit event is at $HJD \approx 2453162.5$ d. The chosen sub-sample of the data are sufficient for testing our image subtraction algorithm and assessing the likely improvements that may be possible in comparison with aperture photometry.

The SuperWASP pipeline [62] starts by classifying and sorting out images as bias, dark, flat and science frames and then it produces a master bias, master dark and master flat for each night. Science images are preprocessed in the standard way by subtracting the master bias and the master dark and then dividing by the master flat. The Starlink EXTRACTOR package is used to detect all objects 4σ above sky in the calibrated science frames.

An astrometric solution is determined for each science image by matching detected objects with known objects in the Tycho-2 [33] and USNO-B1.0 [54] catalogs. Then aperture photometry is performed for all USNO-B1.0 sources brighter than 15th magnitude using 3 circular apertures of radius 2.5, 3.5 and 4.5 pixels. A Fermi-Dirac like function is used to assign weights to pixels lying partially outside the aperture to compensate for different aperture offsets from the centre of a pixel.

Since SuperWASP pixels are of size $13.7''$, object blending can be a serious problem. In order to start to sort out blended and nonblended stars, the following ratios are calculated:

$$\text{Blendex1} = \frac{f_3 - f_1}{f_1} \quad (4.1)$$

$$\text{Blendex2} = \frac{f_2 - f_1}{f_1} \quad (4.2)$$

where f_1 , f_2 and f_3 are the measured fluxes in each of the three apertures. Stars are filtered according to the scheme shown in Figure 4.1 where the two ratios Blendex1 and Blendex2 are plotted against each other. The stars in the locus marked by “0” are considered unblended and those outside this locus are considered blended in some way. Other star types range from “1” to “9” and they are not considered suitable for transit searches. The diagonal line shows where the effect of a nearby companion is detectable in the first aperture.

In the search for transit candidates, only stars classed as unblended are considered, which intentionally neglects many possible stars from the analysis. The above method of separating out blends is essential for the SuperWASP project since they use aperture photometry and reliable photometry is required for the transit search. Also, SuperWASP, and other wide field transit surveys, have deliberately avoided the Galactic plane due to the higher stellar density. The image subtraction method provides the possibility of considering not only the unblended stars, but many of those stars that SuperWASP immediately rejects from the transit search because of visible blending, which image subtraction is not affected by.

The other main advantage of the difference imaging technique as opposed to aperture photometry is that optimal PSF fitting can be applied to the difference images. Optimal PSF fitting achieves considerably better S/N than aperture photometry, especially in the sky noise dominated regime. In fact, for the subsample of SuperWASP data we consider in Section 4.3.1, image subtraction combined with optimal PSF fitting can potentially reach 0.33, 0.48 and 0.62 mag deeper than aperture photometry at RMS accuracies of 5, 10 and 20 mmag. Hence many more stars will have lightcurves of the necessary accuracy in order to detect transit signals, therefore increasing the detection potential of the survey.

4.3 Application of the PASS0 Pipeline

4.3.1 Adapting the PASS0 Pipeline

With the aim of judging the performance of the PASS0 difference imaging pipeline on SuperWASP data, we rereduced the 688 SuperWASP images. The rereduction was carried out using the original raw images and calibration frames from the SuperWASP camera. Standard calibrations of debiasing, dark frame subtraction and flat-fielding were carried out as described in Section 3.1.1. On close inspection of the calibrated SuperWASP images it was noted that the PSF is undersampled with a FWHM on average of around 1.9 pixels and that the images suffer from a strong spatially and time varying sky background. In Figure 4.2, we show the PSF shape as a function of position in the SuperWASP CCD using a 5 by 5 grid of positions taken from a calibrated SuperWASP science image.

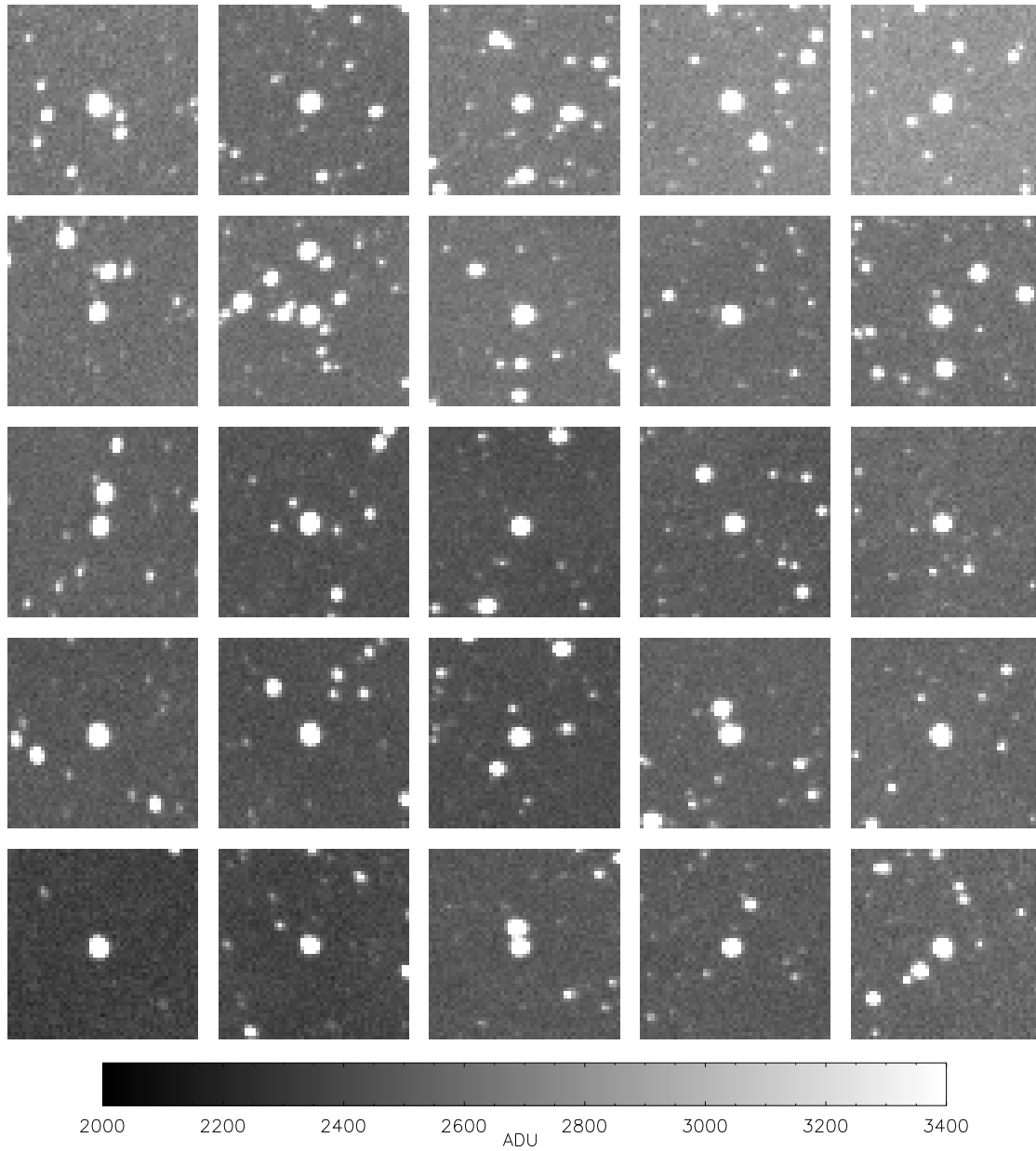


Figure 4.2: A grid of typical star images (PSFs) taken from a corresponding grid of positions on a typical SuperWASP calibrated science image. Each image stamp is 50×50 pixels.

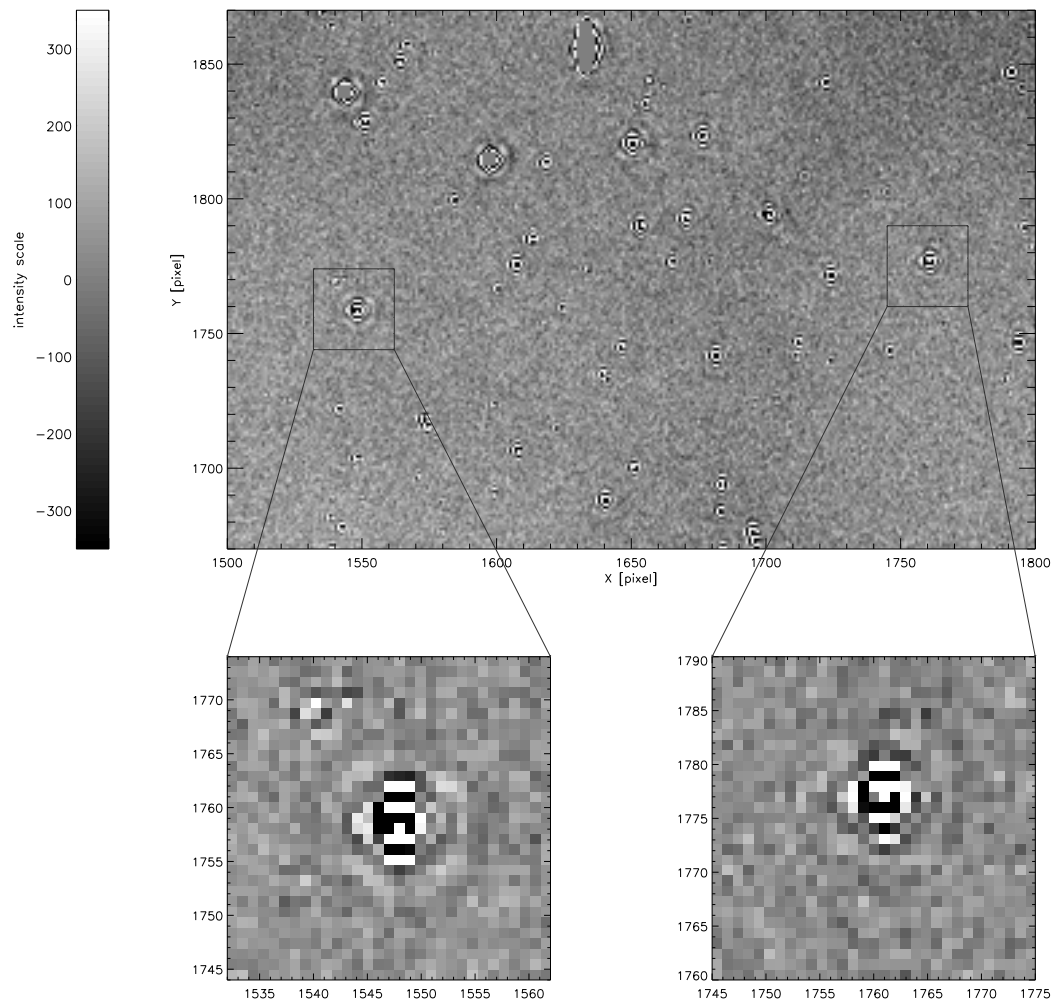


Figure 4.3: A 300x200 pixel subregion of a typical SuperWASP difference image produced by the PASS0 difference imaging pipeline with no image blurring (test N). Highly complicated residuals at the positions of the brighter stars are clearly visible. We supply a zoom on two of the stars to show the residuals in greater detail.

First attempts at using the PASS0 difference imaging pipeline to produce good quality difference images were fruitless. The undersampled PSF on the SuperWASP images made it impossible to derive an accurate convolution kernel. We experimented with different resampling methods for aligning the images and determined that the resampling method was not the cause of the problems with deriving the kernel. We also tried to construct a stacked reference image from a selection of the best-seeing images in order to increase the signal-to-noise of the reference frame, but this failed to solve the problem.

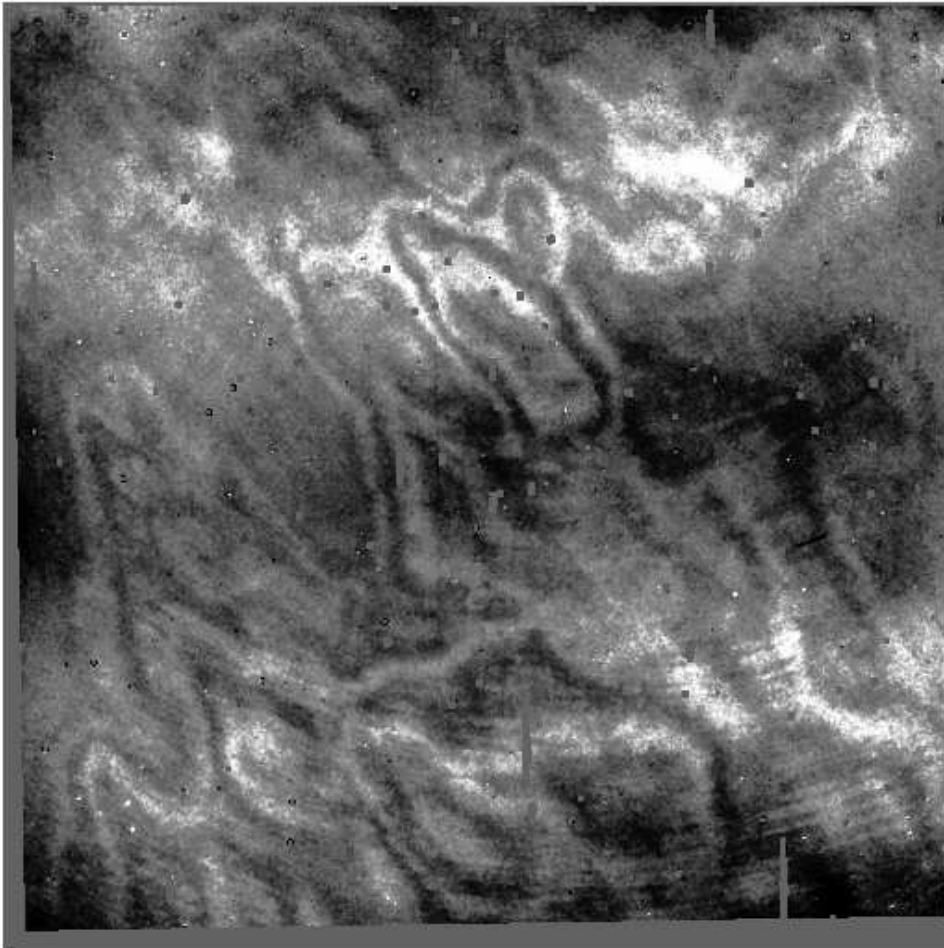


Figure 4.4: A typical SuperWASP difference image produced by the PASS0 difference imaging pipeline. The background residuals range from approximately -80 ADU to 100 ADU, which is the intensity scaling used on this image.

In Figure 4.3 we display a section of a difference image produced with the standard PASS0 difference imaging pipeline. You can clearly see complicated residuals at the positions of the brighter stars. The maximum and minimum scaling on the image is -350 to 350 ADU. In Figure 4.4 we show a full frame typical difference image. It now also becomes clear that SuperWASP images suffer from high spatial frequency fringing at the level of ~ 100 ADU per 50 pixels along with low spatial frequency background variations of the same size.

To attempt to reduce the effect of the undersampling we have taken the approach of blurring each image with a Gaussian convolution kernel. By convolving an image with a Gaussian, we are forcing the image sampling to improve, the amount of which depends on the sigma of the Gaussian used. Since it is not clear what value the sigma of the Gaussian kernel should take, we have tested a grid of values. We also note that because the reference image is required to be the best-seeing image for the technique of difference imaging, we choose to convolve the reference image with a Gaussian that has a smaller sigma than the Gaussian used to convolve the rest of the images.

Since image subtraction is based on the idea of “blurring” the reference image to match the current image, the question arises as to why we pre-blur the reference image with a Gaussian? The reason is that the undersampled nature of the SuperWASP images causes problems for the reference flux analysis of the PASS0 pipeline using DAOFind and DAOPhot. Convolving the reference image with a Gaussian improves the determination of the reference fluxes, which we show later on in Section 4.3.3.

For this test we considered a subset of 198 images from a 3 night period between UTC dates 5th-7th June 2004. This time period includes the most densely covered transit event on the night of 5th June 2004. In Table 4.1 we list the FWHMs of the Gaussians used to blur the reference image and the remaining images, and we include a test V' where we do not blur the reference image in order to analyse what effect, if any, the blurring of the reference image has on the lightcurve accuracy that we obtain.

For each test, the data are reduced using the PASS0 pipeline and blurring is done just before image alignment to the reference image, but after the derivation of the spatial transformation linking the two images. This is to minimise the effect of resampling on a (possibly) undersampled image, but maximise the signal of the stars used for deriving the transformation. The alignment process is very robust since the images are all centred on the same field in the sky and there is very little rotation between images. The blurred reference image is analysed with DAOFind and DAOPhot PSF fitting photometry in exactly the same way as described in Section 3.1.2, except that since the PSFs are circularly symmetric, we use the roundness statistic R between the normal limits of -1 and 1 to detect stars. In this way we construct a list of detected stars on the reference image with associated reference fluxes. Difference images are produced by the PASS0 pipeline which are then measured to produce the difference fluxes for each star. When we scale the empirical PSF to the difference image at the position of each star, we also fit a local sky background as a constant, which removes the need to model the complicated differential background visible in the typical difference image in Figure 4.4.

Constructing lightcurves for the SuperWASP data is much simpler than for the PASS0 data since there is just a single reference image. For each object the total flux $F_{\text{tot}} = F_{\text{ref}} + \Delta f/p$ (see Equation 3.8) at each time is calculated as in Section 3.1.4 and converted to an instrumental magnitude using Equation 3.9. We find that for our particular choice of reference image, by taking

Table 4.1: The list of blur tests using Gaussians of different FWHMs.

Test	FWHM (pix) of Gaussian used to blur the reference image	FWHM (pix) of Gaussian used to blur the remaining images	A (mmag)	B (mmag)	C (mmag)
N	No blurring	No blurring	33.6	9.86	11.3
P	No blurring	0.5	33.4	9.49	11.2
Q	0.5	1.0	26.2	11.0	9.09
R	1.0	1.5	9.96	9.90	7.88
S	1.5	2.0	8.47	11.9	7.04
T	2.0	2.5	7.10	11.2	7.55
U	2.5	3.0	6.78	11.0	8.60
V	3.0	3.5	6.69	10.7	9.68
V'	No blurring	3.5	7.27	10.3	9.72
W	3.5	4.0	6.58	11.8	11.0
X	4.0	4.5	5.91	13.0	12.2
Y	4.5	5.0	5.80	14.3	14.1
Z	5.0	5.5	4.41	16.4	15.3

$M_0 = 19.73$ mag, we bring the lightcurves on to the same magnitude scale as the SuperWASP lightcurves (derived from the 100 brightest star matches).

4.3.2 Comparing the Gaussian Preconvolution Tests

We use an analysis of the RMS diagram for each test in Table 4.1 so that we can assess the quality of the reductions and the noise in the lightcurves as a function of magnitude. In Figure 4.5 we show the RMS diagrams for tests N (red dots), U (green dots) and Z (blue dots). We also show the theoretical noise curve for aperture photometry as the red line (calculated using Equation 2.19, and for optimal PSF photometry as the dashed blue line (calculated using Equations 2.23, 2.17 and 2.18). It is clear that for test N, in which no blurring was carried out, the results are disastrous where at best we achieve an RMS scatter of ~ 0.03 mag at the bright end. Test U, for an intermediate blurring, achieves an RMS scatter close to the theoretical limit for PSF photometry for the stars fainter than ~ 12.5 mags, but only achieves an RMS of ~ 0.007 mag at the bright end. However, we should note that test U actually does better than the theoretical limit for aperture photometry for magnitudes fainter than ~ 12.5 mag. Test Z, for a high blurring, performs with a similar quality as test U for bright stars, but performs considerably worse for magnitudes fainter than ~ 12 mag, because the sky photons become dominant over the star photons for such a large PSF.

The solid curves in Figure 4.5 represent “backbone” fits to the RMS diagram. A “backbone” fit consists of fitting the following model to the RMS diagram using a 3-sigma clip algorithm and the amoeba downhill simplex method to minimise the total of the squared residuals:

$$R(m) = \sqrt{A^2 + (B \times 10^{0.2(m-12.75)})^2 + (C \times 10^{0.4(m-12.75)})^2} \quad (4.3)$$

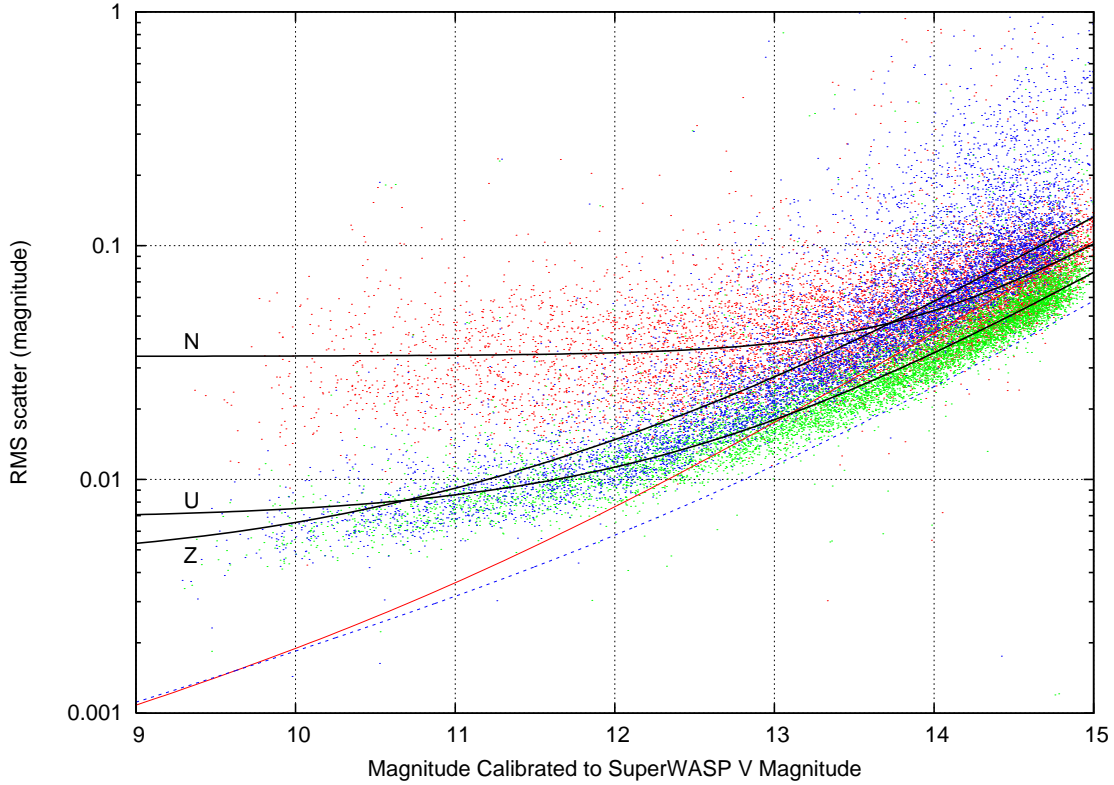


Figure 4.5: The RMS scatter in the lightcurves versus magnitude for tests N (red dots), U (green dots) and Z (blue dots). The theoretical noise curve for aperture photometry is shown as the solid red line and, for PSF photometry, it is shown as the dashed blue curve. The black solid curves represent the “backbone” fits to the data points for each data set.

where m is the magnitude on the SuperWASP magnitude scale, and A , B and C are parameters to be determined. The fitted values of A , B and C are presented in Table 4.1. In fact A corresponds to the total noise contribution from noise sources that are independent of magnitude (for example, readout noise or scintillation). The parameter B corresponds to the Poisson noise from the star photons and the parameter C corresponds to the Poisson noise from the sky photons, both for a star with magnitude 12.75.

We fit the RMS diagram for each of the tests listed in Table 4.1 and hence determine the dependence of the parameters A , B and C on the FWHM of the convolving Gaussian. We expect that if the noise parameter A is dominated by scintillation, then it will be independent of the amount of blurring, since the scintillation occurs before the photons enter the camera. We also expect that B is independent of the amount of blurring since the total number of star photons stays the same. However, we expect that the noise parameter C will be proportional to the blurring FWHM because a blurring by b pixels FWHM increases the number of sky photons by a factor of b^2 and therefore the sky noise by a factor of b .

In Figure 4.6, we show the dependence of the three noise parameters as a function of the

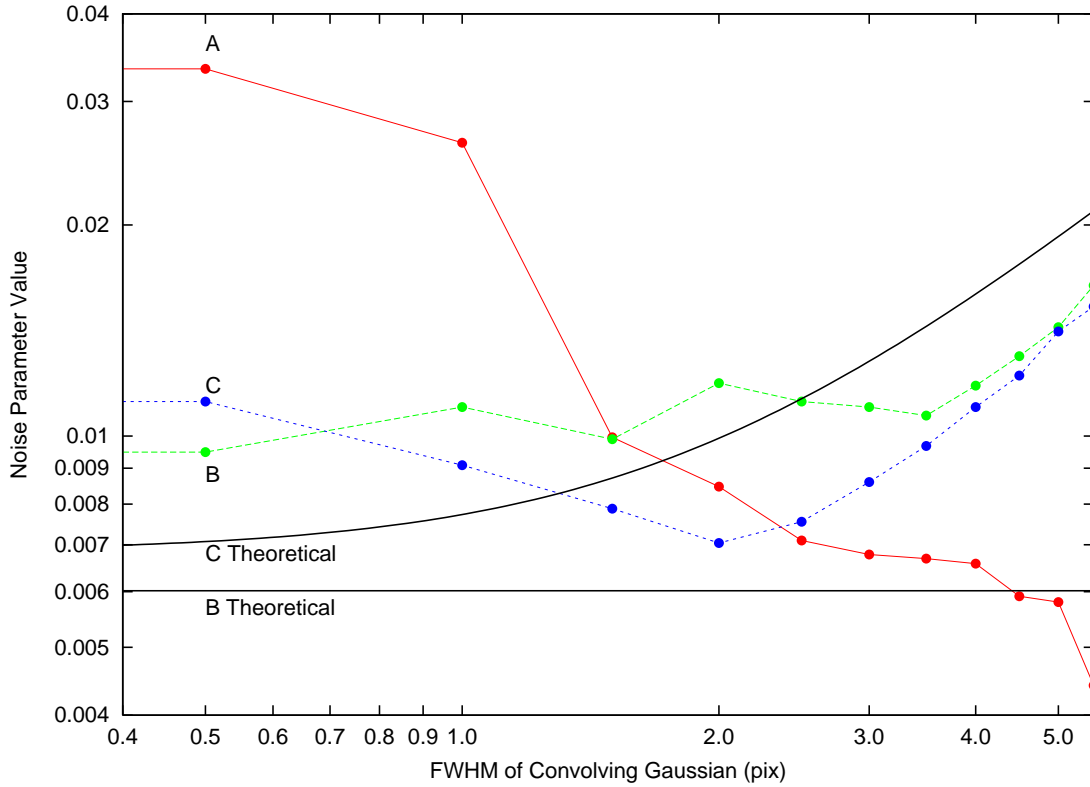


Figure 4.6: The derived values of the noise parameters A , B and C as a function of the FWHM of the convolving Gaussian. The horizontal continuous line represents the expected value of B and the curved continuous line represents the expected behaviour of C .

FWHM of the convolving Gaussian. Parameter A decreases rapidly with FWHM and therefore this magnitude-independent noise term is not dominated by scintillation. Parameter B is approximately constant as expected for $\text{FWHM} \leq 3.5$ pix, but increases rapidly for larger FWHMs. The black horizontal continuous line marks the value of $B = 0.0060$ mag that we expect from Equation 2.23 for a $m = 12.75$ (so that $R(m) = B$ in Equation 4.3) and assuming that the pixel noise is dominated by star photons. Parameter C has an expected value of 0.0064 mag from Equation 2.23 for $m = 12.75$ and no blurring, assuming that the pixel noise is dominated by sky photons. This value for C may then be scaled to other blurring FWHMs by noting that the sky noise scales with the final FWHM of the PSF in the blurred images, and calculating the final FWHM as the square root of the sum of the blurring FWHM squared and the typical PSF FWHM squared. The expected values for C are plotted in Figure 4.6 as the black solid curve. The observed values of B and C do not follow the theoretical predictions which is most likely due to correlations between these quantities when fitting $R(m)$. In fact, when A and C are larger than B , there will be no information in the data concerning B , and the three parameter model leads to unrealistic values for the parameters. This is especially visible in Figure 4.6 for a $\text{FWHM} \geq 3.5$ pix, where the values for B and C follow the same trend.

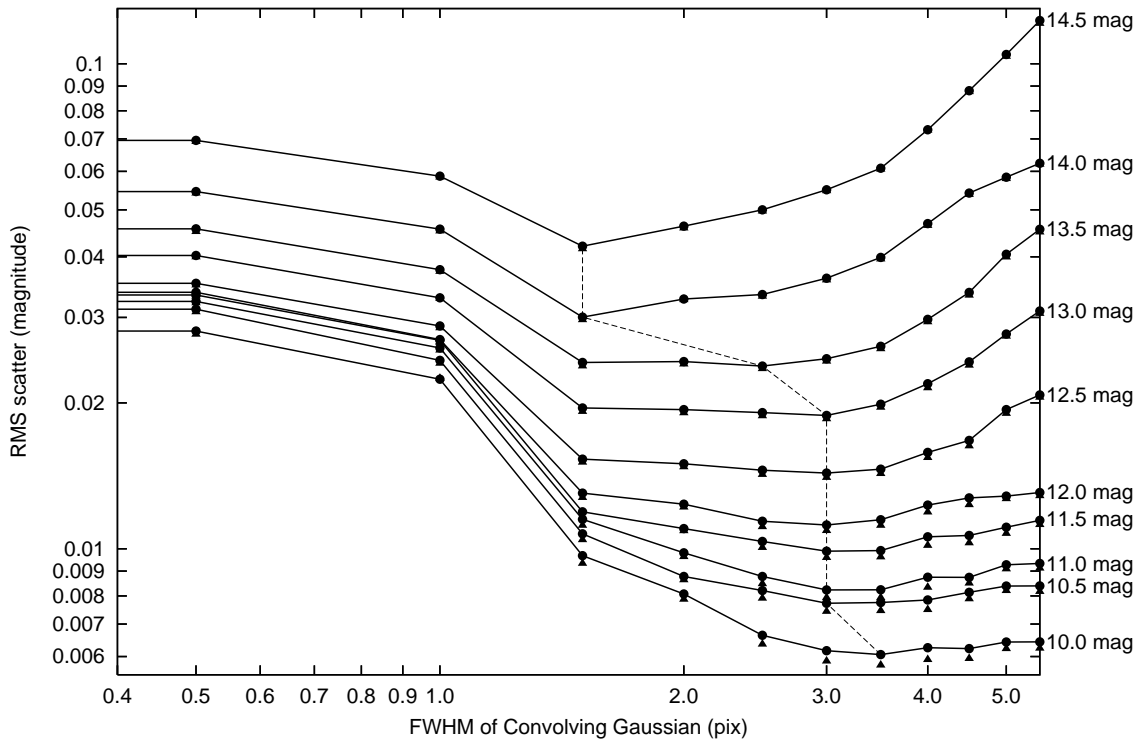


Figure 4.7: Plot of RMS scatter in the lightcurves versus the FWHM of the convolving Gaussian for different groups of stars binned by brightness. Each solid curve and associated data points (filled circles) represents the results for a group of stars with a brightness within 0.25 magnitudes of the magnitude marked at the end of the curve on the right hand side of the plot. The triangles represent how one iteration of the Tamuz post-calibration procedure affects the results. The dashed line links the minima of the solid curves.

At this point, it is clear that some amount of blurring is beneficial in order to be able to apply difference imaging to the SuperWASP data (see Figure 4.5). The question that concerns us is what FWHM should the Gaussian have with which we will convolve the images? Figure 4.7 shows the RMS scatter in the lightcurves as a function of FWHM of the convolving Gaussian and star brightness (each curve is marked at the right hand side of the plot with the centre of its magnitude bin; each magnitude bin is 0.5 mag). It is clear that no blurring or small FWHMs produces very poor results at all magnitudes. We also expect the visible trend that the accuracy of the lightcurves of faint stars is degraded significantly by large amounts of blurring ($\text{FWHM} > 3.5$ pix) because the act of convolution dilutes the star photon signal with sky noise. Brighter stars are less affected by this process and this is also clear in Figure 4.7. The dashed line in Figure 4.7 links the minima of the solid curves and highlights the best FWHM of the convolving Gaussian for each range of star brightnesses. The best results for stars brighter than ~ 13 mag are obtained with a FWHM of 3.0 pix and for stars fainter than this, with a FWHM of ~ 1.5 to 2.0 pix.

We also test the influence of the Tamuz algorithm on the results illustrated in Figure 4.7.

We apply only one iteration of the Tamuz algorithm for test purposes (see Section 4.3.7). The algorithm hardly improves the lightcurve RMS scatter in most cases, and moderately improves the lightcurve scatter for bright stars with large blurring FWHMs. The improvement in this situation reaches $\sim 6\%$. The results from applying the Tamuz algorithm are also shown in Figure 4.7 as the filled triangles that sit just below the filled circles. Hence the use of the Tamuz algorithm will not significantly influence our decision on what is to be the correct blurring FWHM.

Finally, we discuss the results of tests V and V'. The RMS diagrams for both tests are virtually identical to the human eye, and the values of the parameters A , B and C listed in Table 4.1 are equal to within their uncertainties. This observation is reassuring because it shows that the blurring of the reference image has no degrading effects on the subsequent photometry. This is also to be expected because the convolution by a Gaussian and then a derived kernel (test V) is equivalent to convolution by a single derived kernel (test V').

4.3.3 Testing the PASS0 Pipeline on Fake Image Data

Ideally we would like to avoid preconvolution of the SuperWASP images with a Gaussian when applying the image subtraction method since the act of convolution degrades the theoretical accuracy that we may achieve in our lightcurves. However, we have seen that the undersampled SuperWASP images are leading to large systematic residuals on the difference images at the positions of the stars. We decided to investigate what effect this really has on our data, and whether these residuals can explain the very poor ~ 0.03 mag RMS accuracy that we achieve for test N. To do this we consider two noiseless fake data sets that we generate ourselves, one for undersampled image data, and one for oversampled image data. We do not inject fake noise in to our fake images because we are trying to understand the direct effect of undersampling on our results.

To test the PASS0 pipeline in the undersampled case, we choose a Gaussian model with FWHM of 2 pix to represent the PSF with total counts of 10^5 ADU. We generate 121 square images of size 1681×1681 pixels with a fixed sky background of 1000 ADU. Each image is made up of a 41×41 grid of 41×41 pixel sub-squares. At the centre of each sub-square we add a PSF simulating a star with a sub-pixel shift dx and dy , in x and y respectively, that is given by:

$$\begin{aligned} dx &= \frac{G_x - 21}{40} + \frac{(I \bmod 11) - 5}{10} \\ dy &= \frac{G_y - 21}{40} + \frac{I - (I \bmod 11) - 55}{110} \end{aligned} \tag{4.4}$$

where G_x is the grid number in x that runs from 0 to 40, G_y is the grid number in y that runs from 0 to 40 and I is the image number that runs from 0 to 120. In this way, in one image each star is centred at a slightly different sub-pixel phase, where all stars cover a grid of 41×41 sub-pixel phase positions. Also, since each image in the sequence has a slightly different sub-pixel offset, a single star samples a grid of 11×11 sub-pixel phase positions over the image sequence. When calculating the pixel values to be added to each image from the inserted PSF, we supersample the Gaussian by a factor of 10 in x and y to ensure the correct flux integral over each pixel.

We also generate a second set of fake image data to test the PASS0 pipeline in the oversampled case. This is done in an identical way as for the undersampled case, except that we use a Gaussian

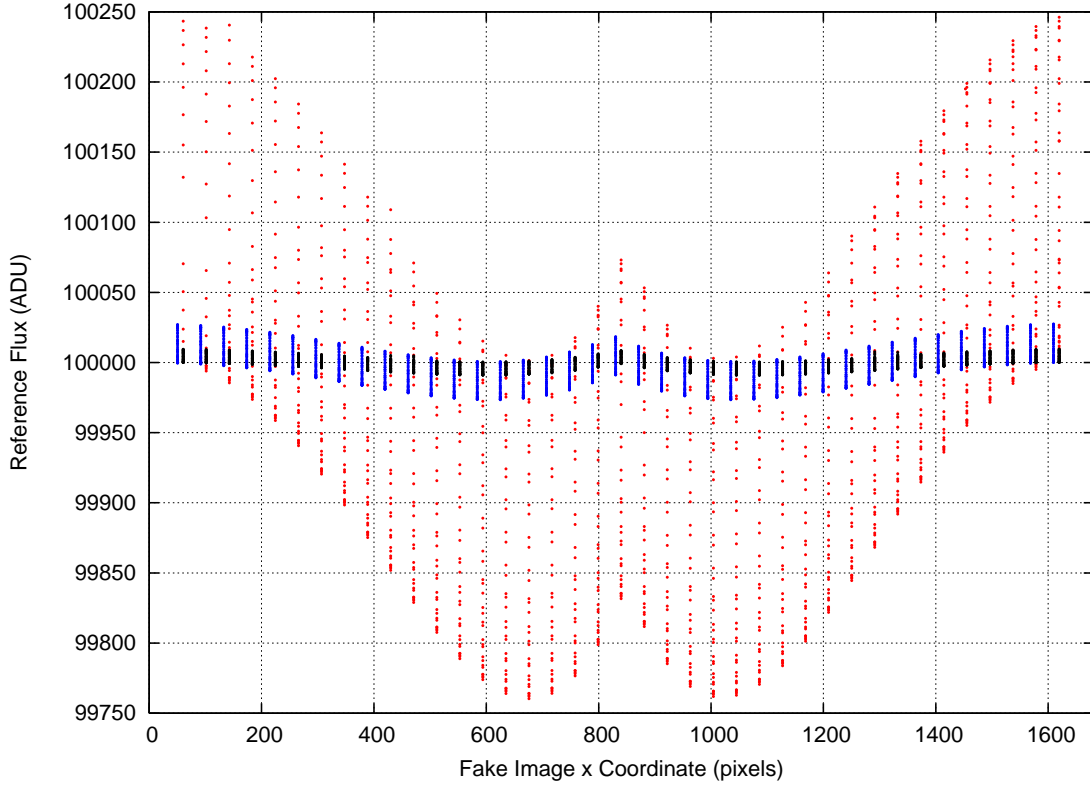


Figure 4.8: Plot of the recovered reference fluxes from the fake image data for the undersampled case with a FWHM of 2 pix with no pre-blurring (red points), for the undersampled case with 3 pix FWHM pre-blurring (blue points) and for the oversampled case with a FWHM of 4 pix (black points).

model with FWHM of 4 pix to represent the PSF, again with total counts of 10^5 ADU. For both cases, we choose the image with $dx = dy = 0$ for the central star as the reference image.

We perform three PASS0 pipeline reduction tests as follows. We reduce the undersampled fake data without pre-blurring the images to simulate test N, and we reduce the undersampled fake data with pre-blurring with a Gaussian of FWHM 3 pix (blurring the reference image by 2.5 pix) to simulate test U. Finally we reduce the oversampled fake data without pre-blurring the images to simulate the case where the SuperWASP camera actually oversamples the image.

On running the fake image data sets through the PASS0 pipeline, we may first compare the reference fluxes we obtain from the analysis of the reference images. We know that each star was injected with total counts of 10^5 ADU. Figure 4.8 shows the recovered reference fluxes for the undersampled image data with no pre-blurring (red points), undersampled image data with 3 pix FWHM pre-blurring (blue points off set by 10 pix in x for clarity) and the oversampled image data with no pre-blurring (black points) as a function of the fake image x coordinate. There is a very clear pattern, which is to be expected from the way the reference image was constructed, and this pattern is very similar to that obtained when plotting the reference fluxes against the y

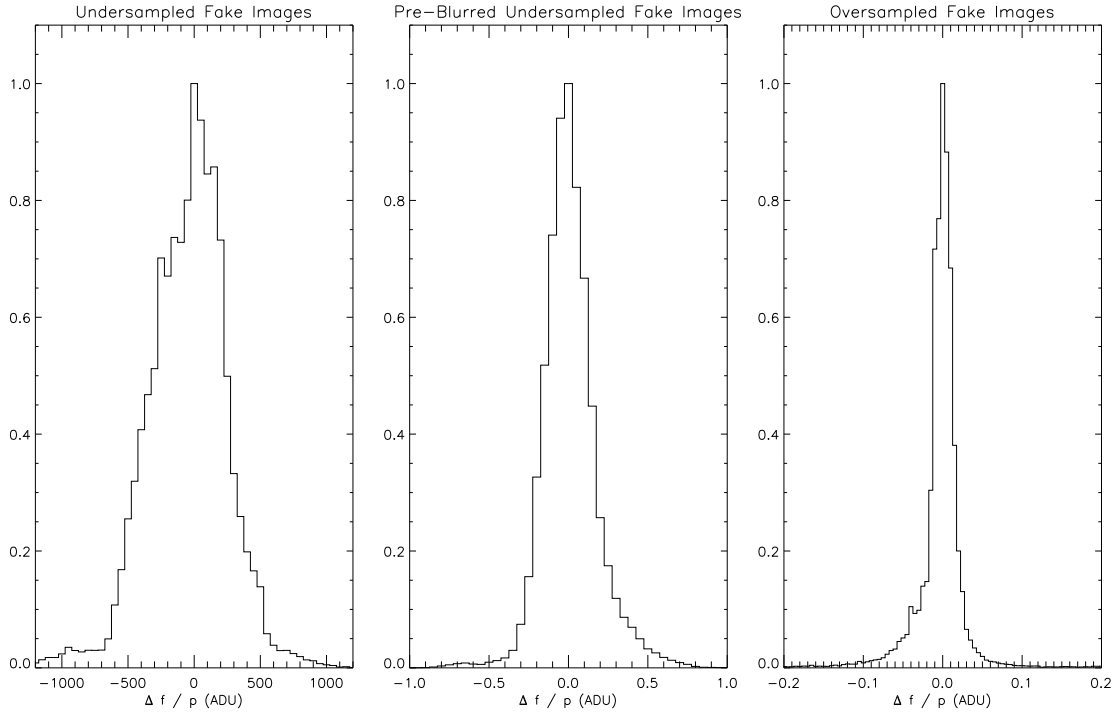


Figure 4.9: Normalised histograms of the recovered difference fluxes from the fake image data for the undersampled case with a FWHM of 2 pix (left), the pre-blurred undersampled case with a FWHM of 2 pix (middle) and for the oversampled case with a FWHM of 4 pix (right). The total number of data points used in each histogram is 203401 (since there are 1681 stars for which each has 121 measurements).

coordinate. What is clear from Figure 4.8 is that the PASS0 pipeline reference image analysis performs much better on the oversampled data and the pre-blurred undersampled data than on the undersampled data alone, since the reference flux values recovered for the oversampled case are all within 10 ADU (or 0.01%) of the correct value and the reference flux values recovered for the pre-blurred undersampled case are all within 30 ADU (or 0.03%) of the correct value, whereas for the undersampled case they can differ from the correct value by up to 250 ADU (or 0.25%). This discovery explains why we chose to pre-blur the reference image as well as the remaining images in the tests performed in Section 4.3.1.

Now we consider the fake lightcurves produced by the pipeline, which should each consist of 121 values of zero for the quantity $\Delta f/p$ (the difference flux normalised by the photometric scale factor). With 1681 test stars, we have 203401 estimates of the difference flux, and we present these measurements in Figure 4.9 as normalised histograms for the undersampled case (left), the pre-blurred undersampled case (middle) and the oversampled case (right). The standard deviation of the $\Delta f/p$ measurements for the undersampled case is ~ 310 ADU, for the pre-blurred undersampled case is ~ 0.173 ADU and for the oversampled case is ~ 0.087 ADU, corresponding

to 0.31%, $1.7 \times 10^{-4}\%$ and $8.7 \times 10^{-5}\%$ of the expected total flux. These results suggest that the pipeline works exceptionally well on the pre-blurred undersampled fake data and the oversampled fake data, recovering the injected fluxes at a precision at least 10^3 times better than we require. However, for the undersampled fake data, systematic errors of the order of 0.31%, with a possible amplitude of up to 1% (from Figure 4.9), are introduced by the pipeline into the lightcurves. These results go some way to explaining the poor RMS accuracy achieved for the SuperWASP lightcurves in test N.

4.3.4 Sub-Pixel Phase Map

As a last attempt to improve the photometry of the SuperWASP images without resorting to image blurring, we investigate how the position of the centroid of each star within a pixel affects the photometry of the star. Considering the lightcurves for test N, we calculate the residual magnitudes around the mean magnitude for each lightcurve. We also consider a single pixel divided up into a grid of 400 square bins such that there are 20 bins along each axis. Using the known position of each star at each epoch in the original images, we can assign each magnitude residual to its corresponding sub-pixel bin using the sub-pixel position of the star. Uncertainties for each magnitude residual are also stored. Since there are $\sim 10^4$ stars with 198 epochs, each sub-pixel bin on average contains ~ 5000 magnitude residuals. The final sub-pixel phase map of magnitude residuals is calculated by taking the optimal inverse-variance weighted mean of the residuals in each sub-pixel bin.

The sub-pixel phase map we obtain is presented in Figure 4.10(a) as a 2×2 pixel grid in order to highlight the structure of the pattern. The maximum and minimum values are 0.0124 and -0.0105 mag respectively. There is clearly a systematic pattern at the ~ 0.005 mag level. We attempt to use this map to correct the test N lightcurves for this systematic error by optimally scaling the pattern to the lightcurve residuals and subtracting, but we find that the correction makes a negligible improvement to the RMS accuracies of the lightcurves. We explain this by considering that a ~ 0.005 mag correction at all epochs cannot drastically improve lightcurves which have RMS accuracies of ~ 0.03 mag and worse.

We also present the sub-pixel phase map that we obtain for test U in Figure 4.10(b). It is clear that the pattern present for test N has disappeared, which is to be expected since the image blurring influences the measured star centroids. Hence we do not attempt to apply any such correction for test U.

4.3.5 Choosing the Best Gaussian Preconvolution

We decide to reduce the 688 images from the full SuperWASP data set using a convolving Gaussian with a FWHM of 3.0 pix for all images except the reference image, which is convolved with a Gaussian with a FWHM of 2.5 pix. This is judged to produce the lowest RMS scatter in the lightcurves for all stars down to a magnitude of ~ 13.25 , and a slightly suboptimal RMS scatter for stars down to ~ 13.75 mag. Below this, the stars are generally too faint to search for transits since the RMS scatter is above 4%. Hence we are not interested so much in the quality of these lightcurves.

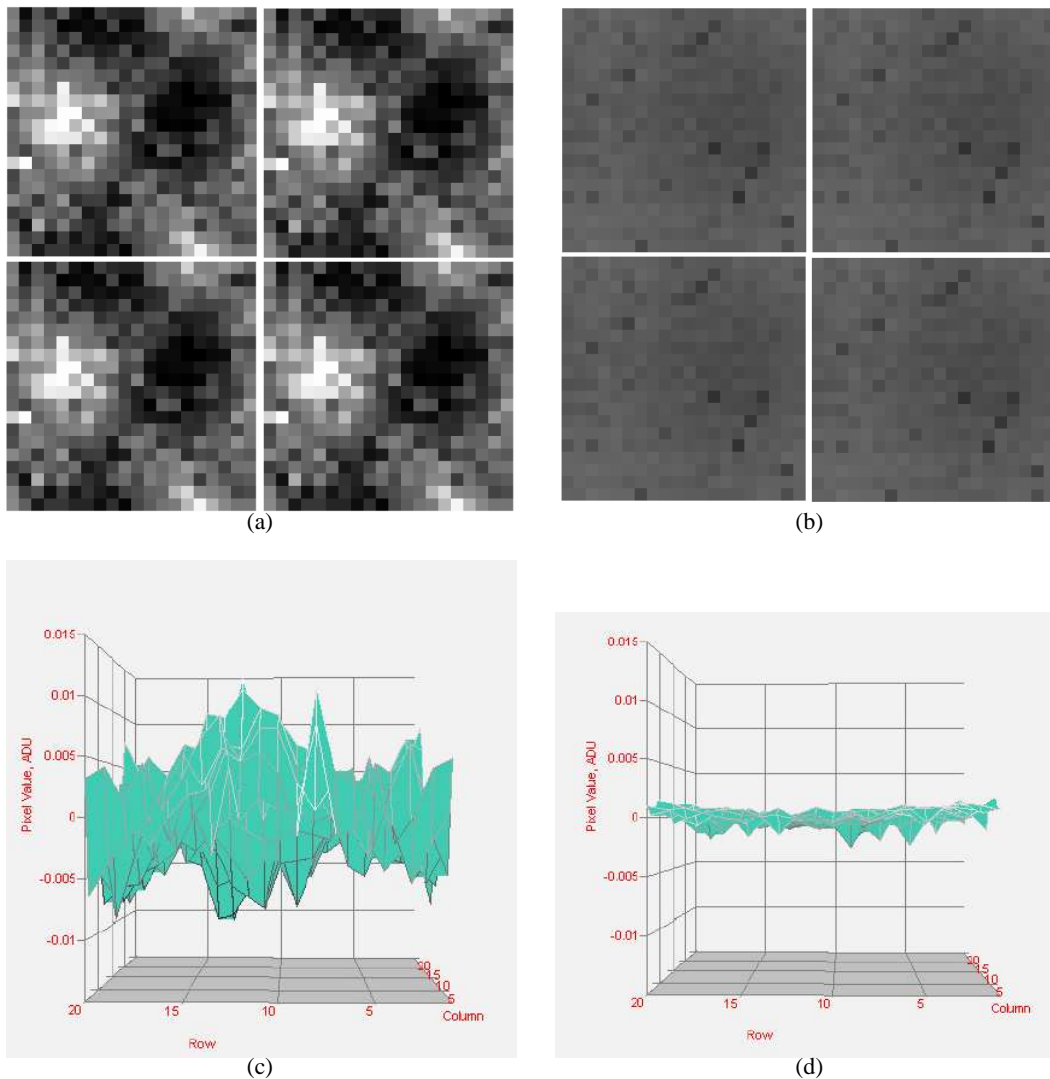


Figure 4.10: **(a)**: Sub-pixel phase map for test N (no image blurring) repeated in a 2×2 pixel grid. Each pixel map represents the optimal mean magnitude residuals as a function of position within a SuperWASP pixel. The image scale is linear from -0.01 to 0.01 mag. **(b)**: Sub-pixel phase map for test U (image blurring with a Gaussian of FWHM 3.0 pix) repeated in a 2×2 pixel grid with the same scale as in (a). **(c)&(d)**: 3D surface plots of a single sub-pixel phase map from (a) & (b).

4.3.6 Image Subtraction Residuals

As with the PASS0 data analysed in Chapter 3, we produce image stamps of the residuals on the difference images for two interesting cases, the star XO-1 and an eclipsing binary. This test is done to check that the PASS0 pipeline is working correctly on the SuperWASP data. In Figure 4.11,

which is based on the same idea as that behind Figure 3.6, we plot 5 image stamps for each epoch and we consider 10 epochs for each of the two stars. Star XO-1 is the star in the centre of the left hand set of stamps and the eclipsing binary is the star in the centre of the right hand set of stamps. Each row of stamps is a different epoch, and these epochs stretch from HJD 2453162.5 d to HJD 2453162.6 d, covering a part of the XO-1 lightcurve going from in-transit to out-of-transit. Note that XO-1 is very close to the edge of the reference image.

The first column of stamps are cutouts from the blurred reference image (the same stamp at each epoch), the second column are cutouts from the science images after blurring and then resampling, and the third column are cutouts from the difference images. The fourth column are cutouts from the difference images, but with the optimally scaled empirical PSF subtracted at the position of the central star and the fifth column is the fourth column normalised by the pixel sigmas determined from the CCD noise model.

The transit signal for XO-1 is not visible to the human eye on the third column of stamps, and hence the fourth column looks the same. However, for comparison, the eclipsing binary, which has a much larger variation amplitude, clearly shows a decrease in brightness over the epochs considered, and the residuals of the fit to the difference image look reasonable in the fourth column. For both stars, the normalised residuals in the fifth column do not stretch to the full ± 3 sigma range since the blurring process has smoothed out the noise (in other words the pixel noise is now correlated between pixels). This may be compared to the fifth column in Figure 3.6 where pixel noise is not correlated. Any fixed pattern that is noticeable in the background on the difference image stamps comes from the subtraction of the pre-blurred reference image, since the reference image has approximately the same signal-to-noise as any other image. These stamps demonstrate that there are not any serious systematic residuals at the position of the stars considered that may affect the PASS0 photometry pipeline.

4.3.7 Further Lightcurve Calibration

Lightcurves from the SuperWASP pipeline are detrended using the algorithm described in Tamuz, Mazeh & Zucker [81]. This algorithm is used to identify and remove systematic effects in large numbers of light curves. As long as the systematic effects are linear and common in most of the stars, then the algorithm will recognize them and remove them. Here we summarise briefly the Tamuz detrending algorithm.

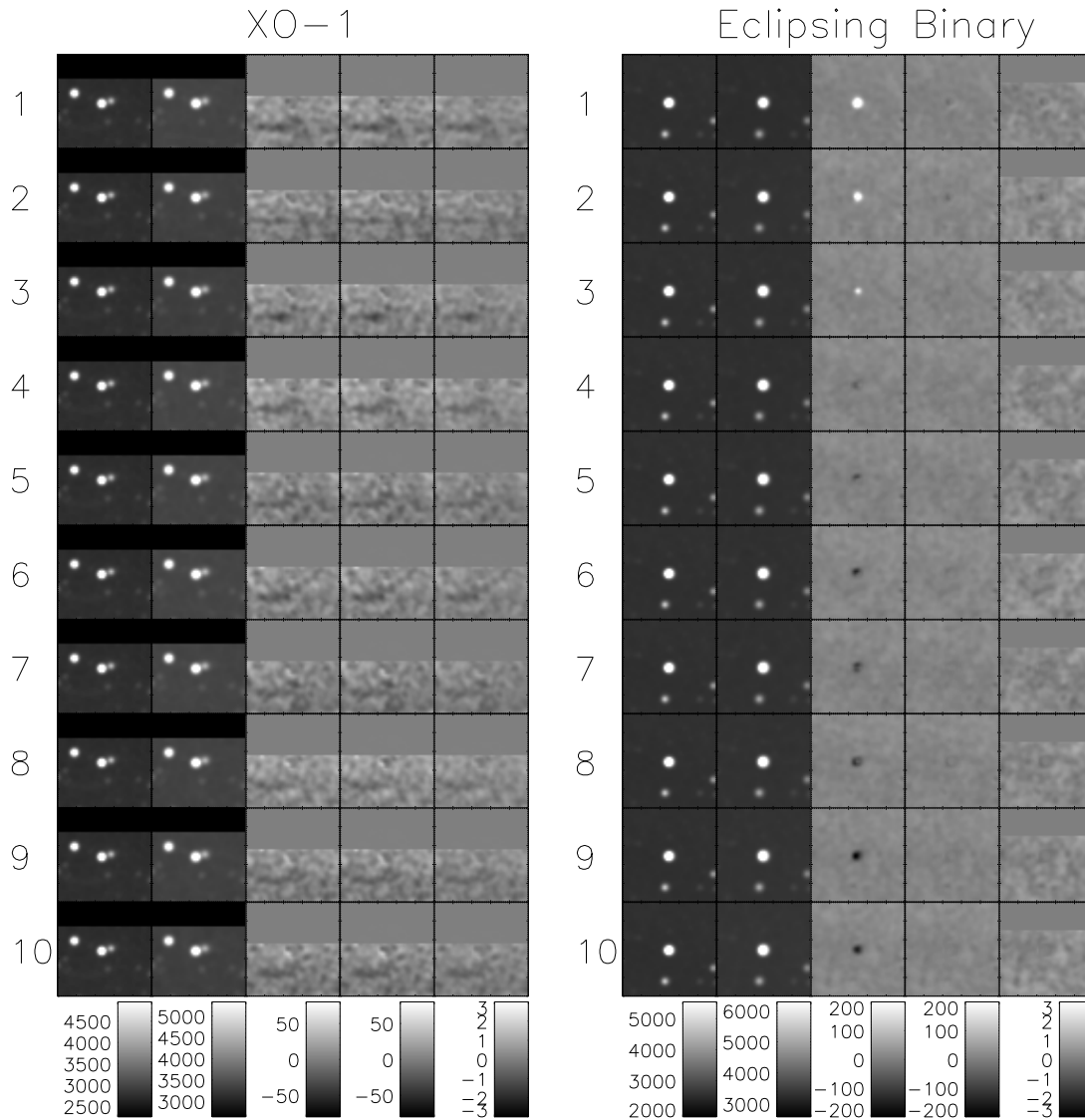


Figure 4.11: Various image stamps for star XO-1 on the left and an eclipsing binary on the right. For each star we show 10 rows of stamps corresponding to 10 epochs from HJD 2453162.5 d to HJD 2453162.6 d, covering a part of the XO-1 lightcurve going from in-transit to out-of-transit. The first column of stamps are cutouts from the blurred reference image, the second column are cutouts from the science images after blurring and then resampling, and the third column are cutouts from the difference images. The fourth column are cutouts from the difference images, but with the optimally scaled empirical PSF subtracted at the position of the central star and the fifth column is the fourth column normalised by the pixel sigmas determined from the CCD noise model.

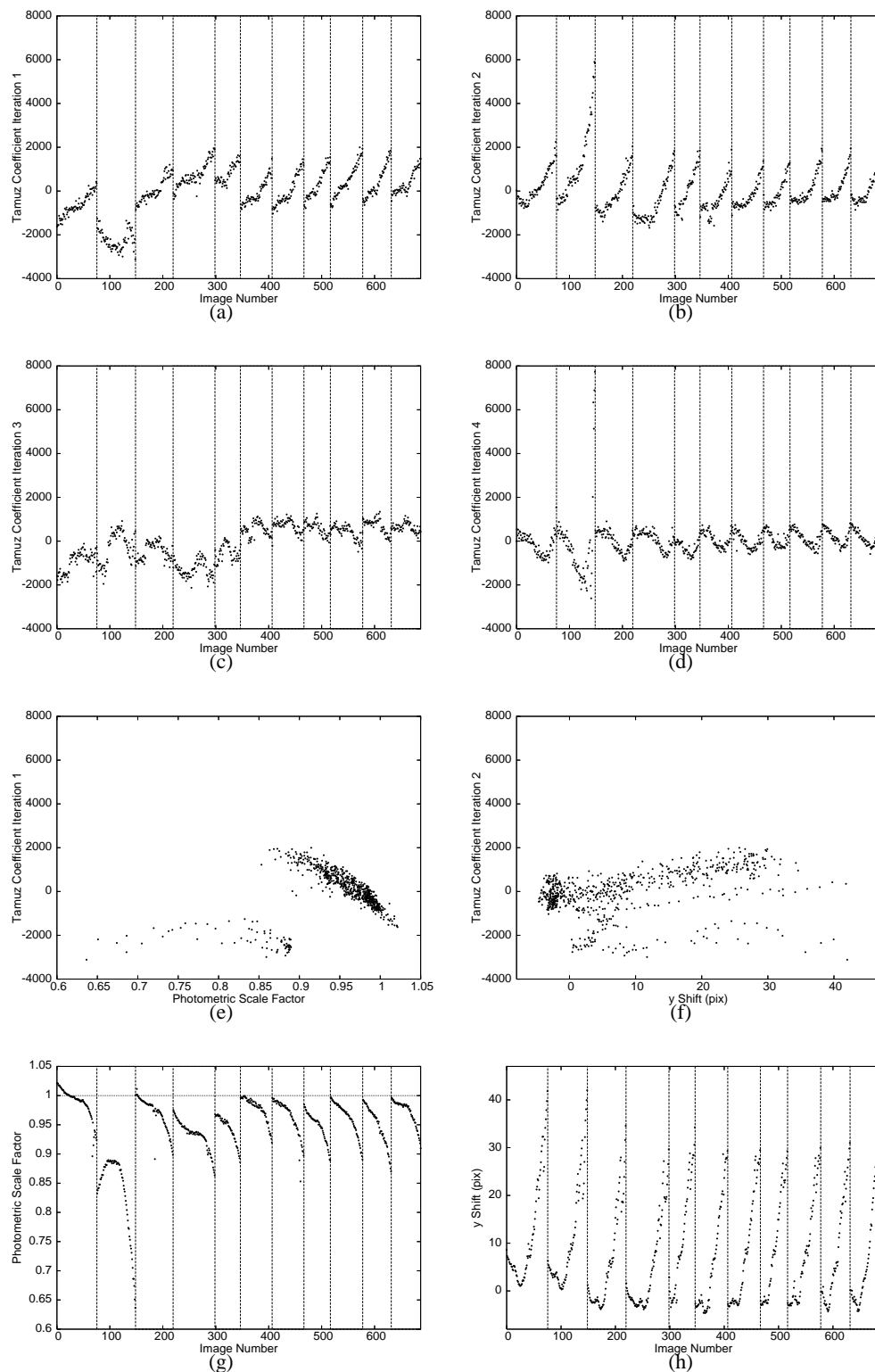


Figure 4.12: (a),(b),(c),(d): Tamuz coefficients against image number. (e): Tamuz coefficients for the 1st iteration against photometric scale factor. (f): Tamuz coefficients for the 2nd iteration against y-Shift. (g): Photometric scale factor against image number. (h): y-Shift against image number.

For a star i and an image j we would like to minimise the chi-squared:

$$\chi_i^2 = \sum_j \frac{(r_{ij} - c_i a_j)^2}{\sigma_{ij}^2} \quad (4.5)$$

where r_{ij} represents the lightcurve residuals after subtracting the mean magnitude for the star. The uncertainties on the lightcurve magnitude measurement are represented by σ_{ij} and the coefficients c_i and a_j may be thought of as the extinction coefficient for each star and the effective airmass of each image respectively.

Starting with an initial guess for the airmasses a_j (using the values recorded in the image headers for instance), we can minimise the χ_i^2 in Equation 4.5 by differentiating the χ_i^2 with respect to c_i , equating to zero and solving for c_i to get:

$$c_i = \frac{\sum_j (r_{ij} a_j / \sigma_{ij}^2)}{\sum_j (a_j^2 / \sigma_{ij}^2)} \quad (4.6)$$

Having solved for the coefficients c_i we can now use a similar method to solve for the most suitable airmasses a_j :

$$a_j = \frac{\sum_i (r_{ij} c_i / \sigma_{ij}^2)}{\sum_i (c_i^2 / \sigma_{ij}^2)} \quad (4.7)$$

The process can then be iterated until convergence is reached on c_i and a_j .

For the SuperWASP pipeline, the Tamuz algorithm is applied four times to the lightcurves removing four components of systematic error, two of which are thought to be caused by airmass variations and thermal changes in the camera focus, but the causes of the other two are unknown [19]. We also apply the Tamuz algorithm to our lightcurves from the PASS0 pipeline for the full SuperWASP data set (688 images) and we find a reasonable improvement in the lightcurve scatter. For a fair comparison of lightcurves and the accuracy we achieve with that of the SuperWASP pipeline, we choose to apply four iterations of the Tamuz algorithm. The results are discussed in Section 4.4.

In Figure 4.12 we present the Tamuz coefficients for the 1st, 2nd, 3rd and 4th iterations in panels (a), (b), (c) and (d). The coefficients are plotted against image number and the vertical dashed lines indicate a change in date. There are clear systematic patterns that are repeated from night to night. We have attempted to find correlations against various quantities corresponding to each image. The quantities we tested were sky background, FWHM, photometric scale factor, and the rotation and xy-shifts transforming the images to the reference image. We find a clear correlation between the Tamuz coefficients from the 1st iteration and the photometric scale factor, which measures the extinction as a function of time (Figures 4.12(g) and 4.12(e)). We also find a correlation between the Tamuz coefficients from the 2nd iteration and the y-shift between images (Figures 4.12(h) and 4.12(f)). The other Tamuz coefficients do not correlate with any of the quantities that we tested.

Table 4.2: The fitted parameters to the final RMS diagrams.

Pipeline	Number of Tamuz Iterations	A (mmag)	B (mmag)	C (mmag)
SuperWASP	4	7.51	5.04	22.6
PASS0	0	5.03	12.1	12.5
PASS0	4	4.52	10.1	12.3

4.4 Comparing the PASS0 and SuperWASP Pipeline Results

4.4.1 Comparing RMS Diagrams

Now we compare the results of our reductions using the PASS0 pipeline of the full SuperWASP data set (688 images) to those using the SuperWASP pipeline and we do this using the RMS diagrams. In Figure 4.13(a) we show the RMS scatter of the lightcurves from the SuperWASP pipeline, including 4 iterations of Tamuz, as the green points. The red points represent the RMS scatter of the raw lightcurves from the PASS0 pipeline which have NOT been calibrated by the Tamuz procedure. We also plot the aperture photometry limit as the solid red line and the PSF photometry limit (no blurring) as the blue dashed line. We include the scintillation noise (solid black line) calculated from Equation 2.46 assuming a lens diameter $d = 11.1$ cm, a median airmass $X = 1.3$ for the image sequence, an observatory height $h = 2400$ m and an exposure time $\Delta t = 30$ s, which gives $\sigma_{\text{SCINT}} \approx 2.2$ mmag. It is clear that at all magnitudes, the PASS0 pipeline, employing the 3.0 pix FWHM image blurring, produces considerably better photometry. For stars at 12th mag and fainter, the PASS0 pipeline starts to do better than the aperture photometry theoretical limit, and we get close to the PSF photometry theoretical limit.

In Figure 4.13(b) we plot the same RMS diagram as in Figure 4.13(a) except that we now show the RMS scatter of the PASS0 pipeline lightcurves after 4 iterations with the Tamuz algorithm. There has been a reasonable improvement to the RMS scatter in the lightcurves. We fit the various sets of points in Figure 4.13 using the three parameter model from Section 4.3.2 and present the fits in Table 4.2.

Finally, in Figure 4.14 we plot the photometry limits and RMS diagram fits relative to the RMS diagram fit for the best result (PASS0 pipeline with Tamuz detrend). Here one can clearly see that our PASS0 pipeline improves on the SuperWASP photometry by up to a factor of ~ 1.7 with a minimum improvement of ~ 1.3 at 11.4 mag. The Tamuz calibration of the PASS0 pipeline lightcurves improves the photometry by a factor of ~ 1.1 across the magnitude range. Our final lightcurves get to within a factor ~ 0.7 of the PSF photometry theoretical limit at the faint end and are more accurate than can be achieved by aperture photometry from ~ 12.2 mag and fainter. However, all pipelines fail drastically to reach the theoretical limits at the bright end suggesting a shortcoming in the theoretical noise models.

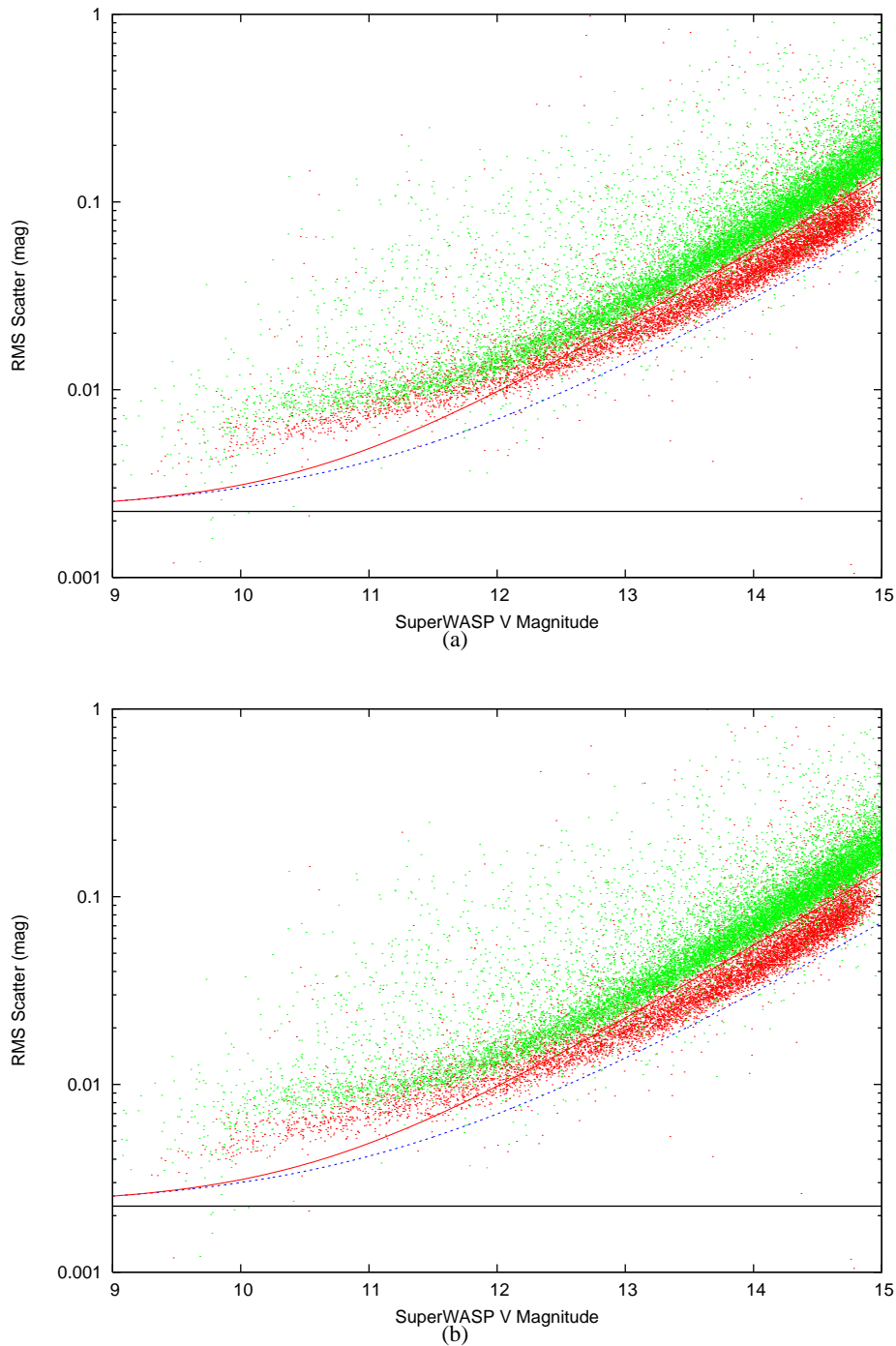


Figure 4.13: **(a)**: RMS scatter in the lightcurves against magnitude for the SuperWASP data for the SuperWASP pipeline (green points) and for the PASS0 pipeline (red points). The solid red line shows the aperture photometry limit, the dashed blue line shows the PSF photometry limit (no blurring) and the solid black line shows the scintillation noise. The SuperWASP pipeline results have been calibrated with four iterations of the Tamuz algorithm and the PASS0 pipeline results have NOT been calibrated by the Tamuz algorithm (i.e. they are the raw pipeline results). **(b)**: The same as (a) except that the PASS0 pipeline results have now been calibrated using four iterations of the Tamuz algorithm so that the results are directly comparable.

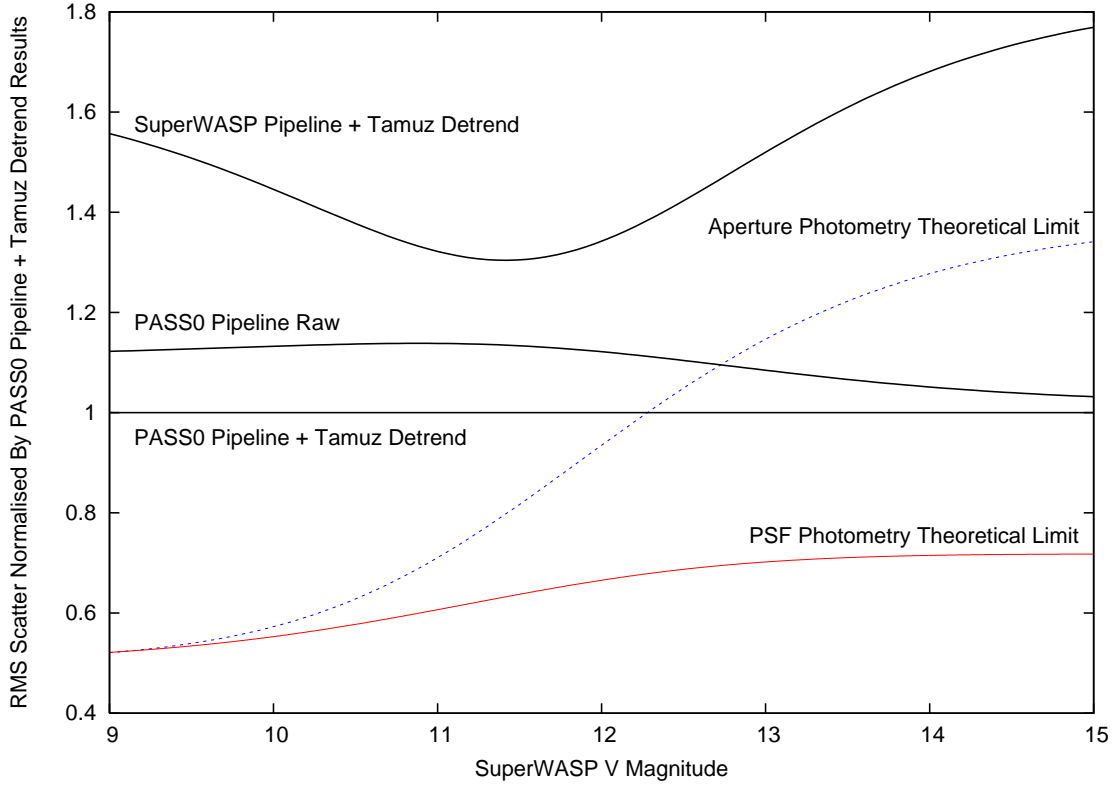


Figure 4.14: A plot of photometric limits and RMS diagram fits as functions of magnitude and normalised by the RMS diagram fit for PASS0 pipeline with Tamuz detrending. Each curve is labelled appropriately.

Now we are in the position to estimate how the improvements in photometric accuracy will affect the planet yield from the SuperWASP survey. From Figure 4.13(b), we can see that on average, for a given RMS accuracy, the corresponding magnitude is ~ 0.7 mag fainter for the reductions using the PASS0 pipeline than for the SuperWASP pipeline. Using this information in Equation 2.37 implies that the distance out to which we can detect planets will have increased by a factor of $10^{0.7/5} \approx 1.4$. Since volume is proportional to the distance cubed, and since the number of stars is proportional to the volume, then we can predict that there will be approximately $10^{2.1/5} \approx 2.6$ times more stars for which we can detect planets, and a corresponding increase in the planet detection efficiency of the SuperWASP survey. Hence our improvements in photometric accuracy have the potential to more than double the planet yield of SuperWASP.

4.4.2 Comparing the Lightcurves of XO-1

We find that our reduction procedure has significantly improved the lightcurve of the star XO-1 compared to the SuperWASP lightcurve. In Figure 4.15(a) we plot the full lightcurve of XO-1 as produced by the SuperWASP pipeline (which includes the Tamuz calibrations) and in Fig-

ure 4.15(c) and 4.15(e) we plot the full lightcurve as produced by the PASS0 pipeline before and after the Tamuz detrending respectively. It is already clear at this stage that the PASS0 pipeline lightcurve is of better quality, with fewer outliers and a slightly smaller scatter. The transits at HJDs of 2453158.5, 2453162.5, 2453166.5 and 2453170.5 days stand out much more in the PASS0 pipeline lightcurve than in the SuperWASP lightcurve.

In the right hand column of plots in Figure 4.15 we plot the same lightcurves but zoomed in on one night including a full transit, and now it is clear that the PASS0 pipeline lightcurve also suffers from less systematic trends than the SuperWASP pipeline lightcurve. For instance, the 0.03 mag brightening of the SuperWASP lightcurve at HJD of 2453162.42 days is not real, and is not present in the PASS0 pipeline lightcurve.

The most obvious visualisation of the improvement is illustrated in Figure 4.16 where we plot the XO-1 lightcurves folded on the period of 3.941534 d. In Figure 4.16(a) we show the full phase and in Figure 4.16(b) we show a zoom on the transit event. In both panels we plot the SuperWASP pipeline lightcurve with red dots, and offset by 0.07 mag for clarity we plot the PASS0 pipeline lightcurve (green points in Figure 4.16(a) and different coloured points in Figure 4.16(b) for each different night of observations). The phased transit event is much clearer in the PASS0 pipeline lightcurve than the SuperWASP pipeline lightcurve.

McCullough et al. 2006 report a transit ephemeris of $T_0 = 2453808.9170$ d and $P = 3.941534$ d in their discovery paper [51]. Further improvements in the ephemeris are not yet available in the literature, although Holman et al. 2006 have produced improved photometry for four transit events which allow them to derive more accurate transit and planetary parameters [34]. These parameters are reported as a planet-to-star radius ratio of 0.13102, an orbital inclination of 89.31° and an impact parameter of 0.14. The impact parameter b is related to the orbital inclination i via $b = a \cos i / R_*$, which means that we can calculate an orbital radius to star radius ratio of $a/R_* = 11.6$. We assume a linear limb darkening coefficient of 0.5 as a decent approximation for a Sun-like star. Then we use the combination of all the above quoted parameters to calculate a model transit lightcurve using the equations of Mandel & Agol 2002 [47]. We plot the model transit lightcurve as the black curve in Figure 4.15 and it is clear that the data follows the model to within the photometric accuracy.

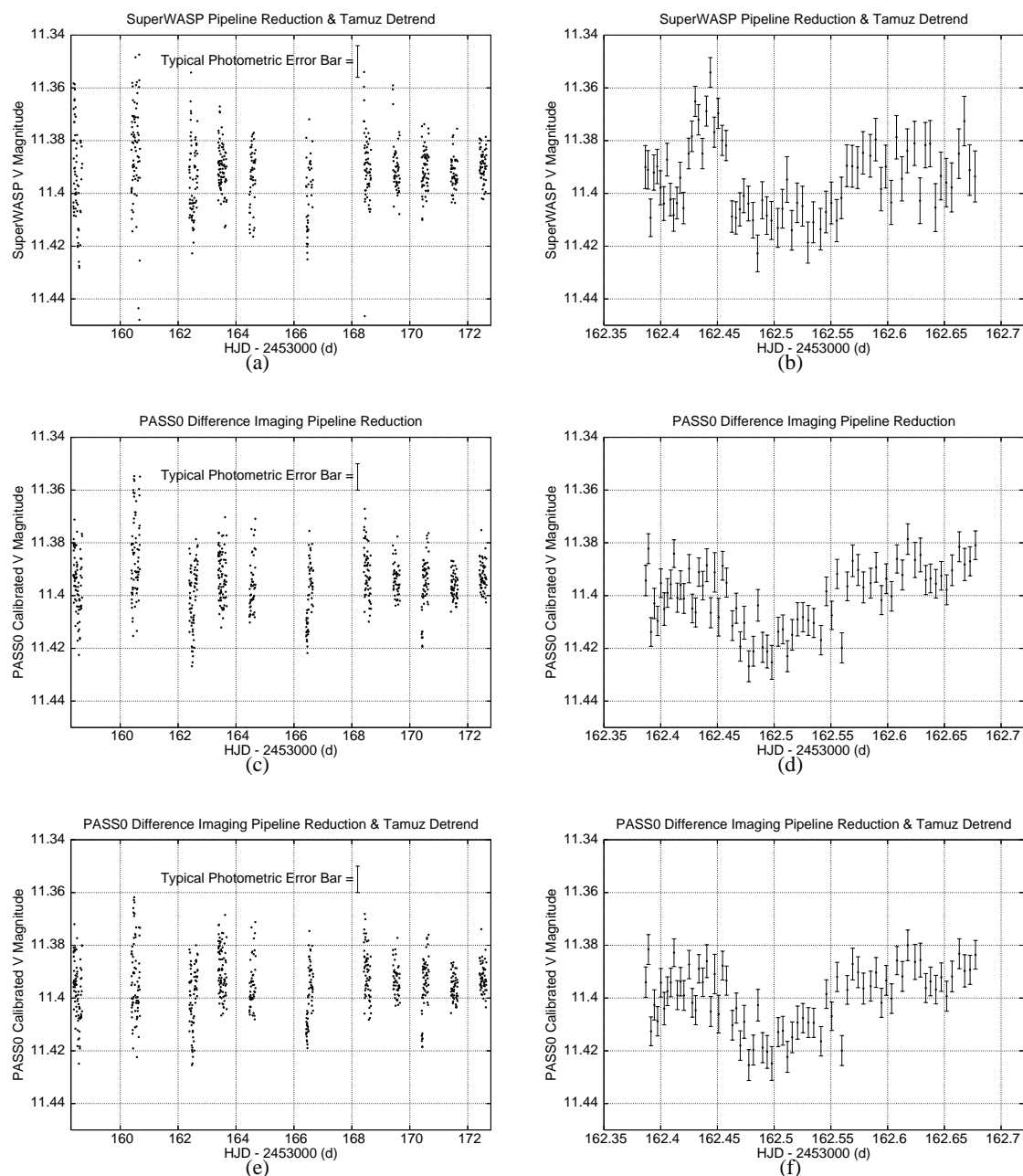


Figure 4.15: **(a)**: Detrended lightcurve of XO-1 from the SuperWASP pipeline. Error bars are not plotted for clarity. Instead, a typical error bar is plotted in the top right hand corner. The time of central transit occurs at $\text{HJD} - 2453000 \approx 162.5$. **(b)**: The third night of the same lightcurve as in (a). **(c)**: Lightcurve of XO-1 from the PASS0 difference imaging pipeline. Again, a sample error bar is plotted in the top right hand corner. No Tamuz detrending has been carried out. **(d)**: The third night of the same lightcurve as in (c). **(e)**: Lightcurve of XO-1 from the PASS0 difference imaging pipeline with Tamuz detrending. **(f)**: The third night of the same lightcurve as in (e).

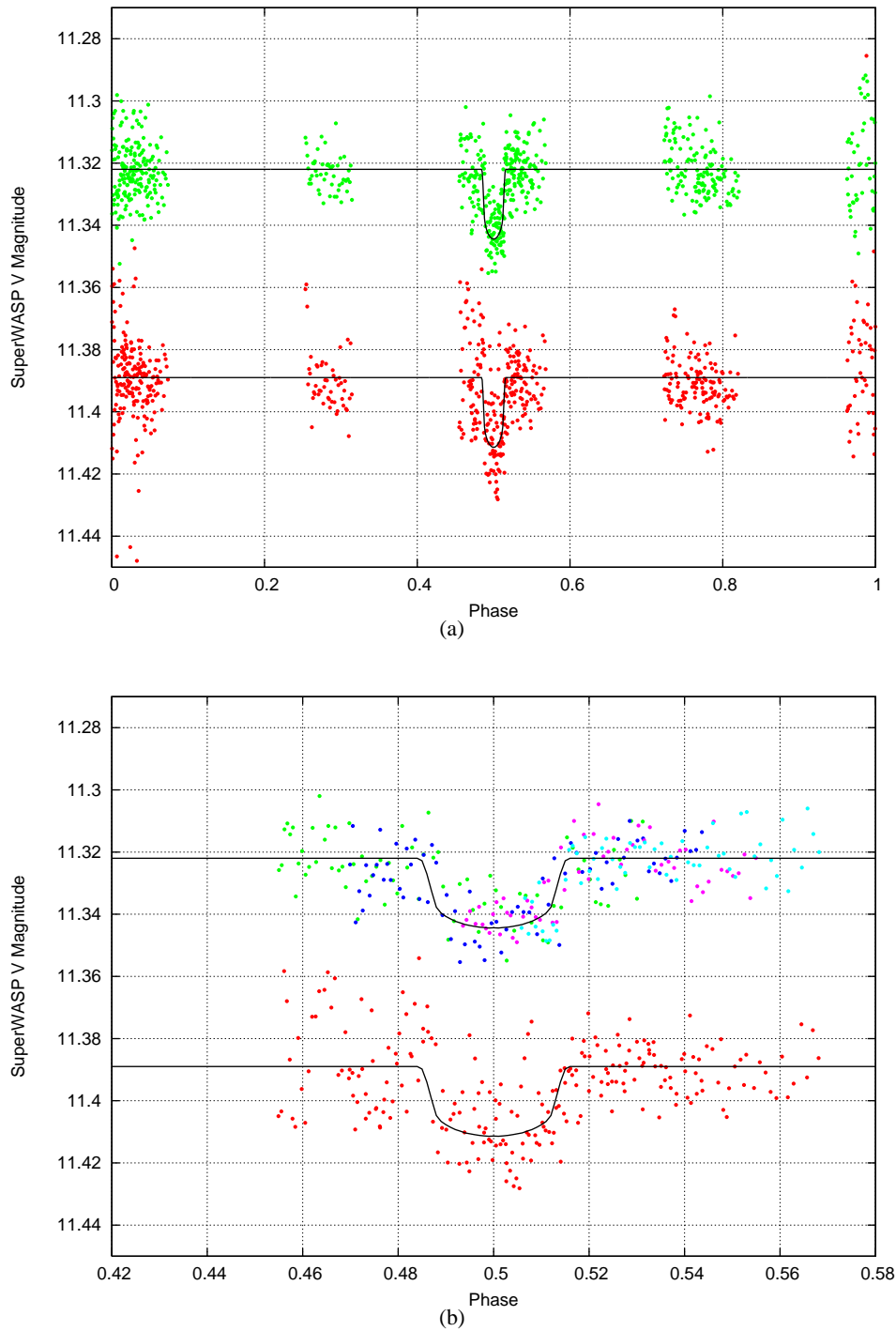


Figure 4.16: **(a)**: Detrended phased lightcurve of XO-1 from the SuperWASP pipeline (red points) and detrended phased lightcurve of XO-1 from the PASS0 pipeline (green points). The black curve is the model lightcurve using published transit parameters. **(b)**: Zoom around the transit event of the detrended phased lightcurve of XO-1 from the SuperWASP pipeline (red points) and of the detrended phased lightcurve of XO-1 from the PASS0 pipeline (various colour points). For the PASS0 pipeline lightcurve, each night has a different colour code. Again the black curve is the model lightcurve using published transit parameters.

Chapter 5

Variable Candidates from the PASS0 and SuperWASP Data

5.1 Introduction

In this Chapter we present a search method for variable stars and apply it to both the PASS0 data and the SuperWASP data that we have analysed in Chapters 3 and 4. We attempt to find periods for the variables using the Lomb-Scargle periodogram [46],[73], and present a short catalogue of variable stars with derived periods where possible. It is understood that most of these variables are likely to be known already since they are stars in the magnitude range from 4th mag to 15th mag.

5.2 Variables in the PASS0 Lightcurve Data

5.2.1 Identifying Variable Stars

The idea behind the method that we use for identifying variables is a simple one. Variable stars should show an RMS scatter in the lightcurves that is above the usual RMS scatter due to noise. We can use the RMS diagrams to find the stars with an RMS that is larger than that of the majority of stars at any particular magnitude.

Firstly we plot a histogram of the number of epochs in the PASS0 lightcurves and decide to consider a variable search in the 12853 lightcurves (out of 13515) with at least 100 epochs (Figure 5.1). Then we plot the RMS diagram for the chosen PASS0 lightcurves (Figure 5.2) and fit it with the model described by Equation 4.3 in Chapter 4, but adjusting the model to take a reference magnitude of 8 rather than 12.75. We obtain $A = 12.1$ mmag, $B = 8.8$ mmag and $C = 7.2$ mmag. The model is plotted on Figure 5.2 as the solid black line.

To identify variables, we need to choose a threshold in RMS above which any stars will be considered as variable. We must be carefull in choosing this threshold because the higher we set this threshold, the more real variables that we will fail to detect, and because the lower we set this threshold, the more constant stars that will contaminate our variable star sample.

It is clear from Figure 5.2 that our variable star detection threshold will need to be a function of magnitude, and we decide to set the threshold as some factor T times the fitted model (solid black

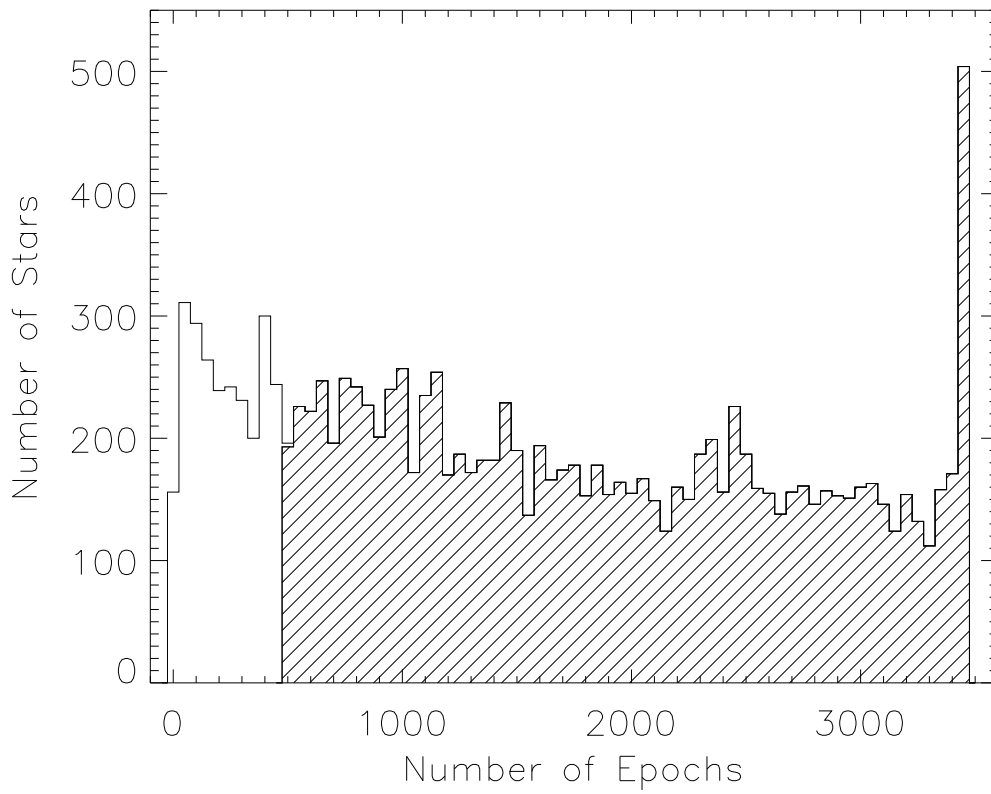


Figure 5.1: Histogram of the number of epochs in the PASS0 lightcurves. The lightcurves with at least 500 epochs are represented by the shaded part of the histogram.

line). In Figure 5.3 we present a normalised cumulative histogram of the ratio of the lightcurve RMS to the model RMS. We compare the normalised cumulative histogram to similar histograms for chi squared distributions with degrees of freedom ranging from 1 up to the number of epochs in the longest PASS0 lightcurve (3426 epochs), where we have normalised the x -axis by the number of degrees of freedom. We find that the chi squared distribution that best fits the normalised cumulative histogram (chosen using least squares) has 27 degrees of freedom. The range in the number of epochs in the PASS0 lightcurves, combined with systematic trends present in the PASS0 lightcurves have served to increase the spread in the RMS values around the model RMS curve, which has resulted in the best-fitting chi squared distribution having an artificially small number of degrees of freedom.

To choose our threshold factor T we consider the probability $P(x > T)$ that the lightcurve RMS to the model RMS ratio x is greater than T , which can be obtained directly from the chi squared distribution with 27 degrees of freedom. The probability that $x \leq T$ for N lightcurves is

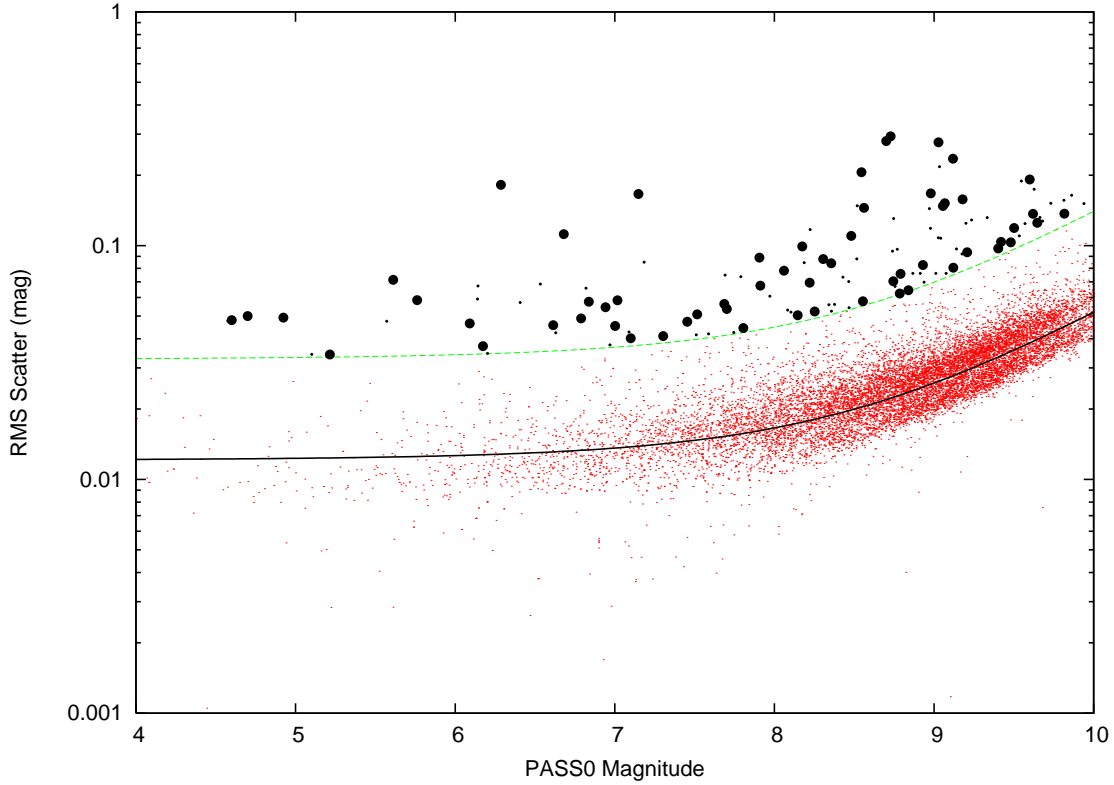


Figure 5.2: Plot of lightcurve RMS scatter against mean magnitude for the PASS0 lightcurves (red dots). The fit to the RMS diagram is shown as the solid black line, and the cut off in RMS for choosing variable star candidates is shown by the green dashed line. Variable star candidates are shown as small filled black circles. Variable star candidates that survive our further cuts in Section 5.2.2 are shown as large filled black circles.

given by:

$$P(x \leq T \text{ for all } N \text{ lightcurves}) = (1 - P(x > T))^N \quad (5.1)$$

Hence the probability that at least one lightcurve exceeds our threshold T is $1 - (1 - P(x > T))^N$, and we choose to require that this false alarm probability is 5%. We can now solve for the probability $P(x > T)$:

$$P(x > T) = 1 - (1 - 0.05)^{1/N} \quad (5.2)$$

and we may then choose T by considering the cut-off value of the chi squared distribution with 27 degrees of freedom. For the $N = 12853$ PASS0 lightcurves that we search for variables we find that we should set $T = 2.71$.

Having chosen our detection threshold for variable stars, we scale up the model represented by the solid black line in Figure 5.2 by a factor of $T = 2.71$, and plot it as the green dashed line. We take all stars with an RMS above this dashed line as candidate variables. This method is similar to that presented in Street et al. 2002 [78]. The 123 candidate variable stars are marked in Figure 5.2

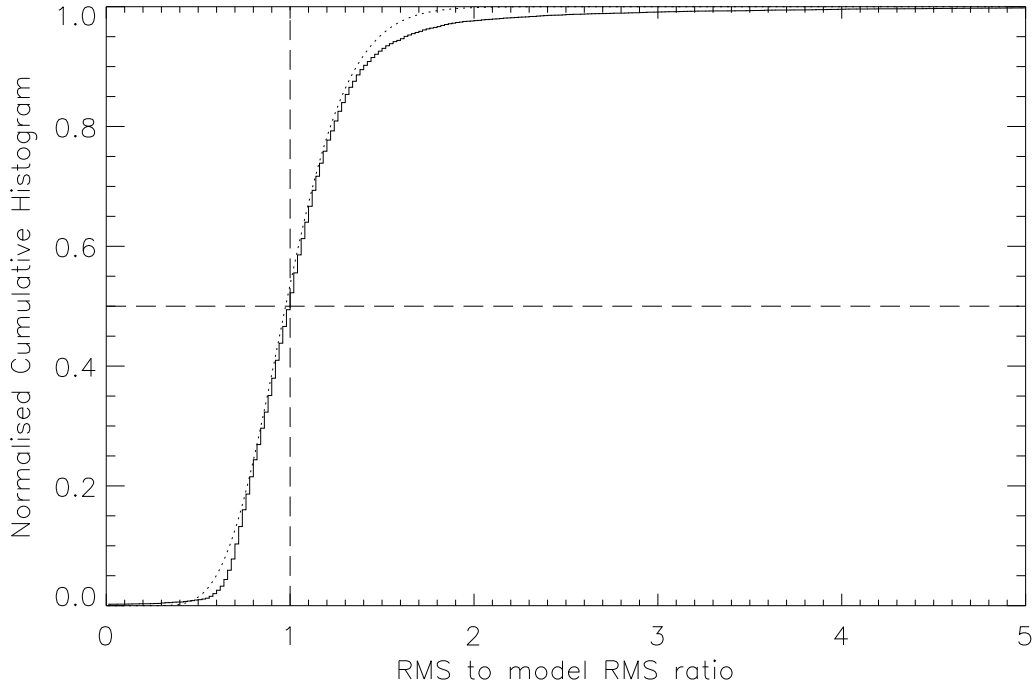


Figure 5.3: Normalised cumulative histogram of the ratio of the lightcurve RMS to the model RMS (solid line). We overplot the best-fit chi squared distribution with 27 degrees of freedom, where the x -axis of this distribution has been normalised by the number of degrees of freedom (dotted line).

as filled black circles, rather than the red dots for all the other stars.

5.2.2 Determining the Period of the Variable Stars

For each variable star candidate we inspect the lightcurve and remove obviously spurious lightcurves. These fake variables show the same large drop in brightness at the end of a night of observations, boosting the RMS of the lightcurve to a large value not representative of the actual scatter in the rest of the lightcurve. We also try and determine a period for each lightcurve using the Lomb-Scargle method [46],[73] via the standard periodogram. For the PASS0 lightcurves it became clear that without at least 500 epochs in a lightcurve, it was impossible to determine a period, mainly because of the poor time sampling of the lightcurves (~ 2 hours in every 24 hours). Hence we further cut the set of variable lightcurve candidates to only those with at least 500 epochs (see Figure 5.1). This left us with 60 variable stars.

The Lomb-Scargle periodogram method attempts to find the best period for a set of time-series data (evenly or unevenly spaced) by fitting sine and cosine curves at different frequencies to the data, and plotting the improvement in the data residuals as a function of frequency. With a clear

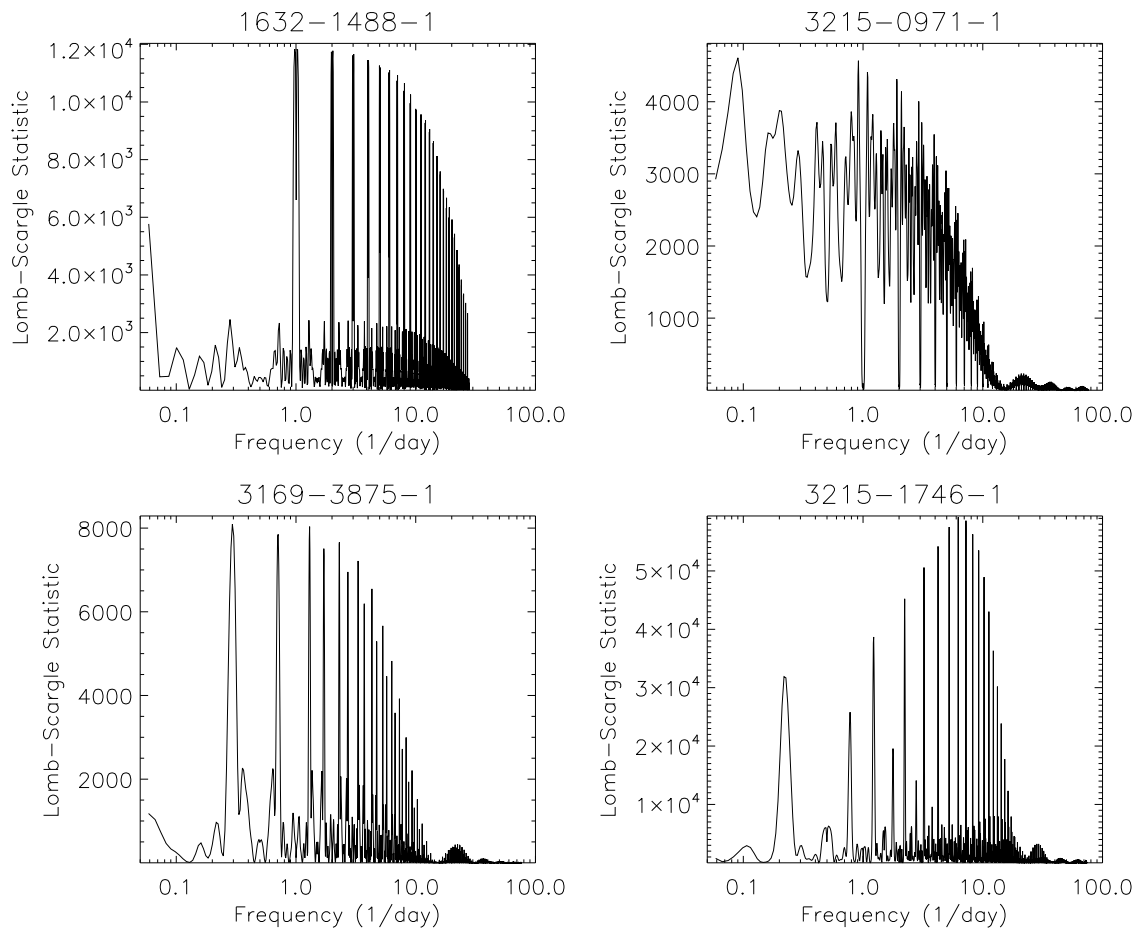


Figure 5.4: Periodograms for PASS0 example variable lightcurves.

periodic signal, the period will be indicated by the peak of the periodogram. However, when the signal is not so strong, there may be multiple periodogram peaks. Also, when the time-series data does not cover the full phase of the actual period, other periodogram peaks of equal strength may appear at integer multiples of the real frequency.

The period search for each variable lightcurve was limited to the range from the Nyquist frequency (half the sampling frequency) to half the time length of the specific lightcurve. In the case of a clear periodogram peak, we take this peak as the period. In the case of multiple equal-strength peaks, we take the peak corresponding to the shortest period as the period. For stars which have periodograms without a clear peak we simply plot the unphased lightcurves.

In Figure 5.4 we plot four example periodograms corresponding to four PASS0 variables. The top left periodogram is for the star 1632-1488-1 (lightcurve in Figure 5.5) which varies on a longer time scale than the length of the observation run. In this case, the periodogram suggests a period of 1 d, which is clearly wrong, and corresponds to the time between different observation nights. Hence we cannot derive a period for this star. The top right periodogram is for the star 3215-0971-

1 (lightcurve in Figure 5.6) which shows an eclipse on the seventh observing night, but is constant otherwise. It is impossible to derive a period with only one eclipse, and the periodogram shows no clear peak but suggests a period of greater than 10 d. Hence we do not adopt a period for this lightcurve. The bottom left periodogram is for the star 3169-3875-1 (lightcurve in Figure 5.8) and it has a clear peak at a period of 3.3979 d. The folded lightcurve is of good quality and therefore we adopt the suggested period. The bottom right periodogram is for the star 3215-1746-1 (lightcurve in Figure 5.7). The strongest peak is at a period of 0.1603 d which produces a beautiful folded lightcurve and therefore we adopt this period.

Of the 60 variable stars, we could derive a period in 30 cases. In Figures 5.5 and 5.6, we plot the 30 unphased variable star lightcurves for which a reliable period could not be found. In Figures 5.7 and 5.8, we present the remaining 30 variable star lightcurves phased on the most reliable period. We mention that for lightcurves like 1635-0568-1, 3155-1202-1 and 1631-0923-1 there seem to be a few copies of the lightcurve pattern shifted in magnitude from the main lightcurve. This is caused by a small subset of the *PASSCAL* factors for the LST correction ($k_1(t)$) being poorly determined for these lightcurves (see Section 3.2.2).

In Tables 5.1 and 5.2, we list the variable stars from the *PASS0* data. We report the celestial coordinates and mean magnitude of each star. We also report the period and amplitude of the lightcurve for those lightcurves for which we could derive a period. In the last column we report the results of a query in the *SIMBAD* astronomical database (<http://simbad.u-strasbg.fr/simbad/>) for the Tycho star identifier and list the variable type if the star is already known as a variable (note that the *SIMBAD* database does not supply the period). We find that 37 out of the 60 variable stars are already known as variables in *SIMBAD*, and it is likely that the remaining 23 variables are known variables that are not reported in *SIMBAD* but elsewhere, simply because these are bright stars (brighter than 10th magnitude). It is not within the range of this thesis to investigate these variables further.

5.3 Variables in the SuperWASP Lightcurve Data

All the lightcurves for the SuperWASP data have 688 epochs and hence it is not necessary to make a constraint on the number of epochs when identifying variable stars. We make a similar RMS diagram plot as for the *PASS0* data in Figure 5.9, and fit the model described by Equation 4.3 (solid black line). We obtain the results $A = 4.5$ mmag, $B = 10.1$ mmag and $C = 12.3$ mmag. We also plot a normalised cumulative histogram of the ratio of the lightcurve RMS to the model RMS in Figure 5.10 and find that the best-fit is a chi squared distribution with 47 degrees of freedom. Theoretically, since each SuperWASP lightcurve has 688 epochs, the best-fit chi squared should have 687 degrees of freedom. The fact that it has only 47 degrees of freedom indicates that systematic errors in the lightcurves have served to increase the spread in the RMS values around the model RMS curve.

We choose the variable star threshold $T = 2.18$ by requiring a 5% false alarm probability and using Equation 5.2 with $N = 9671$ lightcurves. The dashed green line in Figure 5.9 represents the solid black line scaled up by a factor of $T = 2.18$, and all stars above this become our candidate variable stars (filled black circles). With this method we find 287 candidate variables.

However, we find many high scatter lightcurves for the fainter stars and hence we decide to

remove all candidate variables with mean magnitudes of less than 14.5 mag, which leaves 217 candidate variables. We visually inspect the candidate variable lightcurves and remove obviously spurious variables, usually due to a group of outlier data points. We also use the Lomb-Scargle method to determine a period for each lightcurve in exactly the same way as for the PASS0 variable lightcurves in Section 5.2.2.

The results of our variable search in the SuperWASP lightcurves are shown in Figures 5.11 and 5.12 where in Figure 5.11 we plot 11 variable stars for which we could not find a period, and in Figure 5.12 we plot 10 variable stars for which we could find a period. In Table 5.3 we report the properties of the SuperWASP variables in an identical way to Tables 5.1 and 5.2 for the PASS0 variables. We find that 15 out of the 21 variables are already known as variables in the SIMBAD astronomical database. The 21 variables are plotted in Figure 5.9 as large filled black circles.

5.4 Conclusions

In Section 5.2 we search for variables in 12853 PASS0 lightcurves using a fitted model to the RMS diagram. We find 60 convincing variable star candidates and we are able to derive a period for 30 of them. We also find that 37 candidate variables are already known variables according to the SIMBAD astronomical database. In Section 5.3 we perform a similar variable star search in the 9671 SuperWASP lightcurves and find 21 convincing variable star candidates, 15 of which are already known variables according to SIMBAD. The results presented in this Chapter show the potential for variable star discovery and monitoring as a side-product of a wide-field transit survey.

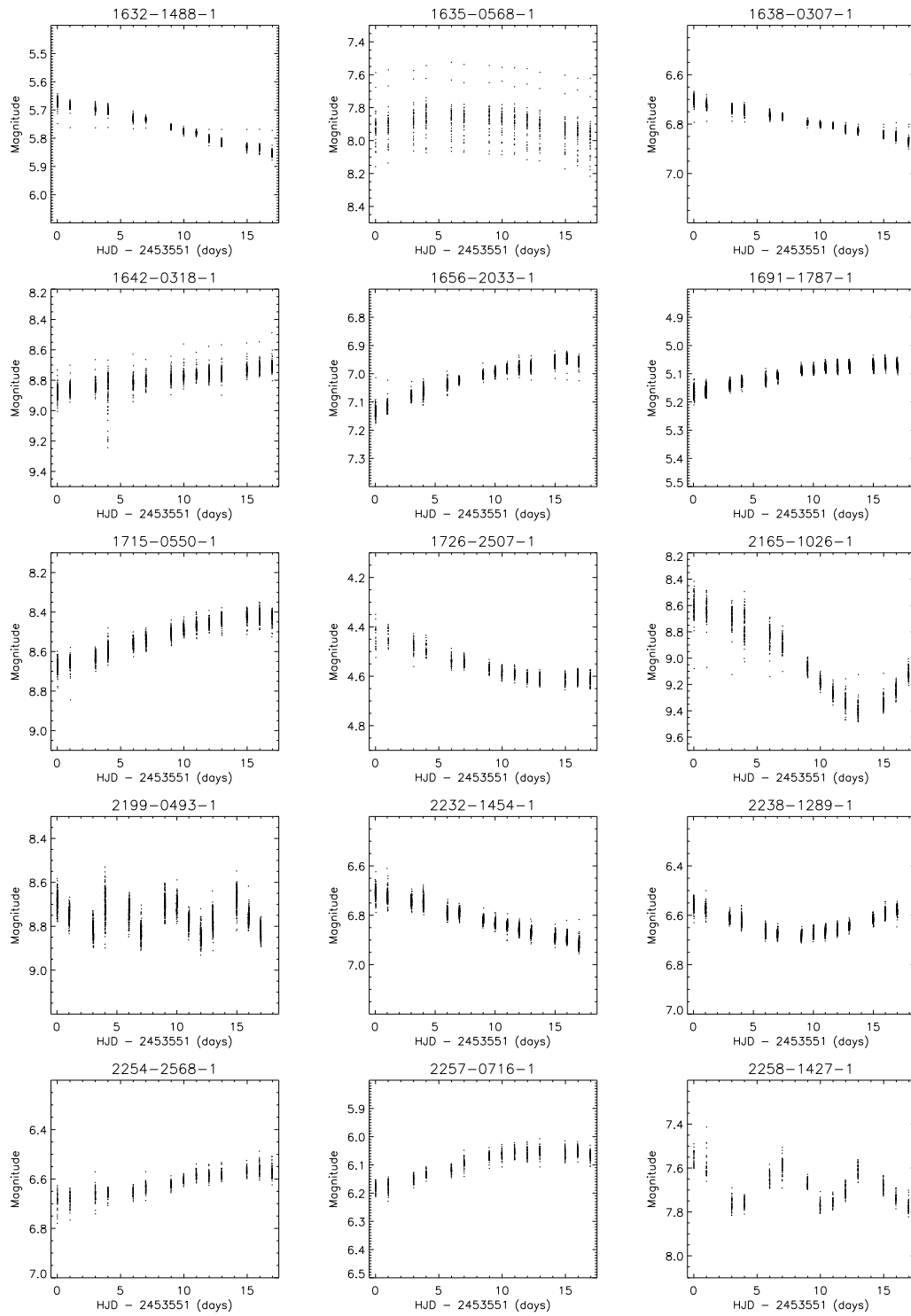


Figure 5.5: Unphased PASS0 variable star lightcurves.

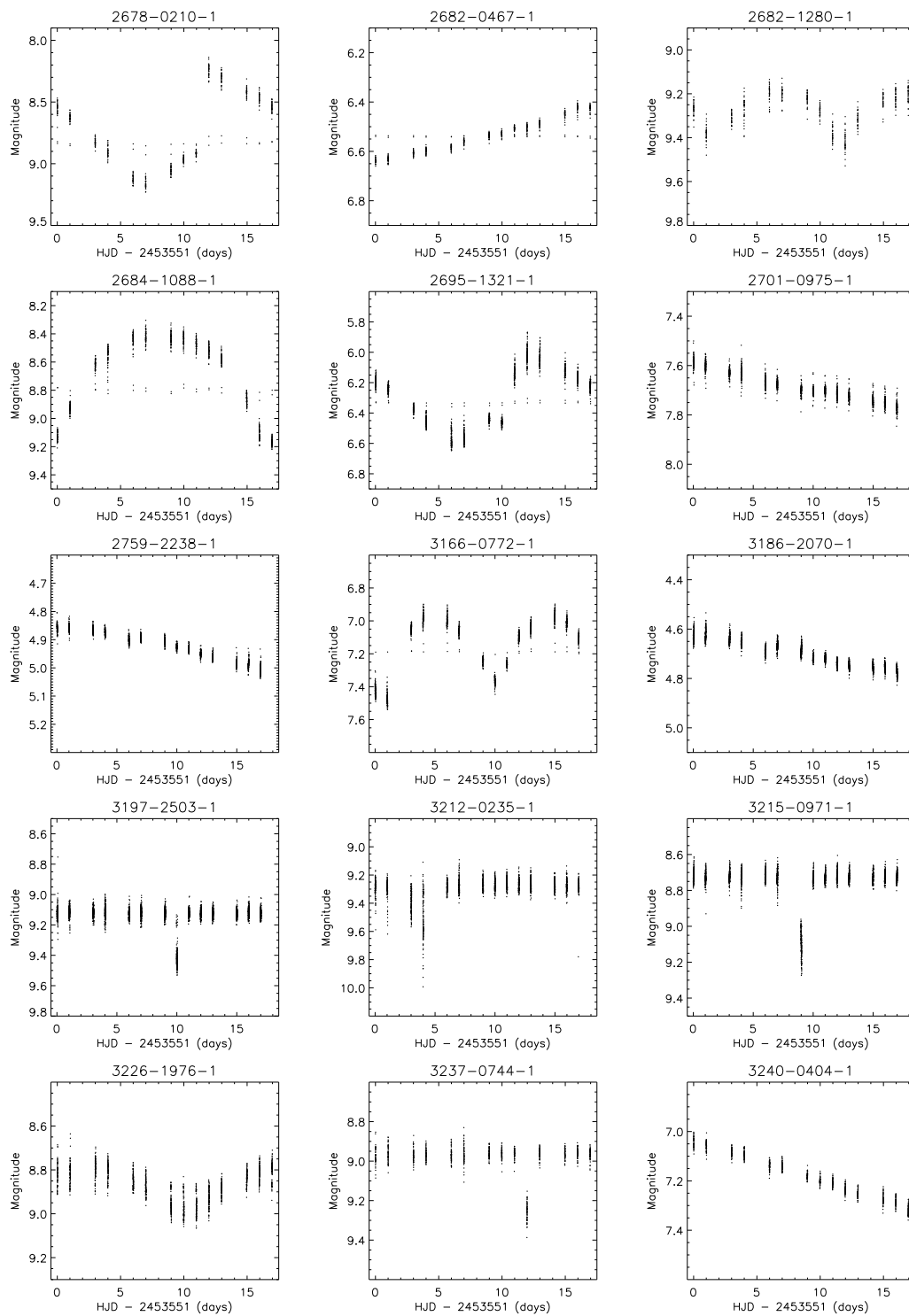


Figure 5.6: Unphased PASS0 variable star lightcurves continued.

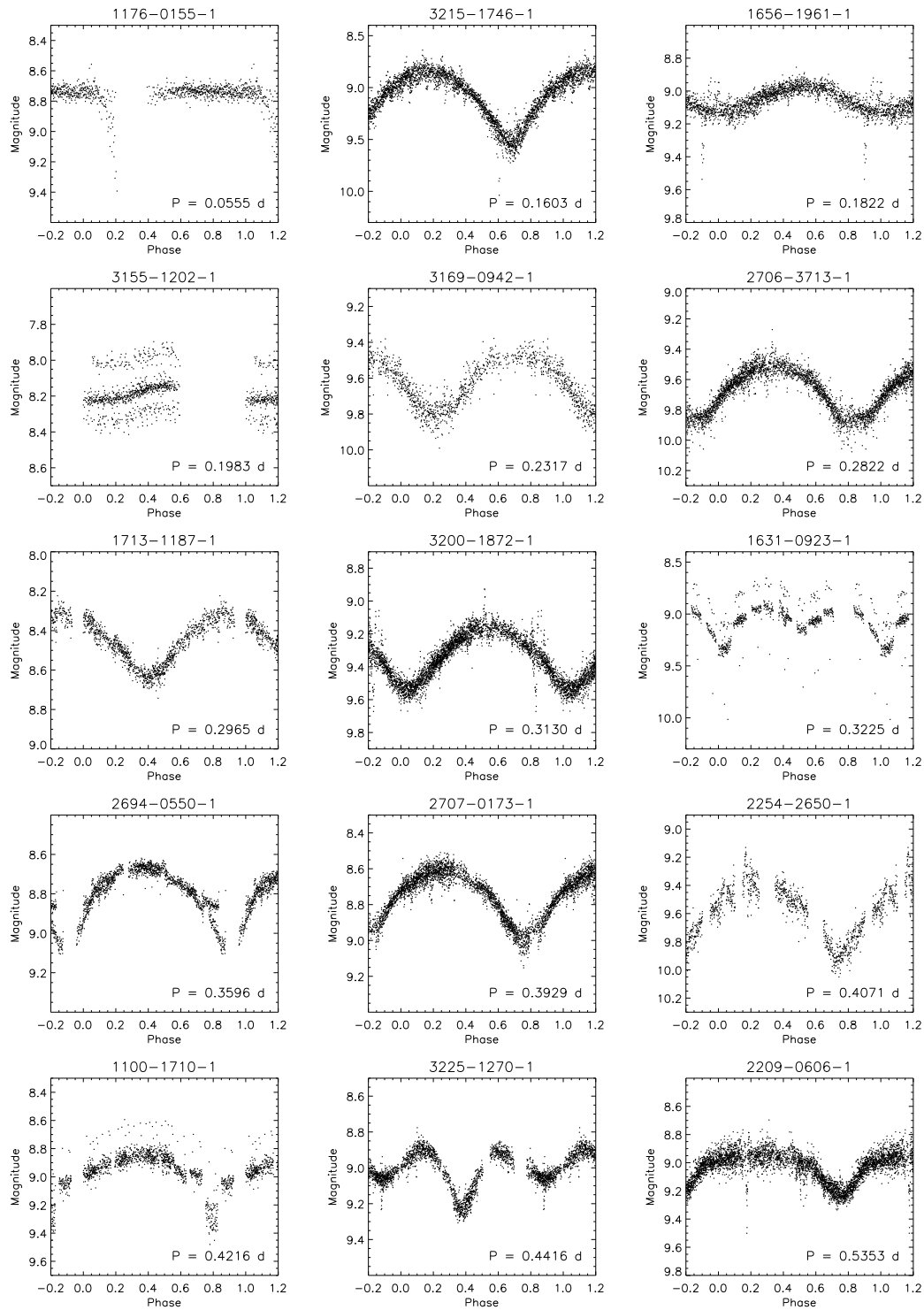


Figure 5.7: Phased PASS0 variable star lightcurves.

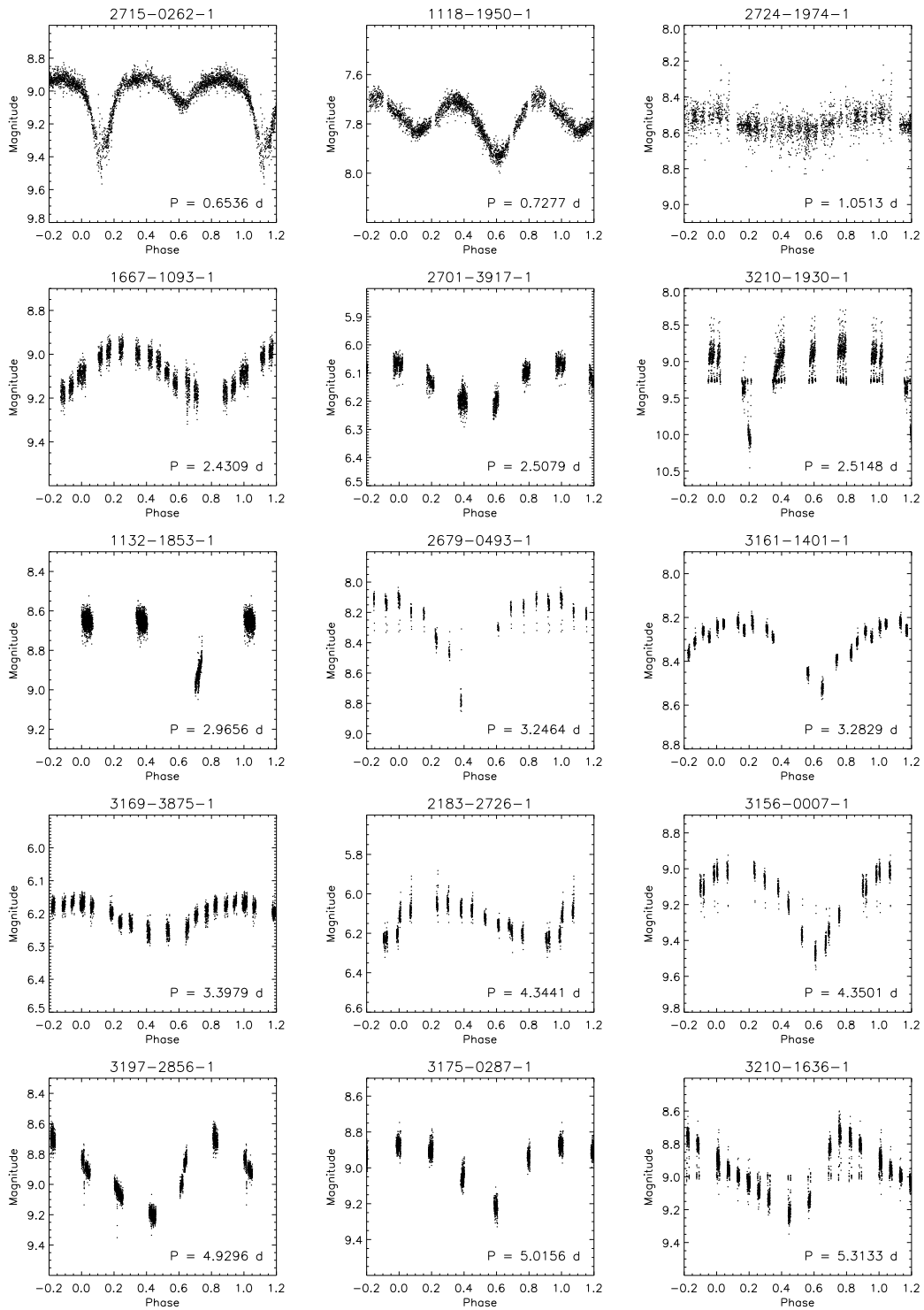


Figure 5.8: Phased PASS0 variable star lightcurves continued.

Table 5.1: Properties of the PASS0 variable stars. The SIMBAD variable type is taken from a query in the SIMBAD astronomical database (<http://simbad.u-strasbg.fr/simbad/>).

Star Name	RA J2000	Dec J2000	Mean Magnitude	Amplitude (mag)	Period (d)	SIMBAD Variable Type
1632-1488-1	20:29:10	16° 16' 25"	5.76	-	-	Semi-Regular Pulsator
1635-0568-1	20:16:30	17° 34' 42"	7.90	-	-	-
1638-0307-1	20:43:05	17° 05' 17"	6.79	-	-	Mira Ceti
1642-0318-1	20:43:50	19° 13' 07"	8.79	-	-	-
1656-2033-1	21:01:53	18° 59' 56"	7.02	-	-	Variable
1691-1787-1	21:52:18	21° 16' 23"	5.10	-	-	Variable
1715-0550-1	23:10:45	19° 19' 22"	8.52	-	-	-
1726-2507-1	23:33:28	22° 29' 56"	4.57	-	-	Variable
2165-1026-1	20:36:32	26° 36' 15"	9.03	-	-	RV Tau
2199-0493-1	21:23:50	28° 28' 15"	8.76	-	-	-
2232-1454-1	22:42:59	28° 09' 26"	6.82	-	-	Semi-Regular Pulsator
2238-1289-1	22:54:40	24° 23' 14"	6.63	-	-	Irregular Variable
2254-2568-1	23:47:23	26° 07' 53"	6.61	-	-	Variable
2257-0716-1	23:46:52	28° 25' 11"	6.09	-	-	-
2258-1427-1	23:55:04	28° 38' 01"	7.69	-	-	RS CVn
2678-0210-1	20:04:27	34° 06' 44"	8.73	-	-	Delta Cepheid
2682-0467-1	20:04:28	36° 49' 00"	6.53	-	-	Semi-Regular Pulsator
2682-1280-1	20:01:43	36° 47' 28"	9.28	-	-	-
2684-1088-1	20:18:47	36° 20' 26"	8.69	-	-	Beta Lyr Eclipsing Binary
2695-1321-1	20:43:35	35° 35' 33"	6.29	-	-	-
2701-0975-1	21:05:49	30° 13' 02"	7.69	-	-	Semi-Regular Pulsator
2759-2238-1	23:10:09	33° 46' 04"	4.92	-	-	Irregular Variable
3166-0772-1	20:48:00	39° 17' 16"	7.15	-	-	Beta Lyr Eclipsing Binary
3186-2070-1	21:22:49	40° 55' 57"	4.70	-	-	Variable
3197-2503-1	21:56:03	43° 19' 22"	9.14	-	-	-
3212-0235-1	22:24:14	44° 02' 49"	9.30	-	-	-
3215-0971-1	22:52:15	38° 44' 45"	8.75	-	-	Eclipsing Binary
3226-1976-1	22:46:18	43° 52' 08"	8.87	-	-	-
3237-0744-1	23:58:58	40° 47' 32"	8.99	-	-	Variable Star
3240-0404-1	23:44:40	42° 03' 32"	7.18	-	-	Variable Star
1176-0155-1	23:45:39	14° 43' 48"	8.75	0.65	0.0555	-
3215-1746-1	22:53:42	37° 56' 19"	9.12	0.70	0.1603	W UMa Eclipsing Binary
1656-1961-1	20:57:10	19° 38' 59"	9.05	0.20	0.1822	W UMa Eclipsing Binary
3155-1202-1	20:10:55	40° 42' 03"	8.17	0.10	0.1983	-
3169-0942-1	21:13:19	37° 34' 08"	9.65	0.35	0.2317	-
2706-3713-1	21:16:22	32° 12' 52"	9.66	0.50	0.2822	-
1713-1187-1	23:25:25	15° 41' 19"	8.48	0.35	0.2965	W UMa Eclipsing Binary
3200-1872-1	22:29:35	37° 57' 31"	9.33	0.35	0.3130	-
1631-0923-1	20:21:35	15° 25' 38"	9.06	0.45	0.3225	-
2694-0550-1	20:37:20	35° 26' 16"	8.77	0.45	0.3596	Beta Lyr Eclipsing Binary

Table 5.2: Properties of the PASS0 variable stars. The SIMBAD variable type is taken from a query in the SIMBAD astronomical database (<http://simbad.u-strasbg.fr/simbad/>).

Star Name	RA J2000	Dec J2000	Mean Magnitude	Amplitude (mag)	Period (d)	SIMBAD Variable Type
2707-0173-1	21:25:00	33° 41' 15"	8.75	0.40	0.3929	W UMa Eclipsing Binary
2254-2650-1	23:45:35	25° 28' 19"	9.60	0.60	0.4071	W UMa Eclipsing Binary
1100-1710-1	20:39:37	14° 25' 43"	8.93	0.50	0.4216	Algol Eclipsing Binary
3225-1270-1	23:16:21	41° 33' 43"	9.03	0.35	0.4416	-
2209-0606-1	22:11:39	26° 07' 32"	9.04	0.25	0.5353	-
2715-0262-1	21:21:24	35° 44' 11"	9.01	0.55	0.6536	Beta Lyr Eclipsing Binary
1118-1950-1	21:26:41	13° 41' 18"	7.79	0.30	0.7277	Beta Lyr Eclipsing Binary
2724-1974-1	22:09:33	33° 05' 28"	8.55	0.10	1.0513	-
1667-1093-1	21:24:00	18° 16' 44"	9.08	0.25	2.4309	W Vir
2701-3917-1	22:15:31	32° 18' 45"	6.14	0.15	2.5079	-
3210-1930-1	22:01:31	43° 53' 26"	9.08	1.10	2.5148	RS CVn
1132-1853-1	21:41:38	14° 39' 31"	8.69	0.35	2.9656	Algol Eclipsing Binary
2679-0493-1	20:06:10	35° 23' 10"	8.26	0.70	3.2464	Beta Lyr Eclipsing Binary
3161-1401-1	20:32:22	41° 18' 19"	8.31	0.35	3.2829	Beta Lyr Eclipsing Binary
3169-3875-1	21:19:22	38° 14' 15"	6.20	0.10	3.3979	Delta Cepheid
2183-2726-1	20:51:28	28° 15' 02"	6.14	0.20	4.3441	Delta Cepheid
3156-0007-1	20:26:21	39° 40' 10"	9.18	0.45	4.3501	-
3197-2856-1	21:51:41	43° 08' 03"	8.98	0.55	4.9296	Delta Cepheid
3175-0287-1	20:55:19	42° 43' 32"	8.98	0.40	5.0156	-
3210-1636-1	21:01:05	40° 15' 35"	8.97	0.30	5.3133	-

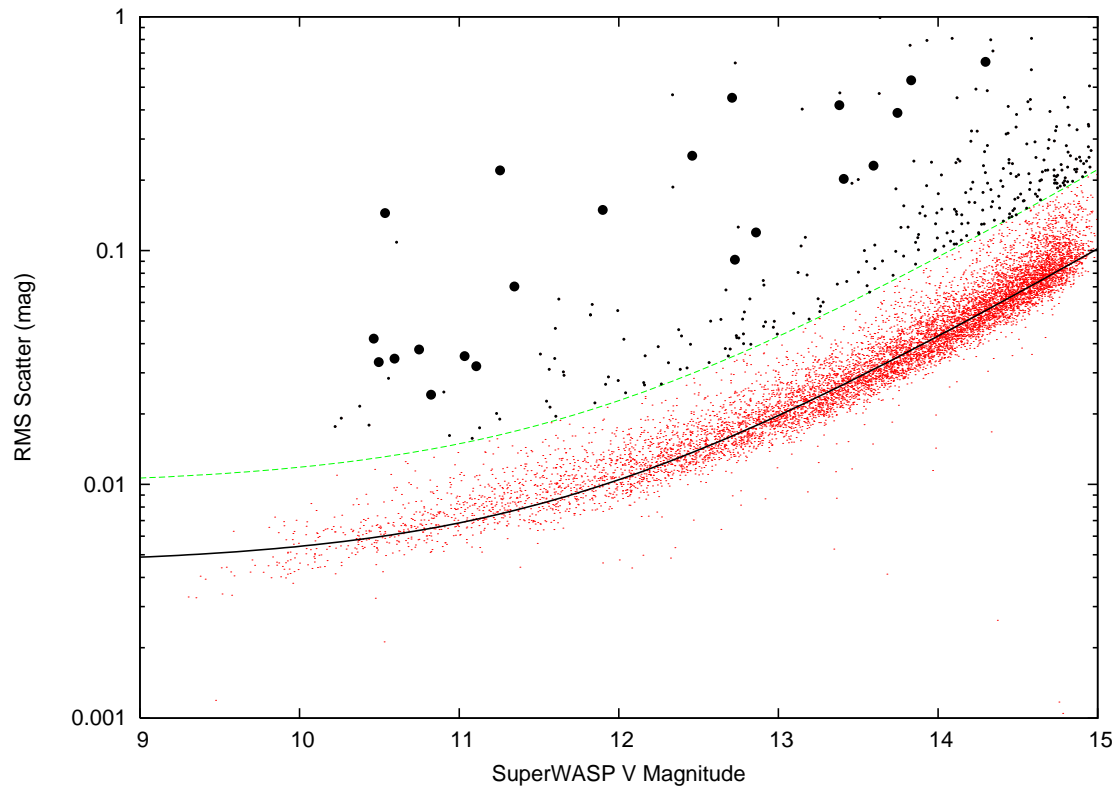


Figure 5.9: Plot of lightcurve RMS scatter against mean magnitude for the SuperWASP lightcurves (red dots). The fit to the RMS diagram is shown as the solid black line, and the cut off in RMS for choosing variable star candidates is shown by the green dashed line. Variable star candidates are shown as small filled black circles. The final set of 21 variable stars are shown as large filled black circles.

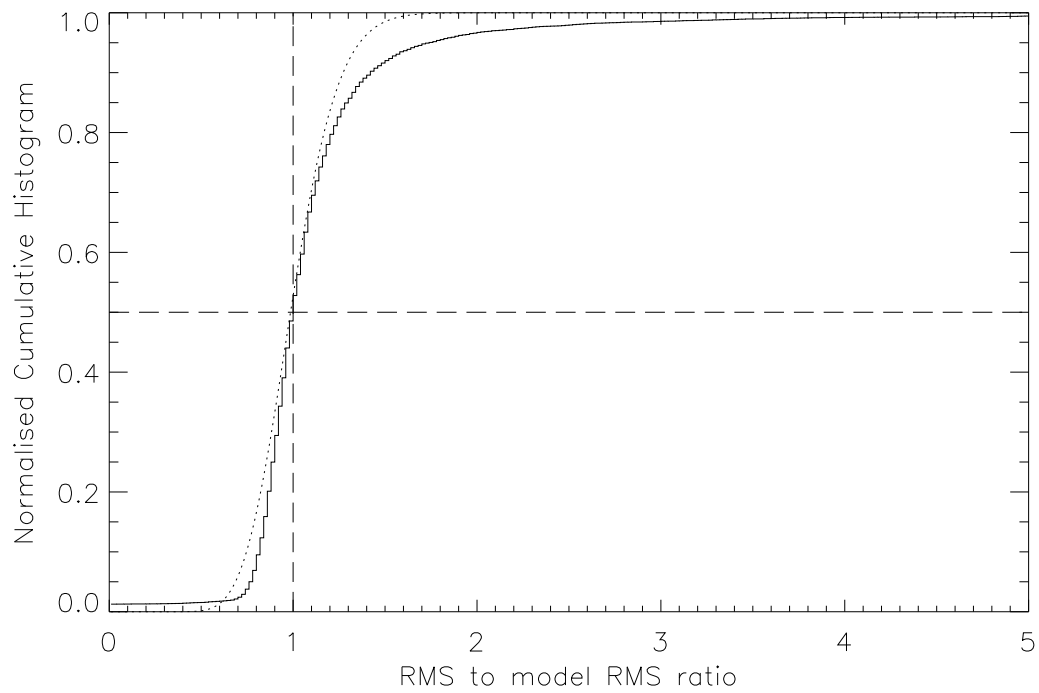


Figure 5.10: Normalised cumulative histogram of the ratio of the lightcurve RMS to the model RMS (solid line). We overplot the best-fit chi squared distribution with 47 degrees of freedom, where the x -axis of this distribution has been normalised by the number of degrees of freedom (dotted line).

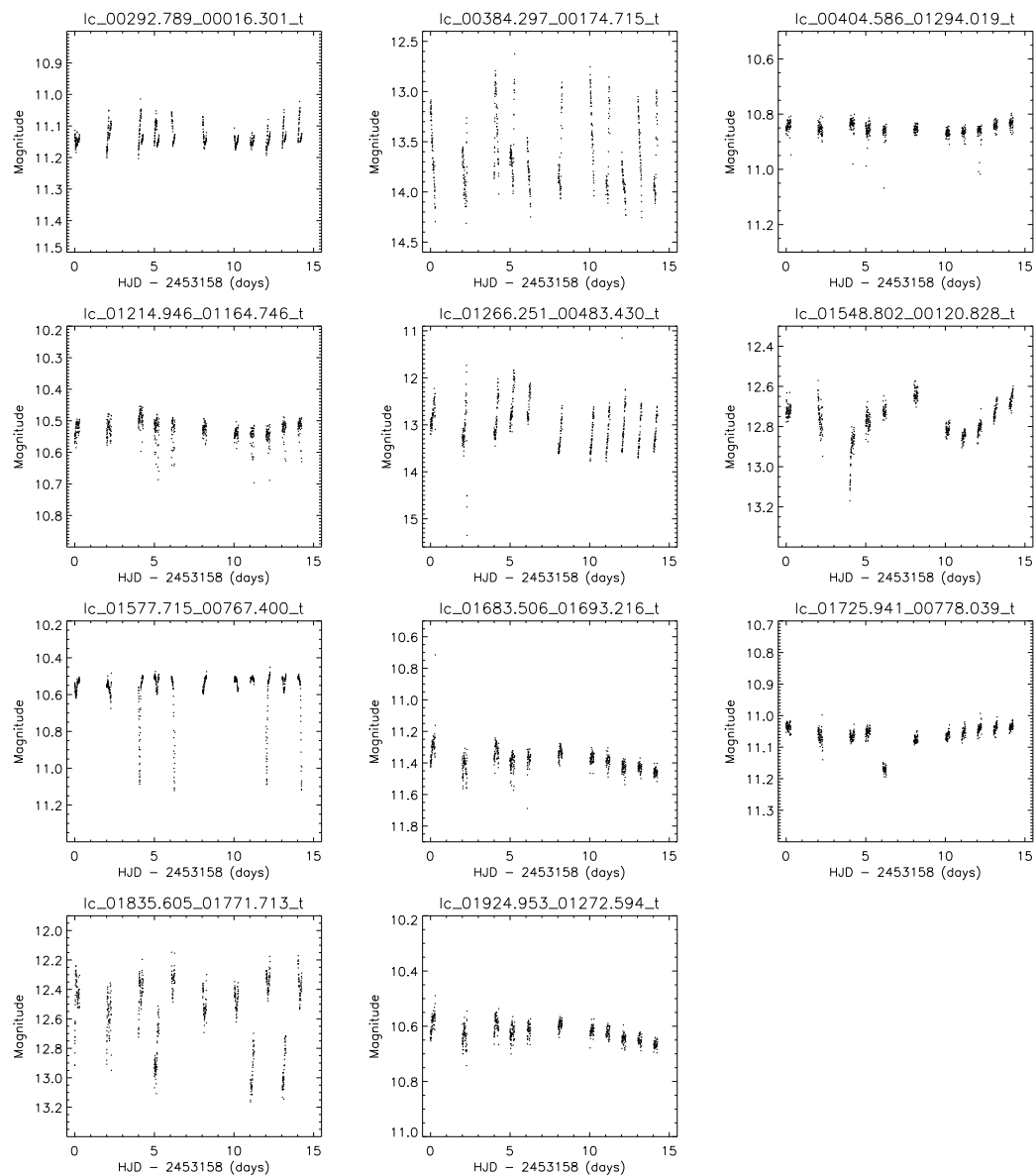


Figure 5.11: Unphased SuperWASP variable star lightcurves.

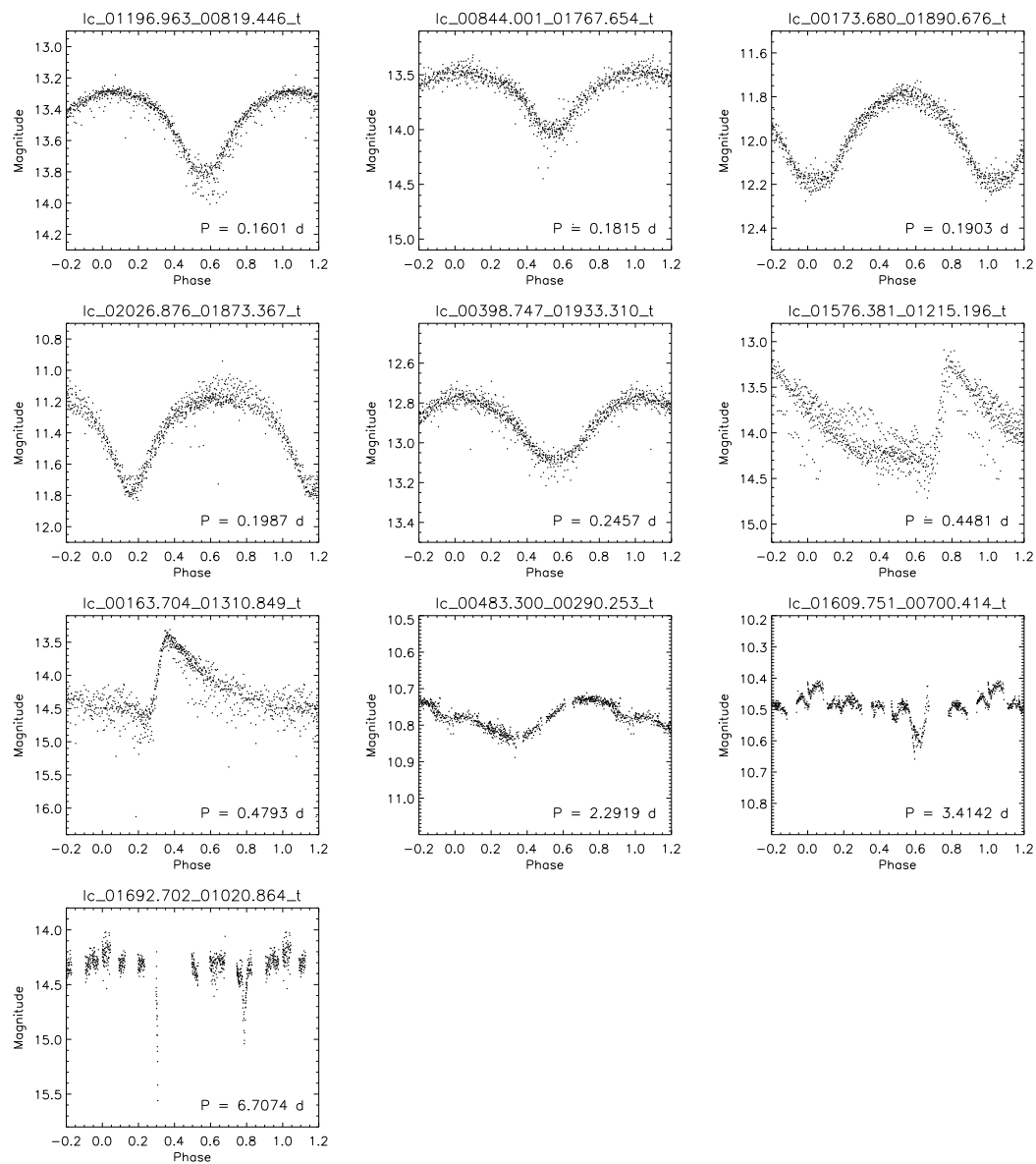


Figure 5.12: Phased SuperWASP variable star lightcurves.

Table 5.3: Properties of the SuperWASP variable stars. The SIMBAD variable type is taken from a query in the SIMBAD astronomical database (<http://simbad.u-strasbg.fr/simbad/>).

Star Name	RA J2000	Dec J2000	Mean Magnitude	Amplitude (mag)	Period (d)	SIMBAD Variable Type
lc_00292.789_00016.301_t	15:24:06.0	34° 34' 11.3''	11.13	-	-	RR Lyrae
lc_00384.297_00174.715_t	15:27:14.3	34° 14' 52.6''	13.63	-	-	RR Lyrae
lc_00404.586_01294.019_t	15:48:22.0	34° 18' 21.6''	10.85	-	-	-
lc_01214.946_01164.746_t	15:46:26.1	31° 05' 36.0''	10.53	-	-	-
lc_01266.251_00483.430_t	15:33:50.9	30° 49' 16.7''	12.99	-	-	-
lc_01548.802_00120.828_t	15:27:28.1	29° 38' 09.3''	12.77	-	-	Galaxy
lc_01577.715_00767.400_t	15:39:16.3	29° 37' 07.6''	10.59	-	-	Algol Eclipsing Binary
lc_01683.506_01693.216_t	15:56:08.0	29° 14' 20.0''	11.38	-	-	Mira Ceti
lc_01725.941_00778.039_t	15:39:26.7	29° 00' 58.9''	11.06	-	-	-
lc_01835.605_01771.713_t	15:57:31.8	28° 38' 00.4''	12.56	-	-	RR Lyrae
lc_01924.953_01272.594_t	15:48:31.7	28° 16' 54.5''	10.62	-	-	Pulsator
lc_01196.963_00819.446_t	15:40:00.8	31° 08' 17.6''	13.49	0.50	0.1601	Eclipsing Binary
lc_00844.001_01767.654_t	15:57:41.0	32° 33' 51.3''	13.69	0.50	0.1815	Eclipsing Binary
lc_00173.680_01890.676_t	16:00:14.5	35° 12' 31.6''	11.96	0.40	0.1903	W UMa Eclipsing Binary
lc_02026.876_01873.367_t	15:59:18.6	27° 52' 15.0''	11.35	0.60	0.1987	W UMa Eclipsing Binary
lc_00398.747_01933.310_t	16:00:58.5	34° 18' 54.3''	12.91	0.35	0.2457	RR Lyrae
lc_01576.381_01215.196_t	15:47:25.9	29° 39' 42.6''	13.98	1.10	0.4481	RR Lyrae
lc_00163.704_01310.849_t	15:49:00.2	35° 15' 59.3''	14.18	1.40	0.4793	RR Lyrae
lc_00483.300_00290.253_t	15:29:32.7	33° 52' 55.5''	10.78	0.10	2.2919	-
lc_01609.751_00700.414_t	15:38:03.0	29° 29' 14.0''	10.49	0.20	3.4142	RS CVn
lc_01692.702_01020.864_t	15:43:54.7	29° 11' 42.4''	14.35	1.20	6.7074	-

Chapter 6

Transit Candidates from the PASS0 and SuperWASP Data

6.1 Introduction

In this Chapter we perform a transit search on the PASS0 lightcurves and the SuperWASP lightcurves. However, we do not expect to find any new transit candidates since the observations do not cover a long enough time period. The ~ 15 night observing runs are unlikely to catch any transiting planet in a ~ 3 day orbit, especially in the case of the PASS0 data since only ~ 2 hours were observed each night. Instead, the aim of the transit search exercise is to see if we can recover any of the known transiting planets and/or transit candidates in the field with a standard transit search method.

6.2 Transit Search Algorithms

Identifying transit candidates from large sets of lightcurves for radial velocity follow-up observations is a difficult procedure. The transit signal is small (of the order of $\sim 1\%$) and it is usually comparable to the noise in the lightcurves. In many cases a single transit is not detectable and the combined signal from observations of many different transits is necessary for the transit candidate to be identified. This implies that a period analysis is required while searching for transits increasing the parameter space to be searched. When searching for a transit we therefore need to scan the parameter space defined by the transit epoch, duration and period.

Transit search algorithms have been studied and reviewed in the literature [84],[85]. One of the most widely used is the box-fitting algorithm (BLS) by Kovacs, Zucker & Mazeh [42]. It has been proven to perform the same or better than any other transit search algorithm in the tests of Tingley (2003; [85]). The BLS method is based on searching the lightcurves for signals that have a periodic alternation between two discrete levels, with much less time spent at the lower level. The method involves choosing a trial period and considering the folded time series of magnitude measurements. A step function is fitted for a grid of phases and transit durations covering the parameter space of these quantities. For each point in the parameter grid, the average weighted squared deviation is calculated and the minimum of this quantity over the parameter grid indicates

the best phase and transit duration. The same procedure is repeated for all trial periods over a given range in which we are searching for planets. The overall minima of the BLS statistic is taken as the best transit signal, with the corresponding period, phase and duration, and fitted out-of-transit and in-transit magnitudes. The BLS method is made even more effective by ignoring any fits that give an increase in brightness at times of “transit” (“the directional correction”, see [85]).

Another method that was not considered in the tests of Tingley [84],[85] is that described by Schwarzenberg-Czerny & Beaulieu 2006 [74]. This method is based on a modification of the analysis-of-variance (AoV) periodogram [75] for the specific purpose of planetary transit searches (AoVtr). This method was published after the comparison paper of Tingley [85] and hence was not included in the tests. The AoVtr method involves choosing a trial period and then binning the lightcurve into $N_H = P/t_T$ bins, where P is the period and t_T is the transit duration. The bin with the faintest mean magnitude is taken as the transit bin, and the out-of-transit mean magnitude is calculated from the remaining data points. Using the division of the data into out-of-transit and in-transit, the AoVtr statistic is calculated (see Schwarzenberg-Czerny & Beaulieu 2006). The maximum of the AoVtr statistic over all test periods indicates the best transit signal for the lightcurve.

Schwarzenberg-Czerny & Beaulieu state that the AoVtr test is more powerful than other methods because it is based on just one parameter fit, the in-transit magnitude. Also, it can be coded to be up to ten times more efficient than other tests, and this efficient code is available from the internet. Hence we have chosen to use the AoVtr method to search for transits in both the PASS0 and SuperWASP lightcurves.

6.3 Transit Candidates in the PASS0 Lightcurve Data

Out of the 13515 PASS0 lightcurves, we decide to search for transits in the 10827 lightcurves that have at least 500 epochs (as with the variable search) and that were not identified as variable candidates via Figure 5.2. By excluding stars with a high RMS, we are hopefully limiting the number of spurious transit candidates that may be detected by removing real variable stars and a large proportion of the stars with drops in brightness at the end of an observing night.

We apply the AoVtr routine to the lightcurves using the values of N_H suggested by Schwarzenberg-Czerny & Beaulieu, 15 and 30. This corresponds to searching for transits with durations that are 1/15 and 1/30 of the orbital period. We scan periods from 1 d (which is slightly shorter than the period of the shortest period known extra-solar planet) up to 8 d (approximately half the duration of the observing run). The frequency resolution used was $5 \times 10^{-4} \text{ d}^{-1}$ which corresponds to a period resolution of $5 \times 10^{-4} \text{ d}$ at a period of 1 d and 0.032 d at a period of 8 d. Both these period resolutions are small fractions of the transit duration for both the $N_H = 15$ and $N_H = 30$ cases, which indicates that we are scanning the period parameter space with sufficient resolution.

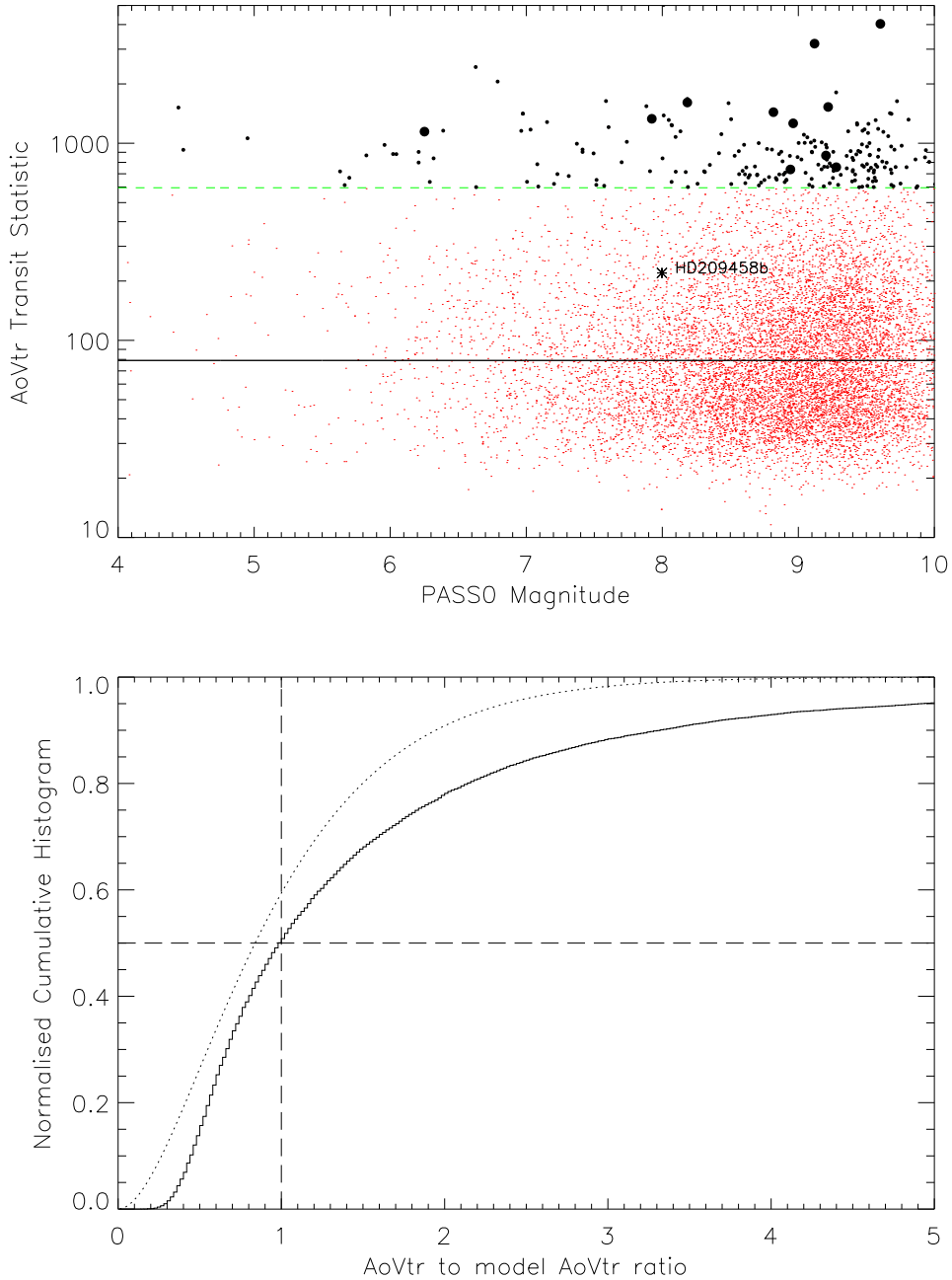


Figure 6.1: **Upper:** The AoVtr statistic plotted against lightcurve magnitude for the 10827 PASS0 lightcurves that we search for transit candidates (red dots). This plot corresponds to the $N_H = 15$ search case. The fitted constant function is plotted as the continuous black line, and the transit candidate threshold is plotted as the green dashed line. The set of initial transit candidates are the filled black circles, and the AoVtr statistic for HD209458 is plotted as an asterisk. The larger filled black circles represent the set of final transit candidates. **Lower:** Normalised cumulative histogram of the ratio of the AoVtr statistic to the model AoVtr statistic (solid line). We overplot the best-fit chi squared distribution with 4 degrees of freedom, where the x -axis of this distribution has been normalised by the number of degrees of freedom (dotted line).

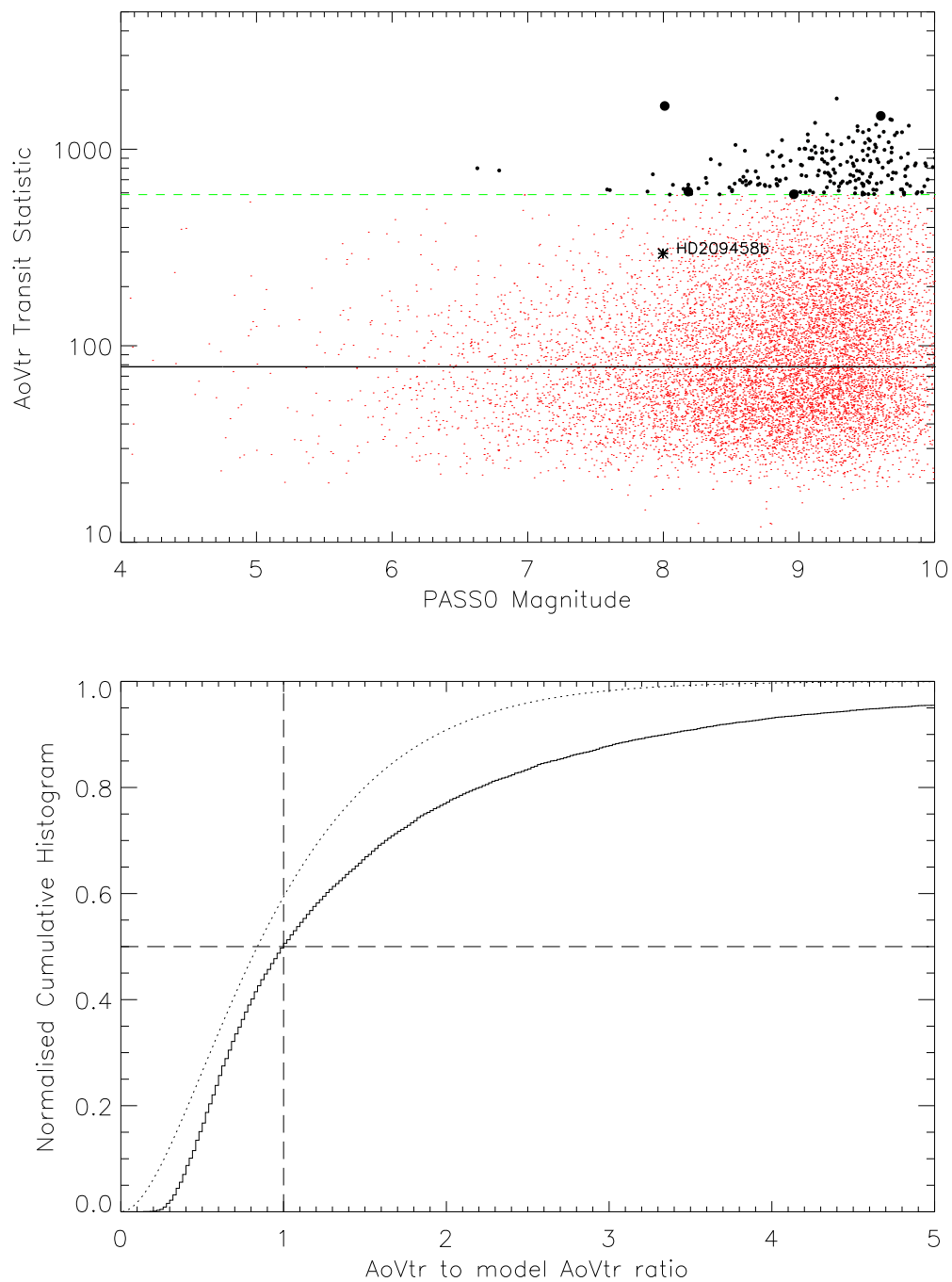


Figure 6.2: **Upper and Lower:** The same as Figure 6.1 except that these plots correspond to the $N_H = 30$ search case.

In the upper panels of Figures 6.1 and 6.2, we plot the AoVtr statistic versus magnitude for both the $N_H = 15$ and $N_H = 30$ cases (red dots). To identify our initial set of transit candidates in both cases, we fit a constant function to the AoVtr versus magnitude diagram using a 3-sigma clip algorithm and the amoeba downhill simplex method to minimise the total of the squared residuals. The idea of the fit is very similar to that of the “backbone” fits to the RMS diagrams described in Section 4.3.2 except that we now use the magnitude-independent model:

$$\text{AoVtr}(m) = A \quad (6.1)$$

where m represents magnitude, and A is a constant to be determined. We find that for $N_H = 15$ we get $A = 79.1$, and that for $N_H = 30$ we get $A = 78.1$. The models for $\text{AoVtr}(m)$ are plotted in both the upper panels of Figures 6.1 and 6.2 as solid black lines.

In the lower panels of Figures 6.1 and 6.2 we plot the normalised cumulative histogram of the ratio of the AoVtr statistic to the model AoVtr transit statistic in Equation 6.1 (solid line). The best-fit chi squared distribution has 4 degrees of freedom (dotted line) in both the $N_H = 15$ and $N_H = 30$ cases. We choose to require a false alarm probability of 5%, which gives $T = 7.52$ using Equation 5.2 and $N = 10827$ lightcurves. Hence we choose our initial set of transit candidates by scaling up the $\text{AoVtr}(m)$ model lines by a factor of 7.52 (green dashed lines) and choosing all lightcurves with the AoVtr statistic above the scaled model. The initial transit candidates are plotted on Figures 6.1 and 6.2 as filled black circles, and we find 221 initial transit candidates for the $N_H = 15$ case and 216 initial transit candidates for the $N_H = 30$ case.

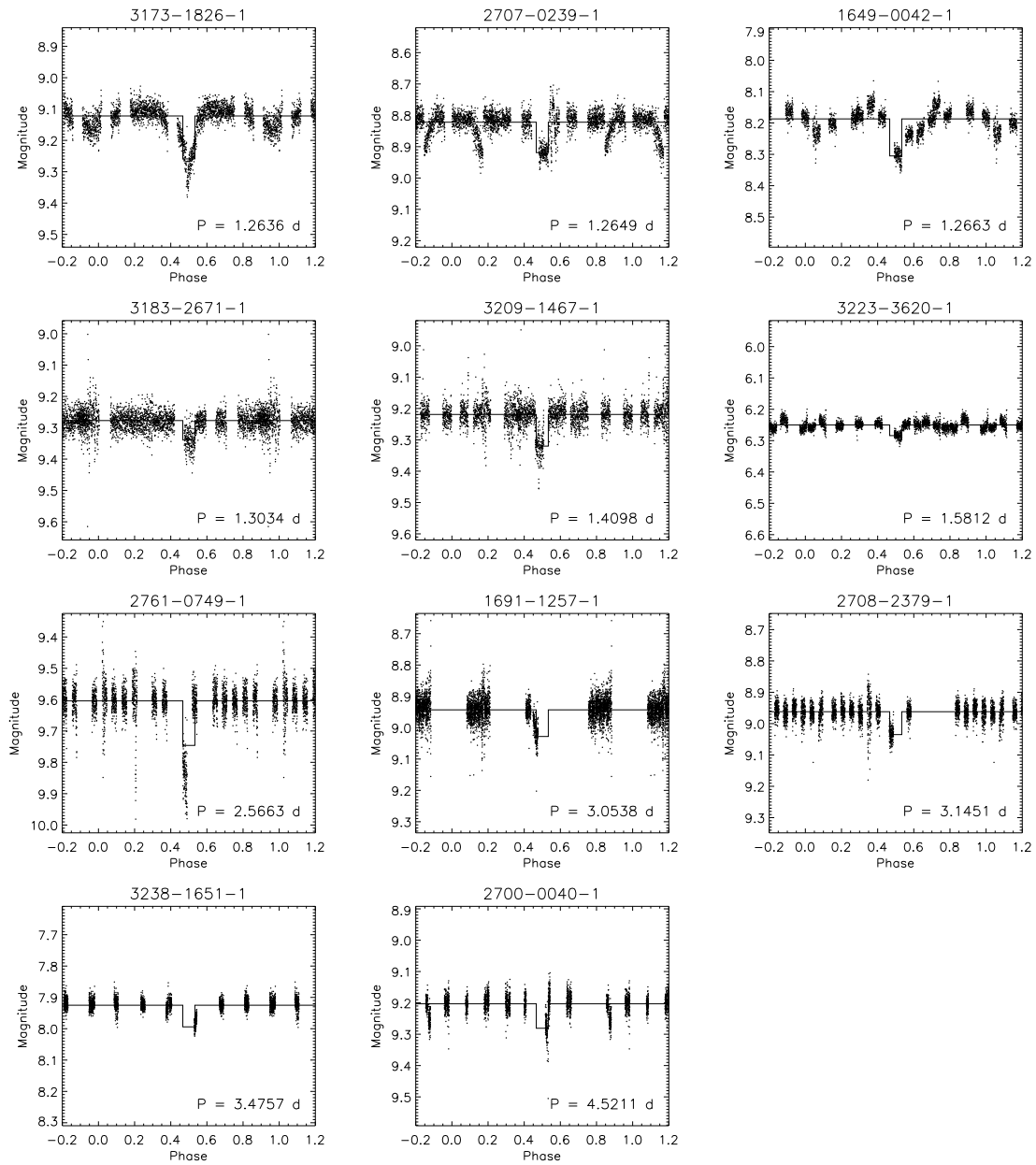
We also plot the AoVtr statistic for HD209458 in the upper panels of Figures 6.1 and 6.2 as an asterisk. It is clear that the transit of HD209458 in the PASS0 data would not have been detected by our method because it lies below the transit candidate threshold for both search cases. This is to be expected since the PASS0 lightcurve of HD209458 only includes the observations of half of one transit which does not give enough signal-to-noise in order for it to be detected.

We inspect all our initial transit candidates and find many spurious lightcurves, either showing the brightness drop at the end of an observing night (as mentioned in section 5.2.2) picked up as a transit by the AoVtr algorithm, or showing a repeating pattern with a period that is close to an integer (1, 2, 3 etc.) or half integer (1.5, 2.5, 3.5 etc.) which indicates the presence of systematic errors repeated from night to night. By removing these fake transit candidates, we are left with 11 transit candidates for the $N_H = 15$ case and 4 transit candidates for the $N_H = 30$ case. Our final transit candidates are plotted in the upper panels of Figures 6.1 and 6.2 as large filled black circles.

We plot the phased lightcurves of the transit candidates for the $N_H = 15$ case in Figure 6.3 and for the $N_H = 30$ case in Figure 6.4. The scale on the magnitude axis always covers a range of 0.7 magnitudes so that the depths of each transit candidate are directly comparable. We also overplot the step function model corresponding to the AoVtr statistic as a continuous black line.

Star 3173-1826-1 is reported by the SIMBAD astronomical database as an irregular type variable, but it is clearly an eclipsing binary with a secondary eclipse. It is interesting to note that this variable star was not detected in our variable search in Chapter 5 but it was detected in our transit search. Star 2707-0239-1 is reported by SIMBAD as a double star, and the lightcurve also suggests that it is an eclipsing binary (note that the AoVtr transit algorithm has chosen the wrong period). Stars 1649-0042-1 and 3223-3620-1 are not constant out of the detected drop in brightness and hence we can exclude these as transiting planets. In fact star 3223-3620-1 is reported as

a Beta Cep type variable by SIMBAD. The remaining stars all show the correct shape for a transit curve, but the phase coverage of the lightcurves is too poor for any real conclusions to be drawn about the nature of the dips, since they are all only partially covered. Of these stars, 1691-1257-1, 3238-1651-1 and 3216-1614-1 are known variable stars in the SIMBAD database. Also, note that three of the four transit candidates for the $N_{\text{H}} = 30$ case are also transit candidates for the $N_{\text{H}} = 15$. Hence, from our 12 different transit candidates, we have 5 for which more observations would be useful to construct their full phased lightcurves. To obtain celestial coordinates of any of the mentioned stars, simply perform a search for the Tycho-2 identifier in the SIMBAD database.

Figure 6.3: Plots of the phased lightcurves of the transit candidates for the $N_H = 15$ search case.

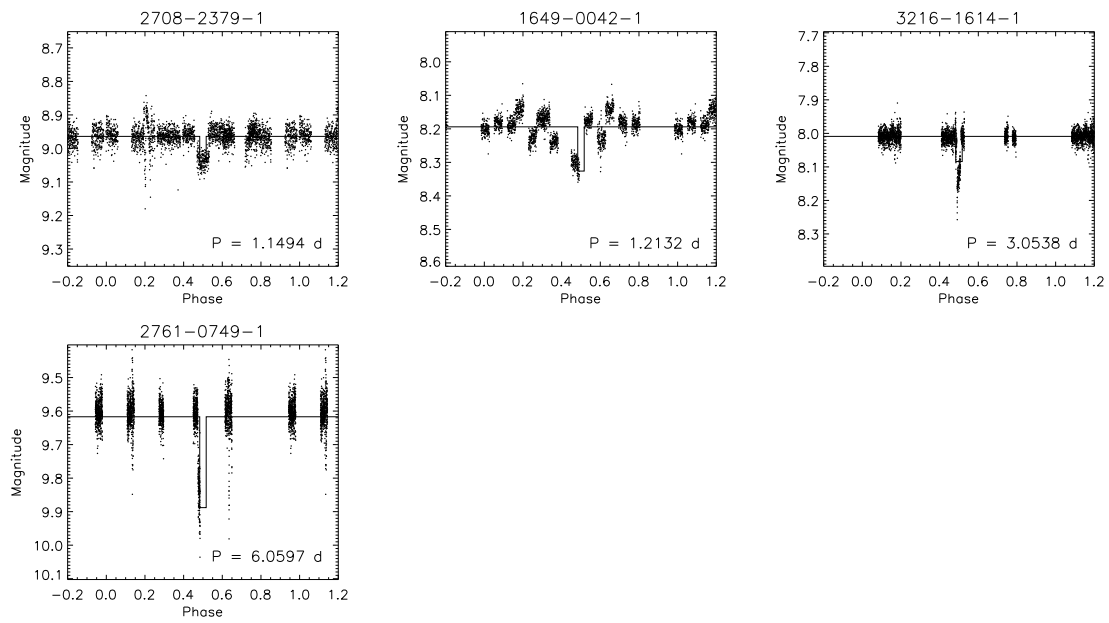


Figure 6.4: Plots of the phased lightcurves of the transit candidates for the $N_H = 30$ search case.

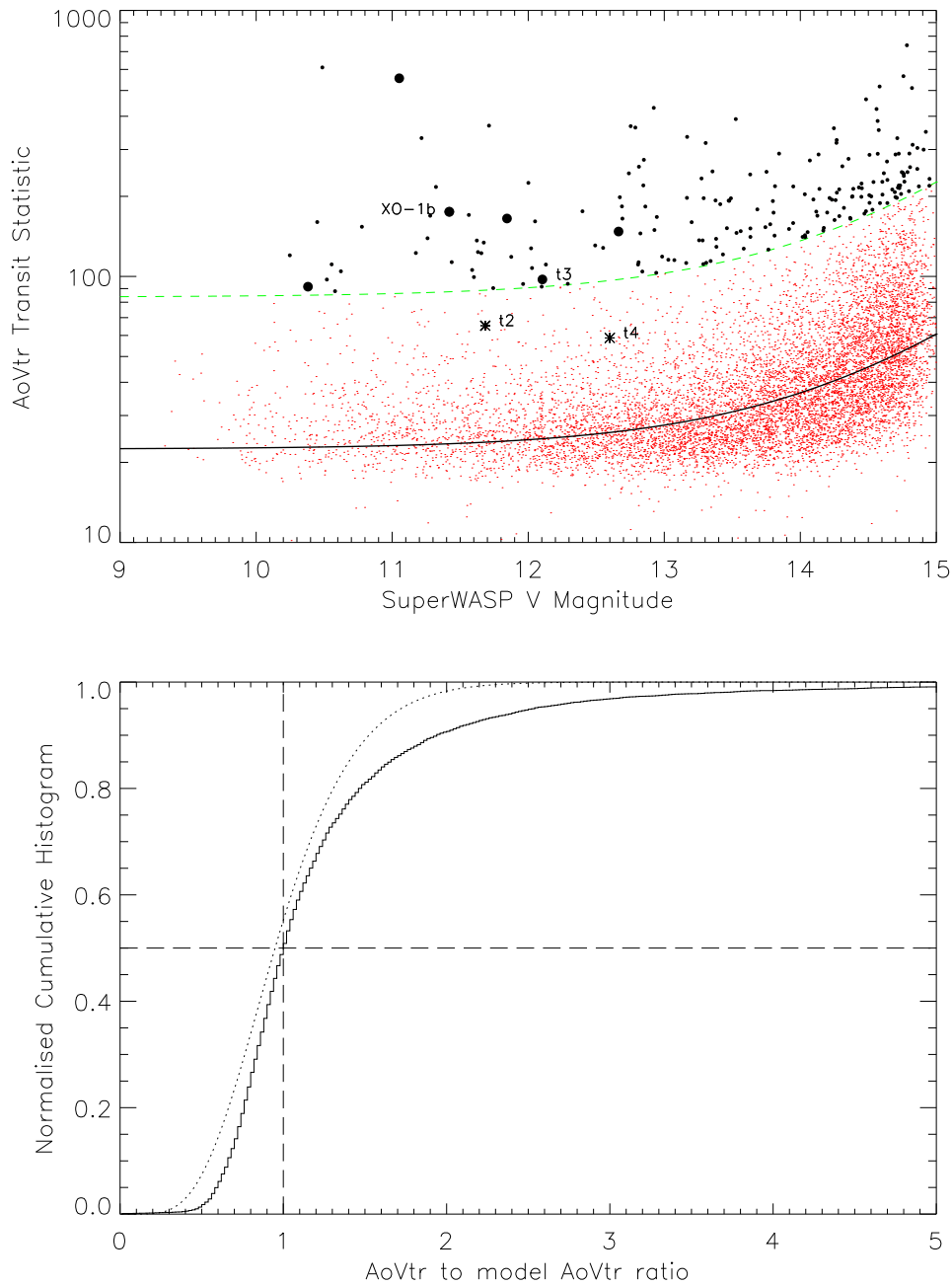


Figure 6.5: **Upper:** The AoVtr statistic plotted against lightcurve magnitude for the 9384 SuperWASP lightcurves that we search for transit candidates (red dots). This plot corresponds to the $N_H = 15$ search case. The fitted exponential function is plotted as the continuous black line, and the transit candidate threshold is plotted as the green dashed line. The set of initial transit candidates are the filled black circles, and the AoVtr statistic for the four transit candidates from K07 are labelled appropriately. The larger filled black circles represent the set of final transit candidates. **Lower:** Normalised cumulative histogram of the ratio of the AoVtr statistic to the model AoVtr statistic (solid line). We overplot the best-fit chi squared distribution with 13 degrees of freedom, where the x -axis of this distribution has been normalised by the number of degrees of freedom (dotted line).

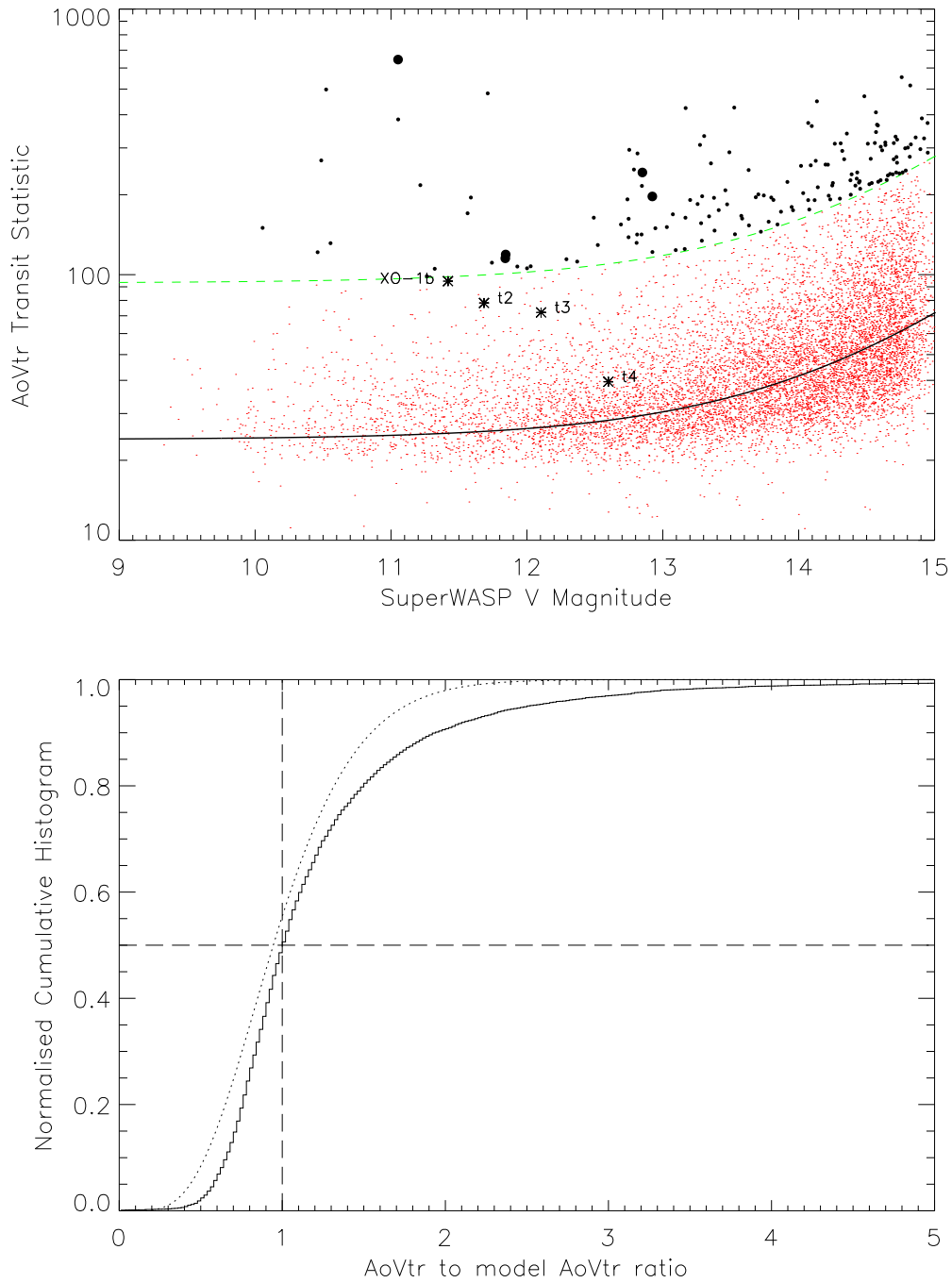


Figure 6.6: **Upper and Lower:** The same as Figure 6.5 except that these plots correspond to the $N_H = 30$ search case, and that in the lower panel the chi squared distribution (dotted line) is for 12 degrees of freedom.

6.4 Transit Candidates in the SuperWASP Lightcurve Data

We search for transits using the AoVtr statistic method in the 9384 SuperWASP lightcurves that were not selected as variable candidates in Chapter 5 (of 9671 lightcurves in total). We use exactly the same values of N_H , the same period range and the same frequency resolution as the transit search in the PASS0 lightcurves (see Section 6.3). In the upper panels of Figures 6.5 and 6.6, we plot the AoVtr statistic versus magnitude for both the $N_H = 15$ and $N_H = 30$ cases (red dots). We fit the following exponential function to the AoVtr versus magnitude diagram using a 3-sigma clip algorithm and the amoeba downhill simplex method to minimise the total of the squared residuals:

$$\text{AoVtr}(m) = A + B \exp(m - 12.75) \quad (6.2)$$

We find that for $N_H = 15$ we get $A = 22.4$ and $B = 4.04$, and that for $N_H = 30$ we get $A = 24.0$ and $B = 5.04$. The models for $\text{AoVtr}(m)$ are plotted in both the upper panels of Figures 6.5 and 6.6 as solid black lines.

In the lower panels of Figures 6.5 and 6.6 we plot the normalised cumulative histogram of the ratio of the AoVtr statistic to the model AoVtr transit statistic in Equation 6.2 (solid line). The best-fit chi squared distribution (dotted line) has 13 degrees of freedom in the $N_H = 15$ case, and 12 degrees of freedom in the $N_H = 30$ case. We choose to require a false alarm probability of 5%, which gives $T = 3.73$ for the $N_H = 15$ case, and $T = 3.88$ for the $N_H = 30$ case, using Equation 5.2 and $N = 9384$ lightcurves. Hence we choose our initial set of transit candidates by scaling up the $\text{AoVtr}(m)$ model lines by the chosen thresholds (green dashed lines) and choosing all lightcurves with the AoVtr statistic above the scaled model. The initial transit candidates are plotted on Figures 6.5 and 6.6 as filled black circles, and we find 195 initial transit candidates for the $N_H = 15$ case and 151 initial transit candidates for the $N_H = 30$ case.

In the upper panels of Figures 6.5 and 6.6, we also plot the AoVtr statistic for the four transit candidates from Table 2 in Kane et al. 2007 ([39]; from now on K07) that lie within the field of the SuperWASP observations that we analysed. These transit candidates are labelled appropriately in Figures 6.5 and 6.6. One of these transit candidates from K07 is actually the transiting planet XO-1b and we detect it in the $N_H = 15$ AoVtr search but not in the $N_H = 30$ AoVtr search (although it is very close to the threshold). It is reassuring that we confidently recover this transiting planet, especially since this detection is using only the 11 nights of SuperWASP data that we analysed.

For the transit candidate J152645.62+310204.3 from K07 (marked as “t2”), our data covers two transit events compared to the 16 transit events used to detect the transit in K07, explaining why we do not detect this event in our transit search. We present the lightcurve folded on the 1.409102 d period and epoch reported in K07 in Figure 6.7. The dip in brightness is visible, and the variations in the out-of-transit lightcurve that lead K07 to reject this candidate as a possible planet are also visible.

For the transit candidate J153135.51+305957.1 from K07 (marked as “t3”), our data covers just one transit event compared to the 10 transit events used to detect the transit in K07. However, the high quality of our lightcurve and the ~ 0.02 mag depth of the event lead it to be detected just above the detection threshold for the $N_H = 15$ transit search (the transit candidate is not detected in the $N_H = 30$ transit search). We present the lightcurve folded on the 4.467224 d period and epoch reported in K07 in Figure 6.7. Again the dip in brightness is clearly visible. K07 rejected this transit candidate because the predicted size of the transiting planet was too large ($\sim 2 R_{\text{JUP}}$).

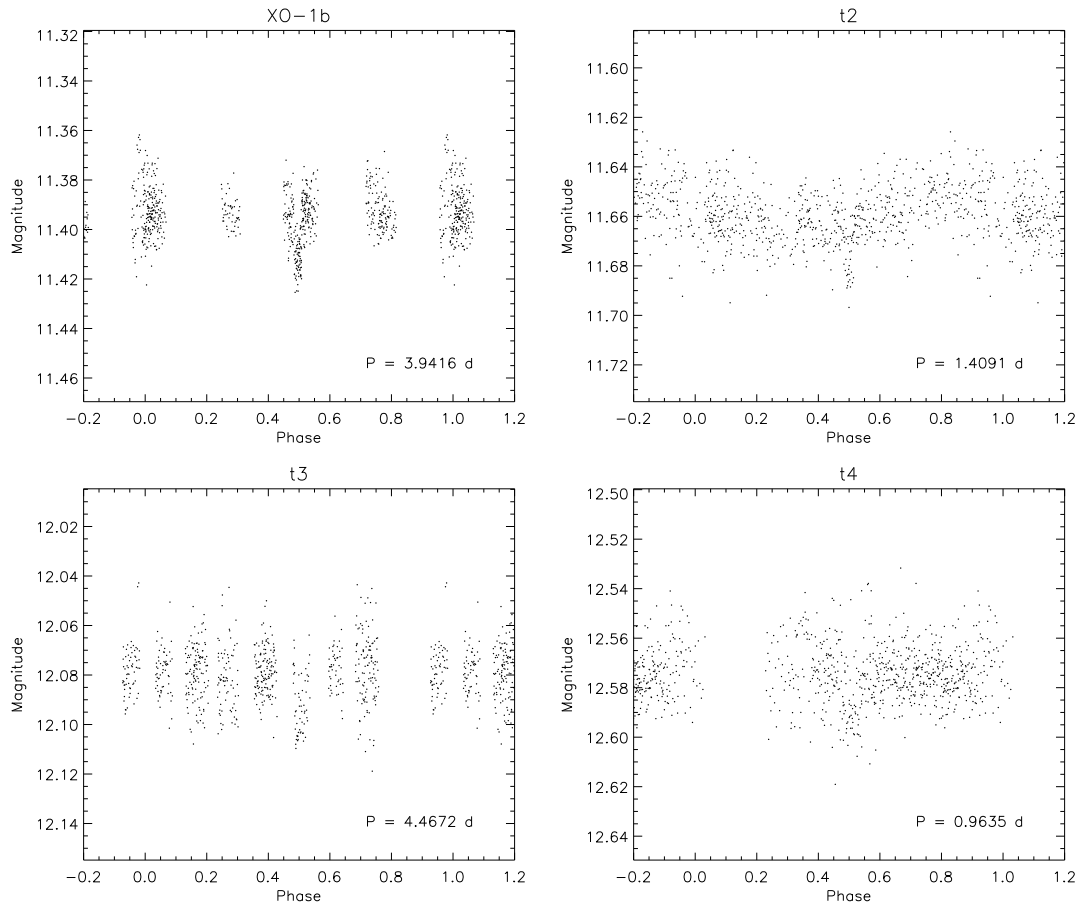


Figure 6.7: The phased lightcurves of the four transit candidates in the field of our SuperWASP data from K07. The dip at phase 0.5 is visible in all four lightcurves. However, only XO-1b and t3 were detected by our transit search because of the small number of observations that we processed. All four lightcurves are plotted with the size of the range at 0.15 mag so that the size of the dips are directly comparable.

For the transit candidate J153741.83+344433.4 (marked as “t4”), our data covers two transit events fully and one partially, compared to the 24 events used to detect the transit in K07, explaining why we do not detect this event in our transit search. We present the lightcurve folded on the 0.963514 d period and epoch reported in K07 in Figure 6.7 and one can clearly see the event. This transit candidate was rejected because of its period, but the fact that the signal is also clearly present in our reductions means that this transit candidate should be reconsidered.

We inspect all our initial transit candidates, and we remove those showing groups of outlier data points being picked up as a transit and those showing a repeating pattern with a period close to an integer or half integer. Our final set of transit candidates are plotted as phased lightcurves in Figure 6.8 for the $N_H = 15$ case and in Figure 6.9 for the $N_H = 30$ case. The scale on the magnitude axis always covers a range of 0.3 mag so that the depths of each transit candidate

are directly comparable. We also overplot the step function model corresponding to the AoVtr statistic as a continuous black line. We find 6 transit candidates for the $N_H = 15$ case and 5 transit candidates for the $N_H = 30$ case.

As we have already mentioned, we detect the transiting planet XO-1b in the AoVtr search with $N_H = 15$, but we detect it at a period of ~ 1.31 d, which is approximately one third of the real period. This is a period alias that has been detected and it occurs because of the sparse phase coverage at the real period. The same has happened for the transit candidate J153135.51+305957.1 from K07 for which our data only covers one transit event. With just one event, the period cannot be determined and so the AoVtr algorithm has picked up a spurious period of 2.7822 d. A search on SIMBAD for the remaining transit candidates does not reveal any known variables so we now discuss each transit candidate in turn.

Star lc_01296.625_01643.003_t is clearly a pulsating variable star and it is detected in both the $N_H = 15$ and $N_H = 30$ transit searches. Star lc_00180.634_01441.525_t shows a V-shaped partial eclipse on one night which is at least 0.06 mag deep and probably deeper. This star is most likely to be an eclipsing binary that we detect in both the $N_H = 15$ and $N_H = 30$ transit searches. Star lc_01265.014_01399.240_t is another pulsating variable star.

Star lc_00582.058_00840.097_t shows a small dip of ~ 0.01 mag on one night, but also shows some possible out-of-transit variations at the same level. The listing for this star in SIMBAD does not give any useful information on the spectral type of the star. More observations will be needed to fully characterise the lightcurve of this star.

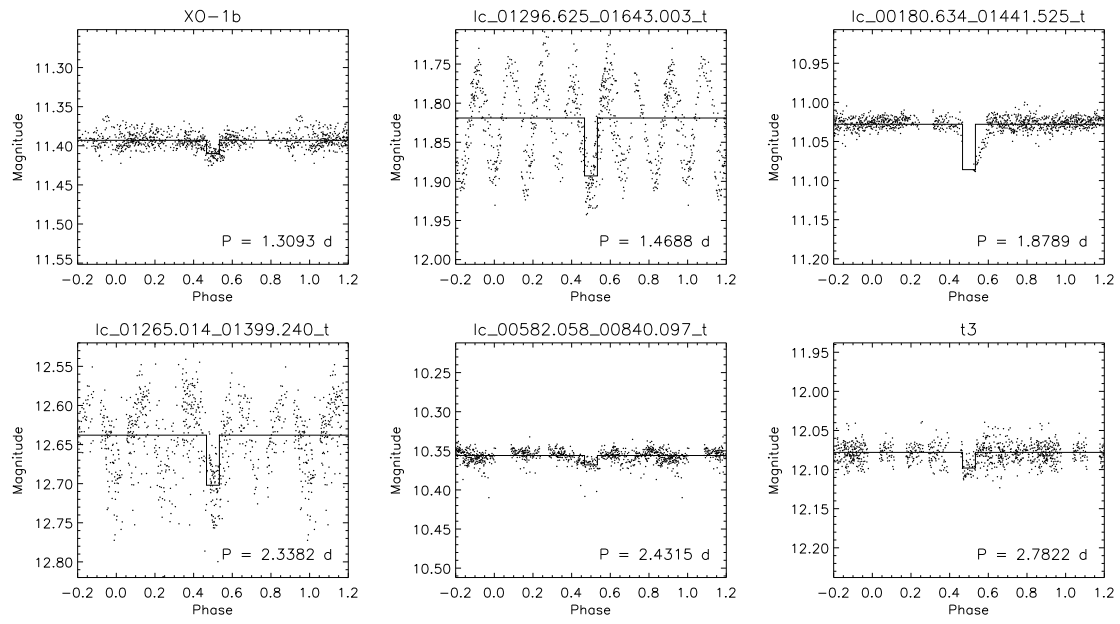
Star lc_01960.713_01889.197_t shows a number of sharp V-shaped eclipses and out-of-transit variation which means that this is most likely an eclipsing binary rather than a transiting planet (note that the AoVtr transit algorithm has clearly picked the wrong period). Star lc_00391.903_00952.326_t also shows a short duration V-shaped eclipse and out-of-transit variation indicating that it is an eclipsing binary. Finally, the suspected ‘‘dip’’ in the lightcurve of lc_00667.887_01922.180_t occurs on one night and on inspection of the lightcurve, it seems to be due to a group of noisy measurements rather than a real effect.

6.5 Conclusions

In Section 6.3 we search for transits in 10827 PASS0 lightcurves using the AoVtr statistic method. We find no convincing candidates and we would require more observations for 5 transit candidates that we could not reject based on their lightcurves. Our findings here are to be expected because we have reduced a test data set from PASS0 that consisted of 14 nights of observations with only 2 hours per night observed. A successful search for transits in PASS0 data would really need a month of observations of one field for full nights.

In Section 6.4 we search for transits in 9384 SuperWASP lightcurves again using the AoVtr statistic method. This data set is also a test data set, but with 11 full nights of observations over a 15 night period. Hence the phase coverage of the lightcurves for 1 to 10 day period planets is better than for the PASS0 lightcurves. We successfully recover the transiting planet XO-1b, but we recover only one of the other three known transit candidates from this field as reported by K07. This is due to too few transit events being observed for each transit candidate. Our search for transits gives 9 unique candidates, one of which is known as a transiting planet (XO-1b), another of

which is a K07 transit candidate, and 5 of which are obviously variable stars. One of the remaining candidates is explained as a group of noisy points that were detected and the final candidate shows a small dip, but also some possible out-of-transit variations, which means that more observations are required to determine the full properties of the lightcurve. Again we conclude that a transit search in this SuperWASP field would require many more observations in order to successfully detect a transiting planet, but with the improvements in the SuperWASP photometry that we have achieved, such a transit search will be more efficient.

Figure 6.8: Plots of the phased lightcurves of the transit candidates for the $N_H = 15$ search case.

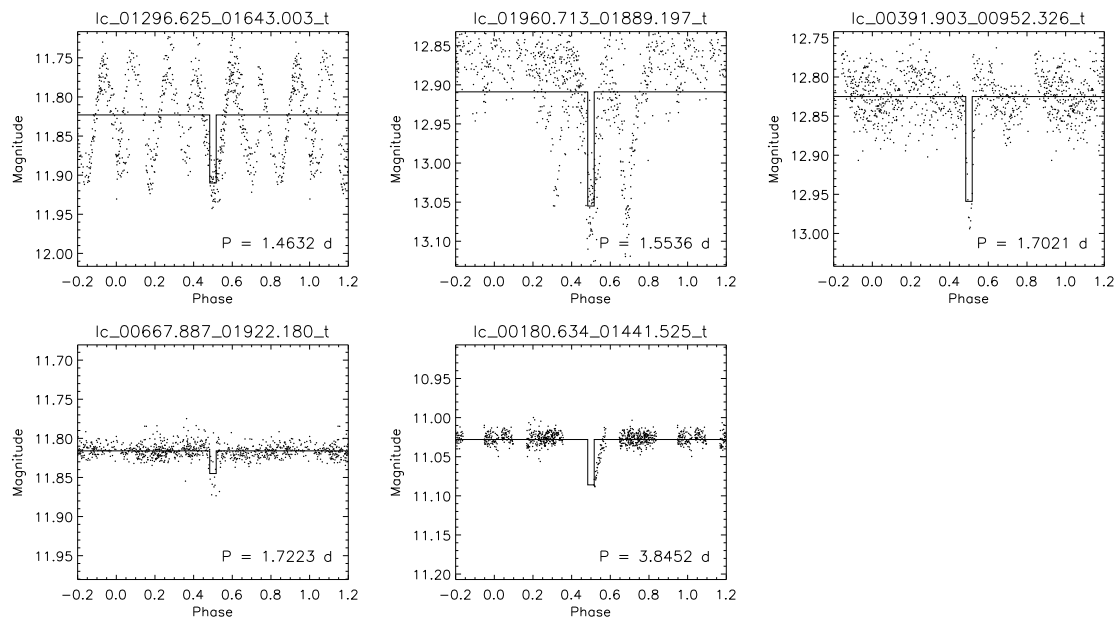


Figure 6.9: Plots of the phased lightcurves of the transit candidates for the $N_H = 30$ search case.

Chapter 7

WASP-7b and WASP-8b

7.1 Introduction

In the last few weeks of writing this thesis, the WASP consortium provided an opportunity to further prove the effectiveness of the DIA method in producing accurate and reliable lightcurves, and this time, the results of the analysis would have an impact on the published parameters of two newly discovered, but unannounced, extra-solar planets. These planets are WASP-7b and WASP-8b, discovered by photometry from the SuperWASP-South station at the South African Astronomical Observatory (SAAO), and confirmed by spectroscopy from the CORALIE spectrograph on the Euler 1.2-m telescope at the La Silla observatory in Chile.

Due to the volume of image data available for these two events, the time available only allowed the transfer of images from the 2007 season to our processing computer and the processing of these images. WASP-7b was observed in 2007 on chips DAS21 and DAS27 from 30th April until 14th October with 7008 images for DAS21 and 6971 images for DAS27. WASP-8b was observed in 2007 on chips DAS21 and DAS22 from 16th June until 28th November with 6290 images for DAS21 and 6289 images for DAS22.

7.2 Reductions

The calibration frames of master bias, master dark and master flat produced by the SuperWASP pipeline for each night were supplied by the WASP consortium. We applied these calibration frames to the raw images in the standard way (see Section 4.2) so that the preprocessing reductions were done in exactly the same way as for the SuperWASP pipeline. We also measured some useful quantities like sky background and FWHM which allowed us to identify some images to be ignored (e.g. some bias images were labelled as science images). In this way, for WASP-7b, we rejected 7 images for DAS21 and 5 images for DAS27, and for WASP-8b, we rejected 8 images for DAS21 and 8 images for DAS22. We chose a reference image for each planet and chip combination with low sky backgrounds (~ 300 ADU) and sharp FWHMs (~ 1.7 pix).

The stars WASP-7b and WASP-8b have magnitudes of ~ 9.6 and ~ 9.9 , which are at the bright end of the stars surveyed by the SuperWASP camera. Considering the analysis we have done in Chapter 4 on optimising the SuperWASP photometry, we can choose the amount of image blurring

to optimise the photometry for our specific targets since we are only interested in the lightcurve of one star from each chip. From Figure 4.7, we can see that for stars of approximately 10th magnitude the best Gaussian blur has a FWHM of 3.5 pix. Hence we blur each image using a Gaussian of FWHM 3.5 pix and we blur the reference image with a Gaussian of FWHM 3 pix. This is in contrast to the recommendation from Chapter 4 to blur each image with a Gaussian of FWHM 3 pix which is optimised for all stars in the field.

To process the order of ~ 26000 images through all stages of the PASS0 pipeline successfully within the two week deadline required considering only a 500×500 pixel cut out of each image around the position of the planet-hosting star on the reference image. Also, to speed up the processing, images were processed in batches on a few different processors in parallel.

Here we report on the reductions for WASP-7b. For DAS21 and DAS27, 2 and 5 images respectively failed to be registered with the reference image due to heavy clouds. Also, 198 images for DAS21 had pixel shifts of above 250 pixels which meant that WASP-7b did not fall within our chosen 500×500 pixel cutout. Normally these images would be successfully processed by the pipeline when considered as full images. Another complication which we only became aware of *after* having done the reductions was that the flat field calibration frames provided by the WASP consortium, and produced by the SuperWASP pipeline, contain of the order of 100 “blank” pixels with no value. The single bad pixels were flagged correctly by our PASS0 pipeline in the calibrated science images, but grew into larger bad pixel areas when each image was preblurred by a Gaussian. The reference images suffered even more because these images are preblurred by a Gaussian and then subsequently blurred by the derived kernel, and the blank pixels grow twice over. As the pointing of the SuperWASP camera drifts during each night, and from night to night, our target star sometimes drifts over a bad pixel area and we lose the photometric measurements for the affected images. Consequently we lost 465 measurements of WASP-7b for DAS21 and 32 measurements for DAS27. In future, if DIA is to be used, the “blank” pixel problem in the SuperWASP calibration frames will have to be solved, possibly by filling in the blank pixels with the median value of the surrounding pixels. At this stage we find we have 6332 lightcurve data points for DAS21 and 6929 lightcurve data points for DAS27.

Now we report on the reductions for WASP-8b. For DAS21 and DAS22, we successfully registered *all* images with the reference image for both chips. However, we then discovered that for DAS22, WASP-8b is only present in the *full* frame for 364 images. Due to the problem with blank pixels in the SuperWASP calibration frames, we lost 136 measurements of WASP-8b for DAS21 and 107 measurements for DAS22. Hence at this stage we find we have 6146 lightcurve data points for DAS21 and 257 lightcurve data points for DAS22.

The final stage of our reductions involves processing the lightcurves for each planet and chip combination through four iterations of the Tamuz algorithm (see Section 4.3.7). We firstly filter out all data points from our lightcurves for which the photometric scale factor is less than 0.3 indicating the presence of cloud cover. It was clear from inspecting a random selection of lightcurves that these low quality data points were producing unrealistic outliers of a few up to a few magnitudes. Removing these data points left us with much cleaner lightcurves with 6139 and 6735 data points for DAS21 and DAS27 respectively for WASP-7b, and 5978 and 257 data points for DAS21 and DAS22 respectively for WASP-8b. At this point we apply four iterations of the Tamuz procedure.

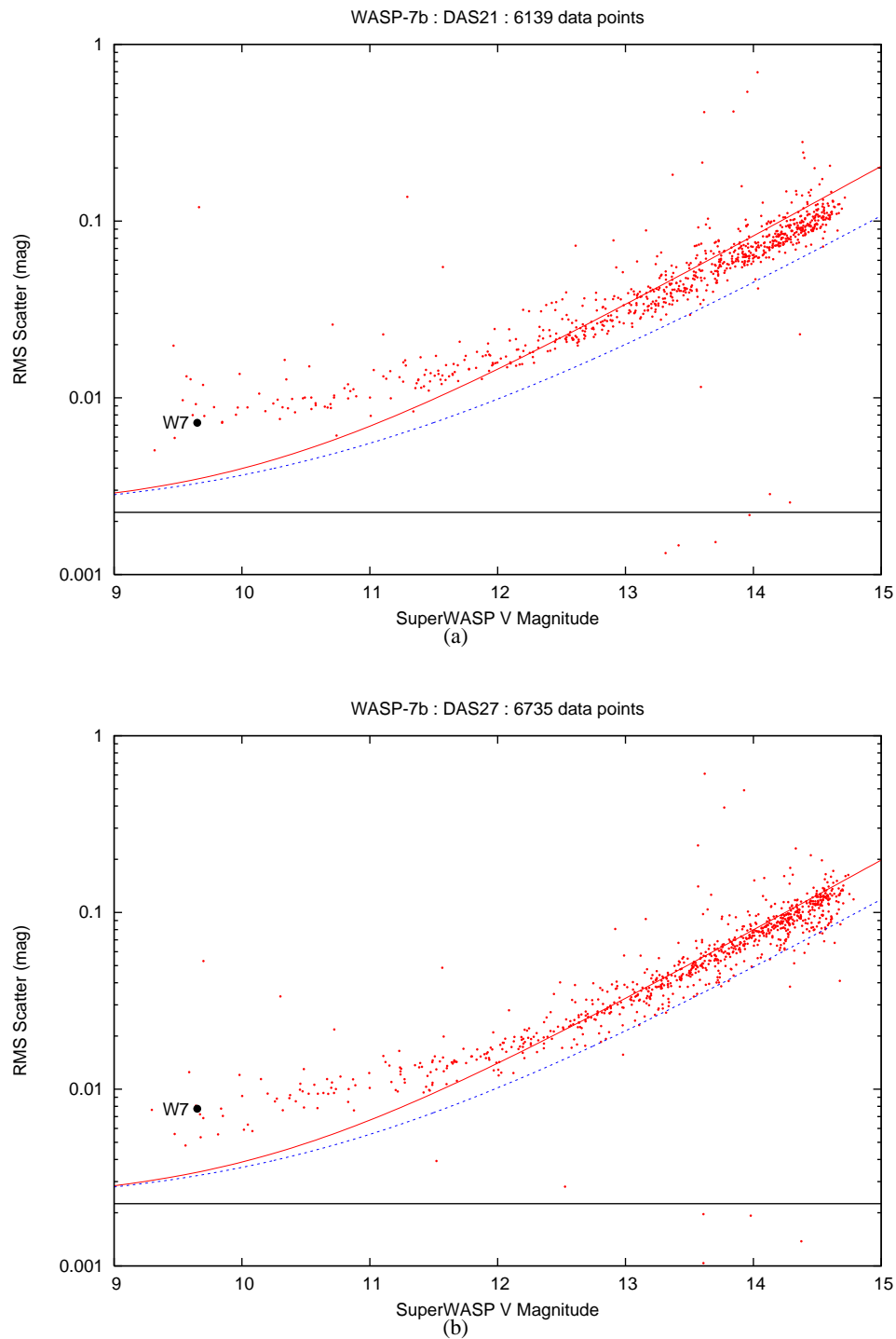


Figure 7.1: **(a)**: RMS scatter in the lightcurves against magnitude for the final set of lightcurves (Tamuz detrended) in the field of WASP-7b for DAS21. WASP-7b is marked by the solid black circle. The solid red line shows the aperture photometry limit, the dashed blue line shows the PSF photometry limit (no blurring) and the solid black line shows the scintillation noise. **(b)**: The same as (a) for the field of WASP-7b for DAS27.

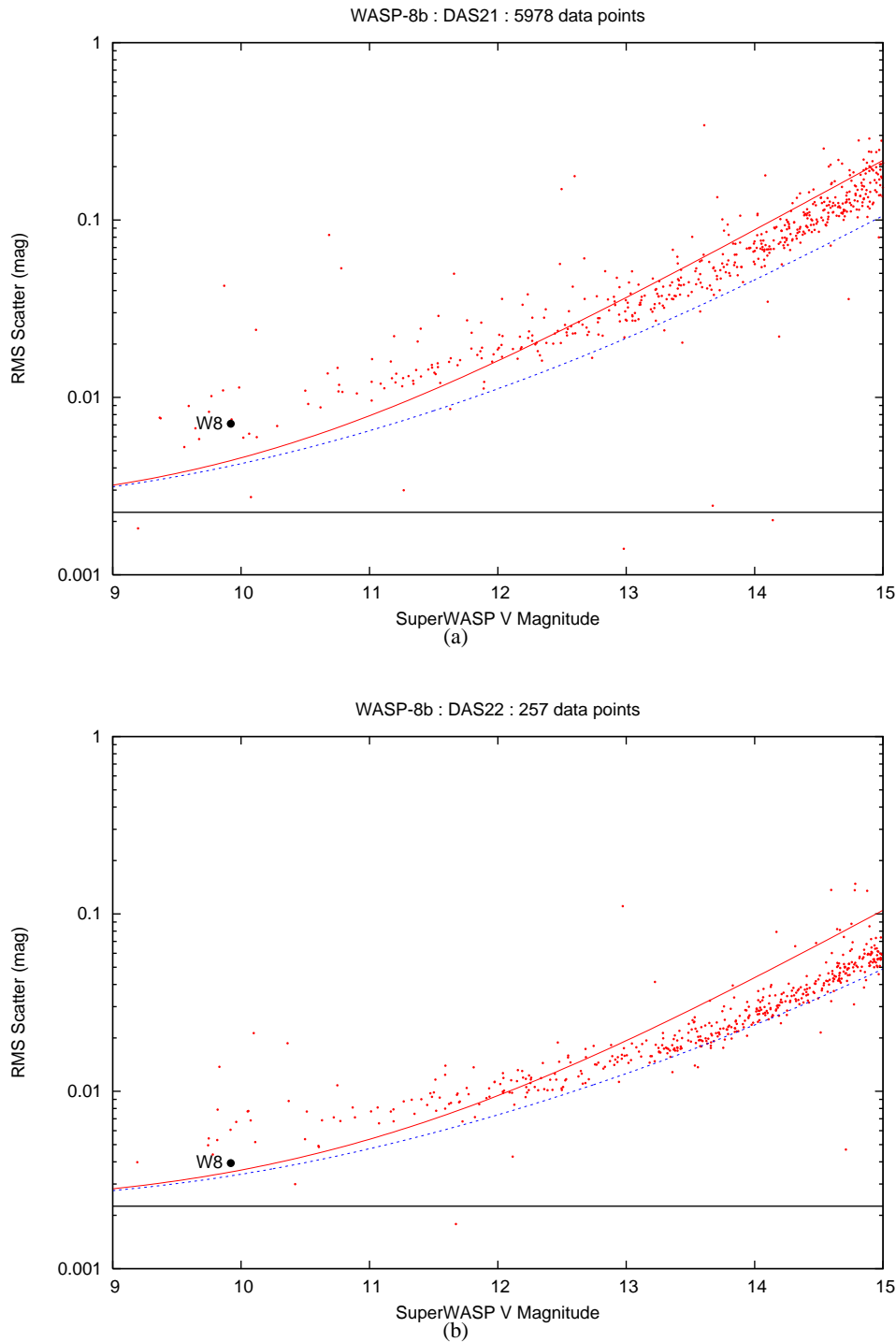


Figure 7.2: **(a)**: RMS scatter in the lightcurves against magnitude for the final set of lightcurves (Tamuz detrended) in the field of WASP-8b for DAS21. WASP-8b is marked by the solid black circle. The solid red line shows the aperture photometry limit, the dashed blue line shows the PSF photometry limit (no blurring) and the solid black line shows the scintillation noise. **(b)**: The same as (a) for the field of WASP-8b for DAS22.

Table 7.1: Comparison of the PASS0 and SuperWASP pipeline results for the WASP-7b lightcurve.

DAS21	PASS0 Pipeline RMS (mag)	SuperWASP Pipeline RMS (mag)	PASS0 Pipeline No. Data Points	SuperWASP Pipeline No. Data Points
Unfiltered lightcurves	0.0072	0.0505	6139 (+465)	6308
Matched unfiltered lightcurves	0.0071	0.0263	5604	5604
Filtered SuperWASP lightcurve	-	0.0059	-	3701
Matched unfiltered DIA lightcurve with filtered SuperWASP lightcurve	0.0057	0.0059	3700	3700
DAS27				
Unfiltered lightcurves	0.0078	0.0415	6735 (+32)	5718
Matched unfiltered lightcurves	0.0078	0.0242	5551	5551
Filtered SuperWASP lightcurve	-	0.0058	-	3867
Matched unfiltered DIA lightcurve with filtered SuperWASP lightcurve	0.0060	0.0058	3852	3852

Table 7.2: Comparison of the PASS0 and SuperWASP pipeline results for the WASP-8b lightcurve.

DAS21	PASS0 Pipeline RMS (mag)	SuperWASP Pipeline RMS (mag)	PASS0 Pipeline No. Data Points	SuperWASP Pipeline No. Data Points
Unfiltered lightcurves	0.0071	0.0680	5978 (+136)	6095
Matched unfiltered lightcurves	0.0071	0.0265	5543	5543
Filtered SuperWASP lightcurve	-	0.0063	-	4706
Matched unfiltered DIA lightcurve with filtered SuperWASP lightcurve	0.0061	0.0063	4677	4677
DAS22				
Unfiltered lightcurves	0.0039	0.0056	257 (+107)	349
Matched unfiltered lightcurves	0.0039	0.0042	243	243
Filtered SuperWASP lightcurve	-	0.0047	-	295
Matched unfiltered DIA lightcurve with filtered SuperWASP lightcurve	0.0041	0.0044	204	204

To bring our instrumental magnitudes approximately into line with the SuperWASP magnitudes we use the known magnitudes of WASP-7b and WASP-8b to derive magnitude zeropoints of $M_0 \approx 18.78, 18.88, 18.69$ and 18.75 for WASP-7b-DAS21, WASP-7b-DAS27, WASP-8b-DAS21 and WASP-8b-DAS22 respectively. We present our final RMS diagrams in Figures 7.1 and 7.2 for WASP-7b and WASP-8b respectively. In each RMS diagram the red points correspond to stars in the field and the solid black circle corresponds to the object of interest (WASP-7b or WASP-8b). Also, the solid red line shows the aperture photometry limit, the dashed blue line shows the PSF photometry limit (no blurring) and the solid black line shows the scintillation noise (calculated from Equation 2.46 assuming $d = 11.1$ cm, $X = 1.3$, $h = 2400$ m and $\Delta t = 30$ s, giving $\sigma_{\text{SCINT}} \approx 2.2$ mmag).

7.3 Comparing the Lightcurves from the PASS0 and SuperWASP Pipelines

The WASP consortium provided us with the lightcurves of WASP-7b and WASP-8b produced by the SuperWASP pipeline and calibrated by the Tamuz algorithm. Hence we can directly compare the PASS0 pipeline lightcurves to the SuperWASP pipeline lightcurves for these two planets. We would like to compare the pipelines for both accuracy *and* reliability. We assess the accuracy of the pipelines by looking at the RMS values of the lightcurves and we assess the reliability of the pipelines by looking at how many data points are produced for each lightcurve.

In Tables 7.1 and 7.2 we present the results of our pipeline comparison for each planet and chip combination (WASP-7b-DAS21, WASP-7b-DAS27, WASP-8b-DAS21 and WASP-8b-DAS22). For each case we present the RMS of the (unfiltered) lightcurves for the PASS0 and SuperWASP pipelines along with the number of data points successfully measured using each pipeline. For the PASS0 pipeline we note in brackets the number of data points lost to the “blank” pixel problem, which can be avoided by producing the appropriate calibration frames free of blank pixels. We also match the data points in the (unfiltered) PASS0 and SuperWASP pipeline lightcurves for a direct comparison of RMS values for common data points and present these results in the Tables. For the purpose of lightcurve fitting, the WASP consortium filters the SuperWASP pipeline lightcurves of WASP-7b and WASP-8b by rejecting all data points with uncertainties greater than 0.02 mag. We show the effect on the SuperWASP pipeline lightcurve RMS values and number of data points in the Tables. Finally we match the (unfiltered) PASS0 pipeline lightcurve with the filtered SuperWASP pipeline lightcurve and present these results in the Tables.

Considering the (unfiltered) lightcurves, it is clear that the PASS0 pipeline achieves much better RMS accuracy than the SuperWASP pipeline, and that the PASS0 pipeline is more reliable than the SuperWASP pipeline because all the PASS0 pipeline lightcurves have more data points than the corresponding SuperWASP pipeline lightcurves (when you take into account the data points lost to the “blank” pixel problem). Matching the unfiltered lightcurves between the pipelines does not affect the RMS accuracy of the PASS0 pipeline lightcurves, but considerably improves the RMS accuracy of the SuperWASP pipeline lightcurves, at the expense of losing of the order of $\sim 10\%$ of the data points. This suggests that the PASS0 pipeline has automatically rejected poor data points whereas the SuperWASP pipeline has included poor data points in the lightcurves, indicating further the better reliability of the PASS0 pipeline.

The WASP consortium has data on WASP-7b and WASP-8b from the 2006 observing season as well as from the 2007 observing season, and they have supplied us with appropriate ephemerides for these planets which are more accurate than what we could derive from the 2007 data alone (C. Hellier, private communication). WASP-7b has a period of $P = 4.9551026$ d with time of mid-transit $T_0 = 2453856.18820$ d, and WASP-8b has a period of $P = 8.1595457$ d with time of mid-transit $T_0 = 2454181.68318$ d. In Figures 7.3 and 7.4 we present the unfiltered phased lightcurves for both pipelines for WASP-7b and WASP-8b respectively. For WASP-7b, DAS21 data points are red and DAS27 data points are green, and for WASP-8b, DAS21 data points are red and DAS22 data points are green. For both planets, it is clear that the PASS0 pipeline lightcurve is much superior to the SuperWASP pipeline lightcurve, which suffers from very serious systematic trends and large outliers in both cases, even after the Tamuz detrending. It is questionable as to how the transiting planets were even detected using the SuperWASP data.

The filtering of the SuperWASP pipeline lightcurves by rejecting all data points with uncertainties greater than 0.02 mag is an effective way of greatly improving the RMS accuracy of the SuperWASP pipeline lightcurves. The improvement is good enough that the filtered SuperWASP pipeline lightcurves have reasonably better RMS accuracy than the (unfiltered) PASS0 pipeline lightcurves. However, the filtering process can remove anywhere from $\sim 15\%$ to $\sim 40\%$ of the data points (WASP-8b-DAS22 and WASP-7b-DAS21 respectively). This strong approach to filtering removes very important data from during the transit event.

When matching between the (unfiltered) PASS0 pipeline lightcurve and the filtered SuperWASP pipeline lightcurve, it becomes clear that the data points in the filtered SuperWASP pipeline lightcurve are contained in the PASS0 pipeline lightcurve (see Tables 7.1 and 7.2). Also, the matched lightcurves in this case are generally slightly better for the PASS0 pipeline than the SuperWASP pipeline. This leads to the conclusion that for the best balance between RMS accuracy and number of data points, the (unfiltered) PASS0 pipeline lightcurves are the best choice. It is now clear that the PASS0 pipeline successfully processes the higher S/N images to a similar accuracy as the SuperWASP pipeline and that the PASS0 pipeline processes lower S/N images to a much better accuracy than the SuperWASP pipeline.

In each panel of Figures 7.5 and 7.6 corresponding to a different planet and chip combination, we plot the filtered SuperWASP pipeline lightcurve magnitudes against the (unfiltered) PASS0 pipeline lightcurve magnitudes for the matching data points. We do this to see what level of correlation the SuperWASP pipeline aperture photometry shows with the PASS0 pipeline DIA-PSF photometry. In all four cases there is a relatively high level of correlation between the lightcurves and this conclusion is supported by the Spearman's rank correlation coefficients shown within the panels. This fact is reassuring for the reliability of the reductions from both pipelines.

At this point we mention that the WASP-7b and WASP-8b host stars are at the very bright end of the stars surveyed by the SuperWASP camera. For these stars it is theoretically possible for aperture photometry to perform as accurately as PSF photometry since the photon noise is dominated by star photons (see Figures 7.1 and 7.2). However, from Figures 7.1 and 7.2 it is clear that if WASP-7b and WASP-8b had been fainter than ~ 12 mag, then the PASS0 pipeline would have provided RMS accuracies significantly better than the SuperWASP pipeline, even after filtering the SuperWASP pipeline lightcurve, since the stars fainter than this limit have RMS accuracies better than the theoretical aperture photometry limit.

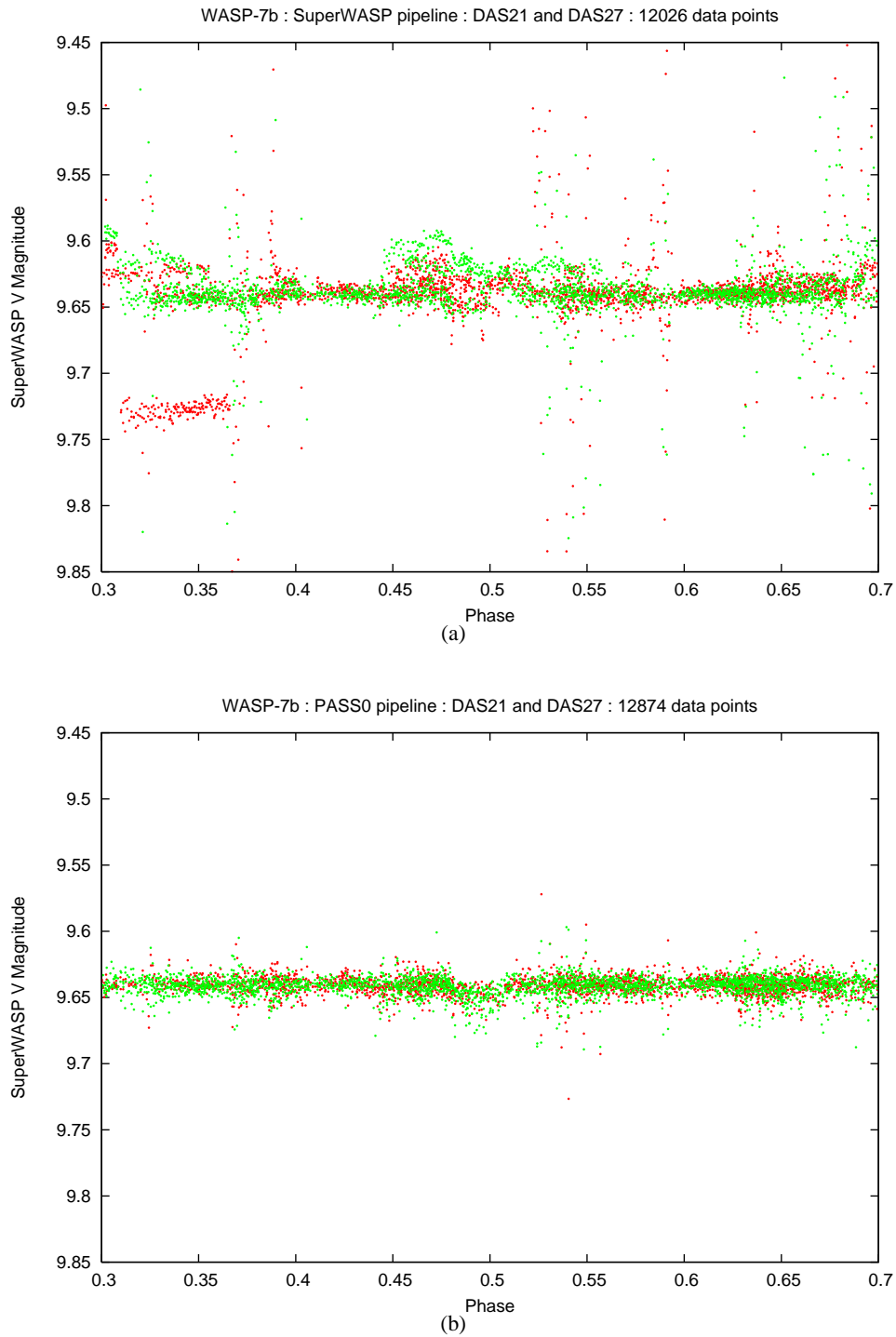


Figure 7.3: **(a)**: Plot of the phased lightcurve of WASP-7b for both chips (red points are DAS21; green points are DAS27) for the SuperWASP pipeline. **(b)**: The same as (a) but for the PASS0 pipeline.

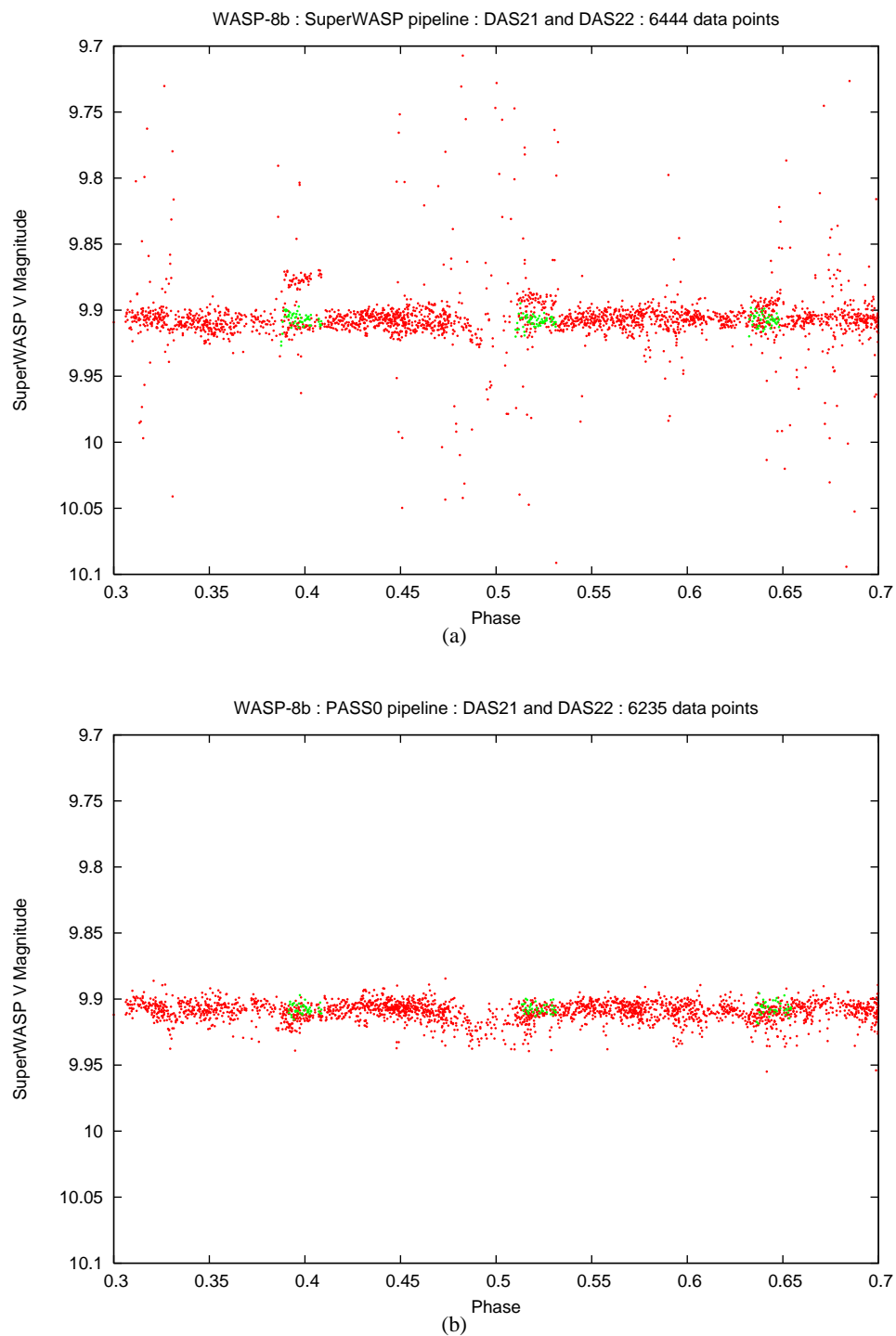


Figure 7.4: **(a)**: Plot of the phased lightcurve of WASP-8b for both chips (red points are DAS21; green points are DAS22) for the SuperWASP pipeline. **(b)**: The same as (a) but for the PASS0 pipeline.

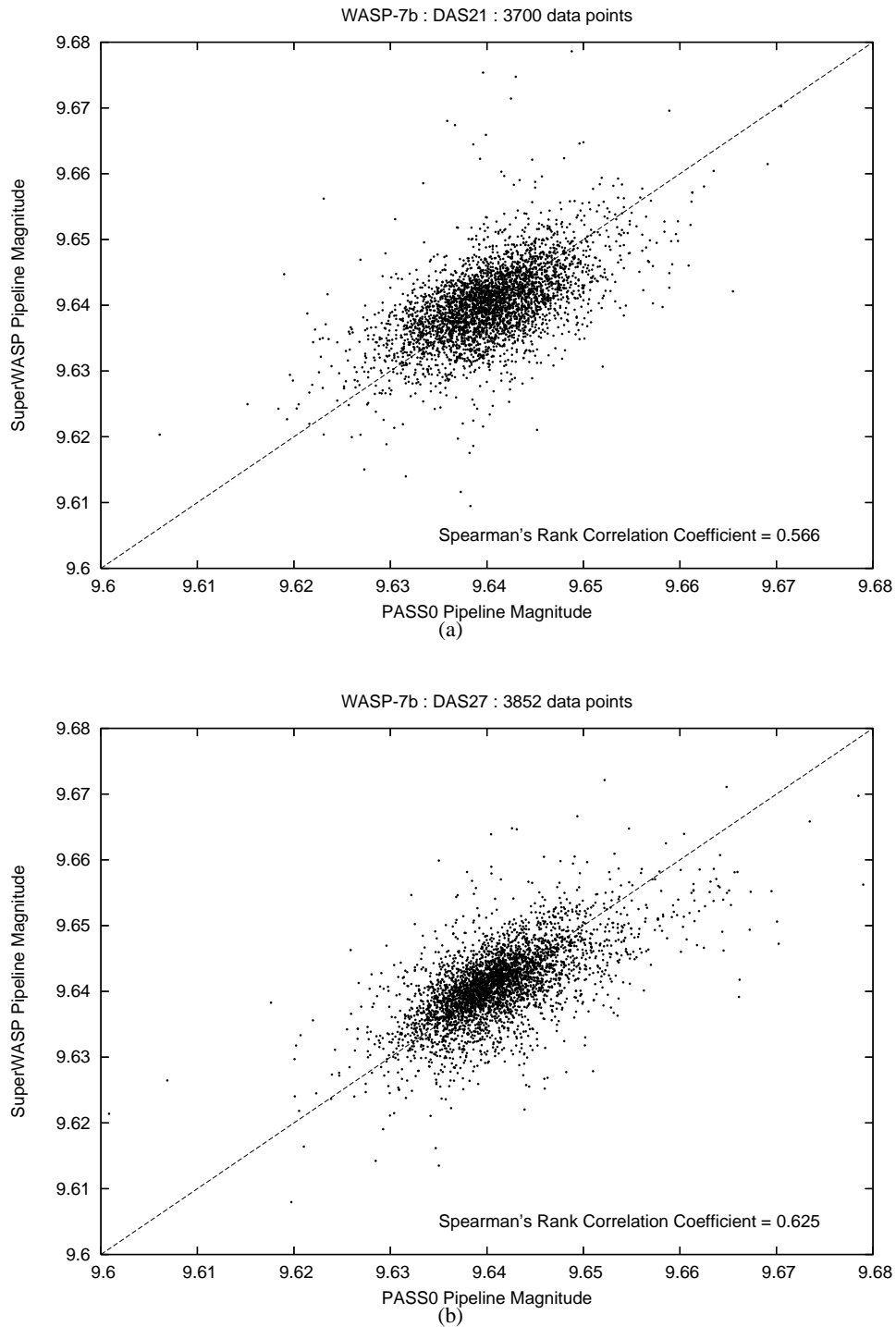


Figure 7.5: **(a)**: Plot of filtered SuperWASP pipeline lightcurve magnitudes against (unfiltered) PASS0 pipeline lightcurve magnitudes for matching data points. This case corresponds to WASP-7b and DAS21. **(b)**: The same as (a) but for WASP-7b and DAS27.

7.3. COMPARING THE LIGHTCURVES FROM THE PASS0 AND SUPERWASP PIPELINES 157

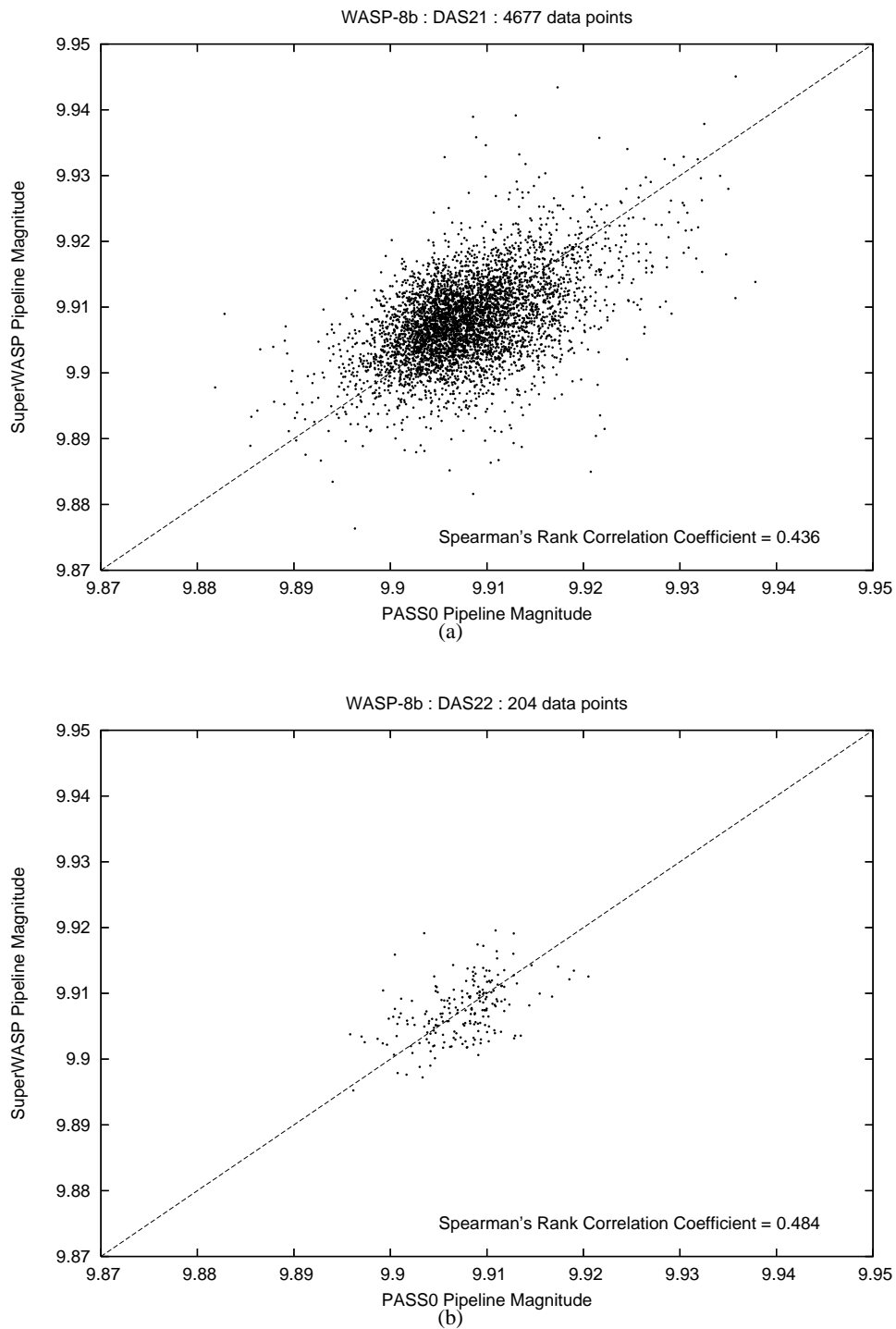


Figure 7.6: **(a)**: Plot of filtered SuperWASP pipeline lightcurve magnitudes against (unfiltered) PASS0 pipeline lightcurve magnitudes for matching data points. This case corresponds to WASP-8b and DAS21. **(b)**: The same as (a) but for WASP-8b and DAS22.

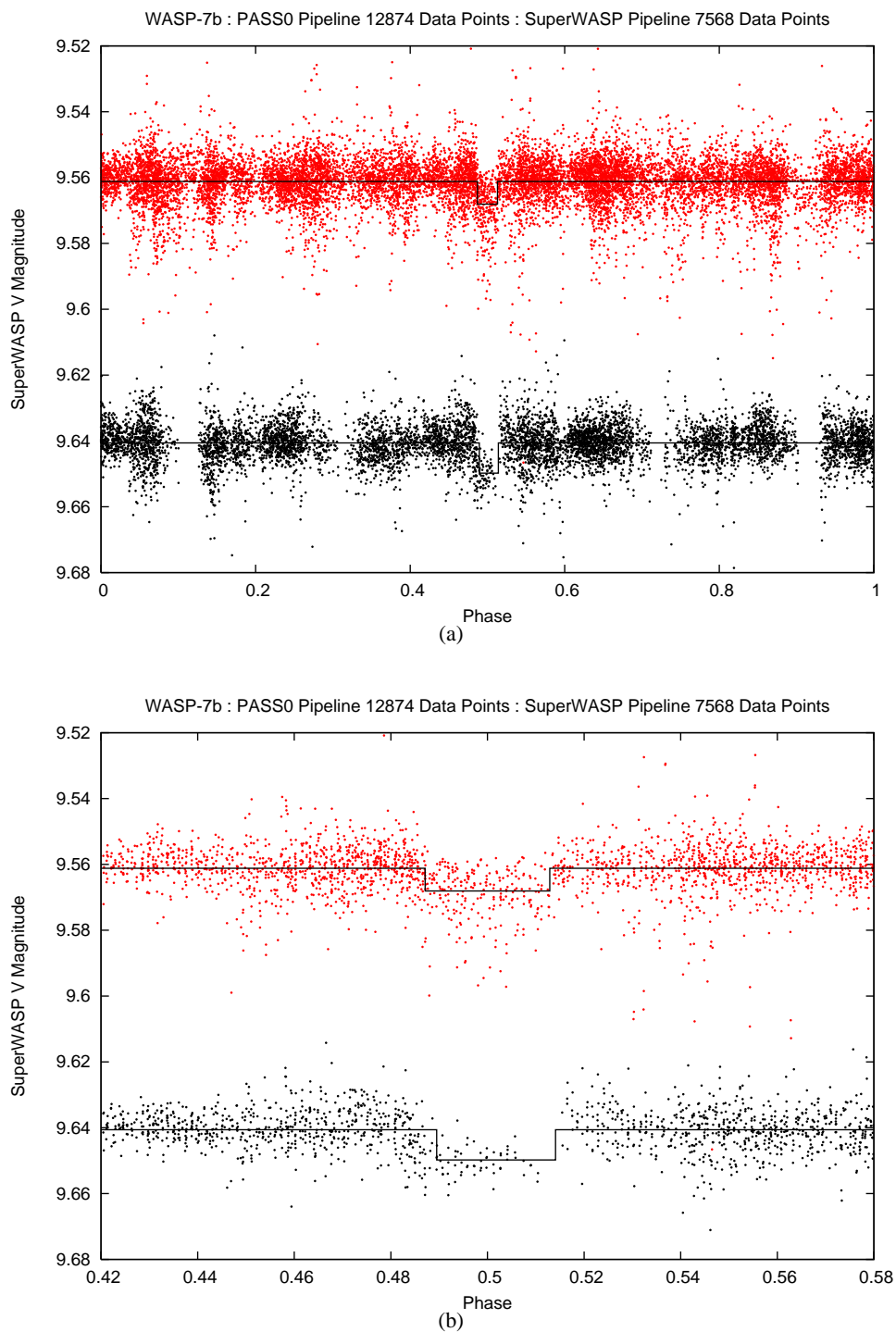


Figure 7.7: **(a)**: Plot of the phased lightcurve of WASP-7b for both chips for the filtered SuperWASP pipeline lightcurve (black points) and the (unfiltered) PASS pipeline lightcurve (red points; offset by 0.08 mag). The best fit step function model is plotted as the solid black curve for both lightcurves. **(b)**: The same as (a) but zoomed in around the transit event.

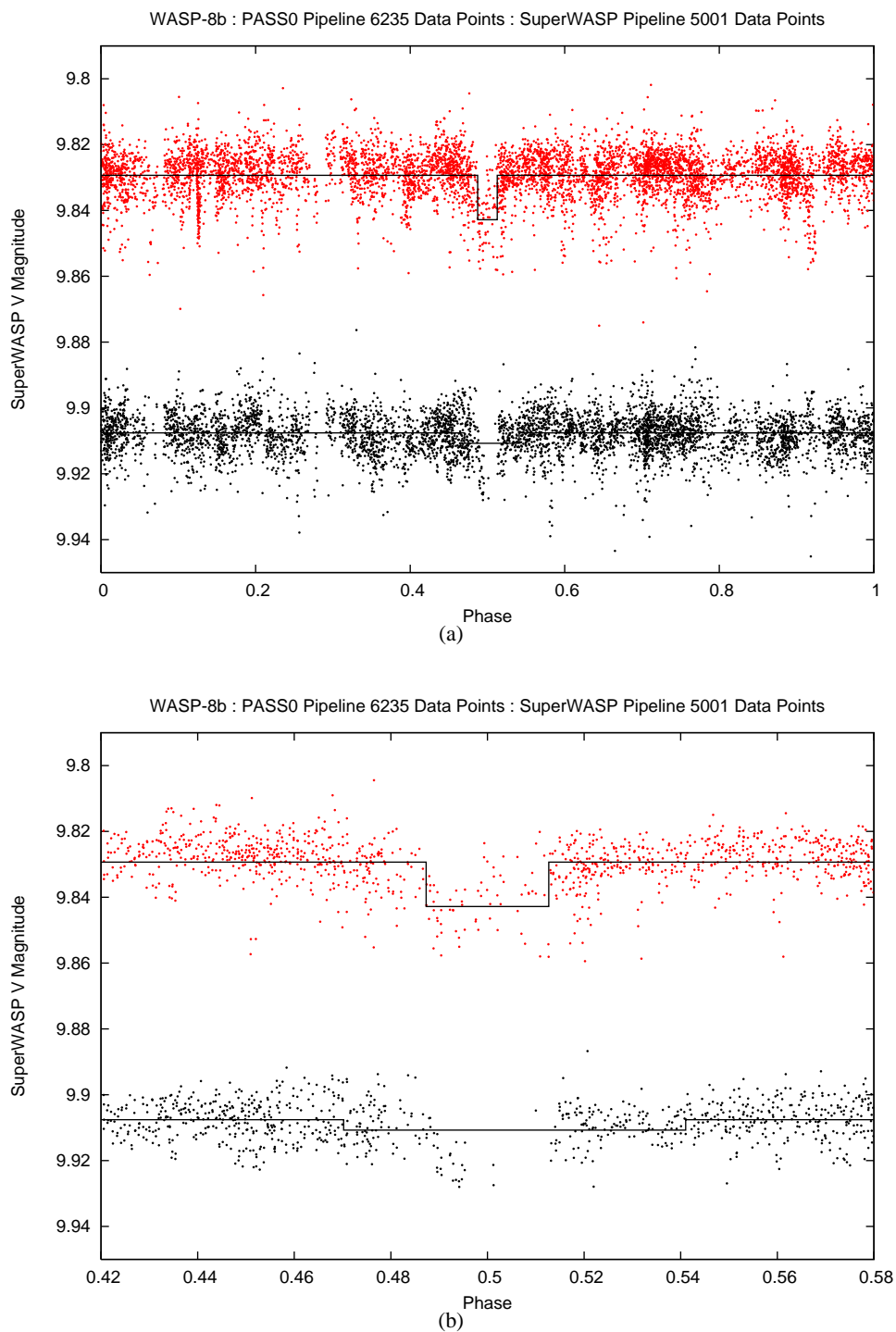


Figure 7.8: **(a)**: Plot of the phased lightcurve of WASP-8b for both chips for the filtered SuperWASP pipeline lightcurve (black points) and the (unfiltered) PASS pipeline lightcurve (red points; offset by 0.08 mag). The best fit step function model is plotted as the solid black curve for both lightcurves. **(b)**: The same as (a) but zoomed in around the transit event.

Table 7.3: The fitted planet parameters for WASP-7b and WASP-8b.

	Transit Depth (mmag)	Transit Duration (h)	Time of Central Transit (d)	Planet Radius (R_{JUP})	Orbital Inclination ($^{\circ}$)
WASP-7b PASS0 pipeline	6.9 ± 0.2	3.07 ± 0.12	2453856.15847	1.00 ± 0.10	87.8
WASP-7b SuperWASP pipeline	9.1 ± 0.5	2.93 ± 0.27	-	1.14 ± 0.12	87.4
WASP-8b PASS0 pipeline	13.5 ± 0.5	4.97 ± 0.35	2453181.65870	1.08 ± 0.11	-
WASP-8b SuperWASP pipeline	3.2 ± 0.3	13.9 ± 0.71	-	-	-

7.4 Fitting the Lightcurves from the PASS0 and SuperWASP Pipelines

In Figures 7.7 and 7.8 we plot the SuperWASP pipeline and PASS0 pipeline phased lightcurves of WASP-7b and WASP-8b respectively. The SuperWASP pipeline lightcurves (black points) have been filtered by rejecting all data points with uncertainties greater than 0.02 mag, and the PASS0 pipeline lightcurves (red points) are presented unfiltered (and offset by 0.08 mag). In Figures 7.3 and 7.4 we noticed that the time of central transit provided to us is slightly in error, and so we have redetermined it in our fits of these lightcurves. The lightcurves presented in Figures 7.7 and 7.8 have been phased on the periods provided by C. Hellier, but using our fitted times of central transit for the PASS0 lightcurves.

Firstly we consider what we can derive from the lightcurves for the planet WASP-7b. We fit a step function to the phased lightcurve with parameters of mean magnitude out-of-transit M_{OUT} , time of central transit T_0 , transit depth Δm and transit duration t_{T} . We do not take a more complicated transit model (by including limb darkening etc.) simply because the data is not of sufficient quality to extract any more than the basic transit properties. To find the best-fit parameters of the step function we step through a fine grid of transit durations from zero to 0.1 in phase and times of central transit from 0.45 to 0.55 in phase. For each trial duration and time of central transit we may calculate the out-of-transit mean magnitude M_{OUT} and the in-transit mean magnitude M_{IN} using optimal means, from which we can also derive the transit depth $\Delta m = M_{\text{IN}} - M_{\text{OUT}}$. Then for each trial duration we use the fitted parameters to calculate the χ^2 , and the best-fit solution corresponds to the step function with the smallest χ^2 .

The fitted step functions are plotted on Figure 7.7 as solid black curves. We find that for the PASS0 lightcurve, the best-fit step function has a transit duration $t_{\text{T}} = 3.07 \pm 0.12$ h and a transit depth $\Delta m = 6.9 \pm 0.2$ mmag. The error bar on Δm was calculated directly from the use of optimal means to calculate M_{OUT} and M_{IN} , and the error bar on t_{T} was estimated by measuring the size of the region where $\chi^2 - \chi_{\text{BEST}}^2 < 1$ (where $\chi^2 = \chi_{\text{BEST}}^2$ for the best-fit solution). We determine a new time of central transit of $T_0 = 2453856.15847$ d. For the SuperWASP lightcurve, the best-fit step function has a transit duration $t_{\text{T}} = 2.93 \pm 0.27$ h and a transit depth $\Delta m = 9.1 \pm 0.5$ mmag. Note that the filtering of the SuperWASP lightcurve has removed a large fraction of important data points during the transit event, which has reduced the accuracy of the derived transit parameters for the SuperWASP pipeline.

The radial velocity method provides no information on the radius of the extra-solar planet whereas the depth of a transit indicates the ratio of the radius of the planet to the radius of the star (see Equation 1.3). For small transit depths we can assume $\Delta m \approx \Delta F/F = (R_{\text{p}}/R_{\text{*}})^2$. With knowledge of the host star radius we can then estimate the planetary radius. Also the transit parameters can be used to estimate the orbital inclination using Equations 1.8 and 1.10.

The host star of WASP-7b is a main sequence star of spectral type F6 with predicted radius $\sim 1.2R_{\odot}$ and mass $\sim 1.29M_{\odot}$ (C. Hellier, private communication). We are not supplied with the uncertainties on the stellar parameters and so we take conservative estimates of 10%. Our results then provide planetary radii estimates of $\sim 1.00 \pm 0.10R_{\text{JUP}}$ for the PASS0 pipeline lightcurve, and $\sim 1.14 \pm 0.12R_{\text{JUP}}$ for the SuperWASP pipeline lightcurve (assuming $R_{\text{JUP}} \approx 0.1R_{\odot}$). We also estimate the inclination as $\sim 87.8^\circ$ for the PASS0 pipeline lightcurve and $\sim 87.4^\circ$ for the

SuperWASP pipeline lightcurve.

For the WASP-8b lightcurves, we use the same method to find the best-fit step function. The best-fit step functions are plotted on Figure 7.8 as solid black curves. For the PASS0 pipeline lightcurve we get $t_T = 4.97 \pm 0.35$ h and $\Delta m = 13.5 \pm 0.5$ mmag whereas for the SuperWASP pipeline lightcurve we get $t_T = 13.9 \pm 0.71$ h and $\Delta m = 3.2 \pm 0.3$ mmag. Again the filtering of the SuperWASP lightcurve has removed essential data points from the transit event, which has left the transit event with too few data points in order to be fit successfully, and the resulting fit is clearly wrong. We determine a new time of central transit of $T_0 = 2454181.65870$ d. The host star of WASP-8b is a main sequence star of spectral type G6 with predicted radius $\sim 0.93R_\odot$ and mass $\sim 0.93M_\odot$. (C. Hellier, private communication). Again we assume that the uncertainties on the stellar parameters are at 10%. Hence we predict a planetary radius of $\sim 1.08 \pm 0.11R_{\text{JUP}}$ from our PASS0 pipeline lightcurve, and we ignore the erroneous results from the SuperWASP pipeline lightcurve. We note that the maximum transit duration which occurs for a central transit is given by $t_T = PR_*/\pi a = 3.48$ h (see Equations 1.8 and 1.10). Hence the duration of the transit fit to the PASS0 pipeline lightcurve (and that of the SuperWASP pipeline) must be in error and we cannot estimate correctly the inclination of the transiting planet. This error has occurred because of the lack of data points available during the transit event.

7.5 Conclusions

In this chapter we have shown again how the DIA-PSF method is more accurate and reliable than the aperture photometry method for SuperWASP data. We have demonstrated this by reprocessing the SuperWASP data for 2007 for two transiting planets that will be announced soon. We find that the PASS0 pipeline lightcurves are of sufficient quality to model the transit events without further filtering of the lightcurves, whereas the SuperWASP pipeline lightcurves require heavy filtering to remove the serious systematic trends that they suffer from. However, by filtering the SuperWASP lightcurves, the number of data points is drastically reduced which means that modelling the transit event becomes much less accurate for the SuperWASP lightcurves (or even impossible in the case of WASP-8b).

We summarise the results of our fits to the various transiting planet lightcurves in Table 7.3. We derive planetary radii of $\sim 1.00 \pm 0.10R_{\text{JUP}}$ and $\sim 1.08 \pm 0.11R_{\text{JUP}}$ from the PASS0 lightcurves for WASP-7b and WASP-8b respectively. We also determine more accurate times of central transit as $T_0 = 2453856.15847$ d and $T_0 = 2454181.65870$ d for WASP-7b and WASP-8b respectively. For WASP-7b we are also able to estimate the orbital inclination as $\sim 87.8^\circ$. Our results show the potential of our PASS0 pipeline to deliver more accurate and reliable planetary parameters than the SuperWASP pipeline.

Chapter 8

Summary

In the first Chapter of this thesis we introduced the field of extrasolar planets and the methods of detection, focussing on the transit method. We described a wide selection of transit search experiments and commented on their potential and success. We discussed what information on extrasolar planets can be determined from the transit lightcurves and mentioned the achievements of various investigators in these areas. We briefly discussed planet formation theory and how this area has been shaken up by the discovery of hot Jupiters. Then we concluded with a discussion of the properties of known extrasolar planets.

The second Chapter is split into two halves. In the first half we introduce CCDs and the theory behind the digital images that they produce, including pixel noise. We look at how to calculate signal-to-noise and derive equations to calculate the noise in lightcurves made from photometric measurements on CCDs. In deriving these equations, which are central to the thesis, we consider two popular methods of photometry, aperture photometry and PSF photometry. In the second half of the Chapter we introduce the Permanent All Sky Survey (PASS) and present the calculations used in considering the design of the experiment. Having chosen the experiment parameters and hardware (U10 CCD and 50mm lens with f-stop 1.2), we consider the effects of the fixed observing mode and star trailing on our expected signal-to-noise. We find that for trailed observations there is an optimal exposure time between 10 s and 25 s depending on the observing site (and we adopt a 20 s exposure time). The optimal exposure time has been chosen to maximise the SNR of the photometric measurements and also to keep the scintillation noise to a minimum. In fact scintillation noise becomes prohibitive for pointings below elevations of 60 deg, and so to create an all-sky survey based on PASS cameras, we suggest a worldwide network of cameras pointing at or near zenith. In fact, we have shown that the most desirable site for a PASS camera is at the North or South pole, with the camera pointing towards the zenith, which minimises the star trailing. Finally we describe our PASS0 test data set of 3426 science images taken from 29th June 2005 to 16th July 2005.

In Chapter 3 we describe in detail each stage of the PASS0 pipeline that we developed in order to successfully process the trailed PASS0 images. The PASS0 pipeline uses difference image analysis to perform differential photometry on the images using the difference images. Images are processed in groups using the LST as the grouping parameter, and full lightcurves are constructed by matching up the starlists between consecutive LSTs. Due to the different reference fluxes mea-

sured for each LST, the full lightcurves require further calibration. We attempt to do this first with the string method, but find that we do not get optimal results, and so with further development of a more logical calibration model, we have developed `PASSCAL`. This program models the lightcurve corrections as functions of LST, observation night and position on the chip, and substantially improves the accuracy of the lightcurves. Our final `PASS0` lightcurves are reaching the theoretical PSF photometry limit from ~ 8.8 mag and fainter, and from ~ 8.2 mag and fainter we are doing better than the theoretical aperture photometry limit. However, at the bright end our photometry has an RMS of ~ 0.01 mag independent of magnitude which suggests that scintillation noise is dominating our photometric accuracy down to ~ 8 th magnitude. As a final proof of the viability of our experiment, we show the lightcurve of HD209458 and see that the transit signature is clearly visible.

In the fourth Chapter we describe a test data set of 688 observations from the SuperWASP experiment of a field containing the transiting planet host star XO-1 which span 15 nights. We find that the undersampled SuperWASP images, processed using the standard `PASS0` pipeline methods, produce very poor DIA photometry. We show that by preblurring the science images, we can force them to be well sampled, and hence we can extract lightcurves close to the theoretical PSF photometry limit. We test various different amounts of preblurring and find that to optimise the RMS accuracy of the lightcurves over as large a range of magnitudes as possible, we should adopt a Gaussian blur with FWHM of 3.0 pix. Our `PASS0` pipeline tests on fake image data confirm that the undersampling of the SuperWASP images is the cause of the problems for the `PASS0` pipeline photometry. As with the SuperWASP pipeline, we use the Tamuz algorithm to further calibrate the lightcurves. We find that the RMS accuracy of the lightcurves from the `PASS0` pipeline is better than the aperture photometry limit for 12th magnitude and fainter, and that the `PASS0` pipeline photometry improves on the available SuperWASP photometry by up to a factor of ~ 1.7 . We estimate that these improvements in photometric accuracy would increase the detection efficiency of the SuperWASP experiment by up to a factor of ~ 2.6 based on signal-to-noise considerations only. The DIA technique would also allow access to planet detections for visibly blended stars simply due to the nature of the technique, something that is impossible with the SuperWASP aperture photometry pipeline. Finally, we show that the `PASS0` pipeline lightcurve of XO-1 is clearly of superior quality than the corresponding SuperWASP lightcurve. Our results suggest that the SuperWASP project could more than **double** its planet detection efficiency from the adoption of the DIA pipeline instead of their standard aperture photometry pipeline.

In the fifth Chapter we present our method for searching for variable stars in both the `PASS0` and SuperWASP lightcurves from Chapters 3 and 4. We choose our variable star detection threshold to keep the false alarm probability at 5%. Where possible we derive periods for the variables using the Lomb-Scargle periodogram method, although this is particularly difficult for the `PASS0` lightcurves with only 2 hours of sampling per day. From 12853 `PASS0` lightcurves, we find 60 convincing variable star candidates, 37 of which are already known variables according to the SIMBAD astronomical database, and we are able to derive a period for 30 of them. From 9671 SuperWASP lightcurves, we find 21 convincing variable star candidates, 15 of which are already known variables according to the SIMBAD astronomical database, and we are able to derive a period for 10 of them. The results presented in this Chapter show the potential for variable star discovery and monitoring as a side-product of a wide-field transit survey.

In Chapter 6 we perform a transit search on the PASS0 and SuperWASP lightcurves from Chapters 3 and 4 using the AoVtr algorithm. We do not expect to detect any new transiting planets in these data sets since the observations do not cover a long enough time period. We choose our transit candidate detection threshold to keep the false alarm probability at 5%. From 10827 suitable PASS0 lightcurves that we search for transits, we find no convincing candidates, and we would require more observations for 5 transit candidates that we could not reject based on their available lightcurves. We do not detect the transiting planet HD209458, but this is to be expected since the observations only cover half of one transit event. From 9384 suitable SuperWASP lightcurves that we search for transits, we successfully recover the transiting planet XO-1, but we only recover one of the other three known transit candidates from this field. This is due to too few transit events being observed for each transit candidate in the test SuperWASP data set. Our search for transits in the SuperWASP lightcurves gives 9 transit candidates, one of which is XO-1, another of which is a known transit candidate, and 5 of which are obviously variable stars. One of the remaining candidates we can explain as a group of noisy data points, and the final candidate requires more observations in order to determine if the out-of-transit lightcurve shows suspected variations. We conclude that more observations of up to one month would be required in order to perform a serious transit search on the data.

In our seventh and final Chapter, we describe our attempts at reducing a full season (2007) of image data for each of the newly discovered, but not yet announced, transiting planets WASP-7b and WASP-8b. We reduced 13979 images for WASP-7b and 12579 images for WASP-8b. By applying a preblurring Gaussian of FWHM 3.5 pix to the science images (which is the most appropriate blurring for the magnitude of the host stars), we obtain a lightcurve RMS of 0.0072 mag and 0.0078 mag for each of the chips containing WASP-7b, and 0.0071 mag and 0.0039 mag for each of the chips containing WASP-8b. This may be compared to the lightcurve RMS from the SuperWASP pipeline of 0.0505 mag and 0.0415 mag for each of the chips containing WASP-7b, and 0.0680 mag and 0.0056 mag for each of the chips containing WASP-8b. It is only with heavy filtering of the SuperWASP pipeline lightcurves that the RMS values are similar to those for the lightcurves from the PASS0 pipeline. Consequently, the higher quality filtered SuperWASP pipeline lightcurve have up to 40% less data points than the PASS0 pipeline lightcurves which creates problems for estimating the correct transit parameters. From the PASS0 pipeline lightcurves we derive planetary radii of $\sim 1.00 \pm 0.10 R_{\text{JUP}}$ and $\sim 1.08 \pm 0.11 R_{\text{JUP}}$ for WASP-7b and WASP-8b respectively. We also determine more accurate times of central transit as $T_0 = 2453856.15847$ d and $T_0 = 2454181.65870$ d for WASP-7b and WASP-8b respectively. For WASP-7b we are also able to estimate the orbital inclination as $\sim 87.8^\circ$.

In this thesis, we have shown that the PASS0 experiment is a difficult challenge, but certainly has the potential for planetary discoveries, especially if it is placed at a site like the North/South Pole, where trailing is not such a problem for non-tracking observations. The difference imaging pipeline and post-calibration programs are designed to overcome the problems inherent in the non-tracking observations and we can reach close to the PSF photometry accuracy limit. We have also shown that the difference imaging analysis technique, through the pipeline we developed for the PASS0 experiment, has the potential to deliver more accurate and reliable lightcurves for the SuperWASP experiment, which will increase the efficiency of the detection algorithms, and will lead to more accurate estimates of the planetary parameters. More importantly, the implementation

of such improvements as the standard in SuperWASP data reduction could more than **double** the planet detection efficiency of the project.

Appendix A

Relation between Gaussian Sigma and FWHM

A Gaussian has an equation:

$$G(x) = A \exp\left(-\frac{x^2}{2\sigma^2}\right) \quad (\text{A.1})$$

We require the value of x at $G(x) = A/2$. Then:

$$A/2 = A \exp\left(-\frac{x^2}{2\sigma^2}\right) \quad (\text{A.2})$$

Solving for x we get:

$$x = \sigma\sqrt{2 \ln 2} \quad (\text{A.3})$$

The full-width half-maximum (FWHM) of the Gaussian is actually $2x$:

$$\text{FWHM} = 2x = 2\sigma\sqrt{2 \ln 2} \quad (\text{A.4})$$

Appendix B

Number of Effective Pixels of a Gaussian PSF

Consider Equation 2.21, which we repeat here for convenience, ignoring the time dependence for the moment:

$$\sigma_{\Delta f}^2 = \frac{1}{\sum_{x,y} P(x,y)^2 / \sigma_X^2(x,y)} \quad (\text{B.1})$$

In the case of a faint star, the sky noise σ_{SKY} dominates the pixel noise so that $\sigma_X^2(x,y) = \sigma_{\text{SKY}}^2$. So we can write:

$$\sigma_{\Delta f}^2 = \frac{\sigma_{\text{SKY}}^2}{\int_{x,y} P(x,y)^2 dx dy} \quad (\text{B.2})$$

and then define the number of effective pixels of the PSF $P(x,y)$ as:

$$N_{\text{eff}} = \frac{1}{\int_{x,y} P(x,y)^2 dx dy} \quad (\text{B.3})$$

Assume that $P(x,y)$ is a 2-dimensional Gaussian:

$$P(x,y) = \left(\frac{1}{2\pi\sigma^2} \right) \exp\left(-\frac{x^2}{2\sigma^2}\right) \exp\left(-\frac{y^2}{2\sigma^2}\right) \quad (\text{B.4})$$

Note the standard result for the integral of a Gaussian is:

$$\int_x P(x) dx = \int_x \exp\left(-\frac{x^2}{2\sigma^2}\right) dx = \sqrt{2\pi\sigma^2} \quad (\text{B.5})$$

For this case, the integral in Equation B.3 can be done as:

$$\begin{aligned} \int_{x,y} P(x,y)^2 dx dy &= \left(\frac{1}{4\pi^2\sigma^4} \right) \int_x \exp\left(-\frac{x^2}{\sigma^2}\right) dx \int_y \exp\left(-\frac{y^2}{\sigma^2}\right) dy \\ &= \frac{\sqrt{\pi\sigma^2}\sqrt{\pi\sigma^2}}{4\pi^2\sigma^4} \\ &= \frac{1}{4\pi\sigma^2} \end{aligned} \quad (\text{B.6})$$

Therefore:

$$N_{\text{eff}} = 4\pi\sigma^2 \quad (\text{B.7})$$

Using Equation A.4 we get:

$$N_{\text{eff}} = \frac{\pi[\text{FWHM}]^2}{2 \ln 2} \quad (\text{B.8})$$

Appendix C

Useful Equations

Definition of chi-squared:

$$\chi^2 = \sum_i \left(\frac{X_i - M_i}{\sigma_i} \right)^2 \quad (\text{C.1})$$

where X_i are the data, M_i are the model or expected values and σ_i are the uncertainties.

Optimal average formula:

$$M = \frac{\sum_i \left(\frac{X_i}{\sigma_i^2} \right)}{\sum_i \left(\frac{1}{\sigma_i^2} \right)} \quad (\text{C.2})$$

where M is the optimal average, X_i are the data and σ_i are the uncertainties.

Optimal scaling formula:

$$f = \frac{\sum_i \left(\frac{X_i P_i}{\sigma_i^2} \right)}{\sum_i \left(\frac{P_i^2}{\sigma_i^2} \right)} \quad (\text{C.3})$$

where f is the optimal scale factor, X_i are the data, P_i are the pattern to be scaled and σ_i are the uncertainties.

Step function:

$$m(x) = \begin{cases} m_{\text{IN}} & \text{for } 0.5 - t_{\text{T}}/2 < x < 0.5 + t_{\text{T}}/2 \\ m_{\text{OUT}} & \text{otherwise} \end{cases} \quad (\text{C.4})$$

where $m(x)$ is the magnitude as a function of phase x , t_{T} is the transit duration in units of phase, m_{IN} is the magnitude in-transit and m_{OUT} is the magnitude out-of-transit.

Acknowledgements

I would like to thank my wife Shaikha Alsubai for her full support during my long journey to the end of my PhD and for being so patient with me along the way. I would also like to thank my supervisor Keith Horne for being so helpful and encouraging me even in the most difficult times. Finally I would like to thank all the English advisors for proof reading my English in this thesis, either from the University of Qatar or from St. Andrews University.

Bibliography

- [1] Agol E. & Steffen J.H., 2007, MNRAS, 374, 941
- [2] Alard C. & Lupton R., 1998, ApJ, 503, 325
- [3] Alard C., 2000, A&AS, 144, 363
- [4] Alonso R. et al., 2004, ApJ, 613, 153
- [5] Bakos G.A. et al., 2002, PASP, 114, 974
- [6] Beaulieu J.P. et al., 2006, Nature, 439, 437
- [7] Biller B.A. et al., 2006, ApJL, 641, 141
- [8] Bond I.A. et al., 2004, ApJL, 606, 155
- [9] Bond I.A. et al., 2001, MNRAS, 327, 868
- [10] Boss A., 1995, Science, 267, 360
- [11] Bramich D.M. et al., 2005, MNRAS, 359, 1096
- [12] Brown T., 2001, ApJ, 553, 1006
- [13] Caldwell D.A. et al., 2003, IAU Special Session 2, Astronomy in Antarctica, 2
- [14] Charbonneau D., Brown T., Latham D. et al., 2000, ApJL, 529, 45
- [15] Charbonneau D. et al., 2002, ApJ, 568, 377
- [16] Chauvin G. et al, 2004, A&AL, 425, 29
- [17] Chauvin G. et al, 2004, A&A, 438, 29
- [18] Cody A.M. & Sasselov D., 2002, ApJ, 569, 451
- [19] Collier Cameron A. et al., 2006, MNRAS, 373, 799
- [20] Deeg H.J., Alonso R., Belmonte J.A., **Alsubai K.**, Horne K. & Doyle L., 2004, PASP, 116, 985

- [21] Deming D. et al., 2005, *Nature*, 434, 740
- [22] Dominik M., Horne K. & Bode M.F., 2006, *Astronomy & Geophysics*, 47, 3.25
- [23] Fischer D. & Valenti J., 2005, *ApJ*, 622, 1102
- [24] Gililand R., Brown T., Guhathakurta P. et al., 2000, *ApJ*, 545, L47
- [25] Gonzalez G., 1997, *MNRAS*, 285, 403
- [26] Gonzalez G., 1998, *A&A*, 334, 221
- [27] Gould A. et al., 2006, *ApJL*, 644, 37
- [28] Guillot T. et al., 1996, *ApJL*, 459, 35
- [29] Gullixson C., in: Howell S. (Ed.) *Astronomical CCD Observing and Reduction Techniques*, ASP Conference Series Vol. 23, 1992, p. 130
- [30] Harrington J. et al., 2006, *Science*, 314, 623
- [31] Halbwachs J.L., Arenou F., Mayor M. et al., 2000, *A&A*, 355, 581
- [32] Henry G., Marcy G., Butler P. et al., 2000, *ApJL*, 529, 41
- [33] Hog E. et al., 2000, *A&A*, 355, L27
- [34] Holman M.J. et al., 2006, *ApJ*, 652, 1715
- [35] Israelian G. et al, 2001, *Nature*, 411, 163
- [36] Kane S.R. et al., 2004, *MNRAS*, 353, 689
- [37] Kane S.R. et al., 2005, *MNRAS*, 362, 117
- [38] Kane S.R. et al., 2005, *MNRAS*, 364, 1091
- [39] Kane S.R. et al., 2007, astro-ph/0711.2581
- [40] Kiss L.L. & Bedding T.R., 2005, *MNRAS*, 358, 883
- [41] Knutson H.A. et al., 2007, *ApJ*, 655, 564
- [42] Kovacs G., Zucker S. & Mazeh T., 2002, *A&A*, 391, 369
- [43] Lafler J. & Kinman T.D., 1965, *ApJS*, 11, 216
- [44] Lin D., Bodenheimer P. & Richardson D.C., 1996, *Nature*, 380, 606
- [45] Lissauer J., 1995, *Icarus*, 114, 217
- [46] Lomb N.R., 1976, *Ap&SS*, 39, 447

- [47] Mandel K. & Agol E., 2002, *ApJL*, 580, 171
- [48] Mayor M. & Udry S., in: Garzon P., Eiroa C., de Winter D. & Mahoney T.J. (Eds.) *Disk, Planetesimals and Planets*, ASP Conf. Ser., 2000
- [49] Mazeh T., Naef D., Torres G. et al., 2000, *ApJ*, 529, L41
- [50] McCullough P.R. et al., *PASP*, 117, 783
- [51] McCullough P.R. et al., 2006, *ApJ*, 648, 1228
- [52] Mochejska B.J. et al., 2002, *AJ*, 123, 3460
- [53] Mojzsis S.J. et al., 1996, *Nature*, 384, 55
- [54] Monet D.G. et al., 2003, *AJ*, 125, 984
- [55] Mortara L. & Fowler A., in: *Solid State Imagers for Astronomy*, Proc. SPIE, 290, 28
- [56] Murray N. et al., 1998, *Science*, 279, 69
- [57] Neuhäuser R. et al., 2005, *A&AL*, 345, 13
- [58] Newberry M., 1991, *PASP*, 103, 122.
- [59] O'Leary M.H., 1981, *Photochemistry*, 20, 55
- [60] Pepper J. et al., 2007, *PASP*, 119, 923
- [61] Pepper J. et al., 2007, astro-ph/0709.2728
- [62] Pollacco D.L. et al., 2006, *PASP*, 118, 1407
- [63] Pollack J.B. & Bodenheimer P., in: Atreya S., Pollack J.K. & Matthews M.S. (Eds.) *Origin and Evolution of Planetary and Satellite Atmospheres*, University of Arizona Press, Tucson, 1989, p. 564
- [64] Pojmanski G., 2001, in: Chen W.P., Lemme C. & Paczynski B. (Eds.) *Small Telescope Astronomy on Global Scales*, IAU Colloq. 183, ASP Conf. Series 246, p. 53
- [65] Pojmanski G., 2002, *Acta Astronomica*, 52, 397
- [66] Pojmanski G., 2003, *Acta Astronomica*, 53, 341
- [67] Quine B. & Durrant-Whyte H.F., 1996, in: Masten M.K. & Stockum L.A. (Eds.) *Acquisition, Tracking and Pointing X*, Proc. SPIE Vol. 2739, p. 351
- [68] Robin A.C., Reyle C., Derriere S. & Picaud S., 2003, *A&A*, 409, 523

- [69] Sackett P.D., in: Mariotti J.M. & Alloin D. (Eds.) *Planets Outside the Solar System: Theory and Observations*, Boston : Kluwer Academic Publishers, 1999, p. 189
- [70] Sahu K. et al., 2006, *Nature*, 443, 534
- [71] Santos N.C., Israelian G. & Mayor M., 2000, *A&A*, 363, 228
- [72] Santos N.C., Israelian G. & Mayor M., 2001, *A&A*, 373, 1019
- [73] Scargle J.D., 1982, *ApJ*, 263, 835
- [74] Schwarzenberg-Czerny A. & Beaulieu J.-Ph., 2006, *MNRAS*, 365, 165
- [75] Schwarzenberg-Czerny A., 1989, *MNRAS*, 241, 153
- [76] Shu P., Najita J., Ostriker E. et al., 1994, *ApJ*, 429, 781
- [77] Stetson P.B., 1987, *PASP*, 99, 191
- [78] Street R.A. et al., 2002, *MNRAS*, 330, 737
- [79] Street R.A. et al., in: Deming D. & Seager S. (Eds.) *Scientific Frontiers in Research on Extrasolar Planets*, ASP Conference Series, 2003, Vol. 294
- [80] Sotin C., Grasset O. & Mocquet A., 2007, *Icarus*, 191, 337
- [81] Tamuz O., Mazeh T. & Zucker S., 2005, *MNRAS*, 356, 1466
- [82] Thorett S. et al., 1999, *ApJ*, 523, 763
- [83] Tinetti G., 2007, *Nature*, 448, 169
- [84] Tingley B., 2003, *A&A*, 403, 329
- [85] Tingley B., 2003, *A&A*, 408, 5
- [86] Torres G., Konacki M., Sasselov D.D. & Jha S., 2004, *ApJ*, 614, 979
- [87] Trilling D., Benz W., Guillot T. et al., 1998, *ApJ*, 500, 428
- [88] Udalski A. et al., 1994, *Acta Astronomica*, 44, 227
- [89] Udalski A. et al., 2002, *Acta Astronomica*, 52, 1
- [90] Udalski A. et al., 2005, *ApJL*, 628, 109
- [91] Vestrand W.T. et al., in: Kibrick R.I. (Ed.) *Advanced Global Communications Technologies for Astronomy II*, Proceedings of the SPIE, 2002, vol. 4845, p. 126
- [92] Vidal-Madjar A. et al., 2003, *Nature*, 422, 143

- [93] Vidal-Madjar A. et al., 2004, ApJ, 604, 69
- [94] Weidenchilling S.J. & Marzari F., 1996, Nature, 384, 619
- [95] Wright J.T., 2005, PASP, 117, 657
- [96] Wolszczan A. & Frail D.A., 1992, Nature, 355, 145
- [97] Wuchterl G., in: Paresce F. (Ed.) *Science with the VLT Interferometer*, ESO Astrophys. Symp., Springer, 1997, p. 64
- [98] Wuchterl G., 1999, BAAS, 31, 36.07
- [99] Young A.T., 1967, AJ, 72, 747
- [100] Zapatero Osorio M.R., Bejar V., Martin E. et al., 2000, Science, 290, 103
- [101] COROT Press Release: <http://exoplanet.eu/papers/PR-CoRoT-1.pdf>
- [102] The Extrasolar Planets Encyclopedia, J.P. Schneider, <http://exoplanet.eu/>.
- [103] pinpoint, <http://pinpoint.dc3.com>
- [104] <http://jilawwww.colorado.edu/pja/planets/extrasolar.html>